

Microwave Plasma
Technology for CO₂ Utilization
Advancing Sustainable Solutions
from Earth to Mars

Elizabeth Rose Mercer

Supervisor Prof. Dr. Annemie Bogaerts

Microwave Plasma Technology for CO₂ Utilization: Advancing Sustainable Solutions from Earth to Mars

Thesis Submitted for the Degree of

Doctor of Philosophy in Science

Defended by

Elizabeth Rose Mercer
Faculty of Science, Department of Chemistry
UNIVERSITY OF ANTWERP

July 4, 2025

Supervisor

Prof. Dr. Annemie Bogaerts



ORCID: 0000-0001-8212-5488

Members of the Jury

Individual Doctoral Commission

Prof. Dr. Vera Meynen, Chair

Laboratory of Adsorption and Catalysis (LADCA) - University of Antwerp

Prof. Dr. Ir. Patrice Perreault

Laboratory for the Electrification of Chemical Processes & Hydrogen (ElectriffHY) and

The Electrification Institute – University of Antwerp

Dr. Georgi Trenchev

Plasma Lab for Applications in Sustainability and Medicine (PLASMANT) and

D-CRBN - University of Antwerp

External Members

Prof. Dr. Ir. Richard van de Sanden

Plasma for Solar Fuel Devices (PSFD) - Dutch Institute for Fundamental Energy Research

Eindhoven Institute for Renewable Energy Systems (EIRES) – Eindhoven University of Technology

Dr. Ramses Snoeckx

Plasma & Coating Group – Swiss Federal Laboratories for Materials Science and Technology (Empa)

Prof. Dr. Ir. Gerard van Rooij

Plasma Chemistry Group, Circular Chemical Engineering - Maastricht University

Funding



Funded by the European Union



Established by the European Commission



The work described in this thesis was supported by the European Research Council (ERC) under the European Union's Horizon 2020 research and innovation program (grant agreement No 810182 – SCOPE ERC Synergy project), and partially by the European Space Agency (ESA) Open Science Innovation Platform study (contract no. 4000137001/21/NL/GLC/ov).



Declaration

The Ph.D. researcher and supervisor declare that the Ph.D. research was conducted according to the principles of scientific integrity, as mentioned in the general Ph.D. regulations and charter for Ph.D. researchers of UAntwerp and the integrity charter for Ph.D. researchers and supervisors affiliated with the University of Antwerp.

Copyright © 2025 E.R. Mercer

All rights reserved. No part of the publication may be reproduced in any form by print, photoprint, microfilm, or any other means without written permission from the author.

Cover Artwork by Cathrin Machin Contemporary Art ©

Ghosts of the Universe

Website: https://catmachin.com/

Summary

This thesis investigates microwave-based plasma technology for carbon utilization, with applications ranging from terrestrial CO₂ conversion to Martian atmosphere processing for in-situ resource utilization. The research explores how thermal management strategies and flow configurations influence the performance of microwave plasma. Key innovations include demonstrating that preheating CO₂ can increase conversion at near-atmospheric pressure by influencing plasma contraction dynamics and expanding the reactive volume. The work further examines post-plasma reactive quenching with CH₄ using a dual injection system in a CO₂ microwave plasma, showing enhancement to CO₂ conversion, with a comparison to conventional (admixing) dry reforming of methane. Through comprehensive spectroscopic analysis, temperature mapping, and product characterization, this work enhances fundamental understanding of microwave plasma chemistry and develops practical strategies for improving conversion. Additionally, we investigated microwave plasma conversion at near Martian atmosphere (25 mbar), demonstrating the technology's potential for space applications. The findings provide valuable insights for designing nextgeneration plasma reactors that can contribute to a circular carbon economy on Earth and support future human exploration of Mars.

Samenvatting

Dit proefschrift onderzoekt microgolfgebaseerde plasmatechnologie voor het benutten van koolstof, met toepassingen variërend van CO₂ conversie op aarde tot het benutten van de Marsatmosfeer voor "In-situ Resource Utilization". Het onderzoek bestudeert hoe warmte-management en stromingsconfiguraties de prestaties van microgolfplasma beïnvloeden. Belangrijke vernieuwingen zijn onder meer de demonstratie dat voorverwarming van CO₂ bij bijna-atmosferische druk de conversie kan verhogen door de contractiedynamiek van het plasma te beïnvloeden en het reactieve volume uit te breiden. Daarnaast onderzoekt dit werk reactieve quenching na het plasma met CH₄ via een dubbel injectiesysteem in een CO₂ microgolfplasma. Hierbij wordt een verbetering van de CO₂ conversie aangetoond en de resultaten worden vergeleken met conventionele droge reforming van methaan. Door middel van uitgebreide spectroscopische analyse, temperatuurmapping en productkarakterisering wordt zowel het fundamentele begrip van microgolfplasmachemie vergroot, en worden ook praktische strategieën ontwikkeld om de conversie te verbeteren. Verder hebben we de CO₂ (en N₂) conversie in microgolfplasma bij een druk in de buurt van de Marsatmosfeer (25 mbar) onderzocht, wat het potentieel van deze technologie voor ruimtetoepassingen aantoont. De bevindingen bieden waardevolle inzichten voor het ontwerpen van de volgende generatie plasmareactoren, die kunnen bijdragen aan een circulaire koolstofeconomie op aarde en tegelijkertijd toekomstige menselijke verkenning van Mars ondersteunen.

Contents

Introduction						
1.1		Freat Energy Transition of the 21 st Century				
1.2						
Refe	rences					
The	eory					
2.1	Essent	cial Aspects of Microwave Plasma Technology				
2.2	Magne	etron vs Solid-State Technology				
	2.2.1	Magnetrons: The Workhorse of the Century				
	2.2.2	Solid-State Generators: The Technology of the Future, or Today? .				
	2.2.3	Dielectric Resonators				
	2.2.4	A Personal Reflection:				
		Field Experience with Solid-State Microwave Plasma Technology $.$				
2.3	Coupl	ing, Contraction, and Flow Dynamics				
	2.3.1	Power Coupling to the Discharge				
	2.3.2	Contraction Dynamics				
	2.3.3	Flow Dynamics				
2.4	Implie	ations for MW-based Plasma Conversion of CO_2				
	2.4.1	Plasma-Based CO ₂ Dissociation				
	2.4.2	Post-Plasma Afterglow Quenching				
	2.4.3	From Earth to Mars: Low Pressure Plasma Applications				
2.5	Ratio	nale of this Thesis				
Refe	rences					
		Management: Enhancing Efficiency Through Preheating				
	rmal I					
The	rmal I	Management: Enhancing Efficiency Through Preheating				
The	rmal I	Management: Enhancing Efficiency Through Preheating auction				
The	Introd Exper 3.2.1	Management: Enhancing Efficiency Through Preheating Juction				
The 3.1 3.2	Introd Exper 3.2.1	Management: Enhancing Efficiency Through Preheating auction				
The 3.1 3.2	Introd Exper 3.2.1 Result	Management: Enhancing Efficiency Through Preheating fuction				
The 3.1 3.2	Introd Exper 3.2.1 Result 3.3.1	Management: Enhancing Efficiency Through Preheating auction				
The 3.1 3.2	Exper 3.2.1 Result 3.3.1 3.3.2 3.3.3	Management: Enhancing Efficiency Through Preheating fuction				

Table of Contents vii

	4.2	Methods	77				
		4.2.1 Experimental Setup	77				
		4.2.2 Model Description	80				
	4.3	Results and Discussion	82				
		4.3.1 Methane as a Reactive Quenching Agent:					
		Absolute CO_2 Conversion	83				
		4.3.2 A Dry Reforming of Methane Perspective:					
		Syngas Ratio and Product Selectivity Analysis	92				
			102				
	4.4		107				
	Refe		119				
5	\mathbf{Bey}	ond Earth:					
	Maı	•	120				
	5.1	Introduction	121				
	5.2	Experimental Methods	123				
	5.3	Results and Discussion	126				
	5.4	Considerations for Plasma-based ISRU on Mars	130				
	5.5	Post-Plasma Separation:					
		Harnessing the Martian Atmosphere	131				
	5.6	Microwave Reactors on Mars	132				
	5.7	Conclusion and Outlook	133				
	Refe	erences	141				
_			1 40				
6	Con	aclusions and Future Outlook	142				
\mathbf{A}	The	ermal Management:					
	Enh	nancing Efficiency Through Preheating	147				
	A.1	Analysis of Thermal Losses	148				
	A.2	Thermometric Probes	149				
		A.2.1 Optical Emission Spectroscopy Data Treatment	149				
		A.2.1.1 Raw Data Acquisition and Pre-Processing	150				
		•	153				
			154				
			155				
			155				
		•	156				
		A.2.3.3 Analytical Uncertainties	157				
		A.2.3.4 Method Validation	157				
	Δ 3	Analytical Techniques and Performance Indicators	158				
	11.0		158				
	A.4		160				
	А.Э	A.5.1 Impact of Preheating at Higher Power	161 161				
		A.5.2 Changes to Reactive Volume and Plasma Size	162				
		A.5.3 Comparative Analysis: Constant Microwave Power vs Constant Total Power	166				
			167				

Table of Contents viii

	Reie	rences		171				
В	Dual Injection in a CO ₂ plasma: Exploring Reactive Quenching							
	B.1	Analys	sis	173				
		B.1.1	Liquid Analysis	173				
		B.1.2	Carbon Analysis	175				
		B.1.3	Optical Emission Spectroscopy Data Treatment	175				
		B.1.4	Secondary Injection Housing	178				
		B.1.5	Gas Chromatography	178				
		B.1.6	Performance Calculations	180				
	B.2	Model	ing	182				
		B.2.1	Water-Gas Shift Equilibrium and H_2O Formation	182				
		B.2.2	Model Projections for Higher SEI Conditions	183				
	B.3	3 Additional Results and Discussion						
		B.3.1	Additional Results	184				
		B.3.2	Carbon Analysis	196				
	Refe	rences		198				
A	cader	nic Bi	ography	199				
Curriculum Vitae								
Acknowledgements								

Chapter 1

Introduction

1.1 The Great Energy Transition of the 21st Century

For over a century, industrial growth has been fueled by carbon-rich fossil resources like coal, oil, and natural gas. These fuels ushered in extraordinary economic expansion and still supply approximately 81% of the world's energy [1]. However, harnessing the energy from fossil fuels requires releasing vast quantities of carbon dioxide (CO₂) and other greenhouse gases, whose accumulation in the atmosphere has driven dramatic changes in the Earth's climate. No longer an abstract prediction but a stark reality affecting communities worldwide, early reports confirmed by the Copernicus Climate Change Service (C3S) show that 2024 is the second year on record to exceed 1.5 °C above pre-industrial levels [2]. This breaches the threshold set by the Paris Agreement in 2015, which aims to limit climate change impacts by achieving net-zero anthropogenic emissions [3]. The manifestation of this warming is evident in the unprecedented frequency and intensity of extreme weather events, underscoring the immediate need for rapid decarbonization of our energy and industrial sectors. A shift from a fossil fuel-dominated system to a sustainable, carbon-neutral future is only possible through collective efforts focused on advancing technologies that enable not just cleaner energy but also a more circular and efficient use of resources, eliminating waste through emissions.

Achieving the net zero climate imperative faces formidable challenges, as fossil fuels remain deeply entrenched in the global economy. Beyond their role in energy production, fossilderived carbon is a fundamental feedstock for the fuels and chemicals that underpin modern industry, a dependence which emphasizes the need for a broader transformation, not just towards clean energy, but also towards sustainable carbon management. Thus, a fully decarbonized electricity sector is a cornerstone of this transition. Electricity powers modern life, and its share of energy consumption is expected to rise from 20% in 2023 to over 50% by 2050, as global demand surges [4, 5]. However, fossil fuels still account for over 60% of electricity generation [5]. In order to align with net zero targets, that share must decline to below 30% by 2030 [5]. While renewable electricity generation has seen remarkable growth in recent years [6], with solar and wind power becoming increasingly cost-competitive, the challenge of decarbonizing the industrial sector remains critical and complex.

The chemical sector alone is responsible for being the largest industrial energy consumer and the third largest industry subsector in terms of direct CO₂ emissions [5]. To meet Paris Agreement targets, emissions must decline by 75% before 2050 [5]. However, because many industrial processes inherently depend on fossil-based carbon, renewable electrification alone cannot fully eliminate fossil fuel use in chemical production. Addressing this challenge requires a transformative model that must prioritize recycling of carbon emissions (e.g., CO₂) into the chemical resources that run our society, thereby reducing or eliminating our reliance on fossil fuels and mitigating impacts of climate change through circularity practices.

The development of efficient Carbon Capture and Utilization (CCU) technologies represents a key pathway towards sustainable resource consumption [5]. The CCU approach fosters systems where carbon is continuously reused rather than 'littered' in our atmosphere. By recycling carbon, such as from CO₂ emissions, into valuable chemical products and fuels, we can both eliminate greenhouse gas emissions and create sustainable alternatives to fossil-based products. However, the chemical stability of CO₂ presents thermodynamic challenges, requiring efficient activation processes that can operate at industrial scales. Furthermore, as renewable energy increasingly penetrates global power infrastructures, technologies capable of absorbing intermittent power supplies while producing valuable chemicals are becoming critical components of a circular carbon economy.

Among various CCU pathways, plasma-based conversion represents a promising approach for coupling renewable electricity to chemical production [7–10]. Plasma is a (partially) ionized gas with free electrons, ions, and neutral species, which offers a unique, reactive environment that is capable of transforming greenhouse gases, such as CO₂, into value-added chemicals using electricity [9]. Since plasmas allow for rapid response to power fluctuations, the technology is compatible with intermittent renewable energy sources [9, 10]. For example, plasma can be used to dissociate CO₂ into CO, producing a feedstock for carbon-neutral fuel synthesis [9], which can be utilized within our existing infrastructure. Furthermore, plasma reactors can be designed for deployment at local or regional scales, further reducing the CO₂ footprint associated with transporting the key chemicals used in industry.

A leading candidate for plasma-based CO₂ conversion in a CCU context is with microwave (MW) plasma, which has demonstrated promising conversion and energy efficiency in laboratory settings due to the high reactivity of plasma [9, 11–16]. While results from MW plasma applications are encouraging, conversion remains highly dependent on specific operating parameters and process design. Consequently, research efforts have increasingly focused on optimizing the dissociation of greenhouse gases, such as CO₂, using MW plasma systems to advance this promising technology [9, 12–31].

While MW plasma technology shows promise for greenhouse gas conversion, reaching industrial viability requires maximizing overall system efficiency. MW plasmas have historically operated under sub-atmospheric conditions, but advances in engineering have extended the stable range of operation, anywhere from very low pressures (< 1 mbar), in which nonequilibrium behavior is induced, up to above-atmospheric pressure (> 1 bar), where high-temperatures around contracted plasma drive thermal chemistry. The dissociation of CO_2 into CO represents a key pathway toward carbon-neutral fuels and chemicals, as the production of CO serves as a versatile chemical building block for numerous industrial applications [9], which would allow for a reduction in our dependence on fossil resources through a circular carbon economy.

1.2 Outline

This thesis investigates the fundamental aspects and practical applications of MW-based plasma technology for carbon utilization, with a specific focus on CO₂ conversion. The overall aim of this research is to advance the understanding of MW plasma systems for greenhouse gas conversion and contribute to the development of more efficient, sustainable processes for chemical production.

The work explores both terrestrial applications for addressing climate change and potential interplanetary applications for In-situ Resource Utilization (ISRU), particularly on Mars. By examining various aspects of MW plasma technology, from process design to operating conditions, this research seeks to identify pathways for improving the performance and practicality of MW plasma-based carbon utilization.

Building on the theoretical foundations presented in Chapter 2, this thesis develops specific research objectives and questions that guide the experimental investigations in the subsequent chapters. The theoretical framework will establish the rationale for focusing on particular aspects of MW plasma systems, such as thermal management and the importance of flow topology on conversion and energy efficiency. Through this approach, the research aims to contribute to the broader goal of developing efficient, scalable technologies for a circular carbon economy and sustainable industrial production, while expanding the potential applications of MW plasma technology on Earth and beyond.

This thesis is organized into six chapters:

Chapter 1: Introduction

Establishes the context of the climate crisis and introduces plasma technology for carbon utilization.

Chapter 2: Theory

Provides the theoretical foundation of MW plasma technology, exploring reactor engineering principles, power coupling, plasma contraction, flow dynamics, and aspects of CO_2 conversion.

Chapter 3: Thermal Management:

Enhancing Efficiency Through Preheating

Examines the potential for heat recovery in plasma systems by investigating the effect of preheating on CO₂ plasma.

Chapter 4: Dual Injection in CO₂ Plasma:

Exploring Post-Plasma Injection of CH₄

Investigates the effects of post-plasma CH₄ injection on conversion and product distribution, with a focus on reactive quenching to improve CO₂ conversion and provides a comparison with conventional (admixing) DRM.

Chapter 5: Beyond Earth:

Martian Atmosphere Conversion for In-Situ Resource Utilization

Explores the adaptation of MW plasma technology for space exploration.

Chapter 6: Conclusions and Future Outlook

Synthesizes the research findings and discusses implications for future development of MW plasma technology.

Bibliography

- [1] International Energy Agency. World energy statistics and balances. Technical report, IEA, 2024. URL https://www.iea.org/data-and-statistics/data-product/world-energy-statistics-and-balances.
- [2] Global climate highlights 2024. Technical report, Copernicus Climate Change Service (C3S), 2025. URL https://climate.copernicus.eu/global-climate-highlights-2024.
- [3] UNFCCC. Paris climate change conference, 2015.
- [4] International Energy Agency. Electricity 2025. Technical report, IEA, 2025. URL https://www.iea.org/reports/electricity-2025.
- [5] International Energy Agency. Tracking clean energy progress 2023. 2023. URL https://www.iea.org/reports/tracking-clean-energy-progress-2023.
- [6] IRENA. Renewable energy statistics 2024. Technical report, International Renewable Energy Agency, 2024.
- [7] A. Bogaerts and G. Centi. Plasma technology for CO₂ conversion: A personal perspective on prospects and gaps. Frontiers in Energy Research, 8:111, 2020. doi: 10.3389/fenrg.2020.00111.
- [8] A. Bogaerts, X. Tu, and T. Nozaki. Plasma-based CO₂ conversion, pages 209–243.
 Springer, 2024. doi: 10.1007/978-981-99-8822-8_10.
- [9] W. Bongers, H. Bouwmeester, A.J. Wolf, F.J.J. Peeters, S. Welzel, D. van den Bekerom, N. den Harder, A. Goede, M. Graswinckel, and P.W. Groen. Plasmadriven dissociation of CO₂ for fuel synthesis. *Plasma Processes and Polymers*, 14(6): 1600126, 2017. doi: 10.1002/ppap.201600126.

[10] R. Snoeckx and A. Bogaerts. Plasma technology – a novel solution for CO₂ conversion? Chemical Society Reviews, 46(19):5805–5863, 2017. doi: 10.1039/C6CS00066E.

- [11] A.P.H. Goede, W. Bongers, M.F. Graswinckel, M.C.M. van de Sanden, M. Leins, J. Kopecki, A. Schulz, and M. Walker. Production of solar fuels by CO₂ plasmolysis. In *EPJ web of conferences*, volume 79, page 01005. EDP Sciences, 2014. doi: 10. 1051/epjconf/20137901005.
- [12] E.R. Mercer, S. van Alphen, C.F.A.M. van Deursen, T.W.H. Righart, W.A. Bongers, R. Snyders, A. Bogaerts, M.C.M. van de Sanden, and F.J.J. Peeters. Post-plasma quenching to improve conversion and energy efficiency in a CO₂ microwave plasma. Fuel, 334:126734, 2023. doi: 10.1016/j.fuel.2022.126734.
- [13] C.F.A.M. van Deursen, H.M.S. Van Poyer, W.A. Bongers, F.J.J. Peeters, F.M.A. Smits, and M.C.M. van de Sanden. Effluent nozzles in reverse-vortex-stabilized microwave CO₂ plasmas for improved energy efficiency. *Journal of CO₂ Utilization*, 88: 102952, 2024. doi: 10.1016/j.jcou.2024.102952.
- [14] G.J. van Rooij, H.N. Akse, W.A. Bongers, and M.C.M. van De Sanden. Plasma for electrification of chemical industry: A case study on CO₂ reduction. *Plasma Physics* and Controlled Fusion, 60(1):014019, 2017. doi: 10.1088/1361-6587/aa8f7d.
- [15] P. Viegas, L. Vialetto, A.J. Wolf, F.J.J. Peeters, P.W.C. Groen, T.W.H. Righart, W.A. Bongers, M.C.M. van de Sanden, and P. Diomede. Insight into contraction dynamics of microwave plasmas for CO₂ conversion from plasma chemistry modelling. *Plasma Sources Science and Technology*, 29(10):105014, 2020. doi: 10.1088/1361-6595/abb41c.
- [16] A.J. Wolf, T.W.H. Righart, F.J.J. Peeters, W.A. Bongers, and M.C.M. van De Sanden. Implications of thermo-chemical instability on the contracted modes in CO₂ microwave plasmas. *Plasma Sources Science and Technology*, 29(2):025005, 2020. doi: 10.1088/1361-6595/ab5eca.
- [17] N.V. Chekmarev, D.A. Mansfeld, A.V. Vodopyanov, S.V. Sintsov, E.I. Preobrazhensky, and M.A. Remez. Enhancement of CO₂ conversion by counterflow gas quenching of the post-discharge region in microwave plasma sustained by gyrotron radiation. Journal of CO₂ Utilization, 82:102759, 2024. doi: 10.1016/j.jcou.2024.102759.

[18] F.A. D'Isa, E.A.D. Carbone, A. Hecimovic, and U. Fantz. Performance analysis of a 2.45 ghz microwave plasma torch for CO₂ decomposition in gas swirl configuration. *Plasma Sources Science and Technology*, 29(10):105009, 2020. doi: 10.1088/1361-6595/abaa84.

- [19] A. Hecimovic, F.A. D'Isa, E.A.D. Carbone, and U. Fantz. Enhancement of CO₂ conversion in microwave plasmas using a nozzle in the effluent. *Journal of CO₂ Utilization*, 57:101870, 2022. doi: 10.1016/j.jcou.2021.101870.
- [20] A. Hecimovic, C.K. Kiefer, A. Meindl, R. Antunes, and U. Fantz. Fast gas quenching of microwave plasma effluent for enhanced CO₂ conversion. *Journal of CO₂ Utiliza*tion, 71:102473, 2023. doi: 10.1016/j.jcou.2023.102473.
- [21] A. Hecimovic, M.T. Mayer, L.G.J. de Haart, S. Gupta, C.K. Kiefer, A. Navarrete, A. Schulz, and U. Fantz. Benchmarking microwave-induced CO₂ plasma splitting against electrochemical CO₂ reduction for a comparison of promising technologies. *Journal of CO₂ Utilization*, 83:102825, 2024. doi: 10.1016/j.jcou.2024.102825.
- [22] C.K. Kiefer, R. Antunes, A. Hecimovic, A. Meindl, and U. Fantz. CO₂ dissociation using a lab-scale microwave plasma torch: An experimental study in view of industrial application. *Chemical Engineering Journal*, 481:148326, 2024. doi: 10.1016/j.cej. 2023.148326.
- [23] H. Kim, S. Song, C.P. Tom, and F. Xie. Carbon dioxide conversion in an atmospheric pressure microwave plasma reactor: Improving efficiencies by enhancing afterglow quenching. *Journal of CO₂ Utilization*, 37:240–247, 2020. doi: 10.1016/j.jcou.2019. 12.011.
- [24] T. Kozák and A. Bogaerts. Evaluation of the energy efficiency of CO₂ conversion in microwave discharges using a reaction kinetics model. *Plasma Sources Science and Technology*, 24(1):015024, 2015.
- [25] J. Li, X. Zhang, J. Shen, T. Ran, P. Chen, and Y. Yin. Dissociation of CO₂ by thermal plasma with contracting nozzle quenching. *Journal of CO₂ Utilization*, 21: 72–76, 2017. doi: 10.1016/j.jcou.2017.04.003.
- [26] A.W. van de Steeg, L. Vialetto, A. Silva, F. Sovelas, P. Viegas, P. Diomede, M.C.M. van de Sanden, and G.J. van Rooij. The chemical origins of plasma contraction and

thermalization in CO₂ microwave discharges. The Journal of Physical Chemistry Letters, 13(5):1203–1208, 2022. doi: 10.1021/acs.jpclett.1c03731.

- [27] A.W. van de Steeg, P. Viegas, A. Silva, T. Butterworth, A. van Bavel, J. Smits, P. Diomede, M.C.M. van de Sanden, and G. van Rooij. Redefining the microwave plasma-mediated CO₂ reduction efficiency limit: the role of o-CO₂ association. ACS Energy Letters, 6(8):2876-2881, 2021. doi: 10.1021/acsenergylett.1c01206.
- [28] D.C.M. van den Bekerom, J.M.P. Linares, T. Verreycken, E.M. van Veldhuizen, S. Nijdam, G. Berden, W.A. Bongers, M.C.M. van de Sanden, and G.J. van Rooij. The importance of thermal dissociation in CO₂ microwave discharges investigated by power pulsing and rotational raman scattering. *Plasma Sources Science and Technology*, 28 (5):055015, 2019. doi: 10.1088/1361-6595/aaf519.
- [29] L. Vialetto. Modelling of plasma for CO_2 conversion: electron kinetics, chemistry and transport. PhD thesis, Eindhoven University of Technology, 2021.
- [30] A.J. Wolf, F.J.J. Peeters, P.W.C. Groen, W.A. Bongers, and M.C.M. van de Sanden. CO₂ conversion in nonuniform discharges: Disentangling dissociation and recombination mechanisms. *The Journal of Physical Chemistry C*, 124(31):16806–16819, 2020. doi: 10.1021/acs.jpcc.0c03637.
- [31] A.J. Wolf, T.W.H. Righart, F.J.J. Peeters, P.W.C. Groen, M.C.M. van de Sanden, and W.A. Bongers. Characterization of CO₂ microwave plasma based on the phenomenon of skin-depth-limited contraction. *Plasma Sources Science and Technology*, 28(11):115022, 2019. doi: 10.1088/1361-6595/ab4e61.

Chapter 2

Theory

This chapter examines the fundamental principles of MW plasma technology for green-house gas conversion, with a focus on CO_2 dissociation. The first sections explore the engineering aspects of MW plasma systems, compare MW generation technologies, and analyze their respective advantages in efficiency, control, and durability. In the second part, we detail the physics of energy coupling mechanisms, plasma contraction dynamics, and flow behaviors that govern reactor performance in MW plasma systems. Finally, in the last section, special attention is given to thermal management strategies in CO_2 conversion, including preheating, reactive quenching techniques, and low pressure applications to enhance conversion. The insights presented are intended to bridge MW engineering with plasma chemistry, providing a theoretical foundation for the work carried out in the following chapters.

2.1 Essential Aspects of Microwave Plasma Technology

As briefly touched upon in Chapter 1, MW plasma technology has emerged as a promising tool for greenhouse gas conversion in a CCU context, demonstrating promising conversion and energy efficiency in laboratory settings due to the high-temperature gradients and fast transport strongly exhibited in this plasma regime [1–5]. Currently, MW plasma-based gas conversion has a Technology Readiness Level (TRL) of approximately 3 (i.e., achieved experimental proof of concept) [6]. Growing commercial interest in nitrogen fixation, carbon utilization, and hydrocarbon (e.g., methane) reforming are expected to drive the general readiness of the technology in the years to come [7, 8].

The benefits of MW plasmas reside in their adaptivity, which allows for large scaling potential and operation under an extensive parameter space (for example, in terms of pressure, flow rates, and configurations) [7–9]. Indeed, MW plasmas can be maintained across an impressively broad pressure range (from high vacuum < 1 mbar, up to well above atmospheric pressure), which affects the plasma dynamics and, thus, the chemistry (see *Section 2.4*). This flexibility allows MW plasmas to be used in a wide range of applications [9–11].

Using electromagnetic radiation in the frequency range ~ 300 MHz – 300 GHz [12], MWs can create and sustain a plasma discharge. In this process, the field accelerates free electrons, which then transfer energy to gas molecules through collisions, leading to ionization, excitation, and dissociation. This is typically achieved through waveguides, which serve to confine and direct MW radiation toward the plasma while preventing energy losses. Furthermore, MW reactors use non-contact energy transfer, eliminating the need for physical electrodes inside the discharge zone. This not only enhances system longevity but also prevents contamination of the plasma and effluent gas mixture due to electrode erosion, a significant advantage in high-purity applications, such as fertilizer production and chemical synthesis. An example of a typical waveguided MW reactor configuration is illustrated in Figure 2.1.

Following Figure 2.1, a generator produces a peak power, which is transmitted through a rectangular waveguide at a designated frequency (e.g., 2.45 GHz). Rectangular waveguides support many modes in either Transverse Electric (TE) or Transverse Magnetic (TM) mode, signifying that either the Electric (E) or Magnetic (M) fields are perpendicular

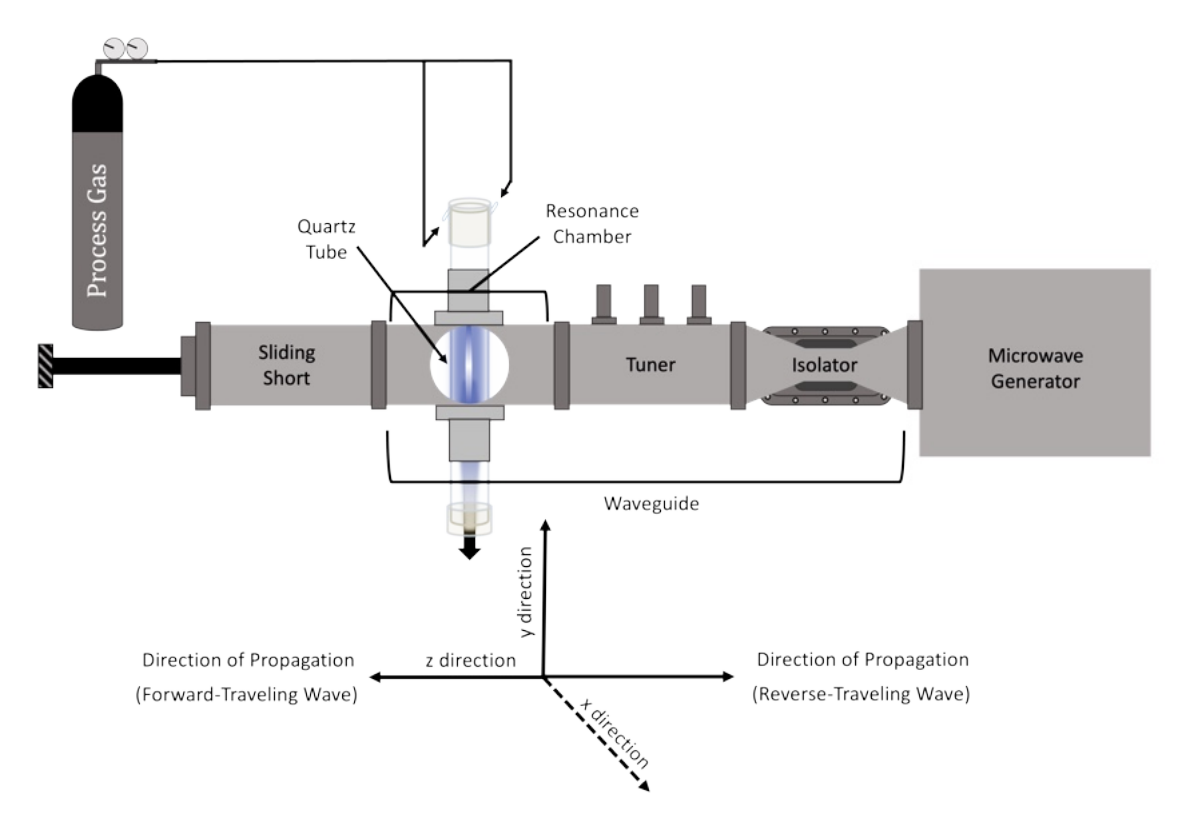


FIGURE 2.1: Schematic of a waveguided MW reactor, with a generator (magnetron or solid-state), and isolator, tuner, resonance chamber (intersected by a quartz tube, where plasma ignition takes place), and sliding short.

to the direction of propagation. In addition, these modes are denoted by nomenclature using the characteristic eigenvalues in a rectangular waveguide derived from the solution of Maxwell's equations governing the propagated wave, e.g., TE_{mn} , where 'm' references the number of maxima in the x-direction, and 'n' references the number of maxima in the y-direction, as shown in Figure 2.1. Typically, the dimensions of a rectangular waveguide are selected such that the TE_{10} mode is the dominant wave propagation mode due to its low cutoff frequency and thus is commonly used for MW plasma reactors. The cutoff frequency defines the mode that will propagate through the waveguide and can be considered like a 'filter' that suppresses other waveforms while allowing for minimum attenuation to the propagation of the signal (i.e., minimal loss of signal through the waveguide). Since this mode offers efficient power transmission with minimal attenuation, it ensures that the power is effectively delivered to the plasma, while minimizing losses [12], as efficient power coupling is critical to MW plasma operation.

To protect the generator from unwanted reflected power downstream, an isolator, which consists of a circulator and a load, is used. The circulator is a non-reciprocal ferromagnetic device that directs power unidirectionally, allowing the transmitted wave to flow from

the generator to the discharge while blocking any reflected waves from traveling back upstream and damaging the generator. Any reflected power is diverted to the load, where it is dissipated. In high-power MW reactors (e.g., above 1 kW), water-cooled loads are commonly used to prevent heat buildup that could damage the circulator.

Further downstream, matching components, such as a stub tuner, are used to optimize impedance matching, ensuring efficient power transfer while minimizing reflection. The tuner, positioned between the generator and the resonance chamber, can be manually adjusted or automatically controlled in modern systems (so called 'auto-tuners'). Many auto-tuners also provide real-time monitoring of forward and reflected power, as well as the applied frequency.

Within the resonance chamber, MW energy is coupled to the gas flow through a MW-transparent medium (e.g., a quartz tube) that traverses the waveguide. The MW field generates an oscillating electric field (E-field), accelerating free electrons, which collide with gas molecules in an avalanche process, leading to ionization and plasma formation, resulting in a sustained discharge consisting of electrons, ions, radicals, and excited species [13]. To ensure efficient confinement of the MW field in the case of rectangular resonance chambers (as illustrated in Figure 2.1), a sliding short (or plunger) can be placed at approximately $\frac{1}{4}$ waveguide wavelength from the discharge region. This component reflects MW energy back into the cavity, creating a standing wave that enhances power density.

However, efficient energy coupling is not solely dependent on waveguide design. It is also influenced by the choice of MW generator, which determines factors such as frequency stability, power tunability, and impedance matching. The two common technologies used for MW plasma generation today are magnetron-based and solid-state sources, each with distinct advantages and trade-offs. In the following section, we explore the differences between a few MW generating technologies and their implications for MW-based plasma applications.

2.2 Magnetron vs Solid-State Technology

2.2.1 Magnetrons: The Workhorse of the Century

The magnetron tube has been a cornerstone of MW technology for over eight decades, demonstrating remarkable versatility across applications ranging from military radar systems to plasma generation. In the early 1940s, magnetrons played a pivotal role in World War II, revolutionizing radar technology. Their ability to generate high-power MW radiation in a compact and efficient form made them indispensable for early high-frequency applications. Following the war, this technology found widespread adoption, with perhaps the most familiar example found in our kitchen as a common household appliance.

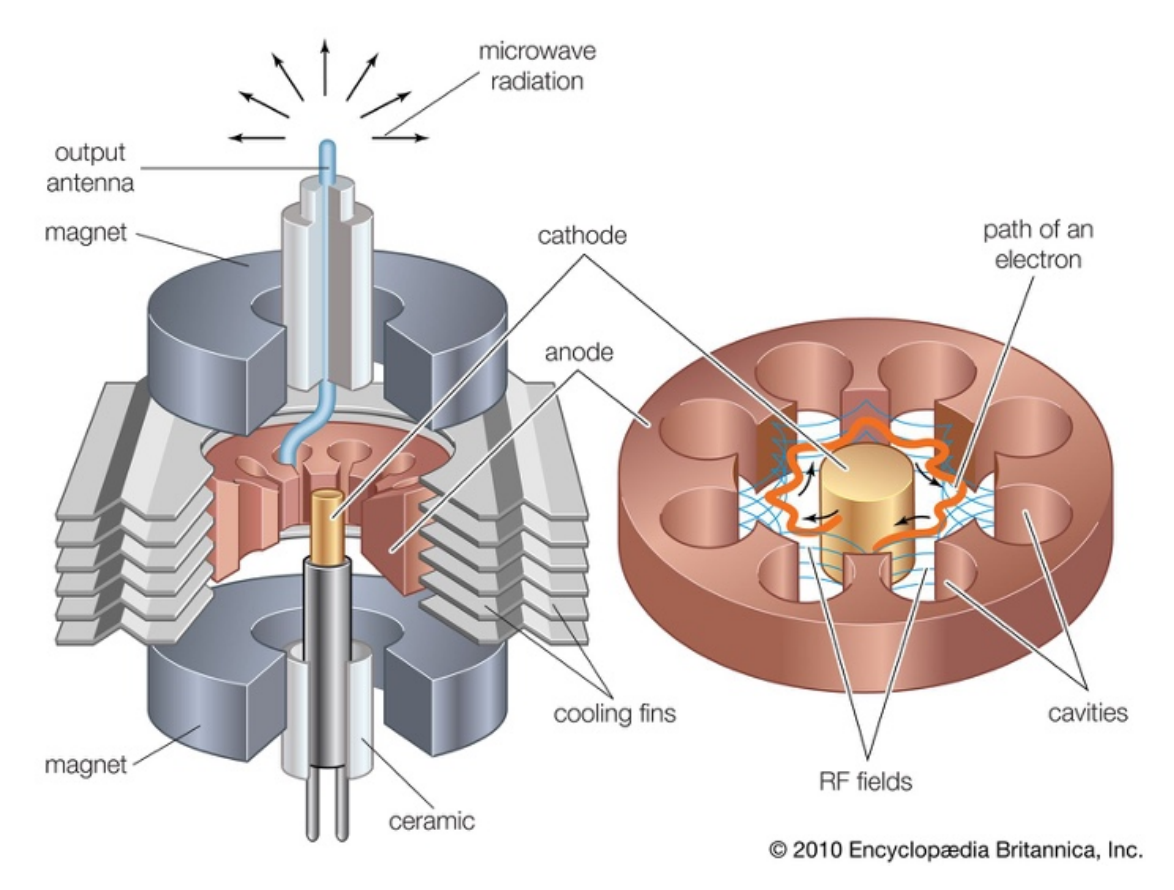


FIGURE 2.2: Typical structure of a magnetron. Image from Encyclopedia Britannica [14]

As *Pozar* describes, there are several types of magnetron tubes; however, all involve the interaction of an electron beam with an electromagnetic field inside a vacuum-sealed envelope [12]. A typical construction of a magnetron is shown in *Figure 2.2*. The high-frequency (HF) energy is coupled outside the envelope, where a hot cathode generates

a stream of electrons by thermionic emission, which is focused to a narrow beam via a high-voltage anode or solenoidal electromagnet [12]. A strong, static magnetic field is applied along the axis, perpendicular to the motion of the electrons. This magnetic field interacts with the E-field created by the high-voltage anode and cathode, forcing the electrons into curved, spiral trajectories [12]. As the electrons pass near the resonant cavities, which set the frequency of oscillation by their geometry (i.e., 2.45 GHz), they transfer kinetic energy in the form of MW radiation [12]. The resulting MW radiation is then extracted via a waveguide, making it available for practical use in plasma reactors. The magnetron is a self-oscillating device requiring no external elements other than a power supply. Additionally, magnetrons can handle very high-power densities in the electron beam, enabling compact high-power output [15]. However, it should be noted that magnetron filaments are sensitive to mechanical shock (e.g., like those created during rocket starts) and have a limited lifetime.

Magnetrons are characterized by their simplicity and efficiency, and a single magnetron tube can directly generate high-power MW (from kW up to MegaW) with source efficiencies of 80% or more [12]. However, as self-oscillating devices, magnetrons inherently operate at a fixed frequency determined by their cavity design. The output of a freerunning magnetron also has relatively high phase noise and some frequency jitter (often described as "noisy" output). The magnetron basically delivers a burst of MWs at its design frequency, and fine control of power is achieved only by adjusting the input voltage to the cathode or via duty cycle modulation (as in pulsing). Rapid or linear power modulation is not a strength of magnetrons; in fact, warm-up times can be \sim 30 minutes or more. Furthermore, magnetrons require high-voltage power supplies (often on the order of several kV) to operate, which adds complexity and safety concerns (e.g., 2 – 4 kV is common for a 1 – 2 kW magnetron) [12]. Modularity is also difficult to achieve with magnetron technology, as it entails bulky waveguide distribution systems.

Another consideration is the fixed lifetime and performance degradation over time, as the cathodes within the magnetron wear with use (through cathode emission degradation or filament burnout) and can suffer from instabilities as they age. A typical magnetron in industrial service might last on the order of a few thousand hours ($\sim 2,000 - 8,000$ hours is common) before needing replacement [12].

While magnetrons commonly dominate the lower MW frequency range (< 1 - 20 GHz,

although higher frequency is possible), gyrotrons represent a specialized class of MW generators capable of operating at significantly higher frequencies (typically ~28 – 500 GHz) and power levels. Interestingly, gyrotrons can be designed to oscillate at multiple frequencies by adjusting operation parameters. Moreover, the higher operating frequencies enable gyrotrons to achieve very high-power outputs, with some systems capable of generating MegaW-level continuous wave (CW) power. Like magnetrons, gyrotrons are vacuum tube devices that rely on the interaction between an electron beam and electromagnetic fields within resonant cavities [12]. However, gyrotrons use solenoidal bias magnets, in which the axial magnetic field forces the electrons into tight spirals down the length of the tube, forcing cyclotron resonance. The electron velocity can become high enough that relativistic effects become important [12, 16].

Despite their impressive power capabilities, gyrotrons present several limitations for plasmabased gas conversion applications. The efficiency of gyrotrons is typically around 50%, considerably lower than the efficiency achievable with magnetrons [12, 17]. This reduced efficiency combined with the complexity and cost of the high-field superconducting magnets required for operation makes gyrotrons economically challenging for plasma-based industrial CO₂ conversion. Furthermore, the higher frequencies can lead to increased power losses in waveguide transmission. Thus, the primary domain for gyrotrons remains in fusion processes. Although some research has explored gyrotron applications in plasma-based gas conversion [18, 19], the combination of lower efficiency, higher complexity, and increased costs generally favors multiple high-power magnetron sources over single-gyrotron systems for industrial CO₂ dissociation applications. Notwithstanding, industrial MW heating and plasma systems have traditionally employed magnetrons because of the technological maturity and low cost. There is a wealth of practical know-how on using magnetrons, and many existing plasma reactors have been designed around them; however, as semiconductor technology continues to advance, the next generation of industrial MW systems appears on the horizon.

2.2.2 Solid-State Generators: The Technology of the Future, or Today?

Recent advances in semiconductor technology have revolutionized the generation of HF energy, enabling a shift from traditional vacuum tube devices to solid-state MW generators. Unlike magnetrons, which operate as self-oscillating devices with fixed frequencies

and high phase noise, solid-state technology leverages transistor-based amplification to provide stable, frequency- and phase-controlled MW power [20], a level of precision and adaptability offers significant advantages for plasma generation.

Solid-state MW sources employ high-power transistors, such as Laterally Diffused Metal-Oxide Semiconductors (LDMOS) and Gallium Nitride (GaN) devices, to amplify an input HF signal to the desired MW power level, with outstanding control over frequency, phase, and power output. This inherent controllability allows solid-state MW sources to operate with low phase noise, and precise power modulation capabilities. By design, solid-state generators can be tuned or adjusted, allowing electronic tuning of frequency (within a certain band, for example, 2.45 ± 0.05 GHz) and can even sweep or hop frequencies rapidly. Thus, power control is vastly superior compared to magnetrons, as the output power can be adjusted linearly. Furthermore, fast variation or pulsing of the MW output is straightforward (since one can drive the transistors with a modulated input or gate bias) [12]. Modern solid-state MW generators offer precise, real-time power control with resolution better than 1% and can achieve micro- and nanosecond response times for pulsing. Solid-state systems also run on low-voltage DC power, eliminating the need for bulky high-voltage transformers and makes the system inherently safer and easier to integrate with digital control circuits. These attributes in a generator should be critically considered for precision-driven applications, like plasma-based research or in space-related endeavors, when, for example, power modulation is key to the process [21].

As solid-state generators are limited in power (e.g., 250 W), they must be coherently combined to scale power output. As a result, substantial efforts have been directed toward increasing output power using various combining techniques [12]. An example of one technique, i.e., an 8-port power combiner used in Chapters 4 and Chapter 5, is shown in Figure 2.3.

Power combining can be achieved either at the device level or the circuit level. At the device level, multiple diode or transistor junctions are electrically connected in parallel within a compact region, effectively operating as a single unit [12]. An example of this approach is shown in *Figure 2.3*, where each 250 W solid-state source is first combined to produce 500 W before being fed through a coaxial cable and further merged at the circuit level. *Figure 2.3* serves to complete this example, where the power amplifiers are placed in parallel, with their output power combined through a specially designed waveguide

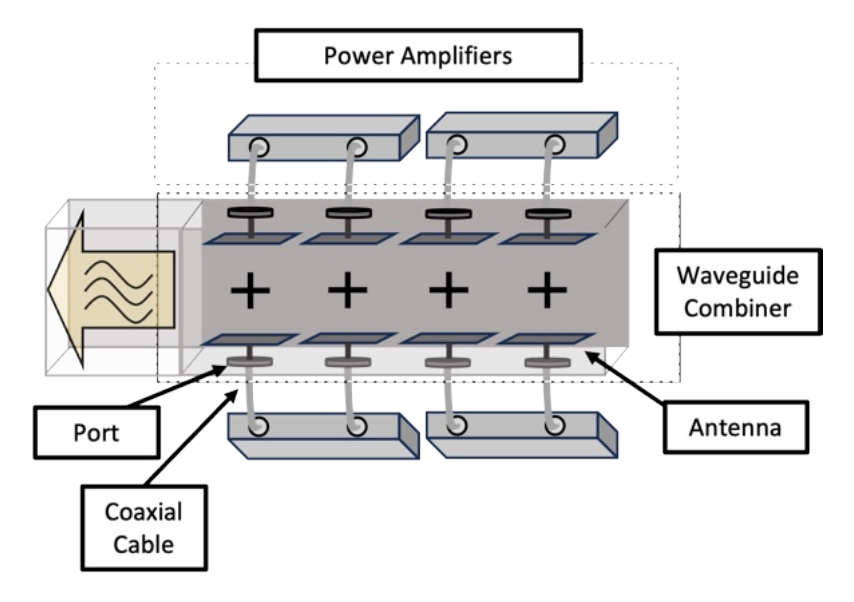


FIGURE 2.3: An example of an 8-port power combiner waveguide. Each power amplifier represents two, 250 W solid-state sources, which are circuit-combined to generate 500 W of power, and then fed through an N-type coaxial cable, which is transitioned to an internal antenna. Each port must be phase-matched (e.g., \pm 180°), and results in combined MW power of ~2000 W.

combiner (cavity combiner) that constructively merges the signals. There is some difficulty in combining amplifiers into a single high-power output, as this requires precise phase matching. Since the technology is also frequency- and phase-stable in coherent systems, it allows the power combining of generators to deliver an extensive power range, opening avenues for distributed power sources into large geometries [20, 22]. There are various power-combining techniques, all which present advantages and disadvantages. Although the depth of this is out of the scope of this thesis, *Pozar's Microwave Engineering* serves as a comprehensive resource for further exploration [12].

In principle, an unlimited amount of HF power can be generated by combining solid-state sources; however, in practice, factors such as combiner losses limit the multiplication factor. This is why high-power solid-state MW devices are not readily commercially available and are extremely costly. Furthermore, the additional components need to be carefully managed, as the phase-matching can be de-calibrated, e.g., due to electromagnetic interference, and properly cooled. The solid-state approach essentially converts the MW generation problem into an electronics and heat management problem, where one needs to deal with cooling of many semiconductor devices to maintain gain and phase balance. From an engineering standpoint, solid-state systems leverage advances in HF electronics, digital control, and thermal management to achieve what magnetrons do with vacuum physics.

Solid-state technology offers much improved operational longevity over magnetrons (i.e., > 100,000 vs. 8,000 hours lifetime) and better mechanical ruggedness. Notably, the magnetron is a 'single point of failure' generator, while solid-state generators typically consist of several sub-units; therefore, if a failure occurs in one or more sub-units, the system can still theoretically function [20]. Although the efficiency of contemporary solid-state MW power supplies is still lower compared to mature magnetron technology in many instances, advances in the field are quickly closing the gap, with some solid-state generators capable of > 60% efficiencies [21, 23]. Furthermore, solid-state systems will not deteriorate in power output or efficiency with time, as is the case with magnetron sources. Moreover, solid-state outshines tube-based amplifiers in modularity, as magnetron-based systems generally entail bulky waveguide distribution systems. As a result, solid-state MW power systems have some enticing advantages, which are particularly interesting for aerospace and ISRU applications, as they are a considerably more compact and portable form compared to high-voltage-powered magnetron systems [20].

This makes solid-state HF generators ideal candidates in ISRU, aerospace, and defense applications. For example, radiation hardness is a concern on Mars due to the lack of a protective ionosphere, which exposes the planet to high-energy radiation [24, 25]. Although radiation does affect semiconductors, smaller devices and active components exhibit reduced sensitivity [21, 25]. As an example, the GaN semiconductor, with its high energy density and small device area per transistor, is remarkably robust against radiation and is already prevalent in advanced aerospace and defense sectors [21, 25]. Furthermore, GaN offers advantages in miniaturization and weight reduction over traditional HF semiconductors (e.g., LDMOS) [21]. In essence, semiconductor-based HF generators hold great potential for Mars ISRU missions. A use case for this will be explored further in Chapter 5.

In summary, these technologies can be scaled to the power levels needed for plasma-based gas conversion, but they do so differently. Magnetron technology is very mature, having been in use for more than 80 years and used in billions of devices (ovens, radar, etc.) [12]. Solid-state technology, while mature in the communication and radar sectors, is relatively new to high-power continuous processing, such as what is needed in plasma-based gas conversion. Only in the last 10 - 15 years have solid-state MW generators at multi-kW levels become commercially viable for plasma applications; however, the

widespread implementation still faces challenges, including cost and availability of high-power devices. Magnetrons currently have the edge in raw high-power availability and efficiency (and cost, allowing cheaper scale-up), and therefore are still most relevant for use in plasma torches and large-scale plasma chemical processes. Solid-state provides a flexible, modular route with unparalleled power control (such as for pulsing, especially on the nanosecond scale), at the expense of greater complexity and currently higher cost. However, as solid-state generators continue to advance, they will offer new capabilities that were previously unavailable in conventional magnetron-based MW plasma systems. In essence, the feasibility for high-power (> 2 kW) plasma reactors is about choosing the right source to meet the process demands (efficiency, stability, maintenance).

2.2.3 Dielectric Resonators

While magnetrons and solid-state devices represent the dominant MW generators for plasma applications, Dielectric Resonator Oscillators (DROs) constitute an emerging class of MW sources that offer several compelling advantages distinct from both approaches. Unlike magnetrons, which are self-oscillating vacuum devices, or solid-state systems that rely on semiconductor amplification, DROs operate through electromagnetic field confinement within high-dielectric-constant ceramic or crystalline materials that serve as frequency-determining elements [26, 27].

The fundamental operating principle involves coupling energy from an external source into the dielectric resonator. At resonant frequencies, the microwaves form standing waves in the resonator, where the confinement mechanism enables precise frequency control while maintaining excellent stability [28]. Since the resonance frequency is primarily determined by the physical dimensions and dielectric properties of the resonator, leading to minimal frequency drift over time and temperature variations. This stability stems from the inherent properties of the ceramic materials used, which can be engineered to exhibit near-zero temperature coefficients, meaning that their dielectric constant and thus their resonant frequency changes very little with temperature. These devices have exceptional temperature stability, very low phase noise, and are compact in size [29]. These characteristics make DROs particularly attractive for applications requiring precise frequency control, such as phase-locked loop systems or frequency synthesis applications.

However, DROs also present critical limitations in terms of power (generally mW to low W range) making them less suitable for plasma-based CO₂ dissociation.

While DROs are not currently viable for high-power MW plasma applications due to their power limitations, they represent an important technological development due to their compact size and frequency stability. For example, this is particularly relevant to the ISRU context discussed in Chapter 5, where the combination of low power consumption, compact size, and exceptional frequency stability could make DROs valuable components in frequency synthesis chains that ultimately drive higher-power solid-state amplifiers. Their reliability and temperature stability characteristics align well with the demanding requirements of space environments, where maintenance and replacement are not feasible. As MW plasma technology continues to evolve toward more sophisticated control and diagnostic systems, DROs may find increasing application.

2.2.4 A Personal Reflection:

Field Experience with Solid-State Microwave Plasma Technology

Having worked extensively with both magnetron and solid-state devices throughout my research career, I present this section to offer practical insights that complement the theoretical discussion above. These experiences may help guide future researchers considering which technology to employ for their specific applications.

The power modulation capabilities of solid-state reactors are indeed unmatched by magnetron devices, as evidenced in the experiments described in subsequent chapters. For example, in Chapter 3, watt-by-watt control proved essential for investigating fundamental aspects of preheating, where minute power adjustments (e.g., 62 W) required precise control beyond magnetron capabilities. For such applications demanding high precision, solid-state technology offers clear advantages.

However, despite their advanced control capabilities, solid-state systems present several operational challenges that reflect current technological limitations. For example, the generator utilized in the Chapter 3 experiments was rated to be a 6 kW source; however, in practice, it was only ever able to deliver a maximum of approximately 5 kW, illustrating the combiner losses discussed in *Section 2.2.2*. Similarly, the 2 kW solid-state source employed in Chapters 4 and 5 reached only about 1.6 kW at maximum output.

These discrepancies highlight the need for careful consideration when specifying power requirements, which will ultimately increase overall system costs.

More significantly, the experimental setup described in Chapter 4 and 5 experienced recurring damage to power amplifiers, with individual channels suffering electronic component failures and coaxial cable damage. Thermal management presented many challenges, such as with cooling system blockages, that ultimately caused catastrophic failure. Post-failure analysis revealed complete burn-through of the coaxial port at the waveguide power combiner shown in Figure 2.3, warpage of the antenna assembly, and irreparable damage to the circulator with multiple fractures to the ferrite assembly. These failures occurred despite operating within the manufacturer's specified parameters, suggesting underlying design vulnerabilities in early-generation solid-state systems. While the initial damage stemmed from cooling system blockages, subsequent investigation revealed an inappropriately high shutdown temperature setting (100°C rather than the safer 70°C threshold). This experience underscores the need for robust cooling solutions with appropriate interlocks and flow meters in high-power solid-state plasma applications, which are not always accounted for in the system design.

Another critical consideration involves component specification. The isolator described in Chapters 4 and 5 was improperly rated (designed for only 3 kW total power without additional water cooling), which proved insufficient during high-reflection incidents, such as with phase mismatches or elevated reflections, which can damage electronic components in power amplifiers, potentially triggering cascading failures downstream without adequate protection.

These experiences align with the broader limitations of current solid-state technology described earlier in this chapter. While offering unprecedented control capabilities, these systems remain more complex, less robust to operational variations, and currently more expensive to repair or replace than their magnetron counterparts. For research applications requiring precise power modulation or high stability, such as those in Chapter 3, these trade-offs may be acceptable. However, for industrial applications or settings with limited technical support, magnetron-based systems still offer compelling advantages in simplicity and resilience.

By comparison, magnetrons offer a more "plug-and-play" approach, albeit with power

instabilities of approximately $\pm 10\%$. While unsuitable for highly precise power requirements, this stability range is adequate for less sensitive metrics. For instance, when studying conversion and energy efficiency, power instability effects average out across multiple measurements, making magnetrons perfectly suitable for many research endeavors.

As solid-state technology continues to mature, addressing these reliability challenges through improved thermal management, enhanced protection, and more robust interface components will be essential to achieve their full potential in plasma applications, but in my opinion, these devices should be considered a research endeavor of their own, requiring excellent technical support and seasoned researchers who understand the complexity and limitations. The integration of flow meters, appropriate interlocks, properly graded components, and more transparent power monitoring would significantly enhance system reliability.

2.3 Coupling, Contraction, and Flow Dynamics

2.3.1 Power Coupling to the Discharge

As discussed, MW plasmas are sustained through the interaction of electromagnetic waves with free electrons, which then transfer energy to the neutral gas molecules via collisions. Power coupling in MW plasmas is a complex process governed by Maxwell's equations, which describe the propagation of electromagnetic fields, and the Boltzmann kinetic equation, which characterizes the energy absorption dynamics of the charged particles [13]. Efficient power coupling is crucial for maintaining the discharge and strongly depends on wave-particle interactions, field penetration, and plasma parameters, such as electron density, pressure, and collisionality.

Maxwell's equations form the framework for understanding power coupling in MW plasmas, describing the propagation of the electromagnetic wave in the plasma medium. In an MW plasma discharge, the oscillating E-field interacts with free electrons, imparting energy through mechanisms such as Ohmic (or Joule) heating and wave-particle resonance (collisionless) heating by the E-field. This energy is subsequently transferred to the bulk gas through elastic and inelastic collisions. The link between Maxwell's equations and

the resonant and absorptive behavior of MW plasma comes from the Helmholtz equation, which describes how electromagnetic waves propagate and couple into a plasma:

$$\nabla^2 \overline{\mathbf{E}} + k^2 \overline{\mathbf{E}} = 0 \tag{2.1}$$

where $\nabla^2 \overline{\mathbf{E}}$ is the vectorized Laplacian of the electric field, $\overline{\mathbf{E}}$ is the electric field vector and k^2 is the square of the complex wave number; k has real (speed of wave propagation) and imaginary (attenuation coefficient) parts, and k^2 is defined as:

$$k^2 = \mu_0 \widehat{\varepsilon} \omega^2 \tag{2.2}$$

where μ_0 is the permeability of free space, ω is the wave frequency ($\omega = 2\pi f$), and where the dielectric permittivity of the plasma is $\hat{\varepsilon} = \varepsilon_0 \hat{\varepsilon}_R$, and with $\hat{\varepsilon}_R$ as a frequency-dependent quantity, i.e.,:

$$\widehat{\varepsilon}_R(\omega) = 1 - \frac{i\omega_p^2}{\omega(\nu_m + i\omega)}$$
 (2.3)

where ν_m is the electron-neutral collision frequency, i is imaginary unit (which satisfies $i^2 = -1$) and ω_p is the plasma frequency defined as:

$$\omega_p = \sqrt{\frac{n_e e^2}{\varepsilon_0 m_e}} \tag{2.4}$$

where n_e is the electron density, e is the electron charge, ε_0 is permittivity in vacuum, and m_e is the mass of an electron, with all other components defined above.

Importantly, whether waves in the plasma can propagate (when $\omega_p^2 > \omega^2 - \nu_m^2$) or whether they reflect ($\omega_p^2 > \omega^2 + \nu_m^2$). In the latter, ε_R becomes negative, which shifts the direction of the E-field [30]. This introduces a cutoff condition for wave penetration that is critical for efficient power coupling. This so-called plasma frequency cutoff acts similarly to a resonance layer where energy can be transferred to electrons via localized field enhancement or mode conversion [13]. The penetration of MW fields into plasma is also constrained by the skin depth (δ) [30, 31]:

$$\delta = \frac{1}{\omega_p} \sqrt{\frac{2\nu_m}{\omega}} \tag{2.5}$$

when $\nu_m > \omega$ (i.e., for high collisionality plasmas), with all variables defined above. As MW frequency increases, the skin depth decreases, leading to more localized energy deposition near the plasma boundary. In high-density plasmas, energy is mostly absorbed within a thin layer, requiring mechanisms such as surface wave excitation or traveling wave discharges to sustain volume ionization [32].

At sufficiently high gas pressure, collisional heating dominates, where electrons oscillating in the E-field continuously gain energy and lose it to collisions with heavy particles (such as neutrals and ions), transferring kinetic energy (which defines the electron temperature) into random thermal energy (defining the gas temperature) [13, 32]. The power absorbed per unit volume can be expressed in a simple steady-state picture, which can be set equal to power losses (through radiation, conduction, etc.), which turns into an energy balance that determines the electron and gas temperature [32]. However, at low pressures, electrons can still be heated through mechanisms like wave-particle resonance (collisionless heating) [13]. Regardless of the mechanism, the result is that electrons gain energy from the field, and these energetic electrons then transfer energy to the rest of the plasma through collisions or collisionless processes, heating the bulk and driving chemistry [13]. This understanding will become important in the following section.

For every system there is an optimum range of pressure and density for efficient power coupling. In MW discharges, there is a distinction between localized coupling (standing wave) and distributed (traveling wave) coupling [13]. The MW field forms standing wave patterns and high field intensities in specific regions [33], which can lead to very efficient local power deposition but potentially lower uniformity. In traveling-wave systems, like a surface-wave plasma, as is described in subsequent chapters, the wave propagates along the plasma, continuously depositing energy [34]. A surface-wave discharge is particularly interesting for coupling at densities beyond the usual cutoff frequency $(\omega_p^2 > \omega^2 + \nu^2)$ [35]. The electromagnetic wave in this case does not propagate through the plasma bulk, but along its surface, with fields decaying into the plasma [35]. This allows the plasma to be "overly dense" and still absorb power as the wave travels on the boundary and ionizes the gas along the way [34, 35]. Such coupling is strongly influenced by pressure and collisions, such that at high pressures, the surface wave is rapidly damped (giving

rise to long and narrow plasma columns, referred to as contracted, see *Section 2.3.2*), whereas at lower pressures the wave can sustain a broader profile (a more diffuse regime, see *Section 2.3.2*) [35].

In practice, ensuring efficient coupling in MW systems often requires impedance matching (e.g., using tuners or matching networks, as introduced in *Section 2.1* of this chapter) so that minimal power is reflected from the plasma. A well-coupled MW plasma can absorb > 90% of the incident power when tuned correctly [12], meaning that the system must also be matched to the characteristic impedance of the waveguide [36].

2.3.2 Contraction Dynamics

Plasma parameters, such as electron density (n_e) , gas pressure (or neutral density, n), and collisional frequency determine which coupling mechanisms dominate and how efficient the power transfer is [37–39]. As discussed in Section 2.3.1, the plasma frequency determines the permittivity of the plasma and thus whether the electromagnetic wave can propagate. As discussed, if n_e exceeds the critical density for a given frequency, a transverse electromagnetic wave will be reflected. In such 'over dense' conditions, coupling can still occur, for example via mode conversion (e.g., a surface wave along the plasma boundary), but it is inherently more challenging to drive energy into the plasma. On the other hand, if n_e is too low, there are not enough charged particles to absorb the power, and most of the field may pass through or remain underutilized. There is often an optimal density range where n_e exhibits a 'sweet spot'. It is low enough for the wave to penetrate, while still high enough to absorb a significant fraction of the power. Once a plasma is sustained, feedback occurs, where higher absorbed power tends to raise n_e , which in turn can increase shielding (reducing penetration). This nonlinear behavior leads to multiple operating modes.

In CO₂ MW plasmas, there are distinct discharge modes characterized into three categories, which are broadly determined by power, pressure, and gas flow rate [31, 37, 39], and images are presented in *Figure 2.3*.

As shown in Figure 2.3 [31], at low pressure (< 100 mbar) or power density, the plasma often remains in homogeneous or L-mode (i and ii), as characterized by uniform temperature, as well as relatively low power density profiles [31]. At low pressure, the collisional

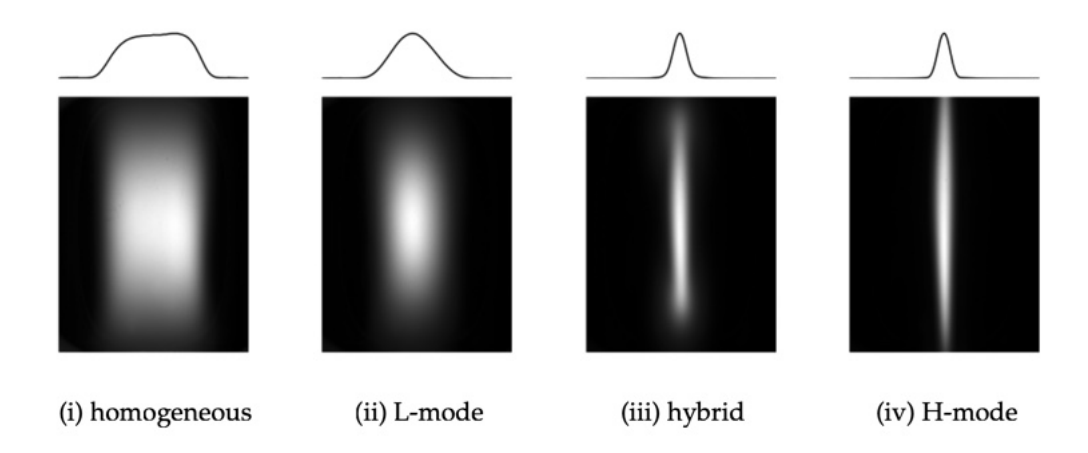


FIGURE 2.4: CCD images of the emission intensity profile of the four stages with increasing pressure (left to right) of vortex-stabilized CO_2 MW plasma. Image courtesy of Wolf et al. [31].

frequency is much smaller than ω , so electrons oscillate 'freely'. In this regime, collisionless heating mechanisms become important, as briefly discussed in Section 2.3.1. The efficiency of power coupling might drop if there is no mechanism for electrons to gain phase-randomized energy; however, discharges tend to always have some inhomogeneity at boundaries that allow phase mixing (e.g., electrons interact with the sheaths or spatial gradients to gain energy). As pressure increases, the hybrid mode arises (iii, typically between 100-200 mbar), balancing partial contraction with sufficient homogeneity to maintain high energy efficiency and mixing [31].

Above ~200 mbar, steep radial gradients arise, leading to a contracted mode (iv, H-mode). These transitions are driven by thermal-ionization instability [31], where localized heating boosts ionization rates, creating dense filaments with elevated temperatures and enhanced microwave absorption [38]. This mechanism favors Ohmic heating, where power coupling is akin to a current driving through a narrow conductor in a resistive medium [39]. High-pressure plasmas thus tend to have more uniform, volumetric heating; however, much of the energy goes into random thermal motion (ultimately gas heating) rather than selective excitation. Additionally, high collisionality means shorter skin depth (better absorption near the edge but potentially preventing the center from receiving field energy).

Several mechanisms govern contraction [1, 31, 37–41]. Electron collisions (particularly in the plasma core) can increase ionization rates, while radial temperature gradients modify the reduced electric field (E/n) and reduce charged-particle losses from the plasma volume [42]. This positive feedback leads to narrow, high-power density regions with significant

temperature elevation; however, it can limit the overall reaction volume, as contracted (H-mode) plasmas exhibit a reduced interface between the reactive high-temperature zone and the bulk gas of the reaction chamber. Consequently, the hybrid regime often emerges as the optimal mode for CO₂ conversion, balancing localized heating with adequate mixing and quenching. However, this regime requires vacuum pumping, which uses additional power from plug to product [43].

2.3.3 Flow Dynamics

Flow dynamics in MW plasmas govern discharge stability, spatial plasma characteristics, and the transport of reactants in and out of the reactive volume. The interaction between gas flow, electromagnetic fields, and plasma contraction mechanisms results in complex behaviors that define reactor performance.

Vortex flows are commonly employed in MW plasma reactors to confine the plasma core and minimize heat loss to the walls. Typically, a vortex is generated through tangential gas injection, with the injection velocity directly influencing vortex strength [44]. This thesis focuses on the 'forward vortex' flow configuration, as illustrated in *Figure 2.4*.

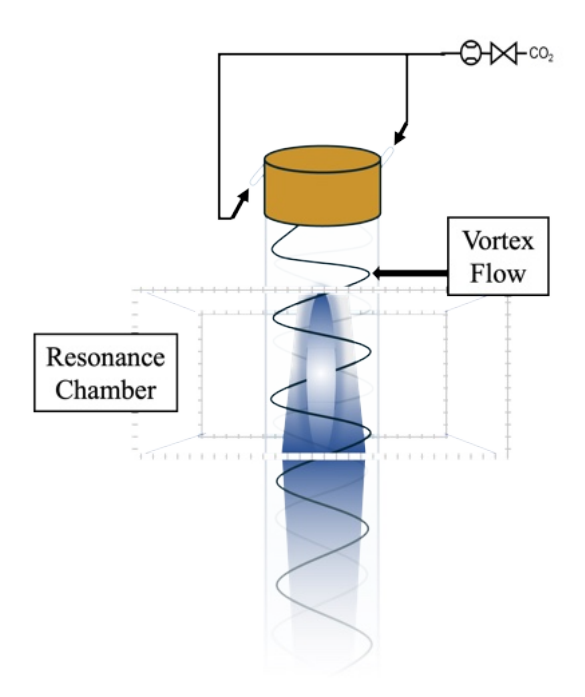


FIGURE 2.5: Schematic of a forward vortex flow in a MW reactor, resulting in a plasma centered in the quartz tube.

In forward vortex stabilized MW plasma systems, the flow strongly influences heat transfer and molecular transport. Tangential gas injection confines the plasma core, promoting steep radial temperature gradients [45]. The gas flow dynamics plays a crucial role in stabilizing the discharge, centering it within the reaction chamber (in our case, a quartz tube), while it transports heat away from the plasma core, creating steep temperature gradients. This in turn enhances radial diffusion and mixing, governing the transport of reactants to and from the reactive volume and facilitates product extraction, which is particularly relevant in CO_2 conversion [46]. The plasma volume exhibits increased kinematic viscosity due to the high temperature (in the range of $\sim 6000 - 8000$ K for contracted discharges), potentially reducing mixing and forming boundary layers. These effects can lead to slippage, wherein a fraction of the gas bypasses the reactive volume along cooler wall regions, limiting overall conversion [4]. Furthermore, there is evidence suggesting that the forward vortex configuration may give rise to recirculation cells near the injection point [47], resulting in partially closed flow lines, and where the plasma may lie in plane with these regions [48].

2.4 Implications for MW-based Plasma Conversion of CO₂

A key challenge in MW plasma-based CO_2 conversion is thermal management. While high gas temperatures ($\gg 3000 \text{ K}$) in the core of a contracted plasma effectively drive CO_2 dissociation through thermal pathways, they simultaneously promote recombination reactions in the afterglow region, limiting overall conversion. Consequently, research efforts have increasingly focused on optimizing the dissociation of CO_2 to CO using MW plasma systems to advance industrial viability, which requires maximizing overall system efficiency [1, 2, 5, 7, 31, 39, 45, 49, 50]. Thus, much of the research emphasis is on progressing the community's understanding of what limits high conversion and energy efficiency [3-5, 37, 38, 42, 43, 51]. Typically, current state-of-the-art approaches achieve conversions below 20% and energy efficiencies well below 50% at atmospheric pressure, with much of the input energy being lost through radiative and conductive pathways [1, 3-5, 31].

2.4.1 Plasma-Based CO₂ Dissociation

The dissociation of CO₂ in plasma follows a complex sequence of energy transfer processes, involving rotational, vibrational, and electronic excitation. Understanding these pathways is crucial for optimizing CO₂ conversion, particularly in MW plasmas. As discussed throughout this chapter, in a MW plasma discharge, free electrons gain energy from the applied electromagnetic field and transfer it to CO₂ molecules through collisions.

Recent experimental evidence has revealed that thermal processes play a dominant role in CO_2 dissociation in contracted MW plasmas (generally, p > 200 mbar), with gas temperatures in the plasma core reaching ~ 6000 K, and temperatures in the surrounding region well above 3000 K [1, 3, 31, 39, 45, 52]. It has indeed been confirmed that MW plasmas under these conditions are fully thermalized and strongly nonuniform due to steep temperature gradients [5, 31, 37–39]. At these conditions, CO_2 follows a thermal decomposition pathway [53]:

$$CO_2 + M \rightleftharpoons CO + O(^3P) + M, \quad \Delta H = 5.5 \text{ eV}$$
 (R2.1)

where M can represent any molecule, and ΔH represents the enthalpy of the dissociation process per molecule [53, 54]. Thermal dissociation of CO_2 occurs when the gas is heated to sufficiently high temperatures, typically $\gg 1500$ K [5], where molecular collisions and energy transfer lead to bond breaking. This process is driven by the high internal energy of the gas and is influenced by heat transfer mechanisms within the plasma. Furthermore, atomic oxygen present within the plasma volume can react with (ground state or vibrationally excited) CO_2 , denoted here as $CO_2(v \ge 0)$, where an additional CO molecule is formed, and energy efficiency is enhanced [53]:

$$O + CO_2(v > 0) \rightleftharpoons CO + O_2, E_q = 0.5 - 3 \text{ eV}$$
 (R2.2)

Indeed, a model presented by van Poyer et al. shows that R2.1 is the main driver to net CO production in the outer regions of the reactive zone; however as temperatures drop sufficiently towards the edges, R2.2 is shown to contribute significantly to CO production [46].

Here, it becomes essential to distinguish between the plasma size and the reactive volume. For thermal processes like CO₂ dissociation, the reactive volume is primarily determined by the temperature distribution rather than the electron density [5, 37, 39]. The temperature-defined 'reactive volume' is fundamental to plasma chemistry and represents the region where chemically active species are present in sufficient concentrations, driving reactions. In MW plasmas specifically, the power absorption profile, heat transfer mechanisms, and gas flow dynamics collectively determine the spatial extent of the plasma volume (contraction state) and reactive volume. We characterize this distinction by noting that while the plasma volume is defined by quasi-neutrality and collective behavior of charged particles, the reactive volume encompasses the entire region where plasma-generated species (including excited neutrals, radicals, and metastable species) participate in reactions that provide products of interest.

For example, in the work of Wolf et al. [31], a plasma diameter of ~ 2.1 mm was obtained at p=500 mbar, P=860 W, and a flow rate = 12 slm. In contrast, spectroscopic measurements from the same study reveal elevated temperatures within a reactive area of ~ 5.0 mm in diameter [31]. Work by van de Steeg et al. showed that within the reactive volume, the temperature dictates the density of species [3], with the plasma volume exhibiting a high fraction of O and CO molecules, as shown in Figure 2.5 [3].

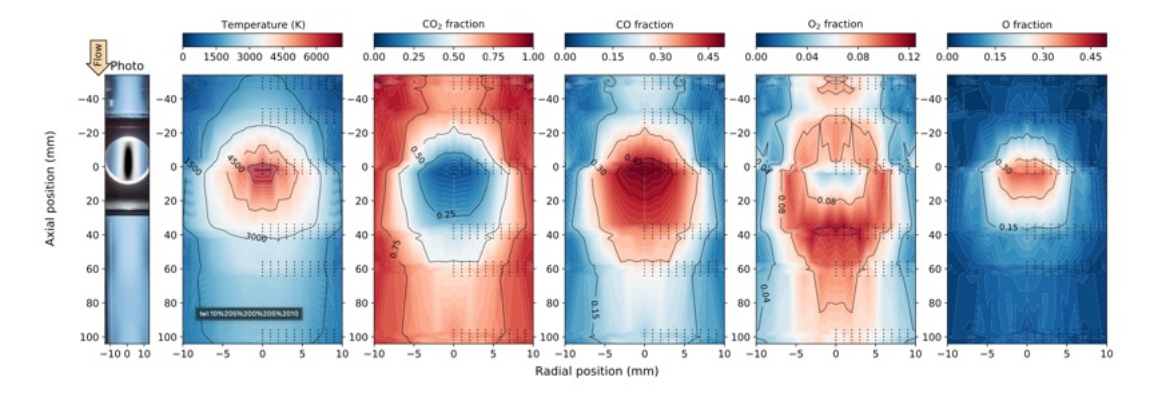


FIGURE 2.6: Image courtesy of van de Steeg et al. [3] showing the plasma emission and spatially resolved Raman results from a 10 slm, 120 mbar, 1000 W $\rm CO_2$ plasma. The map represents the rotational temperature, $\rm CO_2$ fraction, $\rm CO$ fraction, $\rm O_2$ fraction and O fraction. The emission map is an overlay of total emission and 777 nm oxygen emission in the core, with the black dots representing Raman spectra collection.

In Figure 2.5 [3], it is easy to visualize how the reactive volume is characterized by chemical non-equilibrium, as described in the work by van de Steeg et al. Although these conditions are presented for a lower pressure regime (120 mbar) and the core plasma temperature is

much lower ($\sim 3500 - 4000 \,\mathrm{K}$) [3] than is found in a fully contracted H-mode plasma ($\sim 6000 \,\mathrm{K}$) [5, 31], we expect to find greater chemical non-equilibrium in contracted plasmas due to steeper temperature gradients. Recent modeling studies by van Poyer et al. indeed indicate that CO production occurs mainly at the edges of the plasma volume and is driven by net species transport [46]. The temperature profile within the reactive volume peaks with the core plasma temperature and begins a steady decline radially and axially from the plasma volume. Moreover, the work by van Poyer et al. shows that the temperature in the core of H-mode CO_2 plasma leads to full dissociation to C and O or O_2 , which is evident in optical emission spectroscopy measurements with dominant C_2 swan bands [52], further evidence of thermally dominated dissociation processes [55]. These species rapidly diffuse radially out of the plasma volume, recombining to CO_2 or for example, in the case of O or O_2 , resulting in the direct dissociation of CO_2 (R2.2).

The inhomogeneous chemical non-equilibrium behavior is driven by diffusion velocities, and characterized by cylindrical symmetry within the reactor, with the radial direction dominated by turbulent diffusion and the axial direction dominated by the transport of molecules out of the reactive volume into the cooler, post-plasma region where the temperature drops until the chemistry is 'frozen' [5, 46]. As can be observed in *Figure 2.5* [3], radially, from the plasma volume, the fraction of CO₂ increases, until the wall is reached, where unreacted CO₂ molecules dominate, generally referred to as 'gas slippage' in forward vortex stabilized reactors [4]. Gas slippage represents a large fraction of untreated reactant gas and leads to less efficient conversion within the reactor.

2.4.2 Post-Plasma Afterglow Quenching

Once the temperature drops below ~ 3000 K in the reactive volume, CO to CO₂ net recombination competes with dissociation pathways, and energy efficiency may drop due to recombination mechanisms as products (CO) are converted back to reactants (CO₂). This region of intense recombination is called 'burn back', and is typically observed as a blue afterglow in CO₂ MW plasmas (so called 'flame bands' [56]), as shown in *Figure 2.6*.

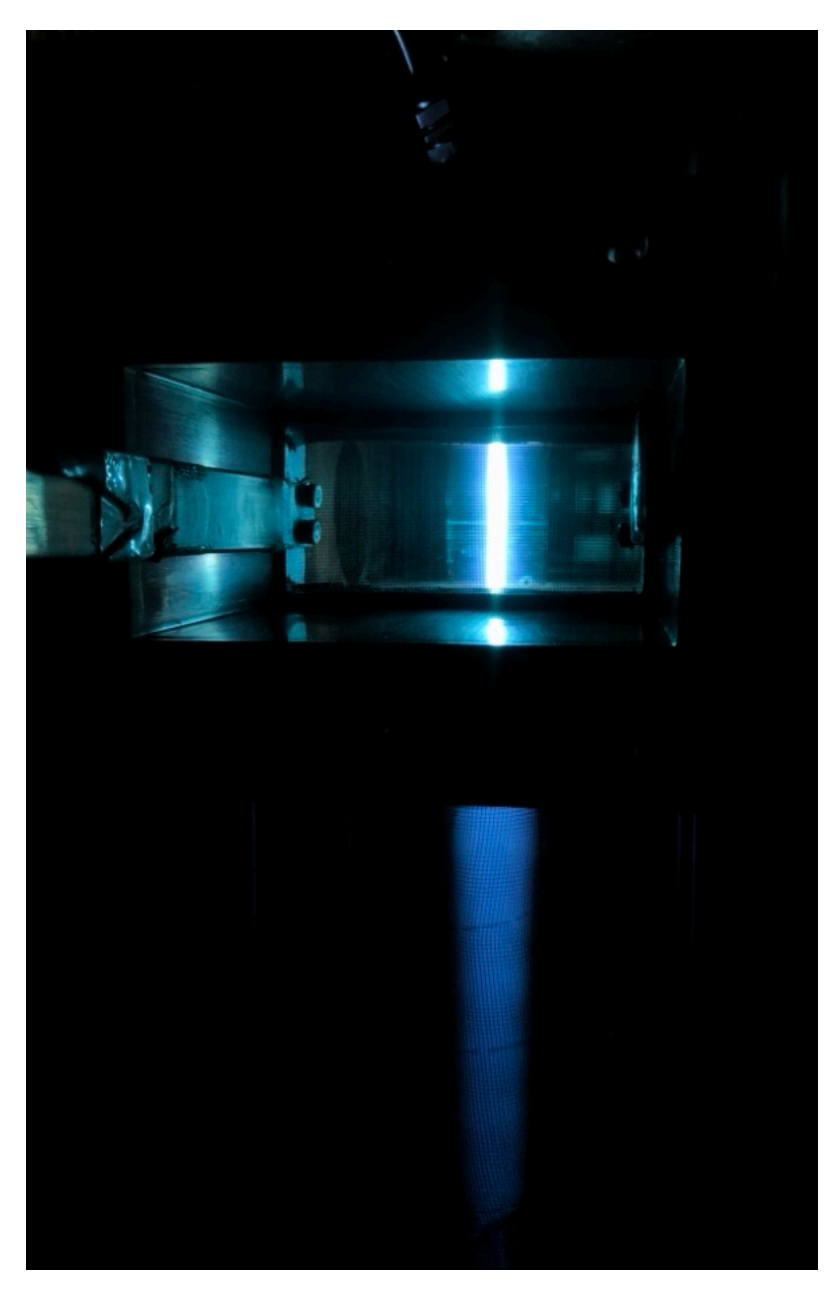


Figure 2.7: Image of a 2.45 GHz MW $\rm CO_2$ plasma with characteristic 'afterglow' resulting from flame band emission.

Flame bands result from the recombination of CO and O to form electronically excited CO_2 , which subsequently emits chemiluminescent radiation across a broad spectral range ($\sim 265-700$ nm), as can be observed in *Figure 2.6*. The emission process follows a reaction chain, as direct recombination to ground state CO_2 is a forbidden transition [56]:

$$CO(^{1}\Sigma_{q}^{+}) + O(^{3}P) + M \rightleftharpoons CO_{2}(1^{3}B_{2}\Sigma_{u}^{+}) + M$$
(R2.3)

$$CO_2(1^3B_2\Sigma_u^+) + M \rightleftharpoons CO_2(1^1B_2\Delta_u) + M$$
 (R2.4)

$$CO_2(1^1B_2\Delta_u) + M \rightarrow CO_2(1\widetilde{X}\Sigma_q^+) + M$$
 (R2.5a)

$$CO_2(1^1B_2\Delta_u) \to CO_2(1^1\widetilde{X}\Sigma_g^+) + h\nu$$
 (R2.5b)

Thus, the recombination process first proceeds via R2.3, where ground state CO and O recombine to excited CO₂ in a triplet state, which can then transition to a singlet state via R2.4 (typically a collisional-induced transition) [56]. Finally, the excited CO₂ can be quenched to the ground state via R2.5a or undergo radiative transition, releasing a photon (R2.5b) [56]. The wavelength-dependent emission intensity (I_{γ}^{λ}) can be described by an Arrhenius-type expression:

$$I_{\gamma}^{\lambda} = \kappa_{\gamma}^{\lambda}(T)[\text{CO}][\text{O}]$$
 (E2.6)

where $\kappa_{\gamma}^{\lambda}(T) = \kappa_0^{\lambda} e^{(-E_a^{\lambda}/T)}$, with κ_0^{λ} and E_a^{λ} representing a wavelength-dependent prefactor and activation energy, respectively [56]. This characteristic flame band emission profile will be further investigated in Chapter 3.

The reader should remember that dissociation and recombination co-occur under these conditions. Still, as we investigate the effects of these mechanisms, we define temperature profiles at which the pathway to conversion or recombination dominates. Where the temperature is between 2000 - 3000 K, the dominant reaction pathway is the recombination of CO with O [3, 5, 31, 46, 56]. If the cooling trajectory in the post-plasma temperature can be quickly cooled or 'quenched' to below 2000 K, O association to O₂ occurs faster than recombination with CO to CO₂, and thus more CO would be retained, given that CO recombination with O₂ has a significant reaction barrier. It is crucial to note that at increased pressures (p > 200 mbar), the required time for chemical reactions to

achieve equilibrium composition (< 0.01 ms at T > 4000 K) is significantly shorter than the expected residence time (> 0.1 ms) of the gas in the reactive volume [5, 31]. This implies that the production of CO within the plasma region is not a limiting factor, and the overall conversion achieved is mainly a function of post-plasma recombination.

These aspects of MW plasmas carry significant implications for the design and optimization of MW reactors. The high temperatures observed in the reactive volume highlight the importance of thermal dissociation pathways and suggest that careful management of gas temperature and thermal loss mechanisms, from inlet to effluent, are critical for improving overall system performance.

2.4.3 From Earth to Mars: Low Pressure Plasma Applications

Beyond terrestrial CCU applications, plasma-based CO_2 conversion holds promise for ISRU on Mars. With the Martian atmosphere having an ambient pressure of approximately 7 mbar and a composition dominated by CO_2 (\sim 96%), the Red Planet presents an ideal case for low-pressure MW plasma applications. The inherent flexibility of MW plasma technology makes it particularly suitable for such extraterrestrial applications of CO_2 conversion.

As described in Section 2.3.1, at significantly low pressures (< 100 mbar), the electronneutral collision frequency (ν_m) decreases significantly, altering the plasma-field interaction. The relationship between ν_m and the wave frequency (ω) determines the dominant coupling mechanism. When $\nu_m < \omega$, as occurs in low-pressure, homogeneous discharges, electrons will be heated through mechanisms like wave-particle resonance [13]. This changes the nature of energy transfer from purely collisional (Ohmic) heating to collisionless heating.

This shift in the energy transfer mechanism has several important consequences. First, the reduced collisional frequency alters the dielectric permittivity of the plasma (ε_R as defined in E2.3), which affects wave penetration and field distribution, characterizing this low-pressure regime as hollow and under-dense and does not follow the thermal-ionization instability due to a lack of self-intensifying electron-density growth [31]. As

discussed in Section 2.3.2, contraction mechanisms are pressure-dependent, where low-pressure discharges are characterized by the homogeneous mode or L-mode (Figure 2.3), and have significantly lower core plasma temperatures ($<\sim3000 \text{ K}$) [31].

As a result, low-pressure MW plasmas feature a pronounced thermal non-equilibrium, with electron temperature substantially exceeding the vibrational temperature, which in turn exceeds rotational and translational temperatures [13]. Thus, it has been hypothesized that if sufficient energy is given to electrons without energy transfer to heat ions and atoms, in principle, higher energy efficiency compared to conventional thermal chemistry can be achieved [13, 53]. Under these conditions, electrons can selectively excite the vibrational modes of CO₂, where vibrational excitation lowers the effective dissociation threshold (e.g., via vibrational ladder climbing), and can enhance dissociation by decreasing the activation barrier [53]:

$$e^{-} + CO_2(v \ge 1) \rightleftharpoons CO + O(^{3}P) + e^{-}$$
 (R2.6)

Thus, enhanced vibrational-translational non-equilibrium at low pressures offers a pathway to overcome the energy efficiency limitation typically observed in thermal-dominated CO₂ conversion at atmospheric pressure [57], a shift which highlights a compelling advantage for applications like Martian ISRU systems, where the ambient pressure (approximately 7 mbar) naturally favors these more efficient conversion pathways [58–63].

Importantly, the flow dynamics in low-pressure (< 100 mbar) also differs markedly from higher pressure operation. For a fixed mass flow rate, the gas velocity increases inversely with pressure, leading to shorter residence times, and likely enhanced periphery quenching effects [5, 31]. This can be particularly beneficial for CO_2 conversion, as it accelerates the extraction of products from the reactive volume before recombination can occur. The rapid cooling trajectory helps preserve CO molecules produced in the plasma by reducing recombination (Section 2.4.2). Additionally, a diffuse plasma takes up a larger reactive volume, increasing the CO production interface [46], which may help mitigate gas slippage, enhancing overall CO_2 dissociation. These differences can be strategically leveraged to enhance CO_2 conversion performance, particularly in specialized applications like Martian resource utilization, which will be explored in greater detail in Chapter 5.

2.5 Rationale of this Thesis

This chapter has established that while MW plasma technology offers remarkable versatility and potential for CO₂ conversion, practical implementation requires careful optimization of multiple interdependent parameters. The theoretical principles of MW plasma technology for greenhouse gas conversion outlined here provide the foundation for the experimental investigations presented in the following chapters. The interplay of plasma contraction and flow dynamics establishes a framework for optimizing CO₂ conversion in MW plasma systems. Understanding these fundamental processes is crucial for addressing key challenges in MW plasma-based CO₂ utilization, such as improving conversion, enhancing energy efficiency, and controlling product formation. By understanding the fundamental mechanisms, we can identify specific opportunities to enhance conversion and energy efficiency through targeted studies.

As discussed in Section 2.4.1, the CO₂ conversion in contracted MW plasmas is largely governed by thermal chemistry, with temperatures in the reactive volume exceeding 3000 K. The significant thermal energy present in these systems suggest that strategic heat recovery could enhance process efficiency. However, the specific effects of preheating on CO₂ MW plasmas remains unexplored. Chapter 3 investigates how preheating the inlet gas affects plasma contraction dynamics, temperature profiles, and conversion. This approach targets the challenge of thermal management outlined in Section 2.4.1 and 2.4.2, evaluating whether redirecting waste heat to preheat the reactant gas can enhance performance, particularly at higher pressures where conversion and energy efficiency typically declines.

Building on our understanding of thermal management, Chapter 4 takes a complementary approach by exploring how thermal energy available in the afterglow might be utilized for additional chemistry through reactive quenching. The concepts described in Section 2.4.2 highlight that post-plasma quenching is important for preserving CO formed in the reactive volume. The temperature profile in the afterglow region, where temperatures between 2000 – 3000 K favor recombination of CO with atomic O, presents an opportunity for chemical trapping. By injecting CH₄ as a reactive quenching agent into the high-temperature afterglow region, we aim to leverage this thermal energy while simultaneously addressing the challenge of product recombination. This approach extends our

understanding of the importance of flow dynamics (Section 2.3.3), exploring how secondary injection affects reaction pathways. Furthermore, this configuration potentially provides a novel approach to Dry Reforming of Methane (DRM) that avoids the plasma instability issues typically encountered with conventional admixing approaches, where solid carbon formation in the plasma volume can couple with the MW field.

The insights gained from manipulating plasma conditions at atmospheric and near-atmospheric pressures naturally lead to questions about performance under more extreme sub-atmospheric pressure conditions. The unique characteristics of MW plasmas at reduced pressures, as described in Section 2.4.3, create opportunities for specialized applications. Moving from the higher-pressure regimes explored in Chapters 3 and 4, Chapter 5 investigates performance under significantly reduced pressure conditions, specifically targeting Martian atmospheric pressure. The Martian atmosphere, with its predominant CO₂ composition and low ambient pressure (approximately 7 mbar), represents an ideal environment for MW plasma-based gas conversion. The non-equilibrium conditions achievable at these low pressures potentially allow for efficient vibrational excitation pathways that may enhance conversion. Furthermore, the low pressures will also enhance flow velocities that could potentially boost periphery quenching. This investigation also provides insight into the potential advantages of solid-state technology (Section 2.2.2) for space applications, where reliability, power modulation, and operational longevity are critical considerations beyond the efficiency metrics that dominate Earth-based applications.

Collectively, this research forms a comprehensive investigation aimed at addressing key challenges in MW plasma-based CO₂ conversion: thermal management, post-plasma chemistry, and specialized low-pressure applications. By systematically examining these aspects, this work aims to enhance conversion and energy efficiency, contributing to the development of MW plasma technology for CO₂ conversion, from Earth to Mars.

By addressing these main questions, the thesis aims to enhance the fundamental understanding of MW-based plasma-chemical conversion and pave the way for future industrial deployment of microwave plasmas in a circular carbon economy.

The following are the focus points of this thesis:

DRM.

1. How can MW plasma technology be optimized to achieve efficient and scalable CO₂ conversion?

This overarching question centers on identifying the key parameters, such as inlet temperature, gas flow configuration, and pressure, that govern MW plasma performance. Specifically, Chapter 3 looks at how inlet gas temperatures affect performance metrics, whereas Chapter 4 investigates gas flow configurations. By systematically exploring how each parameter affects CO₂ conversion and energy efficiency, the work aims to uncover strategies for maximizing industrial feasibility.

- 2. What role does thermal management (e.g., preheating, heat recovery, quenching) play in improving CO_2 plasma conversion and preventing product recombination?

 A central hypothesis explored in Chapter 3 is that preheating the inlet CO_2 stream, or quenching the high-temperature afterglow region as investigated in Chapter 4, could shift the plasma temperature profile in beneficial ways, either by enhancing dissociation or suppressing recombination. Testing this hypothesis clarifies how thermal management techniques can reduce overall energy consumption, extend near-atmospheric operation, and potentially inform reactor-scale solutions.
- 3. Can integrating secondary reactants (e.g., CH₄) in the afterglow through methods of reactive quenching boost conversion and energy efficiency?
 By introducing CH₄ after the plasma core, Chapter 4 investigates whether reactive quenching can harness the plasma's residual heat for additional chemistry while mitigating unfavorable carbon formation normally formed in conventional (admixing)
- 4. How can MW plasma reactors be adapted to the Martian environment in an ISRU context?

Although the thesis primarily addresses Earth-based carbon utilization, it also explores operation at near Martian atmospheric pressure in Chapter 5. The goal is to determine whether sub-atmospheric MW plasma conditions can produce valuable products (i.e., CO, O_2 , and also NO_x , for fertilizer applications) at a competitive energy cost.

Bibliography

- [1] F.A. D'Isa, E.A.D. Carbone, A. Hecimovic, and U. Fantz. Performance analysis of a 2.45 GHz microwave plasma torch for CO₂ decomposition in gas swirl configuration. *Plasma Sources Science and Technology*, 29(10):105009, 2020. doi: 10.1088/1361-6595/abaa84.
- [2] A. Hecimovic, F.A. D'Isa, E. Carbone, and U.Fantz. Enhancement of CO₂ conversion in microwave plasmas using a nozzle in the effluent. *Journal of CO₂ Utilization*, 57: 101870, 2022. doi: 10.1016/j.jcou.2021.101870.
- [3] A. van de Steeg, P. Viegas, A. Silva, T. Butterworth, A. van Bavel, J. Smits, P. Diomede, M.C.M. van de Sanden, and G. van Rooij. Redefining the microwave plasma-mediated CO₂ reduction efficiency limit: the role of o-CO₂ association. ACS Energy Letters, 6(8):2876–2881, 2021. doi: 10.1021/acsenergylett.1c01206.
- [4] C.F.A.M. van Deursen, H.M.S. van Poyer, W.A. Bongers, F.J.J. Peeters, F.M.A. Smits, and M.C.M. van de Sanden. Effluent nozzles in reverse-vortex-stabilized microwave CO₂ plasmas for improved energy efficiency. *Journal of CO₂ Utilization*, 88: 102952, 2024. doi: 10.1016/j.jcou.2024.102952.
- [5] E.R. Mercer, S. van Alphen, C.F.A.M. van Deursen, T.W.H. Righart, W.A. Bongers, R. Snyders, A. Bogaerts, M.C.M. van de Sanden, and F.J.J. Peeters. Post-plasma quenching to improve conversion and energy efficiency in a CO₂ microwave plasma. Fuel, 334:126734, 2023. doi: 10.1016/j.fuel.2022.126734.
- [6] H. Lamberts-Van Assche, G. Thomassen, and T. Compernolle. The early-stage design of plasma for the conversion of CO₂ to chemicals: A prospective techno-economic assessment. *Journal of CO₂ Utilization*, 64:102156, 2022.

[7] W.A. Bongers, H. Bouwmeester, A.J. Wolf, F.J.J. Peeters, S. Welzel, D. van den Bekerom, N. den Harder, A. Goede, M. Graswinckel, and P.W. Groen. Plasmadriven dissociation of CO₂ for fuel synthesis. *Plasma Processes and Polymers*, 14(6): 1600126, 2017. doi: 10.1002/ppap.201600126.

- [8] G.J. van Rooij, H.N. Akse, W.A. Bongers, and M.C.M. van De Sanden. Plasma for electrification of chemical industry: A case study on CO₂ reduction. *Plasma Physics* and Controlled Fusion, 60(1):014019, 2017. doi: 10.1088/1361-6587/aa8f7d.
- [9] R. Snoeckx and A. Bogaerts. Plasma technology a novel solution for CO₂ conversion? Chemical Society Reviews, 46(19):5805–5863, 2017. doi: 10.1039/C6CS00066E.
- [10] M.Y. Ong, S. Nomanbhay, F. Kusumo, and P.L. Show. Application of microwave plasma technology to convert carbon dioxide (CO₂) into high value products: A review. *Journal of Cleaner Production*, 336:130447, 2022. doi: 10.1016/j.jclepro. 2022.130447.
- [11] A.A. Zamri, M.Y. Ong, S. Nomanbhay, and P.L. Show. Microwave plasma technology for sustainable energy production and the electromagnetic interaction within the plasma system: A review. *Environmental Research*, 197:111204, 2021. doi: 10.1016/j.envres.2021.111204.
- [12] D.M. Pozar. Microwave engineering. Fourth Editions, University of Massachusetts at Amherst, John Wiley & Sons, Inc, pages 26–30, 2012.
- [13] A. Fridman. Plasma chemistry. Cambridge university press, 2008.
- [14] Encyclopædia Britannica. Typical elements of a magnetron, 2010. URL https://www.britannica.com/technology/magnetron#/media/1/357510/137.
- [15] R. Ludwig. Rf circuit design: Theory & applications, 2/e. 2000.
- [16] M.V. Kartikeyan, E. Borie, and M.K.A. Thumm. Basic Principles and Gyrotron Cavities. Advanced Texts in Physics. Springer, Berlin, Heidelberg, 2004. doi: 10. 1007/978-3-662-07637-8_3.
- [17] K. Sakamoto, A. Kasugai, K. Takahashi, R. Minami, N. Kobayashi, and K. Kajiwara. Achievement of robust high-efficiency 1 MW oscillation in the hard-self-excitation region by a 170 GHz continuous-wave gyrotron. *Nature Physics*, 3(6):411–414, 2007. doi: 10.1038/nphys599.

[18] N.V. Chekmarev, D.A. Mansfeld, A.V. Vodopyanov, S.V. Sintsov, E.I. Preobrazhensky, and M.A. Remez. Enhancement of CO₂ conversion by counterflow gas quenching of the post-discharge region in microwave plasma sustained by gyrotron radiation. *Journal of CO₂ Utilization*, 82:102759, 2024. doi: 10.1016/j.jcou.2024.102759.

- [19] D. Mansfeld, S. Sintsov, N. Chekmarev, and A. Vodopyanov. Conversion of carbon dioxide in microwave plasma torch sustained by gyrotron radiation at frequency of 24 GHz at atmospheric pressure. *Journal of CO₂ Utilization*, 40:101197, 2020. ISSN 2212-9820. doi: 10.1016/j.jcou.2020.101197.
- [20] R.J. Trew. High-frequency solid-state electronic devices. *IEEE Transactions on Electron Devices*, 52(5):638–649, 2005. doi: 10.1109/TED.2005.845862.
- [21] U.A.K. Betz, L. Arora, R.A. Assal, H. Azevedo, J. Baldwin, M.S. Becker, S. Bostock, V. Cheng, T. Egle, and N. Ferrari. Game changers in science and technology - now and beyond. *Technological Forecasting and Social Change*, 193:122588, 2023.
- [22] V. Ratnaparkhi and A. Hiwale. 35 W GaN solid-state driver power amplifier for l-band radar applications. pages 1–7, 2018.
- [23] G. Kazakevich, R. Johnson, G. Flanagan, F. Marhauser, V. Yakovlev, B. Chase, V. Lebedev, S. Nagaitsev, R. Pasquinelli, N. Solyak, K. Quinn, D. Wolff, and V. Pavlov. High-power magnetron transmitter as an rf source for superconducting linear accelerators. Nuclear Instruments and Methods in Physics Research Section A: Accelerators, Spectrometers, Detectors and Associated Equipment, 760:19–27, 2014. doi: 10.1016/j.nima.2014.05.069.
- [24] D. Beaty, S. Borowski, B. Cataldo, J. Charles, C. Conley, D. Craig, J. Elliot, C. Edwards, W. Engelund, D. Eppler, S. Feldman, J. Garvin, S. Hoffman, J. Jones, F. Jordan, S. Klug, J. Levine, J. Mulqueen, G. Noreen, H. Price, S. Quinn, J. Sanders, J. Schier, L. Simonsen, G. Tahu, and A. Tripathi. Human exploration of Mars design reference architecture. page 406, 2009. URL https://www.nasa.gov/wp-content/uploads/2015/09/373667main_nasa-sp-2009-566-add.pdf?emrc=8b2e96.
- [25] V. Maiwald, D. Schubert, D. Quantius, and P. Zabel. From space back to earth: supporting sustainable development with spaceflight technologies. *Sustainable Earth*, 4(1):3, 2021. doi: 10.1186/s42055-021-00042-9.

[26] K. W. Lee and W. R. Day. Varactor tuned dielectric resonator GaAs FET oscillator in X-band. In 1982 IEEE MTT-S International Microwave Symposium Digest, pages 274–276, 1982. doi: 10.1109/MWSYM.1982.1130688.

- [27] J. Lee, J. E. Andrews, K. W. Lee, and W. R. Day. Digital and analog frequency temperature compensation of dielectric resonator oscillators. In 1984 IEEE MTT-S International Microwave Symposium Digest, pages 277–279, 1984. doi: 10.1109/ MWSYM.1984.1131763.
- [28] A.E. Muhammad-Afifi and W. Ismail. High tuning sensitivity dielectric resonator oscillator from optimization of dielectric resonator $\text{TE}_{01\delta}$ mode. *Microwave Journal*, 52(9):98-116, 2009.
- [29] P. Stockwell, D. Green, C. McNeilage, and J. H. Searls. A low phase noise 1.3 GHz dielectric resonator oscillator. In 2006 IEEE International Frequency Control Symposium and Exposition, pages 882–885, 2006. doi: 10.1109/FREQ.2006.275506.
- [30] W. Zhang, L. Wu, K. Huang, and J. Tao. Propagating modes of the travelling wave in a microwave plasma torch with metallic enclosure. *Physics of Plasmas*, 26(4), 2019.
- [31] A.J. Wolf, T.W.H. Righart, F.J.J. Peeters, W.A. Bongers, and M.C.M. van de Sanden. Implications of thermo-chemical instability on the contracted modes in CO₂ microwave plasmas. *Plasma Sources Science and Technology*, 29(2):025005, 2020. doi: 10.1088/1361-6595/ab5eca.
- [32] M.I. Boulos. *Handbook of Thermal Plasmas*. Springer Nature Switzerland, 2023. doi: 10.1007/978-3-030-84936-8.
- [33] G.J.M. Hagelaar, K. Hassouni, and A. Gicquel. Interaction between the electromagnetic fields and the plasma in a microwave plasma reactor. *Journal of Applied Physics*, 96(4):1819–1828, 2004. doi: 10.1063/1.1769607.
- [34] M. Moisan and Z. Zakrzewski. Plasma sources based on the propagation of electromagnetic surface waves. *Journal of Physics D: Applied Physics*, 24(7):1025, 1991. doi: 10.1088/0022-3727/24/7/001.

[35] M. Moisan, Z. Zakrzewski, and R. Pantel. The theory and characteristics of an efficient surface wave launcher (surfatron) producing long plasma columns. *Journal* of Physics D: Applied Physics, 12(2):219, 1979. doi: 10.1088/0022-3727/12/2/008.

- [36] Waveguide loss spreadsheet, 2015. URL https://www.microwaves101.com/encyclopedias/waveguide-loss.
- [37] A.W. van de Steeg, L. Vialetto, A. Silva, F. Sovelas, P. Viegas, P. Diomede, M.C.M. van de Sanden, and G.J. van Rooij. The chemical origins of plasma contraction and thermalization in CO₂ microwave discharges. *The Journal of Physical Chemistry Letters*, 13(5):1203–1208, 2022. doi: 10.1021/acs.jpclett.1c03731.
- [38] P. Viegas, L. Vialetto, A.J. Wolf, F.J.J. Peeters, P.W.C. Groen, T.W.H. Righart, W.A. Bongers, M.C.M. van de Sanden, and P. Diomede. Insight into contraction dynamics of microwave plasmas for CO₂ conversion from plasma chemistry modelling. *Plasma Sources Science and Technology*, 29(10):105014, 2020. doi: 10.1088/1361-6595/abb41c.
- [39] A.J. Wolf, T.W.H. Righart, F.J.J. Peeters, P.W.C. Groen, M.C.M. van de Sanden, and W.A. Bongers. Characterization of CO₂ microwave plasma based on the phenomenon of skin-depth-limited contraction. *Plasma Sources Science and Technology*, 28(11):115022, 2019. doi: 10.1088/1361-6595/ab4e61.
- [40] O. Biondo, A. Hughes, A. van de Steeg, S. Maerivoet, B. Loenders, G. van Rooij, and A. Bogaerts. Power concentration determined by thermodynamic properties in complex gas mixtures: the case of plasma-based dry reforming of methane. *Plasma Sources Science and Technology*, 32(4):045001, 2023. doi: 10.1088/1361-6595/acc6ec.
- [41] S. Kelly, A. van de Steeg, A. Hughes, G. van Rooij, and A. Bogaerts. Thermal instability and volume contraction in a pulsed microwave N₂ plasma at sub-atmospheric pressure. Plasma Sources Science and Technology, 30(5):055005, 2021.
- [42] L. Vialetto. Modelling of plasma for CO₂ conversion: electron kinetics, chemistry and transport. 2021.
- [43] C.K. Kiefer, R. Antunes, A. Hecimovic, A. Meindl, and U. Fantz. CO₂ dissociation using a lab-scale microwave plasma torch: An experimental study in view of industrial application. *Chemical Engineering Journal*, 481:148326, 2024. doi: 10.1016/j.cej. 2023.148326.

[44] I. Belov, V. Vermeiren, S. Paulussen, and A. Bogaerts. Carbon dioxide dissociation in a microwave plasma reactor operating in a wide pressure range and different gas inlet configurations. *Journal of CO₂ Utilization*, 24:386–397, 2018. doi: 10.1016/j. jcou.2017.12.009.

- [45] D.C.M. van den Bekerom, J.M.P. Linares, T. Verreycken, E.M. van Veldhuizen, S. Nijdam, G. Berden, W.A. Bongers, M.C.M. van de Sanden, and G.J. van Rooij. The importance of thermal dissociation in CO₂ microwave discharges investigated by power pulsing and rotational raman scattering. *Plasma Sources Science and Technology*, 28 (5):055015, 2019. doi: 10.1088/1361-6595/aaf519.
- [46] H.M.S. Van Poyer, I. Tsonev, S.J.R. Maerivoet, M.C.K. Albrechts, and A. Bogaerts. Influence of radial transport and turbulent effects on CO₂ conversion in a microwave plasma reactor: Insights from a multi-dimensional thermo-chemical flow model. Chemical Engineering Journal, 507:160688, 2025. doi: 10.1016/j.cej.2025.160688.
- [47] A. Gutsol and J.A. Bakken. A new vortex method of plasma insulation and explanation of the ranque effect. *Journal of Physics D: Applied Physics*, 31(6):704, 1998. doi: 10.1088/0022-3727/31/6/018.
- [48] P.W.C. Groen, W.A. Bongers, J.F.J. Janssen, T.W.H. Righart, A.W. van de Steeg, A.J. Wolf, M.C.M. van de Sanden, and F.J.J. Peeters. Modelling forward vortex flow in a microwave plasma. *Chemical Engineering Journal*, 503:158072, 2025. doi: 10.1016/j.cej.2024.158072.
- [49] A.P.H. Goede, W.A. Bongers, M.F. Graswinckel, M.C.M. van de Sanden, M. Leins, J. Kopecki, A. Schulz, and M. Walker. Production of solar fuels by CO₂ plasmolysis. 79:01005, 2014. doi: 10.1051/epjconf/20137901005.
- [50] A. Hecimovic, C.K. Kiefer, A. Meindl, R. Antunes, and U. Fantz. Fast gas quenching of microwave plasma effluent for enhanced CO₂ conversion. *Journal of CO₂ Utiliza*tion, 71:102473, 2023. doi: 10.1016/j.jcou.2023.102473.
- [51] A.J. Wolf, F.J.J. Peeters, P.W.C. Groen, W.A. Bongers, and M.C.M. van de Sanden. CO₂ conversion in nonuniform discharges: Disentangling dissociation and recombination mechanisms. *The Journal of Physical Chemistry C*, 124(31):16806–16819, 2020. doi: 10.1021/acs.jpcc.0c03637.

[52] E. Carbone, F. D'Isa, A. Hecimovic, and U. Fantz. Analysis of the c2 (d3g-a3u) swan bands as a thermometric probe in CO₂ microwave plasmas. *Plasma Sources Science* and Technology, 2019. doi: 10.1088/1361-6595/ab74b4.

- [53] A. Bogaerts, X. Tu, G. van Rooij, and M.C.M. van de Sanden. 28. Plasma-based CO_2 conversion, pages 585–634. De Gruyter, 2019. doi: 10.1515/9783110665147-028.
- [54] P.J. Linstrom and W.G. Mallard. The nist chemistry webbook: A chemical data resource on the internet. *Journal of Chemical & Engineering Data*, 46(5):1059–1063, 2001. doi: 10.1021/je000236i.
- [55] S. Soldatov, G. Link, L. Silberer, C.M. Schmedt, E. Carbone, F. D'Isa, J. Jelonnek, R. Dittmeyer, and A. Navarrete. Time-resolved optical emission spectroscopy reveals nonequilibrium conditions for CO₂ splitting in atmospheric plasma sustained with ultrafast microwave pulsation. ACS Energy Letters, 6(1):124–130, 2021. doi: 10. 1021/acsenergylett.0c01983.
- [56] G. Raposo, A.W. van de Steeg, E.R. Mercer, C.F.A.M. van Deursen, H.J.L. Hendrickx, W.A. Bongers, G.J. van Rooij, M.C.M. van de Sanden, and F.J.J. Peeters. Flame bands: CO + O chemiluminescence as a measure of gas temperature. *Journal of Physics D: Applied Physics*, 54(37):374005, 2021. doi: 10.1088/1361-6463/ac0924.
- [57] R. Aerts, R. Snoeckx, and A. Bogaerts. In-situ chemical trapping of oxygen in the splitting of carbon dioxide by plasma. *Plasma Processes and Polymers*, 11(10):985– 992, 2014. doi: 10.1002/ppap.201400091.
- [58] V. Guerra, T. Silva, P. Ogloblina, M. Grofulović, L. Terraz, M.L. da Silva, C.D. Pintassilgo, L.L. Alves, and O. Guaitella. The case for in situ resource utilisation for oxygen production on Mars by non-equilibrium plasmas. *Plasma Sources Science and Technology*, 26(11):11LT01, 2017.
- [59] V. Guerra, T. Silva, N. Pinhão, O. Guaitella, C. Guerra-Garcia, F.J.J. Peeters, M.N. Tsampas, and M.C.M. van de Sanden. Plasmas for in situ resource utilization on Mars: Fuels, life support, and agriculture. *Journal of Applied Physics*, 132(7), 2022. doi: 10.1063/5.0098011.
- [60] S. Kelly, E.R. Mercer, Y. Gorbanev, I. Fedirchyk, C. Verheyen, K. Werner, P. Pullumbi, A. Cowley, and A. Bogaerts. Plasma-based conversion of martian atmosphere

into life-sustaining chemicals: The benefits of utilizing martian ambient pressure. Journal of CO_2 Utilization, 80:102668, 2024. doi: 10.1016/j.jcou.2024.102668.

- [61] S. Kelly, C. Verheyen, A. Cowley, and A. Bogaerts. Producing oxygen and fertilizer with the martian atmosphere by using microwave plasma. *Chem*, 8(10):2797–2816, 2022. doi: 10.1016/j.chempr.2022.07.015.
- [62] S. Kelly and A. Bogaerts. Nitrogen fixation in an electrode-free microwave plasma. Joule, 5(11):3006–3030, 2021.
- [63] G.J.C. Raposo. Plasma in-situ production of fuel and oxygen on Mars. Master's thesis, Técnico Lisboa, 2020.

Chapter 3

Thermal Management: Enhancing Efficiency Through Preheating

In this chapter, we investigate the effects of inlet gas preheating on plasma performance in a vortex-stabilized 915 MHz CO_2 microwave plasma reactor. Spatially resolved spectroscopic measurements of the plasma were employed to understand how preheating affects the temperature profile. Thermographic measurements of the reaction chamber analyzed the losses through the wall, offering deeper insights into the thermal changes within the system. The overall performance was evaluated using gas chromatography. We demonstrate that recycling less than 10% of the input power to preheat CO_2 ($T_{inlet} = 700 \text{ K}$) can increase the energy efficiency of CO_2 conversion by up to ~ 1.7 times at conditions near atmospheric pressure (700 mbar), at moderate microwave power (1132 W). The results indicate that preheating affects plasma fluid dynamics, resulting in shifts in plasma contraction and increased spatial temperature profile, or reactive volume, with higher inlet temperatures. This chapter provides new insights into the potential of integrating heat recycling in plasma reactors, of great interest for future industrial applications.

Cas van Deursen.

Prof. Dr. Ir. Richard van de Sanden, and is in co-first authorship with my esteemed colleague,

This chapter is derived from the following publication:

Preheating applied on a 915 MHz CO₂ Microwave Plasma::
 Unlocking the Potential for Heat Recycling in Plasma Systems
 E.R. Mercer* & C.F.A.M. van Deursen*, F.J.J. Peeters, W.A. Bongers, F.M.A. Smits,
 M.C.M. van de Sanden** & A. Bogaerts** (Submitted Manuscript)
 The work presented in this chapter was carried out at the Dutch Institute for Fundamental Energy Research, in collaboration with the Plasma for Solar Fuels Devices group under the guidance of

3.1 Introduction

As explained in Chapter 2 (Section 2.4.1), it is well established that reactor performance is largely governed by high-temperature thermal chemistry [1-7], and thus, strategic heat recovery could significantly enhance overall system efficiency. Moreover, these insights suggest that preheating the inlet gas could enhance reaction kinetics, while reducing the overall energy requirement for achieving dissociation temperatures. The concept of heat recovery in plasma systems has historical precedents. The Schönherr process for nitrogen fixation, developed in the early 1900s, demonstrated preheating inlet gas using waste heat [8, 9]. Similarly, the Birkeland-Eyde process utilized heat exchangers to improve the efficiency of their atmospheric nitrogen fixation system [10]. The Hüls process for acetylene production from hydrocarbons provides another historical example of successful heat management in plasma processes [11, 12]. These industrial-scale applications demonstrate that careful management of thermal energy is crucial for process economics in plasmabased chemical conversion. Modern industrial applications of plasma technology could benefit from similar heat recovery strategies. Recent studies have shown that gas-to-gas heat exchangers can significantly improve energy efficiencies in chemical processing [13]. In MW plasma systems specifically, the high temperatures achieved in plasma ($\gg 3000$ K) represent a substantial source of thermal energy that could be recovered. While MW plasma technology for CO₂ conversion has been extensively studied, research specifically investigating preheating effects remains limited and has primarily been conducted in other plasma systems.

Shenoy et al. demonstrated the benefits of preheating in a non-thermal gliding arc plasma for natural gas reforming to syngas, showing that preheating up to 800 K could reduce specific energy requirements by enhancing conversion [14]. Cho et al. developed a 'double helix' gas injection system that passively preheats the inlet gas by routing it around the discharge tube before entering the plasma, demonstrating improved CO₂ conversion and energy efficiency compared to conventional MW plasma generators; however, the authors did not report inlet temperatures, so a deeper understanding of the benefits is limited [15]. Jo et al. investigated preheating effects up to 400 K on methane oxidation in gliding arc plasma reforming, showing that identical efficiencies could be achieved with lower total input power by applying some of the power to preheating [16]. In plasma-based reactions, preheating the inlet gas stream has the potential to influence various aspects of plasma

dynamics significantly, such as altering the internal energy distribution, which can affect reaction volume, radiative losses, particle transport, and energy exchange rates.

Systematic investigations of preheating effects, particularly at 915 MHz, have not been reported for CO₂ MW plasmas. Given that preheating could influence plasma behavior by modifying gas density, flow dynamics, and plasma contraction mechanisms, understanding these effects represents a fundamental knowledge gap for optimizing MW plasma reactor performance. The aim of this chapter is to investigate the effects of preheating inlet CO₂ gas in a vortex-stabilized 915 MHz MW plasma reactor and to understand the potential benefits of implementing heat recovery systems in future industrial plasma reactors. The influence of preheating on plasma characteristics is examined with respect to its effects on the reactive volume through an investigation of the spatial temperature distribution. A key consideration is the impact of preheating on thermal management and heat losses at the reactor walls, which could have significant implications for the system's energy efficiency. Additionally, this chapter evaluates the role of preheating in enhancing CO₂ conversion and energy efficiency across various pressure regimes and operating conditions. Finally, the potential for preheating to partially offset MW power requirements while maintaining plasma performance is explored, offering insights into optimizing energy input for sustainable plasma processes.

3.2 Experimental Setup

The experimental setup consists of a vortex-stabilized waveguided MW plasma reactor (Figure 3.1A) with a GaN solid-state MW source with a rated efficiency of $\sim 42\%$ (Wattsine, WSPS-915-5000) that emits an adjustable Continuous Wave (CW) power up to 5 kW at a set frequency of 915 MHz. The MW power is transmitted through a WR975 rectangular waveguide in TE_{10} mode, forming a standing wave. The MW generator is protected by an isolator (Figure 3.1B), which prevents any reflected power from returning upstream. Matching components consist of an automatic stub tuner (HOMER S-TEAM STHT V2.3) (Figure 3.1C) set between the generator (MW source) and the resonance chamber (Figure 3.1D) ensuring a high coupling efficiency by matching the impedance, so that reflected power remains below 1% during experiments. The autotuner also measures the forward and reflected power and frequency applied to the CO_2 gas flow passing perpendicularly through the resonance chamber in a 27 mm inner diameter Quartz Tube

(QT). A QT containing the gas flow traverses the shorted waveguide (Figure 3.1D). The gas is tangentially injected from the preheating section (Figure 3.1E) into the reactor volume by two quartz tubes to create the stabilizing vortex flow. To avoid leak-sensitive material transitions, the preheating section and the reactor section are integrated in a single quartz tube and separated by a quartz disc. The reactor has two diagnostic viewing ports perpendicular to the waveguide formed by open metal rectangular tubes (length 30 cm) in cut-off to prevent MW leakage.

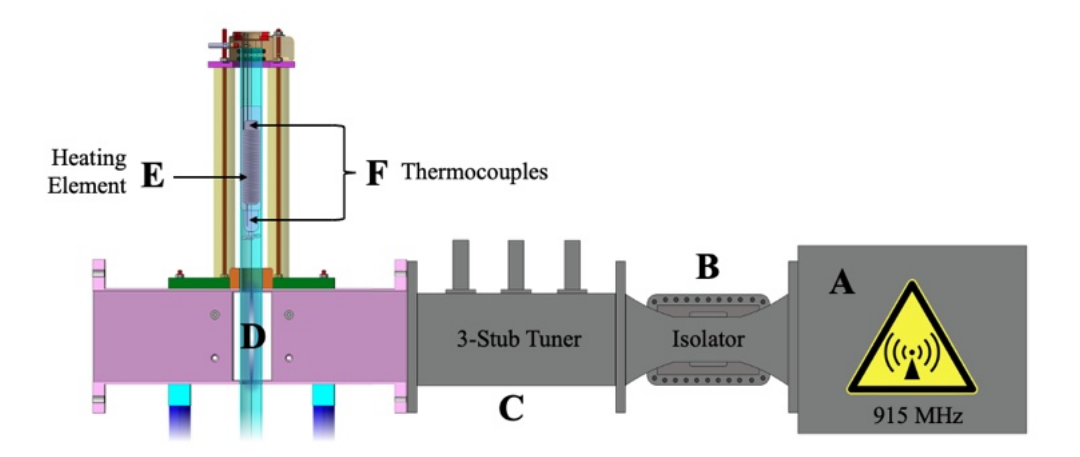


FIGURE 3.1: Schematic overview of the experimental setup. From right to left, (\mathbf{A}) the 915 MHz solid-state MW source (Wattsine, WSPS-915-5000), (\mathbf{B}) the isolator, (\mathbf{C}) the automatic stub tuner (HOMER S-TEAM STHT V2.3), and (\mathbf{D}) the 27 mm inner diameter QT viewed though the cut-off tube. The (\mathbf{E}) heating element and (\mathbf{F}) thermocouples are positioned above the reaction chamber.

The preheating system consists of a custom-designed heating element (Figure 3.1E) positioned 200 mm above the resonance chamber (Figure 3.1D) of the waveguide. The heating element is constructed from 1 mm diameter Kanthal A1 (FeCrAl) wire with a measured total resistance of 3.5 Ω . The wire is insulated with alumina beads (to prevent shorting), supported by an alumina tube, and secured in place using high-temperature ceramic adhesive. Temperature monitoring of the inlet gas utilizes K-type thermocouples (TC Direct) (Figure 3.1F). One thermocouple measures the heater temperature directly, while a second thermocouple is positioned immediately upstream of the tangential gas injection to measure the gas inlet temperature (T_{inlet}). This T_{inlet} measurement provides an accurate representation of the gas temperature immediately before entering the reaction chamber. To enhance thermal efficiency and minimize heat loss, the QT surrounding

the heating element is insulated with aluminum oxide wool. This insulation significantly improved heating efficiency by reducing radiative and convective heat losses through the quartz walls.

3.2.1 Diagnostics and Performance Metrics

A comprehensive overview of the experimental diagnostics setup, including thermographic measurements and collection optics is presented in *Figure 3.2*. The diagram illustrates the spatial arrangement and configuration of all measurement instruments used to characterize system performance.

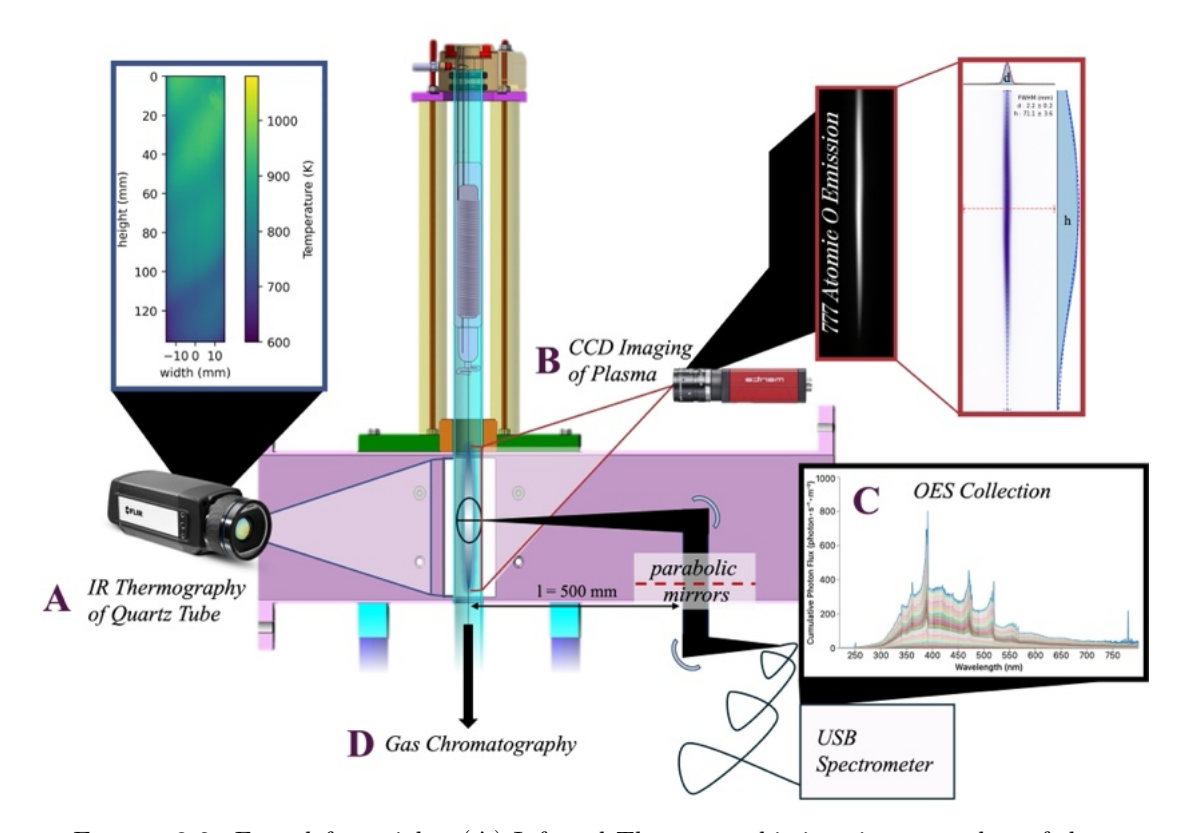


FIGURE 3.2: From left to right: (A) Infrared Thermographic imaging was taken of the QT to calculate the thermal losses through the wall, (B) plasma imaging of the 777 nm atomic oxygen emission was collected using a CCD camera, treated to derive the plasma diameter (d) and the height (h) based on the intensity profile, (C) radially resolved OES was collected using stages that scan the plasma profile using optics consisting of parabolic mirrors and a fiber attachment with a focal point calculated to be 0.5 mm. The collected spectra were pretreated and then fit the C_2 Swan bands for the central temperature profiles using MassiveOES as well as with the flame band model for the periphery temperatures. Gas chromatography (D) was utilized to measure the effluent gas stream.

The total dissipated power lost through the QT wall was measured using an InfraRed (IR) thermography camera (FLIR A655sc) equipped with a 41.3 mm lens and an open

calibrated filter with a spectral range of $7.5-14 \,\mu\mathrm{m}$ (Figure 3.2A). The collected data from IR measurements aids in understanding the power loss to the environment through the QT at the height of the plasma and its impact on system performance. The radiated power was calculated using Stefan-Boltzmann's Law. The reported radiated power and temperature loss through the wall were calculated using the method reported in van Deursen et al. [17]. The convection losses through the wall were calculated using the method outlined in Appendix A,Section A.1. As shown in Figure 3.2B, the optical plasma emission was captured using a CCD camera (Allied Vision Manta G-146B) equipped with a 780 nm narrow bandpass interference filter to isolate oxygen lines at 777 nm and a neutral density filter to prevent overexposure of the CCD. The emission intensity was utilized to derive the shape, size, and volume of the plasma profile. Reported plasma height and diameter were derived using the method described by Wolf et al [18].

An optical stage was used to scan the QT (the reaction chamber) using optical emission spectroscopy (OES) at the height of the plasma through the viewing ports (Figure 3.2C) using an Ocean Insight mini spectrometer (FLAME-S) with an optical resolution of 0.9 nm equipped with a custom 20 cm, 400 μ m high-OH core fiber (Thorlabs FG400AEA). The radial temperature profile is derived using two unique spectral characteristics commonly found in contracted CO₂ MW plasmas. Additional details on the optics and preprocessing of the spectral data can be referenced in the Appendix A, Section A.2.1. One dominant emission profile is the C_2 $(d^3\Pi_q - a^3\Pi_u)$ Swan band system, which can be utilized to derive the rotational and vibrational temperatures [19]. We can, therefore, exploit this spectral feature to derive the core plasma temperature profile, under the assumption that the rotational temperature is equal to the gas temperature. Details of the data processing and uncertainty of the MassiveOES fits can also be found in Appendix A, Section A.2.2. Flame band emission spectroscopy was utilized as a secondary temperature diagnostic to capture the periphery temperatures surrounding the core plasma region. Flame band spectroscopy measures the emission intensity from the radiative transition of excited CO₂ to ground-state CO₂ after recombination of CO and O [20]. Details of the data processing, fitting routine, error analysis, and uncertainty of the flame band fitting can also be found in Appendix A, Section A2.3.

Finally, we utilize Gas Chromatography (GC) (G.A.S. Compact GC 4.0) to measure the composition of the post-plasma effluent mixture (*Figure 4.2D*). From this, the conversion and energy efficiency were calculated using the methods outlined by *Wanten et al.* [21].

Appendix A, Section A.3 outlines further details on analytical techniques and performance calculations. The methods used to calculate the power to heat CO_2 (P_{CO_2}) can be referenced in Appendix A, Section A.4. To comprehensively assess the preheating effects on CO_2 conversion in a MW plasma, two experimental series were investigated:

- 1. Constant MW Power Measurements: In this series of experiments, the MW power (P_{MW}) was held constant, while the inlet mass flow rate of CO_2 was preheated to set temperatures. This approach simulates scenarios where heat recycling could be leveraged to enhance conversion, while providing insight into overall changes in performance. Since the P_{CO_2} used for preheating is assumed to originate from waste heat recovery, it is excluded from the energy efficiency calculation, which normally only accounts for the MW power coupled to the chemistry. By maintaining constant P_{MW} , this experiment is designed to isolate the thermal enhancement effects on plasma performance.
- 2. Constant Total Power Measurements: The total input power to the system $(P_{total} = P_{MW} + P_{CO_2})$ was held constant, isolating the role of preheating in reducing the required MW power on conversion rate. This set of experiments directly evaluates whether preheating allows for a proportional reduction in P_{MW} , while maintaining or improving dissociation efficiency. The assumption remains that P_{CO_2} originates from heat recovery and is therefore decoupled from the energy efficiency calculation, ensuring that any observed gains in performance reflect the redistribution of power rather than an increase in total energy input.

The benchmark condition with a T_{inlet} of 300 K serves as the baseline reference and is represented in green throughout the text.

3.3 Results and Discussion

The results presented in this section were investigated at varying power levels and T_{inlet} with a mass flow rate (ϕ_{CO_2}) of 10 normal liters per minute (ln/min – STP IUPAC, 0 °C, 1 bar) [21]. First, we discuss the reactor performance, analyzed in terms of CO₂ conversion (χ) and energy efficiency (η); calculations are available in Appendix A, Section A.3. Next, we explore the effects of preheating on the plasma characteristics, focusing

on changes to the reaction volume ($T_{gas} > 1500$ K, where dissociation of CO₂ to CO becomes significant) and plasma size (diameter and length as determined by the FWHM of the 777 nm atomic oxygen emission intensity), as well as the effects on radiated power through the reactor wall as measured by IR thermography. The performance metrics are correlated with the radial gas temperature profiles at the plasma height, and the heat flux through the reaction chamber wall, where we analyze the overall impact of gas preheating on conversion, energy efficiency, and plasma dynamics.

3.3.1 Preheating Effects on Conversion and Energy Efficiency

Figure 3.3 presents a comparative look at conversion and energy efficiency between constant P_{total} and P_{MW} . All conditions are represented with a $\phi_{\text{CO}_2} = 10 \text{ ln/min}$, and varying inlet temperatures (T_{inlet}) = 300 (green), 500 (yellow), and 700 K (orange), which correspond to $P_{\text{CO}_2} = 0$, 62, and 132 W, respectively. The results for constant $P_{total} = 1132$ W are shown on the lefthand side (3.3A and 3.3B), while constant $P_{MW} = 1000 \text{ W}$ is on the righthand side (3.3D). A visualization of the plasma imaging defined by the 777 nm atomic oxygen emission is shown for p = 150 mbar and different T_{inlet} (3.3C).

Figure 3.3A and 3.3B reveal that at near-atmospheric pressure (700 – 900 mbar), preheating provides modest but measurable benefits to the energy efficiency. When P_{total} is kept constant, conversion increases by $\sim 15\%$ at 700 mbar for $T_{inlet} = 700$ K and $\sim 10\%$ at 900 mbar for $T_{inlet} = 500$ K compared to baseline conditions. The data for $T_{inlet} = 700$ K at p = 900 mbar is unavailable due to plasma instability. On the other hand, at low pressure (200 mbar), preheating reduces conversion at higher T_{inlet} , with values dropping from $23.92 \pm 0.09\%$ at 300 K to $18.26 \pm 0.07\%$ at 700 K. Figure 3.3D shows larger improvements to the conversion and energy efficiency at constant $P_{MW} = 1000 \text{ W}$, which is logical, because the power used to preheat the inlet CO₂ is 'freely' added to the system, enhancing conversion, and it is not used to calculate energy efficiency, which thus rises to the same extent as conversion (see Appendix A, Section A.3 and A.4, for additional information on the calculations used). However, at low pressure (p < 200 mbar), elevated inlet temperatures (500 K and 700 K) negatively impact energy efficiency and conversion. For example, at 150 mbar, increasing T_{inlet} from 300 K to 700 K reduces conversion from $22.35 \pm 0.09\%$ to $18.26 \pm 0.09\%$. This is likely a consequence of the plasma contraction state.

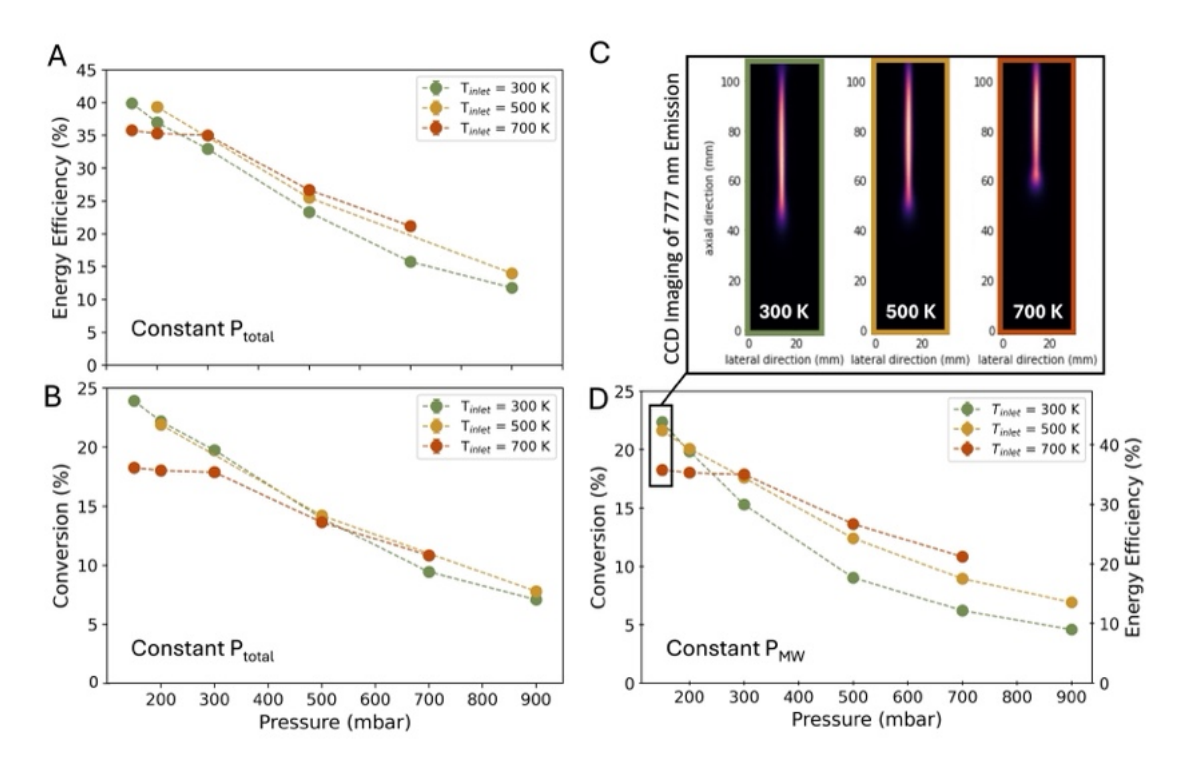


FIGURE 3.3: Conversion and energy efficiency for $T_{inlet} = 300$ K (green), 500 K (yellow), 700 K (dark orange) as a function of pressure, at constant $P_{total} = 1132$ W (A, B) or constant $P_{MW} = 1000$ W (D). Panel C represents the CCD images of the plasma emission profile for the atomic oxygen (777 nm) for the indicated data points at 150 mbar. All conditions were taken with $\phi_{\text{CO}_2} = 10$ ln/min. Error bars are given but fall under the data markers in all cases.

Indeed, it is well documented that CO_2 MW plasmas exhibit distinct discharge modes characterized into three categories, which are broadly determined by power, pressure, and gas flow rate [4, 18, 22]. As also explained in Chapter 2 (Section 2.3.2), at low pressure (< 100 mbar) or power density, the plasma often remains in homogeneous or L-mode, as characterized by uniform temperature, as well as relatively low power density profiles [22]. As pressure increases, the hybrid mode arises (typically between 100 – 200 mbar), balancing partial contraction with sufficient homogeneity to maintain high energy efficiency and mixing [22]. We observe that the benchmark condition for 150 mbar shows hybrid characteristics, where the center region of the filament is contracted but grows outward towards the tip of the column (Figure 3.3C). With increasing T_{inlet} these characteristics become more pronounced, accompanied by a notable decrease in the plasma length (axial direction), as defined by the FWHM of the 777 nm atomic oxygen emission profile for all conditions presented (see again Figure 3.3C). The decrease in plasma length (along with a drop in radial temperature profile, i.e., reactive area) may explain the observed decline in performance at 150 mbar (Figure 3.3D), due to the reduced reactive

volume.

Above ~ 200 mbar, steep radial gradients arise, leading to a contracted mode (H-mode). These transitions are driven by thermal-chemical instability [18, 22–24], where localized heating boosts ionization rates, creating dense filaments with elevated temperatures and enhanced microwave absorption [23]. We see the trend of conversion and energy efficiency upon preheating reverses as the pressure increases and the hybrid mode shifts to fully contracted H-mode, resulting in preheating enhancing both conversion and energy efficiency. Notably in Figure 3.3D, for $P_{MW} = 1000 \text{ W}$ at near-atmospheric pressure (900 mbar), $T_{inlet} = 500 \text{ K}$ achieves a 1.5 relative increase in conversion compared to 300 K (6.92 \pm 0.02% vs. $4.58 \pm 0.01\%$, respectively). A similar pattern is observed at 700 mbar, where $T_{inlet} = 700 \text{ K}$ demonstrates a 1.7 fold improvement over the baseline of 300 K (10.82) $\pm 0.04\%$ vs. $6.21 \pm 0.02\%$, respectively). Several mechanisms govern contraction. Electron collisions (particularly in the plasma core) can increase ionization rates, while radial temperature gradients modify the reduced electric field and reduce charged-particle losses [25]. This positive feedback leads to narrow, high-power density regions with significant temperature elevation; however, it can limit the overall reactive volume, as contracted (H-mode) plasmas will exhibit a reduced interface between the reactive volume and the bulk gas of the reaction chamber. Consequently, the hybrid regime often emerges as the optimal mode for CO₂ conversion, balancing localized heating with adequate mixing and quenching. However, this regime requires vacuum pumping, which uses additional power from plug to product [26].

Despite the change in power distribution (whether constant P_{total} or P_{MW}), we observe that preheating the inlet gas has a marked improvement on conversion and energy efficiency at near-atmospheric pressure, while at low pressure ($\leq 200 \text{ mbar}$) there is a decline in performance. Our results suggest that partial substitution of MW power with direct gas heating can improve conversion and energy efficiency at higher pressures, which is especially important when considering that operating at higher pressures also reduces power consumption needed for vacuum pumping. The modest improvements shown with $P_{total} = 1132 \text{ W}$ at near-atmospheric pressure likely stem from compounding mechanisms, such as the potential for increased post-plasma recombination or reduced gas residence time within the reactive volume. Therefore, a deeper understanding of the underlying mechanisms is crucial for optimization. These effects will be further investigated in the following sections.

Having established the baseline behavior for constant P_{total} and P_{MW} , we will now examine how these preheating effects manifest at slightly higher power. Increasing the input power while maintaining the same mass flow rate provides insight into whether the observed preheating benefits scale with specific energy input. Furthermore, we captured additional T_{inlet} conditions to broaden the parameter space and our understanding of the effects of preheating. Figure 3.4 presents experimental results obtained for $P_{total} = 1500 \text{ W}$, $\phi_{\text{CO}_2} = 10 \text{ ln/min}$, $T_{inlet} = 300 \text{ K}$ (green), 500 K (yellow), 700 K (orange), and 850 K (brown) at varying pressure.

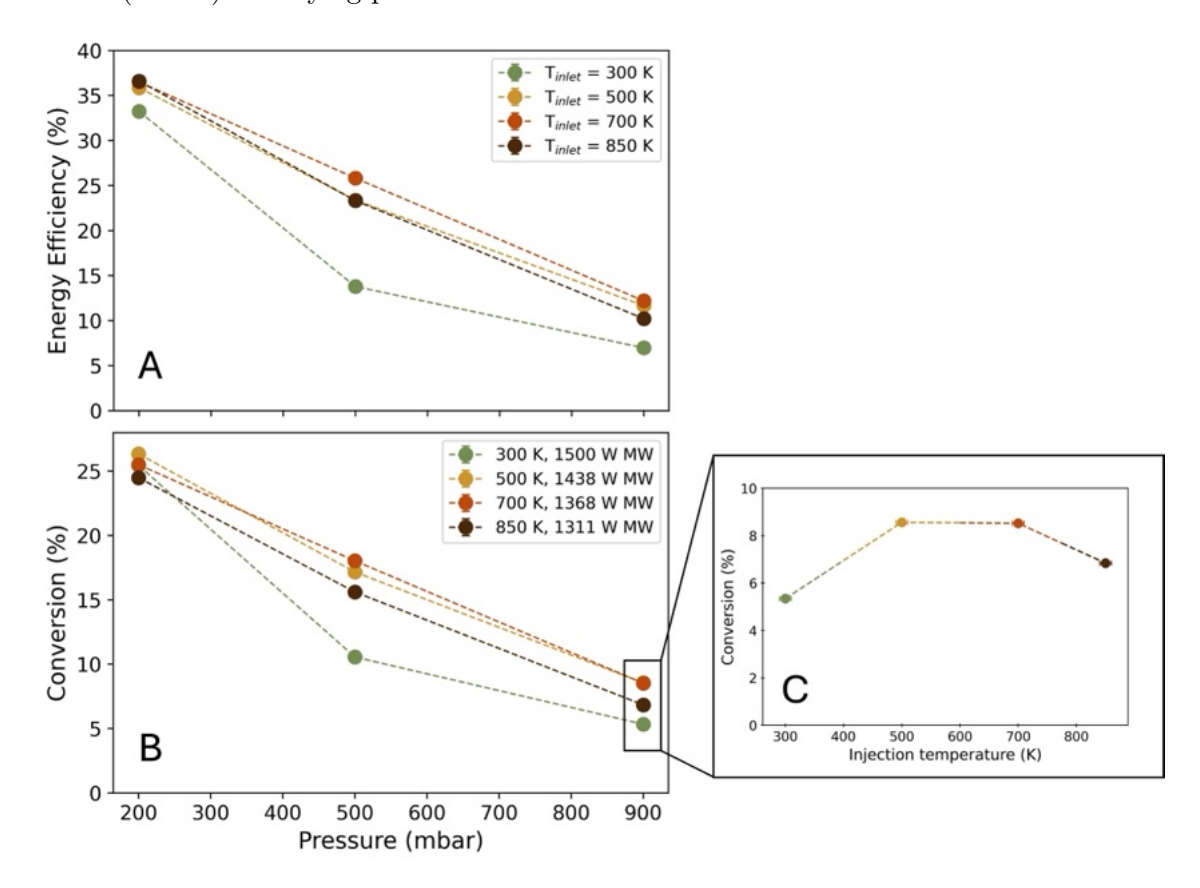


FIGURE 3.4: (A and B) Energy efficiency and conversion as a function of pressure, for $P_{total} = 1500 \text{ W}$, $\phi_{\text{CO}_2} = 10 \text{ nlm}$, $T_{inlet} = 300 \text{ K}$ (green), 500 K (yellow), 700 K (orange) and 850 K (brown). (C) shows the conversion for p = 900 mbar as a function of T_{inlet} , to highlight the decrease in conversion observed at $T_{inlet} = 850 \text{ K}$. The total power added to the system was kept constant across all measurements. Error bars are given but fall under the data markers in all cases.

Figure 3.4A and 3.4B reveal several important trends in how T_{inlet} affects CO₂ conversion and energy efficiency across different pressures. The most striking observation is that $T_{inlet} > 300$ K and within the contracted plasma regime (p > 200 mbar) consistently yields better energy efficiency and conversion (Figure 3.4A,B). An investigation into the effects of increasing the input power and mass flow rate can be reviewed in Appendix

A, Section A.5; however, the reader should note that the conclusions remain consistent with the main findings reported in this section. At p=200 mbar, conversion peaks around 25% ($T_{inlet}=300$ K, 500 K, 700 K, and 850 K give 25.45 \pm 0.11%, 26.34 \pm 0.11%, 25.50 \pm 0.11%, 24.49 \pm 0.10%, respectively), showing relatively small variation between different inlet temperatures. As pressure increases, the performance advantage of preheated conditions becomes more pronounced. As also shown in Figure 3.4C, the divergence between the baseline and preheated conditions (500 - 850 K) grows larger at higher pressures, with preheated conditions maintaining significantly better conversion up to 900 mbar ($T_{inlet}=300$ K, 500 K, 700 K, and 850 K give 5.34 \pm 0.02%, 8.56 \pm 0.03%, 8.52 \pm 0.03%, 6.84 \pm 0.02%, respectively). Thus, preheating extends the pressure range for efficient conversion, although the data shows the highest inlet temperature, $T_{inlet}=850$ K, does not yield the highest conversion (Figure 3.4C), indicating an optimal ratio between P_{CO_2} and P_{total} .

3.3.2 Preheating Effects on the Reaction Volume

Radial scans at the height of the plasma were performed using OES to explore the connection between preheating and plasma behavior. Figure 3.5 shows the radial temperature profiles at $P_{MW}=1000$ W, $\phi_{\text{CO}_2}=10$ ln/min, and p=700 mbar, for three T_{inlet} conditions. Radially resolved C₂ Swan band emissions (shown as the circle data points) provided plasma core temperatures ($T=\sim6000-7000$ K), while flame band emissions (shown as triangular data points) characterized peripheral temperatures (T<1500 K).

In Figure 3.5, the shaded regions within the center of the radial temperature profile represent the plasma diameter determined by the 777 nm atomic oxygen emission captured by CCD imaging. Here, we must make a distinction between the plasma diameter and the elevated temperature region, which extends out of the cylindrical plasma volume and which we denote as the 'reactive volume', where $T_{gas} \gg 1500$ K, i.e., the threshold temperature for CO₂ dissociation [7]. In Figure 3.5, we observe that the plasma diameter increases with increasing T_{inlet} , being 2.0 \pm 0.1, 2.3 \pm 0.2, and 2.4 \pm 0.2 mm, at 300, 500, and 700 K, respectively. We also note a clear difference in the overall reactive area (represented by the last data point from the C₂ Swan band emission) between different T_{inlet} , where the spatial temperature distribution becomes broader with increasing T_{inlet} . This is most

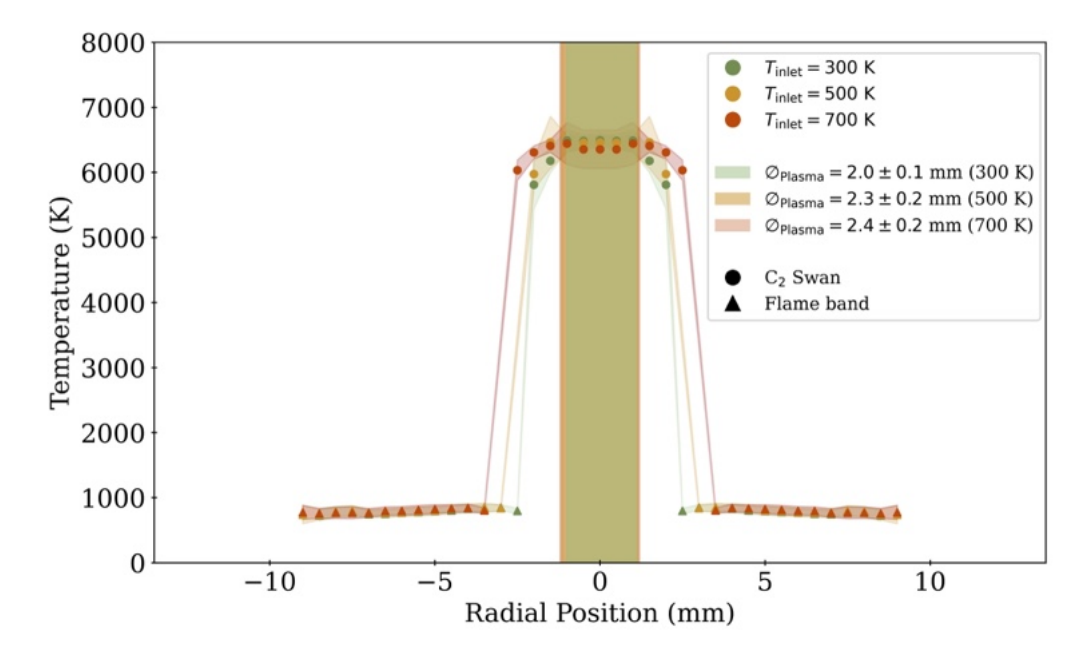


FIGURE 3.5: Radial temperature profiles for $P_{MW}=1000~\rm W,\,\phi_{CO_2}=10~\rm ln/min,\,T_{inlet}=300~\rm K$ (green), 500 K (yellow), 700 K (dark orange) for p = 700 mbar. The centershaded region represents the plasma diameter, determined by the FWHM of the emission intensity of the 777 nm atomic oxygen line captured by CCD imaging. The temperatures derived from the C₂ Swan band emission are represented as circles and from the flame band as triangles.

easily observed in the transparent connections between the C_2 swan-derived temperatures (circles) and the flame band-derived temperatures (triangles); however, it should be stressed that these connections are for visualization purposes only. These results further indicate that preheating affects plasma contraction dynamics, likely due to increased volumetric flow rates driven by higher T_{inlet} . Since elevated T_{inlet} reduces gas density (n), there will be a proportional increase in the volumetric flow rate $(Q = \phi_{mass}/n)$ at a constant mass flow rate (ϕ_{mass}) . Consequently, the average gas velocity rises at a fixed cross-sectional area, likely shortening the residence time (τ) of reactants in the plasma, potentially affecting conversion. The broadening of the temperature profile shown in Figure 3.5 suggests enhanced convective cooling, as well as (turbulent) mixing due to high surface to volume ratio, such that heat is removed more efficiently from the plasma volume, reducing the local temperature gradient that drives contraction. Further evidence of this can be explored in Appendix A, Section A.5.

Two critical observations remain consistent across all conditions. First, the core temperature remains consistent at ~ 6000 K regardless of T_{inlet} , indicating that electron-neutral coupling in the plasma core remains unaffected by preheating. Second, the peripheral temperatures derived from flame band emission measurements remain below 1500 K for

all T_{inlet} . This temperature is sufficiently low to effectively quench products radially diffusing from the reactive volume [7]. These findings suggest that while preheating notably influences the spatial distribution of the plasma and reactive volume, it does not fundamentally alter the core plasma properties or peripheral quenching conditions. Moreover, a clear correlation emerges between the broadened temperature profile observed in Figure 3.5 and the enhanced conversion under these conditions. As discussed in Figure 3.5, in all cases, the reactive area is larger than the dimensions of the plasma filament determined by the 777 nm atomic oxygen emission. For example, at $T_{inlet} = 700 \text{ K}$, the plasma diameter was found to be 2.4 mm versus 5.0 mm as derived from the C_2 swan band temperature profile. To explore this further, we consider the available temperature data, where $T \gg 3000 \text{ K}$ and CO_2 dissociation becomes significant, as a 'slice' of the reactive volume. As a first estimate, we utilize the extrapolated radial position of the cross-section where T = 3000 K (the shaded line connecting the C_2 Swan band and the flame band temperatures) to approximate the reactive area at the height of the plasma, as shown in Figure 3.6.

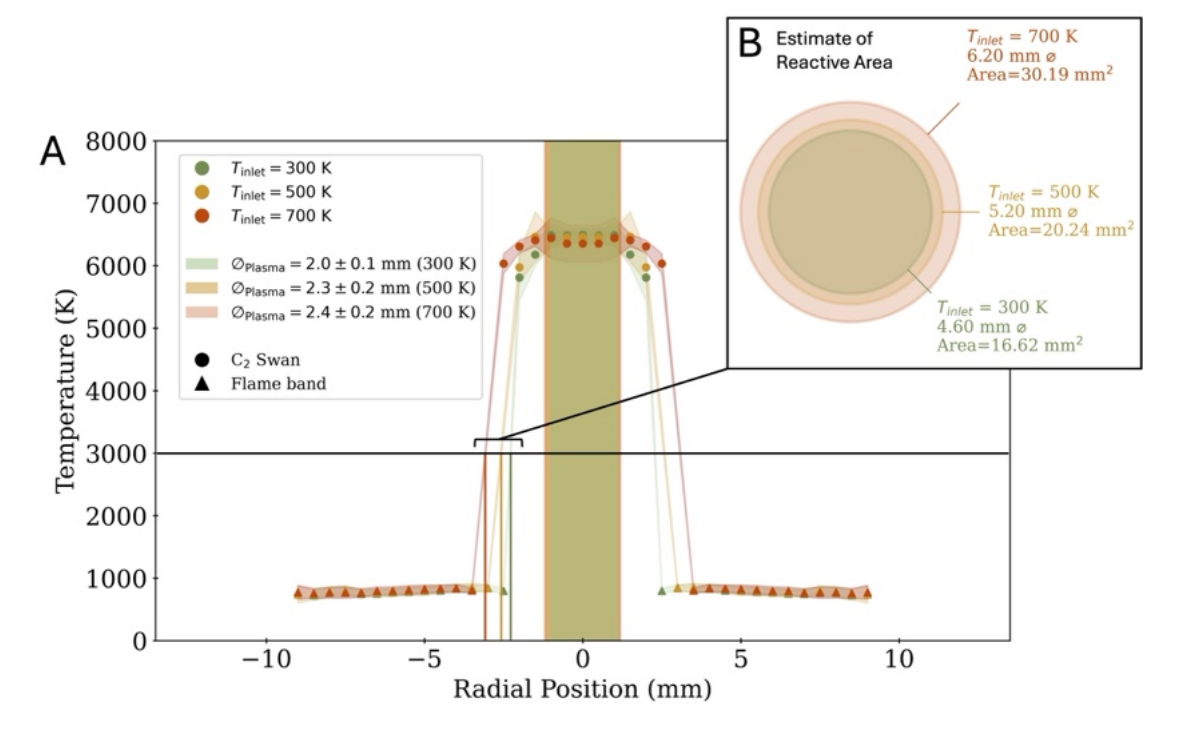


FIGURE 3.6: Reactive area (T \gg 1500 K) for $P_{MW}=1000$ W, $\phi_{\text{CO}_2}=10$ ln/min, $T_{inlet}=300$ K (green), 500 K (yellow) and 700 K (dark orange), for p = 700 mbar, where (A) indicates the temperature cutoff taken as an approximation for a slice of the reactive volume. The radial position of the collected data is used to calculate the reactive area, visualized in (B).

In Figure 3.6, we observe that the estimated reactive area is ~ 30 , 20, 17 mm² for $T_{inlet} = 700$, 500, and 300 K, respectively. As an example, the difference in reactive area between

 $T_{inlet} = 700$ and 300 K accounts for a relative increase of ~ 1.8 , whereas the values between $T_{inlet} = 500$ and 300 K account for a ~ 1.2 increase. We would like stress that this is a first estimate for these values; however, we observe that the trend in the relative increase of the reactive area correlates to the increased conversion observed in Figure 3.3D.

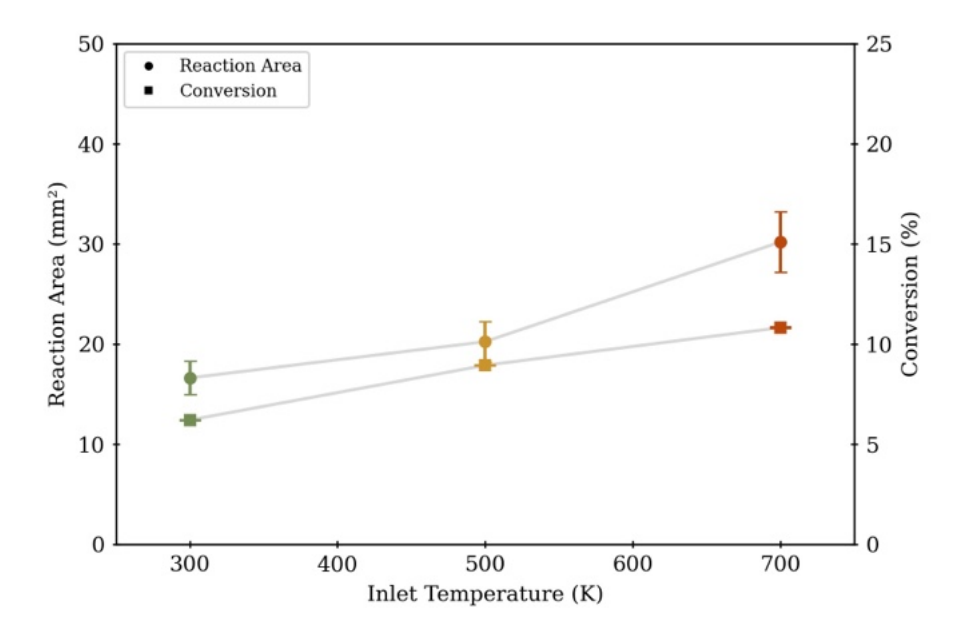


Figure 3.7: Estimated reactive area and conversion plotted as a function of T_{inlet} (K). A clear correlation emerges between the reactive area and conversion.

As shown in Figure 3.7, the expansion of the reactive area with $T_{inlet} = 700$ K and 500 K trends correlate with the increased conversion at these conditions, where an improvement of approximately 1.7 and 1.4, respectively, over baseline conditions (cf. also Figure 3.3D) was reported at 700 mbar. Preheating influences both volumetric flow rate and mass transport. Considering an equal mass flow rate, preheating the inlet gas will increase the volumetric flow rate, thereby enhancing convective cooling and allowing for more efficient heat removal from the reactive volume. This will thereby decrease the local temperature gradient that induces plasma contraction and distributes heat over a larger area. These findings support the hypothesis that preheating the inlet gas leads to a broader reactive volume, which likely contributes to the improved conversion observed at these conditions. The expanded interface between the reactive volume and the cooler periphery region could enhance mixing between the reactive molecules and the bulk gas, leading to additional products being carried out of the reactive volume.

3.3.3 Preheating Effects on Power Loss Through the Wall

The thermal behavior of the reactor walls during plasma operation provides additional insight into how preheating affects overall system performance and energy distribution. Figure 3.8 shows thermal imaging of the QT inside the waveguide at different inlet temperatures, for $P_{total} = 1500 \text{ W}$, $\phi_{\text{CO}_2} = 10 \text{ ln/min}$, p = 900 mbar and $T_{inlet} = 300, 500, 700$, and 850 K, corresponding to preheating power $(P_{\text{CO}_2}) = 0, 62, 132, \text{ and } 189 \text{ W}$, respectively.

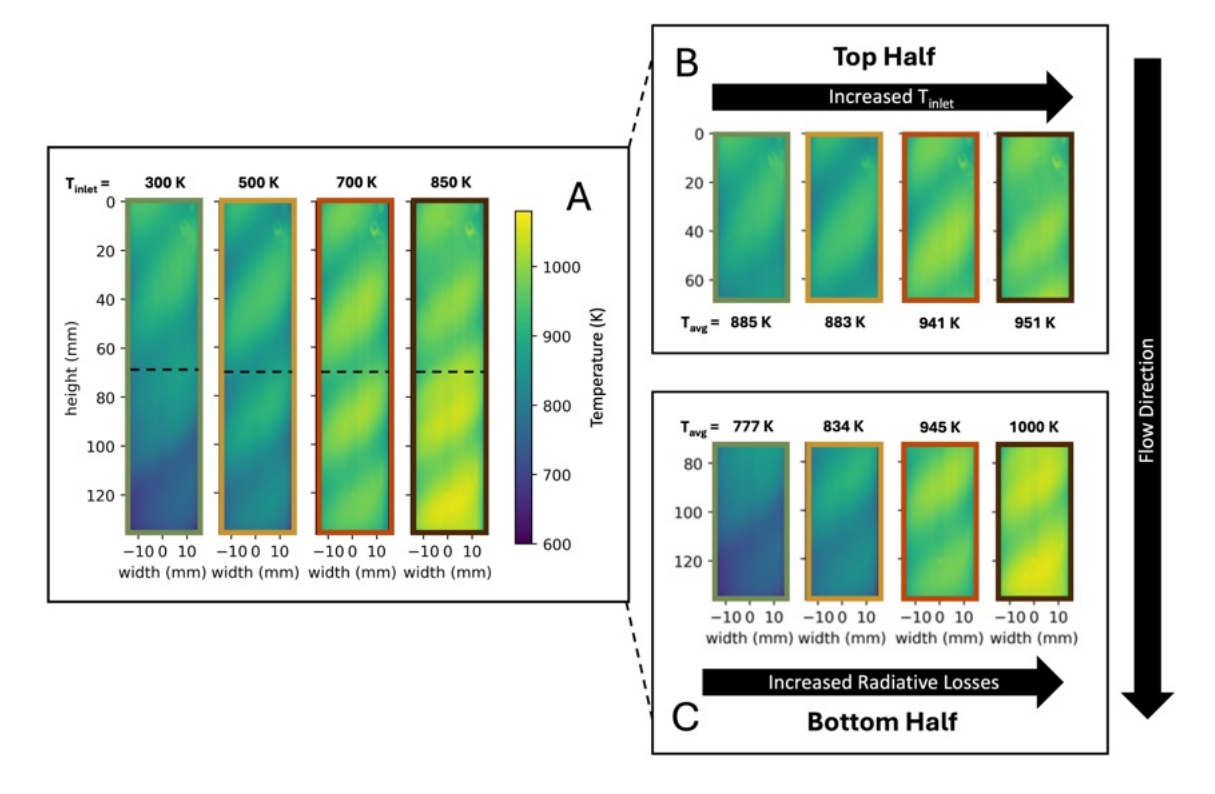


FIGURE 3.8: (A) Thermal images of the QT inside the waveguide at different inlet temperatures, for $P_{total} = 1500$ W, $\phi_{\text{CO}_2} = 10$ ln/min, p = 900 mbar, and $T_{inlet} = 300$, 500, 700, and 850 K, where $P_{\text{CO}_2} = 0$, 62, 132, 189 W, respectively. The images show a downward shift in the position of peak wall temperature with increasing T_{inlet} , and they also illustrate the heating and cooling caused by the flow lines of the helical vortex, visible in the IR images. A pixel-by-pixel analysis (right) provides an average temperature (T_{avg}) for the top (B) and bottom half (C) of the thermographic image, showing the correlation with increasing T_{inlet} (top half, B) and increased exothermic recombination (bottom half, C). For reference, the reported OES measurements were taken in the middle of the waveguide, where the dashed line is indicated.

The results presented in Figure 3.8 reveal two key phenomena: 1) a downward shift in the position of the peak wall temperature with increasing T_{inlet} that falls inside the vortex flow lines, demonstrating the heating and cooling on the surface QT and 2) increased radiative losses with increasing T_{inlet} , as calculated by Stefan-Boltzmann's law. These observations can be explained through several mechanisms. First, the preheated input

flow is the likely culprit for the slight increase in the average temperature observed in the top half of the reaction chamber (Figure 3.8B). For example, at $T_{inlet} = 300 \text{ K}$, the T_{avg} is 885 K vs at $T_{inlet} = 850$ K, the T_{avg} increases to 951 K. However, the downward migration of the peak temperature zone observed (Figure 3.8C) cannot be attributed solely to the preheated inlet gas flow, which would primarily affect the upper region of the tube. Furthermore, in Figure 3.5, we observed that the periphery temperatures derived from the flame band emission remain relatively consistent regardless of T_{inlet} , which is further demonstrated by additional data provided in Appendix A, Section A.5. Therefore, we consider this increased temperature on the surface of the QT is likely caused by an increase in exothermic recombination reactions, consistent with previous observations by Wolf et al. [7] and van Deursen et al. [17]. It is also worth noting that the helical vortex flow structure remains clearly visible in all IR images throughout the entire QT, from top to bottom. The darker spiral bands indicate where the cooler input gas flows along the QTwalls, demonstrating that the vortex structure maintains its integrity as it passes around the reactive volume. This visualization of the flow lines provides important evidence supporting our analysis of the temperature distribution patterns observed in Figure 3.8B and 3.8C, helping to explain the downward migration of peak temperatures with increasing T_{inlet} , as the helical flow patterns appear to influence heat transfer and reaction zone positioning throughout the reactor. This hypothesis is further substantiated when we consider the relationship between the total dissipated power (radiative + convective) with T_{inlet} , as well as between the radiated power for the top half and bottom half of the QT with T_{inlet} , as shown in Figure 3.9(A,B).

Figure 3.9A shows the total dissipated power (W) from the QT as a function of T_{inlet} from 300 K to 850 K. While Figure 3.9B shows the radiative losses for the top and the bottom half (see legend), as split in Figure 3.8B. Both curves show an overall increasing trend in the radiated power as T_{inlet} increases, but the rise is more pronounced for the bottom half. These findings suggest that preheating primarily affects the upstream flow dynamics, which then influences the reactive cross section (Figure 3.5) and thus the reactive volume interface (Figure 3.6). This is further validated by the increase in total losses being greater than the power added through preheating, suggesting that this increase is due to changes in flow dynamics and/or an increase in recombination. The radiated heat pattern (Figure 3.8) also provides evidence for significant atomic oxygen recombination (R3.1) or atomic oxygen recombination with CO, the origin of chemiluminescent flame

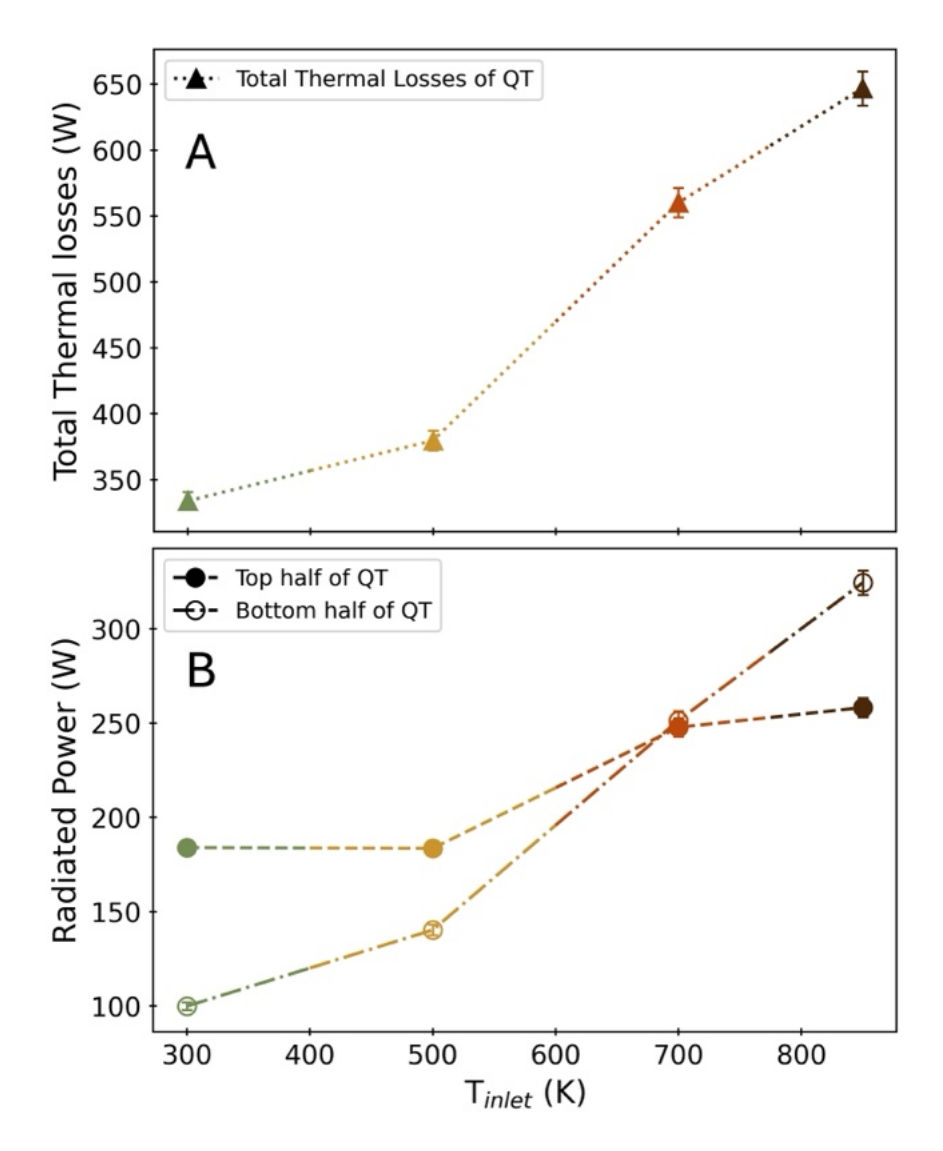


FIGURE 3.9: (A) Total dissipated power (radiative + conductive) as a function of T_{inlet} , showing that the total losses increase with increasing T_{inlet} , (B) Radiated power (calculated using Stefan-Boltzmann's law from the calculated pixel-by-pixel T_{avg} , indicated in Figure 3.8) for both top and bottom half, as a function of T_{inlet} . The increase of the radiative power for the top half and the bottom half of the QT reaches an inflection point at $T_{inlet} = 700 \text{ K}$.

band emission, simplified as (R3.2) between the plasma and downstream region:

$$O + O + M \rightarrow O_2 + M, \ \Delta H = -5.18 \text{ eV}$$
 (R3.1)

$$CO + O + M \to CO_2 + h\nu + M, \ \Delta H = -5.53 \text{ eV}$$
 (R3.2)

as atomic oxygen, produced at the same rate as CO, would generate substantial heat during recombination [5, 7, 27].

Furthermore, these reactions will increase with pressure due to the third body collisional factor. Therefore, any gains in conversion due to increases in the reactive volume are likely lost due to downstream recombination. *Vertongen et al.* showed that although atomic oxygen plays a crucial role in efficient CO₂ dissociation, the presence of atomic oxygen in the effluent also enhances the rate of recombination, decreasing overall conversion [28].

In summary, the observed downward shift in temperature distribution with increasing T_{inlet} confirms that complex interactions exist between flow patterns and heat transfer. These findings demonstrate that preheating effects on plasma behavior are highly pressure dependent. Moreover, the temperature profiles reveal that peripheral temperatures remain below 1500 K across all T_{inlet} conditions, maintaining effective quenching capability for the back reaction of CO + O. However, thermal imaging shows that preheating increases radiative losses through the reactor walls and shifts the peak temperature zone downward. This redistribution of thermal energy suggests modified flow patterns and potentially accelerated recombination processes in the downstream region, particularly evident in the enhanced heat release patterns observed with higher inlet temperatures. The preservation of the peripheral temperature profile, and its relation to effective quenching, despite increased T_{inlet} , is particularly noteworthy, as it indicates that preheating primarily influences upstream flow dynamics and reactive volume distribution, without compromising conversion to CO. However, the increased wall losses and evidence of enhanced recombination suggest that optimizing thermal management in the downstream region becomes increasingly critical at higher T_{inlet} .

3.4 Conclusions and Outlook

This chapter investigates inlet gas preheating in a 915 MHz CO₂ MW plasma, which reveals distinct effects on the spatial temperature distribution or the 'reactive volume' around the plasma. At low pressures (< 200 mbar), when plasma is noted to be in a hybrid contraction state [22], preheating adversely affects performance by decreasing the radial temperature profile (reactive area) and the axial plasma profile, resulting in a reduced reactive volume, which correlates to reduced conversion. However, at higher pressures (> 300 mbar), when the plasma is fully contracted, preheating demonstrates substantial benefits by expanding the spatial temperature profile, or the reactive volume, which relates to improved conversion.

For example, at 700 mbar under constant $P_{MW} = 1000 \text{ W}$, preheating to 700 K increases conversion by ~ 1.7 compared to baseline conditions. This was found to correlate directly with an increase in the reactive area of ~ 1.5 compared to baseline conditions. Similar improvements were observed at 900 mbar with only 500 K preheating. Furthermore, the expanded reactive volume observed with preheating modifies the reactive volume-bulk gas interface, creating a larger region where temperatures exceed the CO₂ dissociation threshold (> 1500 K). The spectroscopic measurements reveal that preheating primarily affects the spatial distribution of thermal energy rather than core plasma properties, as the core plasma temperature was consistently reported to be between $\sim 6000 - 7000 \text{ K}$, regardless of T_{inlet} , while peripheral temperatures remained below ~1000 K, maintaining effective quenching capability. This suggests that the classical description of thermal instability-driven contraction should be expanded to include upstream flow considerations, particularly with the interplay between convective cooling, temperature gradients, and reactive volume formation. The pressure-dependent response to preheating reveals that gas density and flow dynamics play critical roles in determining the spatial temperature distribution beyond what electron density alone would predict. This means that the high-temperature reactive volume, in which CO₂ dissociation is dominated, is not limited to the plasma volume as defined by the electronically excited atomic oxygen 777 nm emission. The observed correlation between T_{inlet} , reactive volume expansion, and conversion challenges the conventional understanding of contracted plasma behavior.

Moreover, the relationship between preheating and performance follows a non-linear pattern. At higher power conditions ($P_{total} = 1500 \text{ W}$), conversion at 900 mbar shows a decline at higher T_{inlet} (850 K), suggesting that 850 K is above the optimal inlet temperature range. Thermographic imaging provides additional insights into this behavior, revealing a downward shift in peak wall temperature with increasing T_{inlet} and enhanced thermal losses through the walls, which correlate directly with reduced conversion. This redistribution of thermal energy suggests modified flow patterns and accelerated recombination processes in the downstream region. The increased wall losses and evidence of enhanced recombination suggest that implementing effective downstream quenching strategies, such as effluent nozzles, could further improve overall system performance by mitigating product loss. This highlighting the critical role of upstream thermal management in determining downstream conversion, providing a theoretical foundation for

optimizing plasma-chemical processes through strategic heat distribution rather than increased power input.

Our findings demonstrate that recycling even small amounts of the input power (< 14%) for preheating can significantly improve energy efficiency and conversion. This suggests that strategic implementation of heat recovery from downstream processes could substantially improve overall system efficiency in industrial applications. The observed pressure-dependent effects also indicate that preheating, if optimized, could extend high energy efficiency operation into the near-atmospheric pressure regime, reducing pumping power requirements. A comprehensive understanding of these aspects will be crucial for translating the observed benefits of preheating into practical improvements for industrial MW plasma-based CO₂ conversion, ultimately contributing to the development of sustainable technologies for carbon utilization and renewable energy storage.

Bibliography

- [1] W.A. Bongers, H. Bouwmeester, A.J. Wolf, F.J.J. Peeters, S. Welzel, D. van den Bekerom, N. den Harder, A. Goede amd M. Graswinckel, and P.W. Groen. Plasmadriven dissociation of CO₂ for fuel synthesis. *Plasma Processes and Polymers*, 14(6): 1600126, 2017. doi: 10.1002/ppap.201600126.
- [2] F.A. D'Isa, E.A.D. Carbone, A. Hecimovic, and U. Fantz. Performance analysis of a 2.45 GHz microwave plasma torch for CO₂ decomposition in gas swirl configuration. *Plasma Sources Science and Technology*, 29(10):105009, 2020. doi: 10.1088/1361-6595/abaa84.
- [3] J. Li, X. Zhang, J. Shen, T. Ran, P. Chen, and Y. Yin. Dissociation of CO₂ by thermal plasma with contracting nozzle quenching. *Journal of CO₂ Utilization*, 21: 72–76, 2017. doi: 10.1016/j.jcou.2017.04.003.
- [4] E.R. Mercer, S. Van Alphen, C.F.A.M. van Deursen, T.W.H. Righart, W.A. Bongers, R. Snyders, A. Bogaerts, M. C. M. van de Sanden, and F.J.J. Peeters. Post-plasma quenching to improve conversion and energy efficiency in a CO₂ microwave plasma. Fuel, 334:126734, 2023. doi: 10.1016/j.fuel.2022.126734.
- [5] A. van de Steeg, P. Viegas, A. Silva, T. Butterworth, A. van Bavel, J. Smits, P. Diomede, M.C.M. van de Sanden, and G. van Rooij. Redefining the microwave plasma-mediated CO₂ reduction efficiency limit: the role of O–CO₂ association. ACS Energy Letters, 6(8):2876–2881, 2021. doi: 10.1021/acsenergylett.1c01206.
- [6] D.C.M. van den Bekerom, J.M.P. Linares, T. Verreycken, E.M. van Veldhuizen, S. Nijdam, G. Berden, W.A. Bongers, M.C.M van de Sanden, and G.J. van Rooij. The importance of thermal dissociation in CO₂ microwave discharges investigated by power pulsing and rotational raman scattering. *Plasma Sources Science and Technology*, 28 (5):055015, 2019. doi: 10.1088/1361-6595/aaf519.

- [7] A.J. Wolf, F.J.J. Peeters, P.W.C Groen, W.A. Bongers, and M.C.M Van De Sanden. CO₂ conversion in nonuniform discharges: Disentangling dissociation and recombination mechanisms. *The Journal of Physical Chemistry C*, 124(31):16806–16819, 2020. doi: 10.1021/acs.jpcc.0c03637.
- [8] O. Schönherr and J. Hessberger. Production of long stable electric arcs, 1909.
- [9] The manufacture of nitrates from the atmosphere. Nature, 89(2227):463-465, 1912.doi: 10.1038/089463a0.
- [10] K.H.R. Rouwenhorst, F. Jardali, A. Bogaerts, and L. Lefferts. From the birkeland–eyde process towards energy-efficient plasma-based NO_X synthesis: a technoeconomic analysis. *Energy & Environmental Science*, 14(5):2520–2534, 2021. doi: 10.1039/D0EE03763J.
- [11] M.I. Boulos, P.L. Fauchais, and E. Pfender. Handbook of Thermal Plasmas. Springer Nature Switzerland, 2023. doi: 10.1007/978-3-030-84936-8.
- [12] L. Kerker and R. Müller. Plasma reforming process for the production of reducing gases. Stahl Eisen; (Germany, Federal Republic of), 104(22), 1984.
- [13] B. Cárdenas, S.D. Garvey, B. Kantharaj, and M.C. Simpson. Gas-to-gas heat exchanger design for high performance thermal energy storage. *Journal of Energy Storage*, 14:311–321, 2017. doi: 10.1016/j.est.2017.03.004.
- [14] S.B. Shridhar, A. Rabinovich, A. Fridman, and H. Pearlman. Process optimization of methane reforming to syngas using gliding arc plasmatron. *Plasma Processes and Polymers*, 16(4):1800159, 2019. doi: 10.1002/ppap.201800159.
- [15] C.H. Cho, J.H. Kim, J.K. Yang, I.S. Park, Y-S Choi, and I.J Kang. Dry reforming process using microwave plasma generator with high carbon dioxide conversion efficiency for syngas production. *Fuel*, 361:130707, 2024. doi: 10.1016/j.fuel.2023.130707.
- [16] S. Jo, D.H. Lee, and Y-H Song. Effect of gas temperature on partial oxidation of methane in plasma reforming. *International Journal of Hydrogen Energy*, 38(31): 13643–13648, 2013. doi: 10.1016/j.ijhydene.2013.08.049.

- [17] C.F.A.M. van Deursen, H.M.S. Van Poyer, W.A. Bongers, F.J.J. Peeters, F.M.A Smits, and M.C.M van de Sanden. Effluent nozzles in reverse-vortex-stabilized microwave CO₂ plasmas for improved energy efficiency. *Journal of CO₂ Utilization*, 88: 102952, 2024. doi: 10.1016/j.jcou.2024.102952.
- [18] A.J. Wolf, T.W.H. Righart, F.J.J. Peeters, P.W.C. Groen, M.C.M van de Sanden, and W.A. Bongers. Characterization of CO₂ microwave plasma based on the phenomenon of skin-depth-limited contraction. *Plasma Sources Science and Technology*, 28(11): 115022, 2019. doi: 10.1088/1361-6595/ab4e61.
- [19] E. Carbone, F. D'Isa, A. Hecimovic, and U. Fantz. Analysis of the C_2 $d^3\Pi_g a^3\Pi_u$ swan bands as a thermometric probe in CO_2 microwave plasmas. *Plasma Sources Science and Technology*, 2019. doi: 10.1088/1361-6595/ab74b4.
- [20] G. Raposo, A.W. van de Steeg, E.R. Mercer, C.F.A.M van Deursen, H.J.L. Hendrickx, W.A. Bongers, G.J. van Rooij, M.C.M. van de Sanden, and F.J.J. Peeters. Flame bands: CO + O chemiluminescence as a measure of gas temperature. *Journal of Physics D: Applied Physics*, 54(37):374005, 2021. doi: 10.1088/1361-6463/ac0924.
- [21] B. Wanten, R. Vertongen, R De Meyer, and A. Bogaerts. Plasma-based CO₂ conversion: How to correctly analyze the performance? *Journal of energy chemistry*, 2023. ISSN 2095-4956.
- [22] A.J. Wolf, T.W.H. Righart, F.J.J. Peeters, W.A. Bongers, and M.C.M. Van De Sanden. Implications of thermo-chemical instability on the contracted modes in CO₂ microwave plasmas. *Plasma Sources Science and Technology*, 29(2):025005, 2020. doi: 10.1088/1361-6595/ab5eca.
- [23] P. Viegas, L. Vialetto, A.J. Wolf, F.J.J. Peeters, P.W.C. Groen, T.W.H. Righart, W.A. Bongers, M.C.M van de Sanden, and P. Diomede. Insight into contraction dynamics of microwave plasmas for CO₂ conversion from plasma chemistry modelling. *Plasma Sources Science and Technology*, 29(10):105014, 2020. doi: 10.1088/1361-6595/abb41c.
- [24] O. Biondo, A. Hughes, A. van de Steeg, S. Maerivoet, B. Loenders, G. van Rooij, and A. Bogaerts. Power concentration determined by thermodynamic properties in complex gas mixtures: the case of plasma-based dry reforming of methane. *Plasma Sources Science and Technology*, 32(4):045001, 2023. doi: 10.1088/1361-6595/acc6ec.

- [25] L. Vialetto. Modelling of plasma for CO_2 conversion: electron kinetics, chemistry and transport. PhD thesis, Eindhoven University of Technology, 2021.
- [26] C.K. Kiefer, R. Antunes, A. Hecimovic, A. Meindl, and U. Fantz. CO₂ dissociation using a lab-scale microwave plasma torch: An experimental study in view of industrial application. *Chemical Engineering Journal*, 481:148326, 2024. doi: 10.1016/j.cej. 2023.148326.
- [27] K. Wang, S. Ceulemans, H. Zhang, I. Tsonev, Y. Zhang, Y. Long, M. Fang, X. Li, J. Yan, and A. Bogaerts. Inhibiting recombination to improve the performance of plasma-based CO₂ conversion. *Chemical Engineering Journal*, 481:148684, 2024. doi: 10.1016/j.cej.2024.148684.
- [28] R. Vertongen, G. Trenchev, R. Van Loenhout, and A. Bogaerts. Enhancing CO₂ conversion with plasma reactors in series and O₂ removal. *Journal of CO₂ Utilization*, 66:102252, 2022. doi: 10.1016/j.jcou.2022.102252.

Chapter 4

Dual Injection in a CO₂ Plasma: Exploring Reactive Quenching

In this chapter, we investigate dual injection in a 2.45 GHz CO₂ microwave plasma, where CH₄ is injected into the afterglow region as a novel approach to utilize the high post-plasma temperatures for additional chemistry with reactive quenching. The experiments were conducted at various pressures, powers, and CO₂:CH₄ ratios. We find that this approach effectively enhances absolute CO_2 conversion, with a maximum reported value of $\sim 55\%$ at 1250 W, 500 mbar, and a $CO_2:CH_4$ ratio of 7:7 slm. Furthermore, we compare our dual injection method with the approach of admixing Dry Reforming of Methane (DRM), using a comprehensive analysis of gaseous and liquid products, as well as carbon structure and morphology, with the latter exhibiting a fused amorphous structure, formed under fast cooling conditions. Using chemical kinetics modeling we identify key pathways, explaining the enhanced CO_2 conversion by the removal of O atoms and O_2 molecules, which prevents participation in recombination reactions, while supplying H atoms upon CH_{λ} dissociation. This results in the reverse water-gas shift reaction, which lowers the syngas ratios compared to admixing DRM. Nonetheless, the model predicts that increasing the specific energy input may achieve more competitive syngas ratios. Our findings represent an advancement toward precise control of microwave-based plasma chemistry.

This chapter is derived from the following publication:

[•] Dual Injection in a CO_2 Microwave Plasma: Exploring Post-Plasma Quenching with CH_4 and Comparison with DRM (Submitted Manuscript)

E.R. Mercer, M. Albrechts, R. De Meyer, I. Fedirchyk, E. Morais, S. Bals, A. Bogaerts

4.1 Introduction

As discussed in Chapter 2 (Section 2.4.2), recent studies have highlighted the importance of post-plasma quenching in CO_2 plasma to maximize conversion and energy efficiency, with many experimental studies focused on rapidly decreasing the extreme temperatures measured in the afterglow region (typically T >> 1500 K) by enhanced mixing of cool periphery flows and the hot reactive volume using nozzles [1–6]. The goal of such strategies is to reduce 'burn back', typically observed as a blue afterglow in CO_2 MW plasmas, resulting from the chemiluminescent recombination of CO + O to CO_2 [7]; however, such high temperatures observed in the downstream afterglow region have the potential to transfer the exergy into additional chemistry, using methods of reactive quenching (also known as chemical trapping) [8–11]. Moreover, the removal of O atoms and O_2 molecules through reactive quenching in the afterglow of CO_2 plasma has been found to enhance the retainment of CO [12–16].

One effective example of reactive quenching is placing a carbon bed in the afterglow region of CO₂ plasmas [14–17], which has been shown to significantly improve the yield of CO by removing O atoms and O_2 molecules while reducing the overall energy cost. Girard-Sahun et al. [14] showed that a carbon bed placed directly after a Gliding Arc Plasmatron (GAP) reactor enhances the CO₂ conversion while achieving an oxygen-free effluent. This research successfully demonstrated how eliminating O atoms and O₂ molecules in the post-plasma gas mixture not only enhances CO output, but also eliminates the need for one of the most expensive separation steps required for industrialization [18], while simultaneously lowering the energy cost of the conversion process. Follow-up research by Biondo et al. [15] revealed that reducing the distance between reactor outlet and carbon bed further enhances performance by facilitating direct interaction between the carbon pellets and the reactive species in the afterglow. Moreover, O'Modhrain et al. [16] demonstrated the effects of bed size and insulation, noting the influence of higher postplasma temperature (as a result of the choice of power source) on conversion, and included a detailed study on the positive effects associated with bed insulation and preheating the carbon prior to entry into the bed, highlighting essential aspects of thermal management in plasma systems. This emphasizes the importance of reactive quenching and thermal management in controlling recombination in the post-plasma region.

The literature for post-plasma reactive quenching using a secondary gas injection (i.e., via dual injection) is limited. A study by Chekmarev et al. [19] demonstrated a threefold increase in CO_2 conversion by injecting nitrogen (N_2) as a quenching gas in the post-plasma region. Although the authors reported that the dissociation of N_2 was minor, they successfully showed an increase in conversion and energy efficiency as a function of the secondary injection of N_2 flow rates. Another study by Mansfeld et al. [20] showed that using argon (Ar) as a post-plasma quenching agent was also successful at reducing recombination, with observed reduction of the characteristic flame band afterglow from recombination to CO_2 [7] and an accompanying enhancement in conversion. These examples highlight the importance of understanding the role of secondary injection quenching in plasma-based chemical conversion.

As research has demonstrated, controlled manipulation of the post-plasma environment by introducing improved mixing, thermal management, and oxygen scavenging in the CO₂ afterglow region can significantly improve conversion [1–5, 14–16, 19, 21], helping to optimize process performance in plasma systems. This begs the question of whether the strategy of introducing a reactive quenching gas, such as an oxygen scavenger like methane (CH₄), shows the same promise for enhancing reactor performance. Experimental and modeling investigations by Aerts et al. [22] reveal that in-situ scavenging of O atoms and O₂ molecules via a hydrogen source (e.g., CH₄), provides an oxygen-free effluent mixture that can be more easily separated using existing technologies [18, 23, 24]. When CO₂ is combined with CH₄, the reaction produces a mixture of CO and hydrogen (H₂), which is a versatile precursor for fuels and chemicals, known as synthesis gas (syngas). This reaction is widely known as Dry Reforming of Methane (DRM); however, controlling the syngas ratio and dealing with solid carbon formation at higher CH₄ fractions [25–35].

The difficulty in controlling the produced syngas ratio (i.e., H₂/CO) presents a critical limitation when admixing CO₂ and CH₄ in plasma-based DRM. This is because, in ideal DRM, the stoichiometric reaction yields a syngas ratio of 1; therefore, to achieve higher syngas ratios, e.g., around 2, which is required for methanol synthesis or the Fischer-Tropsch process [36], significantly more CH₄ must be converted over CO₂. However, when admixing CO₂ and CH₄, increasing the CH₄ fraction reduces the absolute conversion of this reactant [26, 28], as well as increases solid carbon formation. For instance, *Kelly et al.* [28] reported energy costs as low as 2.8 eV/molecule for MW plasma-based DRM,

with CO_2 and CH_4 conversions of 49% and 67%, respectively. However, the authors reported significant plasma instability at CH_4 fractions exceeding 45%, attributed to solid carbon formation in the plasma region [28]. The syngas ratio in the product stream remained at $\lesssim 1$, consistent with other reports in literature [5, 30]. The formation of solid carbon in plasma-based DRM creates operational instability, affecting power coupling and destabilizing the plasma [26, 28, 32, 33, 35]. This carbon formation not only reduces process efficiency but also requires frequent maintenance of reactor components. Wanten et al. [33] performed experiments in an Atmospheric Pressure Glow Discharge (APGD), and reported that increasing the CH_4 fraction led to an increasingly unstable plasma due to the formation of solid carbon. This negatively affected the conversion and reactor performance in general and limited their experiments to CH_4 fractions < 35% [33]. This is particularly relevant in MW plasma-based DRM, as carbon particles formed during the reaction interact with the MW field, in turn destabilizing the discharge [26, 28, 37].

Several efforts to mitigate carbon formation in plasma-based DRM have been reported. Biondo et al. [26] showed that reverse vortex flow configurations can successfully suppress carbon formation at reduced pressures, suggesting that the flow typology plays a critical role in carbon nucleation in MW plasmas [38, 39]. Macrivoet et al. [35] demonstrated that the addition of O₂ to DRM (so-called OCRM) in an APGD resulted in the oxidation of solid carbon, allowing for more stable conditions; however, the results also revealed a higher selectivity to water (H₂O). In another APGD experiment, Wanten et al. [32] suppressed soot formation by admixing H₂O vapor to the reactive gas stream (in so-called bi-reforming, BRM), both enhancing plasma stability and increasing syngas ratios. In this chapter, we seek to mitigate the instability attributed to high CH₄ fractions and the resulting solid carbon formation by injecting CH₄ into the post-plasma region as a reactive quenching agent. An example of post-plasma CH₄ injection in literature was conducted by Cho et al. [27], where the authors ran experiments in a system utilizing dual injection for DRM with a 1:1 CO₂:CH₄ ratio in a 2.45 GHz MW reactor. The study explored a two-phase system: within the resonance chamber, a CO₂ plasma was first generated utilizing a double helix injection at atmospheric pressure, followed by an injection of CH₄ at the start of an insulated stainless steel reforming reaction chamber [27]. The novel double-helix type plasma generator from this work reported high conversion and energy efficiency, and serves as an example of an extended reaction chamber, with two processes in series. This contrasts with the system we propose, which uses direct post-plasma reactive quenching with the goal of reducing the post-plasma temperatures quickly to mitigate recombination reactions. We introduce dual injection in a CO_2 MW plasma by injecting CH_4 into the high-temperature post-plasma region as a reactive quenching agent. Our experimental results are supported by modeling, performed by Matthias Albrechts (Ph.D. student within PLASMANT), which further investigates the reaction pathways. This configuration leverages the thermal energy of the plasma afterglow (T > 1500 K). We hypothesize that CH_4 will act as an effective quenching agent for O atoms and O_2 molecules generated in the primary CO_2 plasma, enhancing CO_2 conversion by suppressing CO_3 recombination back to CO_2 .

This chapter aims to understand how this approach measures against pure CO₂ conversion. Furthermore, by enabling the treatment of larger CH₄ fractions (without plasma destabilization by carbon deposition), we also aim to determine how this might be beneficial in a DRM context, in relation to the syngas ratio, process stability, energy cost, and product selectivity compared to conventional (admixing) DRM. In this respect, we also investigate the liquid byproducts and solid carbon formation. We gain deeper insights into the experimental results by using a 0D chemical kinetics model designed to investigate the post-plasma reactions in a dual injection system. The model examines the mixing of the thermal CO₂ plasma effluent with cold CH₄ injection in the post-plasma region. As established in the Chapter 1 and Chapter 2, we hope to advance the practical implementation of these technologies for CO₂ utilization, representing a step toward more precise control of plasma chemistry, and investigating new pathways for the selective production of fuels and chemicals from greenhouse gases.

4.2 Methods

4.2.1 Experimental Setup

As shown in Figure 4.1, the MW plasma reactor is powered by a custom-designed 2.45 GHz solid-state source composed of a collection of LDMOS power amplifiers with a rated efficiency of $\sim 54\%$ (LDMOS PAs, right side of Figure 4.1) from which the output is combined in a specialized 8-port WR340 combiner waveguide (see Chapter 2, Section 2.2.2), which is protected from reflected power by an isolator. The absorbed and reflected power (< 5% for all results reported) were measured using the Homer series auto-tuner from

S-TEAM labs. Together, the auto-tuner, impedance analyzer, and adjustable short tune the electric field to optimal conditions for electrical breakdown and to sustain the plasma. The tapered resonance chamber is intersected perpendicularly by a 16 mm inner diameter quartz tube, where the CO₂ plasma is formed as a surface-wave discharge. Directly after the plasma, CH₄ is injected into the afterglow region, which was monitored via the 'afterglow viewing quartz' to observe carbon formation.

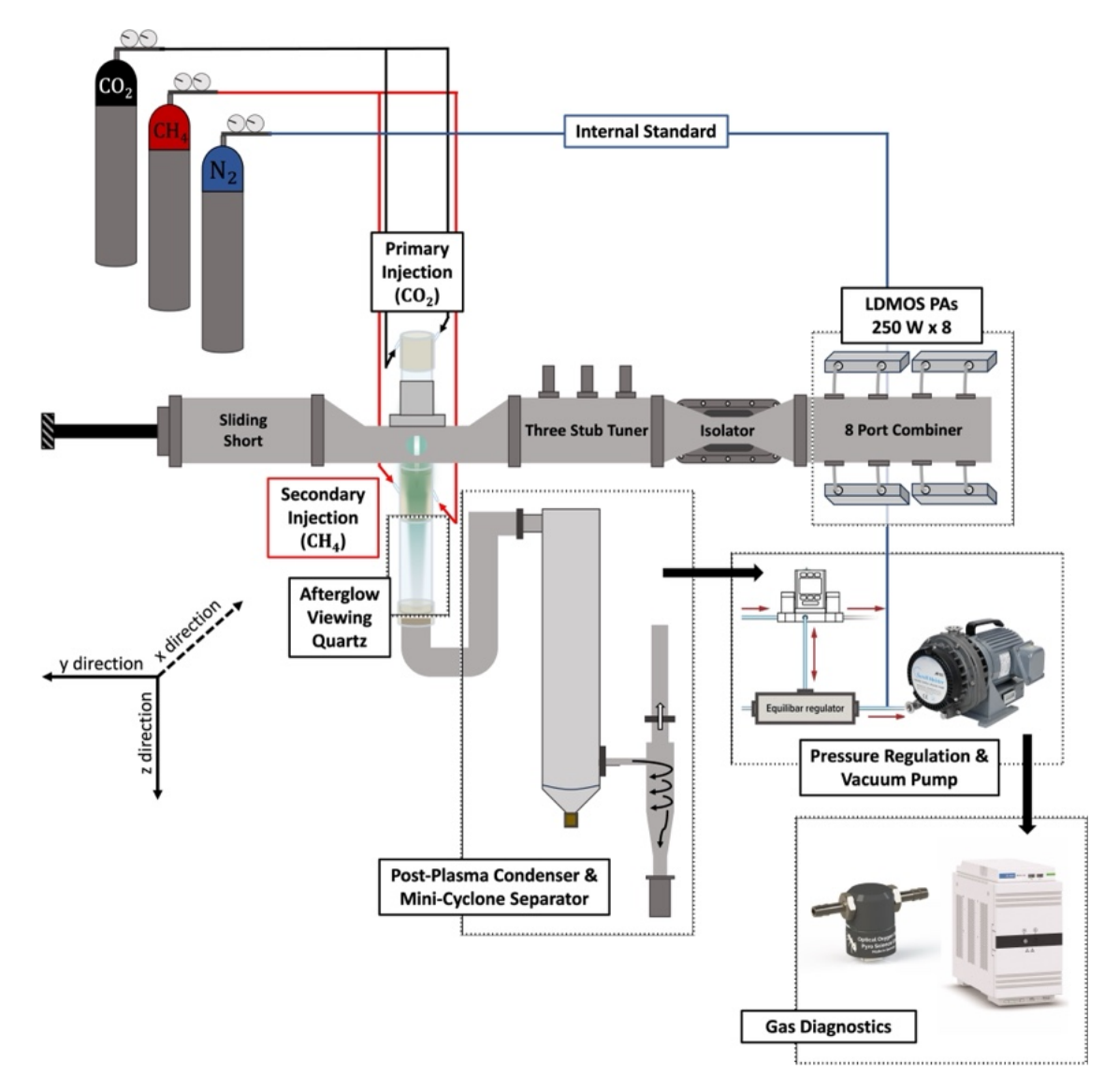


FIGURE 4.1: Overview of the experimental setup.

As shown in Figure 4.1, the product stream is fed into a post-plasma condenser, which collects the liquid products, analyzed using a series of diagnostic techniques outlined in Appendix B, Section B.1.1. The cooled gas then moves to a miniature cyclone separator, which was designed to collect carbon particles down to 1 μ m with 95% efficiency [40]. The deposited carbon in the post-plasma region and cyclone separator is analyzed using two

methods, Scanning Electron Microscopy (SEM) and Transmission Electron Microscopy (TEM) [28]. All solid carbon related analysis was performed by Robin De Meyer (Ph.D. student within PLASMANT). Additional information on the carbon characterization can be found in Appendix B, Section B.1.2.

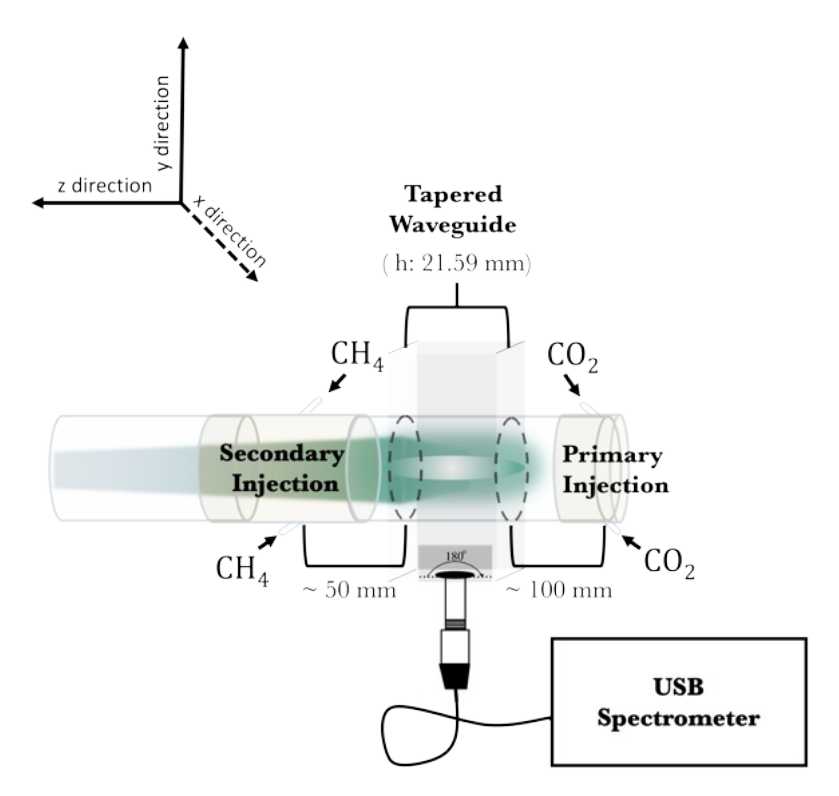


Figure 4.2: Schematic view of the dual injection system with optical emission spectroscopy.

A zoomed-in image of the injection setup is shown in Figure 4.2, where the primary injection of the reactant gas (CO₂) is fed through the quartz discharge tube via a helical swirl inlet, at the right of Figure 4.2. Upon ignition, a surface-wave sustained mode is generated, with an axially elongated warm plasma filament located in the center of the quartz tube, isolated from the tube walls by the vortex generated from the swirl inlet. Within the resonance chamber, Optical Emission Spectroscopy (OES) is performed to analyze the spectrum generated by the plasma using an Ocean Insight mini spectrometer (HR-4UVV250-5) equipped with a solarization-resistant fiber with a diameter of 400 μ m (QP400-2-SR) and a cosine corrector with Spectralon diffusing material (CC-3-UV-S). Additional information on the optical techniques is available in Appendix B, Section B.1.3. A secondary counter-flow tangential injection of CH₄ with 1 mm inlets is initiated in the afterglow region, 5 cm from the waveguide, where temperatures exceed 1500 K (see Appendix B, Section B.1.4, for a detailed schematic of the secondary injection housing).

The afterglow is viewed through a secondary quartz tube placed after the secondary injection housing, where we were able to observe irradiation from solid carbon (forming within the post-plasma) and any deposits on the quartz tube wall in real-time. A thermocouple placed ~ 200 mm downstream measures the post-secondary injection temperature.

An internal standard, used to determine the expansion coefficient in order to correctly calculate the performance metrics [41], is introduced before the vacuum pump (ISP 500C Scroll Meister, Figure 4.1). The pressure in the system is monitored and adjusted by a membrane-controlled pressure regulator (see Figure 4.1; Equilibra Regulator, GSD Series Precision Back Pressure Regulator), which allowed a range between ∼1 mbar and atmospheric pressure. It is well known that CO₂ conversion declines with increasing pressure [1, 2, 42, 43], therefore in this study, we investigate how this changes with quenching by introducing a pressure series from 200 – 900 mbar. Although calculations of the estimated mixture in relation to the explosion regime were completed, there were still safety concerns about injecting CH₄ into the post-plasma afterglow. Therefore, we limited the testing to quasi-atmospheric pressure (900 mbar), as this has been shown to have the same KPIs as atmospheric pressure [44], so that a larger safety protocol could be implemented for overpressure events that would occur in the instance of an explosion. The product gas stream is analyzed using an optical oxygen sensor (Pyroscience, GmbH FDO2), and Gas Chromatography (GC, two-channel, Agilent 990 MicroGC, Appendix B, Section B.1.5). Additional details on the diagnostic techniques and performance analysis can be found in Appendix B, Section B.1.6.

4.2.2 Model Description

The modeling work carried out in this chapter was performed by Matthias Albrechts to gain deeper insights into the experimental results. We perform modeling calculations using a 0D chemical kinetics model in the framework of the *Chemical Reaction Engineering* module of COMSOL Multiphysics [45]. The model solves the 0D mass balance equations for all species in a batch reactor, given by:

$$\frac{d(c_i V)}{dt} = R_i V \tag{E4.1}$$

where c_i is the species molar concentration, V denotes the simulation volume and R_i is the species rate expression resulting from chemical reactions. We adopt the GRI-Mech 3.0 reaction mechanism [46] to describe the kinetics of the DRM chemistry, as was also done in *Albrechts et al.* [8].

The initial composition for the simulation is the chemical equilibrium composition of CO_2 at 7000 K, based on our OES measurements, which indicate a peak temperature between \sim 7000 – 8000 K (See Appendix B, Section B.1.3), representing the hot plasma core created by the contracted CO_2 plasma. Since our reactor does not utilize heat recovery of the wall losses in the plasma discharge, we assume that 20% of the energy input is lost through the quartz tube wall, as neglecting heat losses leads to overestimation of the total conversion, and the value of 20% gave reasonable agreement with experiments. For simplicity, this value is assumed constant across all pressures. Therefore, the Specific Energy Input (SEI, as the amount of power applied to the chemistry in a single pass through the reactor) to the discharge gas (CO_2 primary injection), used to calculate the fraction of CO_2 heated to 7000 K in this work, is multiplied by 0.8:

$$0.8 \times \text{SEI} = x_p \left(n_{eq} H_{CO_2, eq} (7000 \text{ K}) - H_{CO_2} (300 \text{ K}) \right)$$
 (E4.2)

In E4.2, x_p represents the molar fraction of CO₂ gas heated to 7000 K, $H_{CO_2,eq}$ indicates the enthalpy of the dissociated CO₂ equilibrium mixture (J/mol), and n_{eq} is a factor that accounts for the increase in the number of particles of the dissociated chemical equilibrium mixture.

At the beginning of the simulation, cold CO₂ (300 K) is added via an exponentially decaying source rate, simulating the mixing of the hot CO₂ gas core with the cold surrounding CO₂ flow, as is commonly observed in vortex-stabilized MW plasmas. After a period of 0.67–3.00 ms, depending on the pressure, cold CH₄ (300 K) is introduced to the simulation, according to E4.3. This represents the post-plasma CH₄ injection occurring approximately 5 cm downstream of the waveguide, as reported in the experiments, initiating the DRM chemistry:

if
$$t > t_{off}$$
: $R_m = \frac{n_{CH_4}}{\tau_{mix}} e^{-(t - t_{off})/\tau_{mix}}$ (E4.3)

where t is the simulation time, $t_{\rm off}$ indicates the time interval before the secondary injection of CH₄, R_m represents the mixing rate, i.e., the rate of CH₄ addition to the simulation (mol/s), $n_{\rm CH_4}$ is the total amount of CH₄ added to the system, and $\tau_{\rm mix}$ is the characteristic mixing time. We selected a $\tau_{\rm mix}=10$ ms at the highest pressure of 900 mbar, consistent with the values used in Albrechts et al. [8] at atmospheric pressure. The mixing time is scaled proportionally with pressure, as $\tau_{\rm mix}$ is inversely proportional to the diffusion constant, which itself is inversely proportional to pressure [8]. The $t_{\rm off}$ is set to 3 ms at the highest pressure of 900 mbar, and is scaled proportionally with pressure, similar to $\tau_{\rm mix}$.

The temperature in the simulation decreases due to mixing with the cold gas (upon secondary injection) and conductive heat losses to the wall, eventually quenching the reactive mixture, at which point the simulation is stopped. The model framework used in this study is thoroughly described in *Albrechts et al.* [8]. As explained above, several modifications were implemented, adapting the model to describe our experimental setup, which differs from the configuration used by *Cho et al.* [27], investigated in the previous modeling work [8].

4.3 Results and Discussion

This section presents our experimental findings of post-plasma reactive quenching with CH₄ in a 2.45 GHz CO₂ MW plasma under two absorbed power (P) conditions, 1000 and 1250 W, supported by modeling investigations performed by M. Albrechts (Ph.D. fellow in PLASMANT; see ref [8] for additional details), to explain the underlying mechanisms. Two primary (inlet with pure CO₂) mass flow rates were tested, 10 and 7 standard liters per minute (slm, EU, 20°C, 1 atm) under varying pressure, and with different secondary injection flow rates (inlet with pure CH₄) to investigate how different ratios of reactive quenching in the afterglow change performance metrics. Our results are organized to address the effects of dual injection on absolute CO₂ conversion and energy cost across various operating conditions, followed by a product distribution analysis, including syngas composition, liquid product formation, and carbon analysis.

4.3.1 Methane as a Reactive Quenching Agent: Absolute CO_2 Conversion

The data presented in Figure 4.3 demonstrates the influence of pressure on CO_2 conversion for a primary flow rate (CO_2) of 10 slm at P = 1000 W. We first compare our results with a benchmark measurement of pure CO_2 conversion without secondary injection of CH_4 .

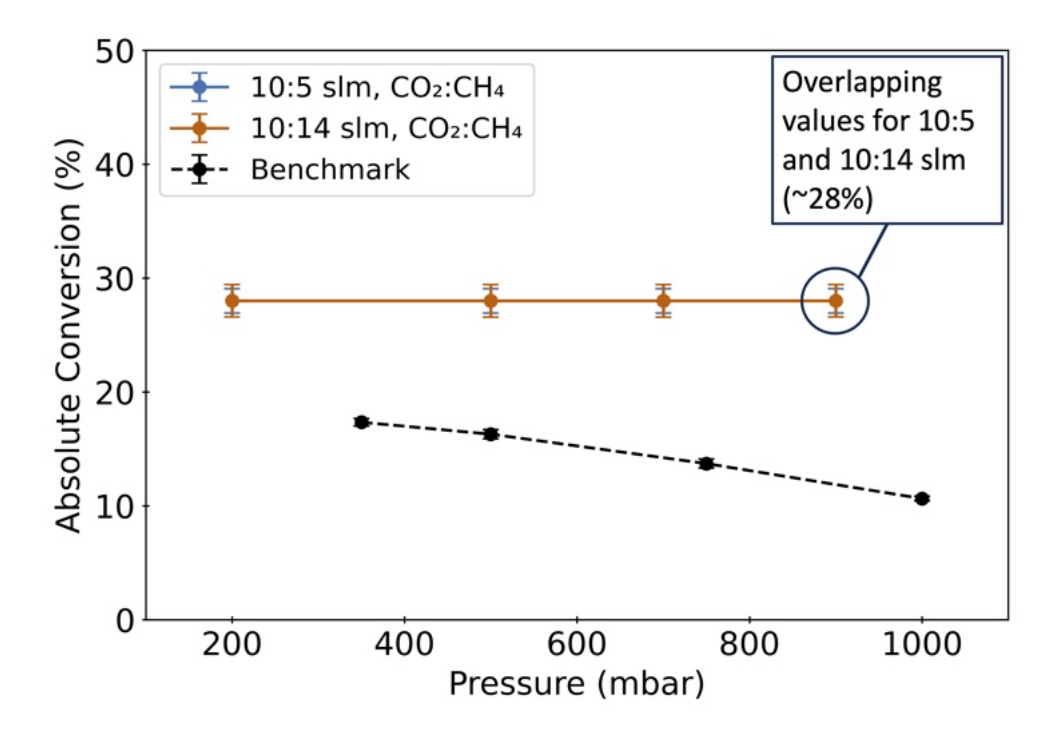


FIGURE 4.3: Absolute CO_2 conversion as a function of pressure for 10:5 and 10:14 slm ratios (CO_2 :CH₄) for a primary flow rate (CO_2) of 10 slm and 1000 W, compared to pure CO_2 plasma under the same conditions with no secondary injection (Benchmark). As shown, the data points for the two ratios (10:5 slm and 10:14 slm CO_2 :CH₄) are identical (\sim 28%) across all pressures.

In the case of the pure CO_2 plasma without a secondary injection of CH_4 (Figure 4.3, dashed line), we observe the characteristic pressure dependence of conversion commonly reported in literature [42, 43], where, upon increasing pressure, conversion decreases due to enhanced product recombination [10, 43, 47, 48]. Notably, the conversion in the pure CO_2 plasma without post-plasma CH_4 injection is lower across all pressure conditions, ranging from $\sim 18\%$ at 200 mbar to $\sim 10\%$ at atmospheric pressure. For both the 10:5 and 10:14 slm, CO_2 : CH_4 ratios, we observe the same results for conversion (~ 28), with no dependence of absolute CO_2 conversion on pressure across the entire range studied (200 – 900 mbar), and regardless of the secondary injection flow rate of CH_4 . This

pressure-independent behavior suggests that introducing CH₄ in the post-plasma region effectively mitigates the recombination processes that typically limit CO₂ conversion at higher pressures, even at low flow rates of 5 slm (half the CO₂ flow rate at the inlet). Under these *SEI* conditions, we observe that the higher flow rate with the secondary injection of CH₄ (14 slm) does not show additional benefits to absolute CO₂ conversion compared to the lower flow rate (5 slm) of CH₄, both resulting in an almost 3-fold increase in conversion compared to pure CO₂ plasma at atmospheric pressure. This suggests that, beyond a certain threshold, increasing the flow rate of the secondary injection does not promote additional CO₂ conversion, possibly due to saturation of the quenching effect or limitations in the mixing dynamics between the afterglow and the secondary injection.

Figure 4.3 clearly illustrates that CH_4 can successfully be used as a quenching gas for CO_2 conversion. The underlying mechanisms are explained in Figure 4.4, showing the net rates of different CO_2 conversion reactions as a function of time when CH_4 or Ar are used as a quenching gas, as obtained from our model, for a CO_2 : CH_4 (or CO_2 :Ar ratio) of 10:14 slm, power of 1250 W, and pressure of 700 mbar. We present this condition as a representative example and note that the relative contributions of the different rates are similar across all conditions. To account for changes in simulation volume over time (due to gas expansion from reactions and temperature increase), we scale the reaction rates by multiplying them by the actual volume and then divide this product by the total number of moles of CO_2 fed into the system throughout the entire simulation, as previously reported in Albrechts et al. [8], resulting in the rate of CO_2 conversion expressed in s^{-1} .

The dominant reactions governing CO₂ conversion in our model are:

$$CO_2 + M \rightleftharpoons CO + O + M$$
 (R4.1)

$$CO_2 + O \rightleftharpoons CO + O_2$$
 (R4.2)

$$CO_2 + H \rightleftharpoons CO + OH$$
 (R4.3)

where reaction R4.1 shows the thermal dissociation reaction (collision with a third body is denoted as M), reaction R4.2 represents dissociation upon collision with O atoms, and reaction R4.3 is H-mediated conversion. Indeed, we can assume that the chemistry is thermal, both inside the plasma (due to the high temperatures of 7000 K) and in the afterglow (where electrons and ions are no longer present). The rate coefficients

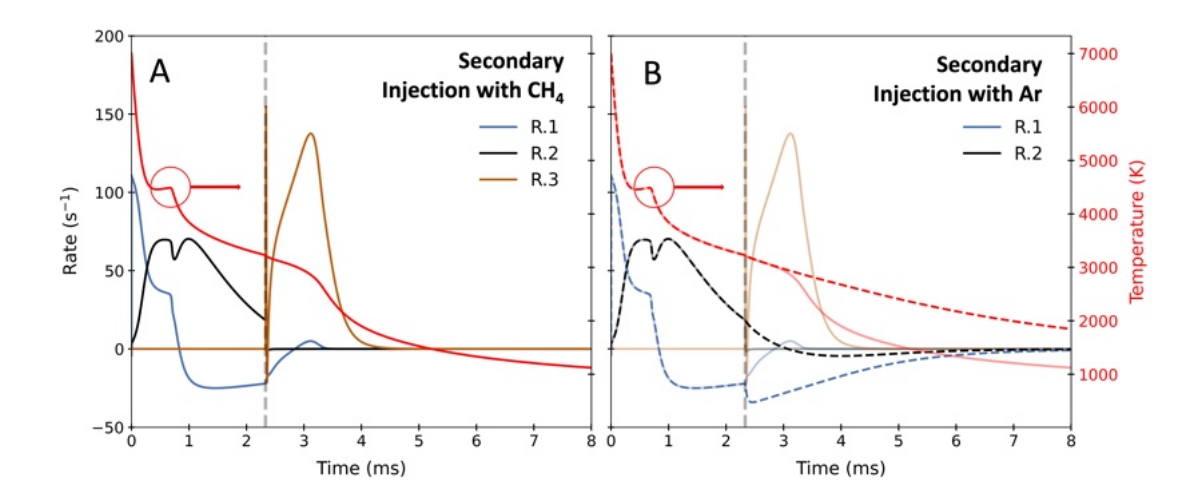


FIGURE 4.4: Calculated net rates of CO_2 conversion as function of time, for secondary injection quenching with CH_4 (4.A, solid lines) and Ar (4.B, dashed lines), at a p = 700 mbar, P = 1250 W, and CO_2 :CH₄ (or CO_2 :Ar) ratio of 10:14 slm. The temperature is plotted on the right y-axis. The vertical dashed grey line indicates the instance of CH_4 (or Ar) injection (t=2.33 ms). The reference rates for CH_4 quenching have been shaded in Figure 4.4.B for easy reference. The graph demonstrates that the temperature decreases more rapidly when CH_4 is used as a quenching gas, due to its higher heat capacity compared to Ar.

are defined by the GRI-Mech 3.0 reaction mechanism [46], where the reverse rates are calculated according to the principle of detailed balance.

As shown in Figure 4.4.A, at the start of the simulation, CO_2 is primarily converted through thermal dissociation (R4.1) due to the very high temperatures (T > 5000 K). As the temperature decreases due to the addition of cold CO₂ (grey vertical dashed line), the contribution of thermal dissociation decreases, and the reaction of CO_2 with O(R4.2), which has a significantly lower energy barrier, becomes the dominant CO₂ conversion pathway. Around t = 0.83 ms, the rate of R4.1 becomes negative, indicating that the reverse reaction becomes dominant, as there is insufficient energy for efficient thermal dissociation of CO₂, resulting in net creation of CO₂ by this reaction. Initially, the temperature is sufficiently high for the O atoms to convert more CO₂ via R4.2; however, as the temperature decreases, the destruction of CO via the reverse reaction of R4.1 (which has a significantly lower energy barrier) becomes more prominent compared to the forward rate of R4.2, leading to net CO₂ production when the temperature drops below approximately 3000 K, as indicated by the model. This is where cold CH₄ is introduced into the simulation, i.e., at t = 2.33 ms, representing the post-plasma injection of CH₄, as indicated by the sudden presence of CO₂ conversion by H atoms (R4.3). One of the reasons for using CH₄ as a quenching gas for CO₂ conversion is to remove O atoms through

CH₄ oxidation, thereby preventing it from reacting with CO to form CO₂ and enhancing the net CO₂ conversion. This is evident from Figure 4.4.A, which shows that the net rate of CO destruction via R4.1 rapidly goes to zero after CH₄ injection, preserving more of the CO produced in the hot CO₂ mixture. The results presented in Figure 4.4 demonstrate that CH₄ injection provides enhanced performance through two complementary chemical pathways: 1) effective suppression of CO recombination reactions, and 2) additional CO₂ conversion via the Reverse Water-Gas Shift (RWGS) reaction.

To further elucidate the specific advantages of using CH₄ as a reactive quenching agent, we conducted additional modeling calculations comparing CH₄ injection with inert Ar quenching under identical conditions to the 10:14 slm, CO₂:CH₄ ratio at 1250 W and 700 mbar, as shown in Figure 4.4.B. This comparison reveals two distinct mechanisms by which CH₄ enhances CO₂ conversion compared to thermal quenching. Figure 4.4.A presents the calculated net rates of CO₂ conversion reactions for both CH₄ (transparent solid lines) and Ar (dashed lines) quenching. When cold Ar gas is injected as a quenching agent, significant CO recombination occurs through the reverse of R4.1. This is evidenced by the pronounced negative peak at $t = 2.33 \ ms$, corresponding to the moment of injection, which destroys $\sim 30\%$ of the CO present upon injection of Ar. In contrast, when CH_4 is used, CO destruction due to recombination with O atoms is negligible (< 1%), owing to the efficient scavenging of O atoms through CH₄ oxidation. We observe that CH₄ effectively scavenges these O atoms through oxidation reactions (e.g., $CH_4 + O \rightarrow CH_3 +$ OH), before they can participate in recombination with CO, resulting in < 1% destruction of CO upon CH_4 injection. In addition to suppressing CO recombination, Figure 4.4.A highlights a substantial additional CO₂ conversion attributed to reactions with H atoms, linked to the RWGS reaction. This reaction accounts for approximately 33% of total CO production, effectively generating an additional 50% of the CO present at the instance of quenching. These combined effects lead to a notably higher CO₂ conversion of 36.1% when CH₄ is used as a quenching agent, compared to only 15.8% when cold Ar is injected post-plasma.

The calculation from Figure 4.4.B demonstrates that the temperature decreases more rapidly when CH₄ is used as a quenching gas, due to its higher heat capacity compared to Ar; however, it is important to note that the enhanced cooling effect of CH₄ as a quenching agent contributes minimally to the mitigation of CO recombination. Although CH₄ provides a higher cooling rate compared to Ar, the temperature profiles remain similar

during the critical time frame of t < 3.3 ms due to compensatory exothermic oxidation reactions. During this timescale, all O atoms undergo recombination, making CO recombination (R4.1) insignificant when temperature divergence begins, highlighting the importance of not only fast cooling but also quickly removing O atoms in the afterglow region. As a result, we conclude that the stronger cooling effect of CH₄ does not significantly influence CO₂ conversion when CH₄ is injected at this distance from the waveguide. The model convincingly demonstrate that reactive quenching with CH₄ effectively removes the O atoms, thus preventing them from the undesirable recombination reaction, CO + O \rightarrow CO₂. In addition, the dissociation/oxidation of CH₄ supplies H atoms, which contribute to additional CO₂ dissociation (R4.3). Both mechanisms predicted by the model explain the enhanced CO₂ conversion upon post-plasma CH₄ injection.

In Figure 4.5, we investigate the overall changes to the absolute conversion of CO_2 and CH_4 as a function of plasma power, for a primary flow rate (CO_2) of 10 slm. The data is organized into two graphs by the secondary injection flow rate of CH_4 (Figure 4.5A 10:5 slm, CO_2 : CH_4 and Figure 4.5B 10:14 slm, CO_2 : CH_4), for two power conditions (1000 W, solid and 1250 W, striped). The data at p = 500 mbar, 1250 W for 10:5 slm, CO_2 : CH_4 is unavailable. A clear trend emerges when comparing the effect of the secondary injection of CH_4 : increasing the flow rate consistently decreases its absolute conversion, observed both in the experiment and modeling results. This is likely a result of the lower effective SEI (i.e., total SEI distributed between both reactant gases). Note that the CO_2 conversion without post-plasma CH_4 injection is between $\sim 18 - 10\%$ (respective to increasing pressure, see also Figure 4.3) across all conditions, demonstrating a clear enhancement from reactive quenching, which is most pronounced at higher power, and, thus higher SEI.

For example, at P = 1250 W, p = 900 mbar with a primary flow rate of 10 slm CO_2 , we observe the highest absolute CH_4 conversion ($\sim 34 \pm 4\%$) when using a relatively low secondary injection flow rate (10:5 slm, CO_2 : CH_4 , Figure 4.5A), with a clear increase compared to P = 1000 W, p = 900 mbar conditions ($\sim 24 \pm 4\%$). As mentioned, we also observe that the absolute conversion of CH_4 drops significantly when the secondary injection increases to 14 slm. For example, at P = 1250 W, p = 900 mbar, the absolute conversion of CH_4 is $\sim 14 \pm 2\%$ (10:14 slm, CO_2 : CH_4 ratio, Figure 4.5 B). We note that increased power directly enhances conversion, which can be observed in Table 4.1,

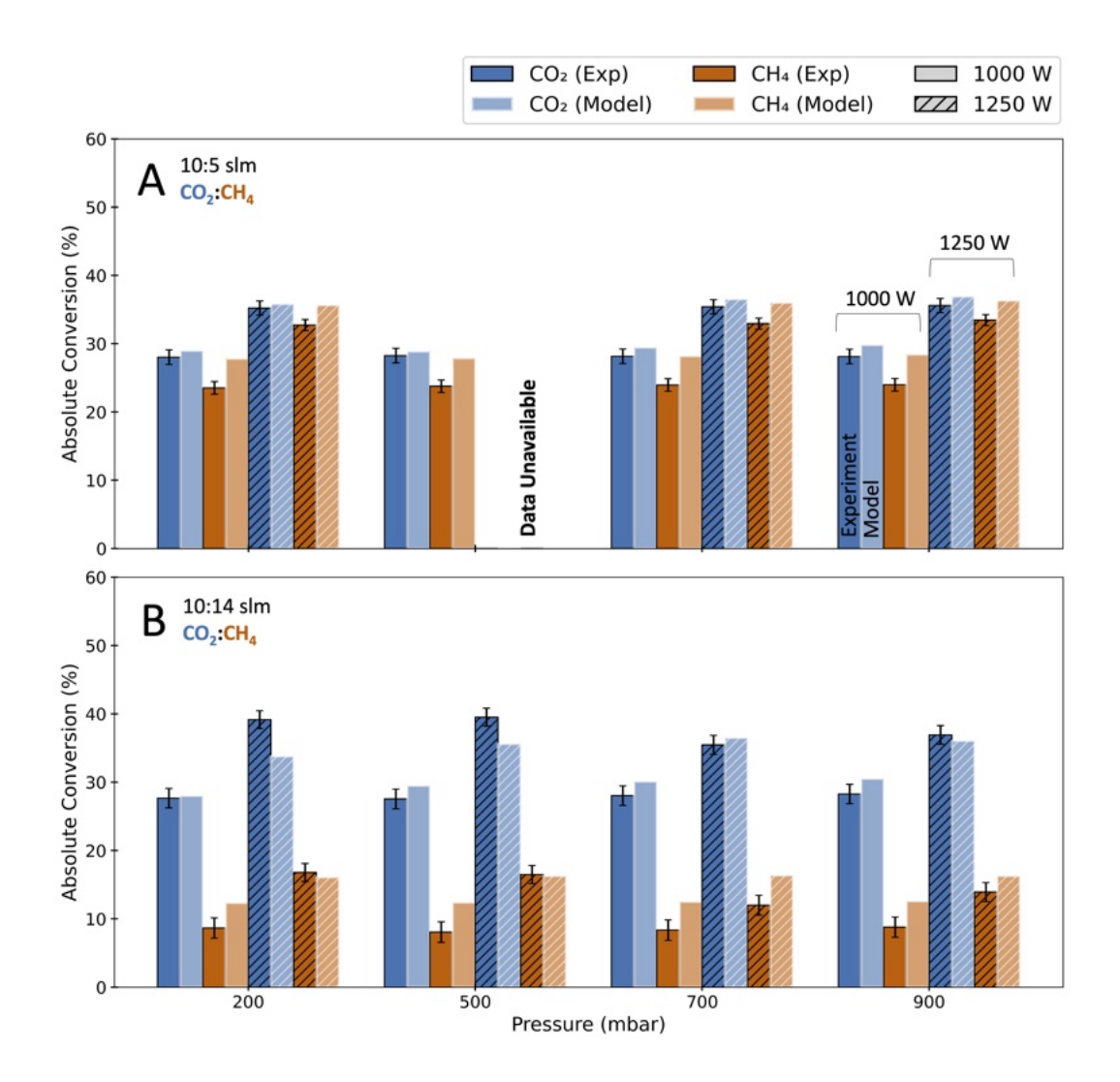


FIGURE 4.5: Comparison of the absolute CO_2 and CH_4 conversion for a primary flow rate (CO_2) of 10 slm with two different post-plasma injections of CH_4 A) 10:5 slm CO_2 : CH_4 (1000 W, solid and 1250 W, striped), and B) 10:14 slm CO_2 : CH_4 (1000 W, solid and 1250 W, striped). The modeling results are presented directly next to the corresponding experimental data. In cases where data collection was not possible due to technical constraints, the corresponding data points are marked as 'Data Unavailable.'

where we show the absolute increase of conversion between 1250 W and 1000 W for the conditions presented in *Figure 4.5*.

Importantly, we note that the model correctly captures the absolute CO_2 conversion under the conditions presented in Figure 4.5 A, B, but is not able to capture the slight increase in CO_2 conversion upon decreasing pressure in Figure 4.5 B, P = 1250 W, p = 200 mbar, see also Table 1. However, overall, there is reasonable agreement between the absolute conversion of both CO_2 and CH_4 calculated by the model and those measured experimentally. Furthermore, the trends presented in Figure 4.5 suggest that there may

Ratio	Pressure	CO ₂ Conversion	CH ₄ Conversion
$(CO_2:CH_4, slm)$	(mbar)	Absolute Increase (%)	Absolute Increase (%)
10:5	200	7	9
10:5	500	N/A	N/A
10:5	700	7	9
10:5	900	7	9
10:14	200	12	8
10:14	500	12	8
10:14	700	7	4
10:14	900	8	5

TABLE 4.1: Absolute increase (%) of conversion between 1000 W and 1250 W for the conditions presented in Figure 4.5 (10 slm primary inlet of CO₂).

be an optimal ratio between the injection of the primary flow rate and the secondary flow rate that maximizes the conversion of both feed gases, for example, when the secondary injection flow rate is smaller than the primary injection flow rate. The reader should note that when the secondary gas flow rate is lower than the primary flow rate, pressure gradients can develop that may destabilize the plasma, potentially extinguishing the discharge. Therefore, the stability of this dual-injection configuration depends critically on the positioning of the secondary injection. In our experimental setup, we mitigated this by placing the secondary injection approximately 5 cm downstream from the waveguide, providing sufficient distance to maintain stable plasma operation across all tested conditions; however, moving the secondary injection closer to the plasma may also serve to enhance conversion of the secondary reactant. We will now examine the results for increased SEI, with a primary flow rate of 7 slm, shown in Figure 4.6.

Higher SEI to the discharge gas presented in Figure 4.6, where the data is organized in the same manner as described in Figure 4.5. The results show deviations from some of the findings with a primary flow rate of 10 slm (Figure 4.5). First, in Figure 4.6 we note that higher SEI to the discharge gas consistently shows better absolute conversions compared to the conditions presented in Figure 4.5 across all flow configurations. For example, the best overall performance shown in Figure 4.6 A is noted for P = 1250 W (7:7 slm, $CO_2:CH_4$), where the absolute conversions of CO_2 and CH_4 reach $\sim 55 \pm 1\%$ and $\sim 37 \pm 2\%$, respectively, at p = 500 mbar. Notably, under these conditions, the pressure-independent conversion deviates slightly, with enhanced absolute conversion of CO_2 and CH_4 with decreasing pressure from 900 mbar, which can also be observed in the absolute increase shown in Table 2. We will examine these findings in greater detail in Section 4.3.2 below.

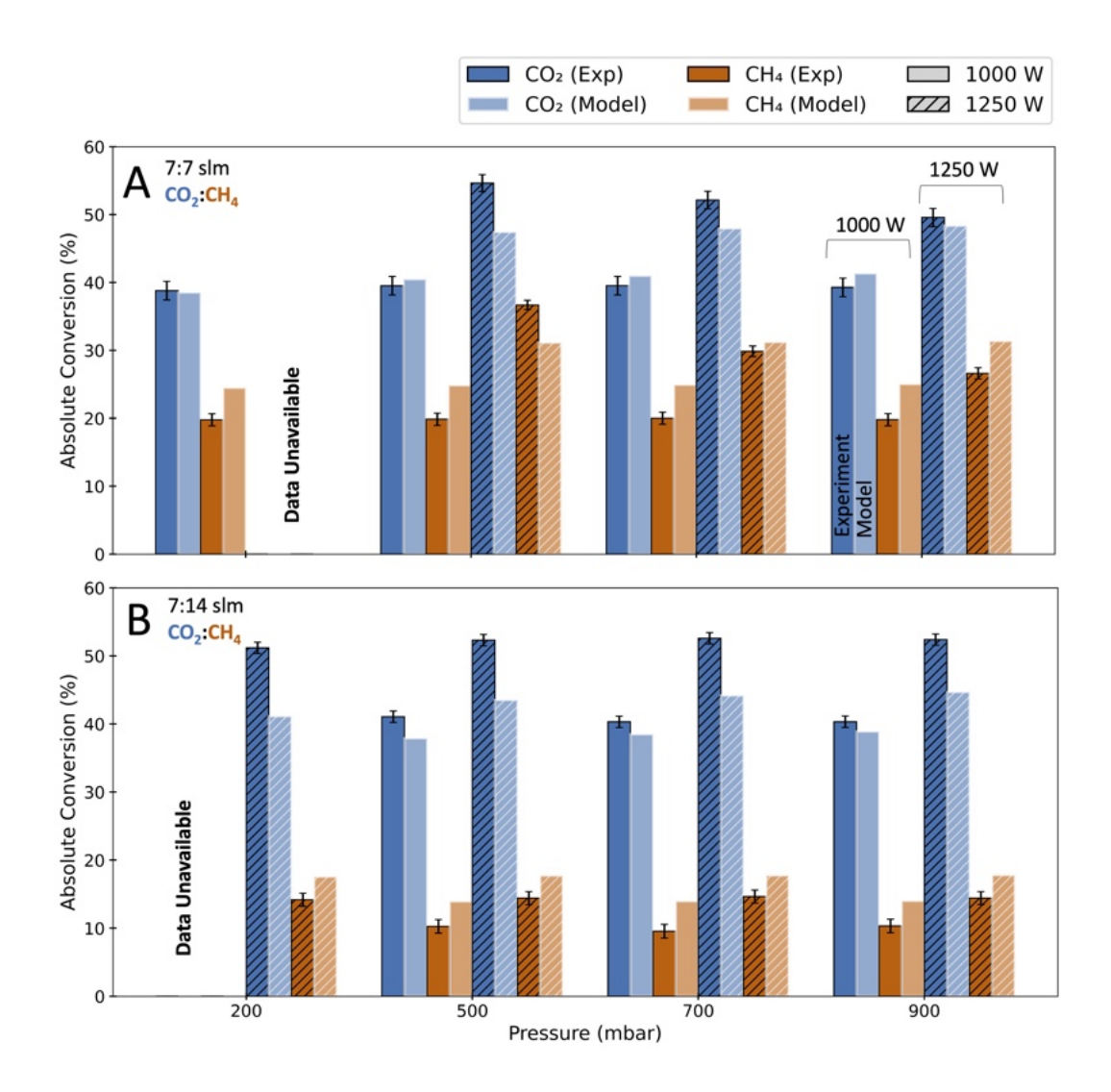


FIGURE 4.6: Comparison of absolute CO_2 and CH_4 conversion for a primary flow rate of 7 slm of CO_2 with different post-plasma flow rate injections of CH_4 , for two power conditions (1000 W and 1250 W). A) 7:7 slm CO_2 : CH_4 and B) 7:14 CO_2 : CH_4 . In cases where data collection was not possible due to technical constraints, the corresponding data points are marked as 'Data Unavailable.

It is clear from these results that a higher SEI to the discharge gas facilitates an increase in CO_2 dissociation within the reactive volume and will subsequently increase the temperature of the afterglow region, in turn allowing more energy exchange and greater conversion of both the primary reactant (CO_2) and the reactive quenching gas (CH_4) . As discussed in Section 4.2.1, the secondary injection housing was designed to monitor the afterglow region for carbon formation in real time, with an additional quartz tube placed downstream of the secondary injection. Although a qualitative observation is all we can make regarding carbon formation, we feel it is worth noting that during the experiments, no carbon formation was visible below 700 mbar. Upon transition between 700 to 900

Ratio	Pressure	CO ₂ Conversion	CH ₄ Conversion
$(CO_2:CH_4, slm)$	(mbar)	Absolute Increase (%)	Absolute Increase (%)
7:7	200	N/A	N/A
7:7	500	15	17
7:7	700	13	10
7:7	900	10	7
7:14	200	N/A	N/A
7:14	500	11	4
7:14	700	12	5
7:14	900	12	4

Table 4.2: Absolute increase (%) of conversion between 1000 W and 1250 W for the conditions presented in Figure 4.6.

mbar, characteristics of irradiance of carbon particles appeared in the afterglow region, noted as an orange 'flame-like' plume, which became more pronounced as the pressure increased to 900 mbar. This plume was the largest at higher power conditions (1250 W); however, overall, the accumulation of carbon particulates was still found to be minimal, only appearing downstream as a 'light' deposit along the walls. Most importantly, by injecting CH_4 into the post-plasma region, we observe that the carbon formation occurs downstream of the discharge; therefore, whatever carbon is formed does not interact with the MW field and thus allows for higher CH_4/CO_2 feed gas ratios, resulting in higher syngas ratios (see Section 4.5.2).

In summary, we examined how injecting CH_4 as a reactive quenching agent into the postplasma region affects the absolute CO_2 conversion under various operating conditions. We saw in Figure 4.3 that when CH_4 is used as a reactive quenching agent, the CO_2 conversion remains constant (\sim 28%) across all pressures (200 – 900 mbar), regardless of the CO_2 : CH_4 ratio. This contrasts with pure CO_2 plasma, where the final conversion decreases with increasing pressure due to recombination; therefore, we attribute the pressure-independent conversion to effective mitigation of the recombination processes that typically limit CO_2 conversion at higher pressures through reactive quenching with CH_4 , confirmed by modeling. Chemical kinetics modeling shows that CH_4 injection enhances the CO_2 conversion through two mechanisms: (1) removing O atoms that would otherwise cause CO to recombine back to CO_2 , and (2) providing H atoms through CH_4 dissociation, which further promote CO_2 conversion. Higher power and higher SEI show improved absolute CO_2 conversion, with the best performance (\sim 55%) achieved at 500 mbar with a 7:7 slm, CO_2 : CH_4 ratio. Having established that injecting CH₄ as a reactive quenching agent into the high-temperature afterglow region of a CO₂ plasma enhances CO production, we will now examine how this approach performs as a method for DRM. By analyzing key performance metrics such as syngas ratio and product selectivity, we can fully understand both the potential and limitations of this dual injection approach compared to the conventional (admixing) DRM processes.

4.3.2 A Dry Reforming of Methane Perspective: Syngas Ratio and Product Selectivity Analysis

As discussed in Section 4.1, the difficulty in controlling the produced syngas ratio (i.e., H₂:CO) presents a critical limitation when admixing CO₂ and CH₄ in plasma-based DRM. Therefore, we explore the effect of the ratio of primary and secondary injection on the syngas fraction, shown in Figure 4.7, for 900 mbar, where we were able to investigate up to a 1:2 ratio (7:14 slm) CO₂:CH₄. All syngas ratios can be found in Appendix B, Section B.3.1 for further analysis.

Figure 4.7 presents an analysis of both the Energy Cost (EC, in kJ/mol and eV/molecule, primary y-axis, calculated accounting for both reactants, CO₂ and CH₄) and the syngas ratio (H₂:CO, secondary y-axis). Further details on the calculations can be found in Appendix B, Section B.1.6. The data reveals a direct correlation between the secondary CH₄ flow rate and the H₂:CO ratios, confirming that increasing the post-plasma CH₄ injection does increase the syngas ratio; however, the maximum syngas ratio observed at 900 mbar was only 0.37 ± 0.02 , at the highest CH₄ fraction (1:2 ratio, 7:14 slm) and P = 1250 W.

Although the SEI varies slightly between our conditions (i.e., SEI = 132 kJ/mol at a 7:7 slm, CO_2 :CH₄ ratio) and those reported by $Kelly\ et\ al.$ for conventional DRM ($SEI = \sim 144$ kJ/mol) [28], our EC is higher at p = 900 mbar, P = 1000 W (346 \pm 17 kJ/mol) compared to values ~ 200 - 369 kJ/mol at the same power in $Kelly\ et\ al.$ [28]. However, under the same conditions (SEI = 132 kJ/mol, 7:7 slm, CO_2 :CH₄) at lower pressure (500 mbar), we obtained an EC as low as 289 ± 15 kJ/mol, with a syngas ratio of 0.38 ± 0.04 , see Appendix B, $Section\ B.3.1$. This is the same condition discussed in $Section\ 4.3.1$ where we observed an absolute CO_2 conversion of $\sim 55\%$ (see $Figure\ 4.6B$). Importantly, the highest H_2 :CO ratio for our quasi-atmospheric results, i.e., 0.37 ± 0.02 (for 7:14 slm

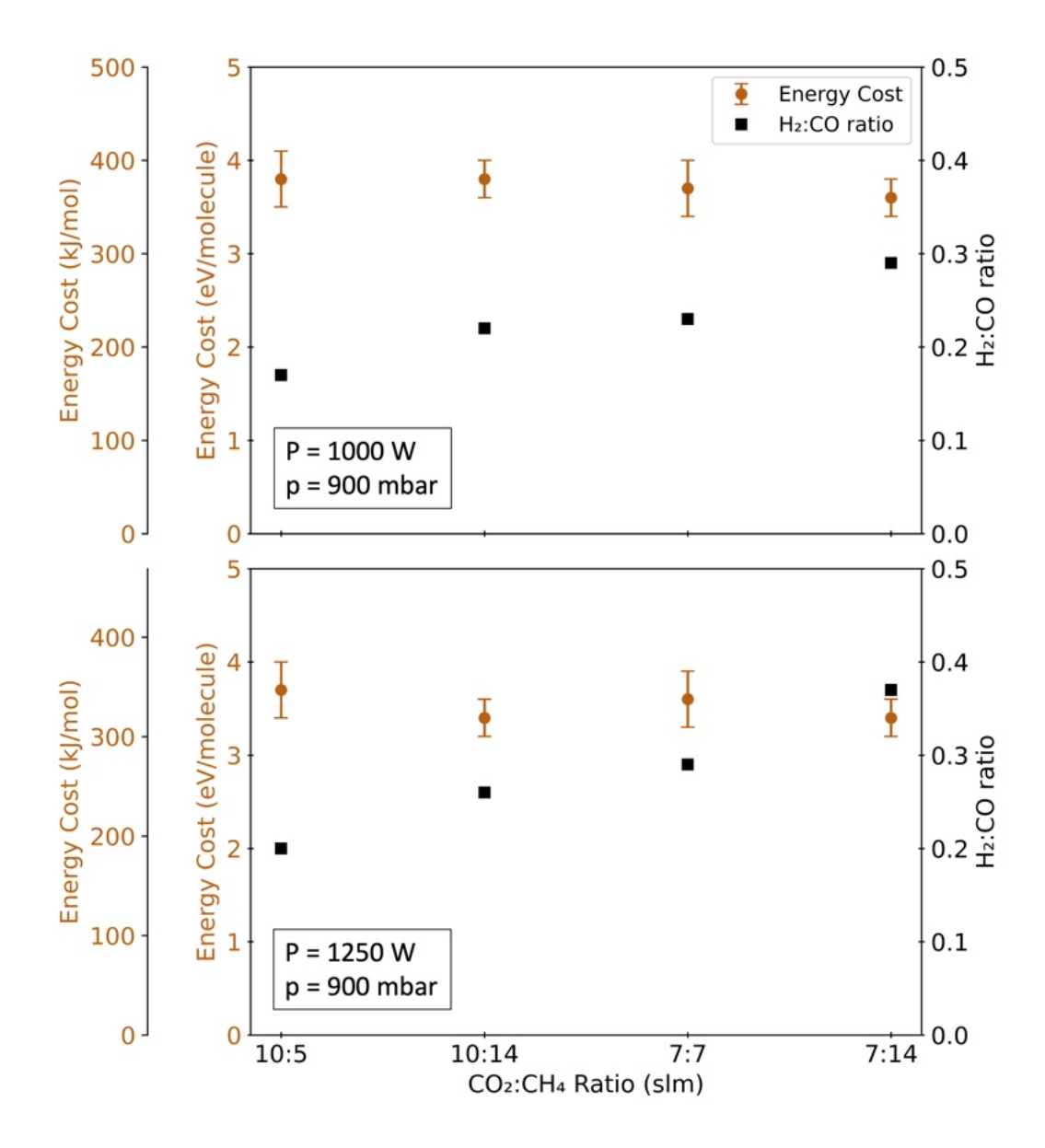


FIGURE 4.7: Energy cost (kJ/mol and eV/molecule) on the primary y-axis, and $\rm H_2/CO$ (syngas) ratio on the secondary y-axis as a function of the $\rm CO_2$:CH₄ ratio, at 900 mbar. A primary flow rate of 10 slm is represented in the 10:5 slm and 10:14 slm data points (left most markers), and of 7 slm in the 7:7 slm and 7:14 slm data points (right most markers), for A) 1000 W and B) 1250 W.

 $CO_2:CH_4$, $SEI = 89 \pm 4$ kJ/mol; $EC = 325 \pm 16$ kJ/mol), is less than half of the best reported value for conventional (admixing) DRM in the MW plasma, reported by Kelly et al. [28], and the dual injection with the extended reforming chamber reported in Cho et al. [27] (1:1 $CO_2:CH_4$, syngas ratio of ~ 1 , EC = 245 kJ/mol). This is likely due to a limitation of operational conditions (lower SEI achievable in our reactor), and the quenching effect limiting the conversion of the quenching reactant, CH_4 , in the afterglow.

Figure 4.8 presents a comprehensive analysis of product selectivity of gaseous products as well as unknown fractions at P = 1250 W across different pressure conditions and flow configurations. Calculations were made based on GC measurements of gas phase species. Tables with the values can be referenced in Appendix B, B.3.1. The data is organized by the primary flow rate of CO_2 (10 slm in Figure 4.8A and 4.8B; 7 slm in Figure 4.8C and 4.8D) and the secondary flow rate of CH_4 (lower in Figure 4.8A and 4.8C; higher in Figure 4.8B and 4.8D).

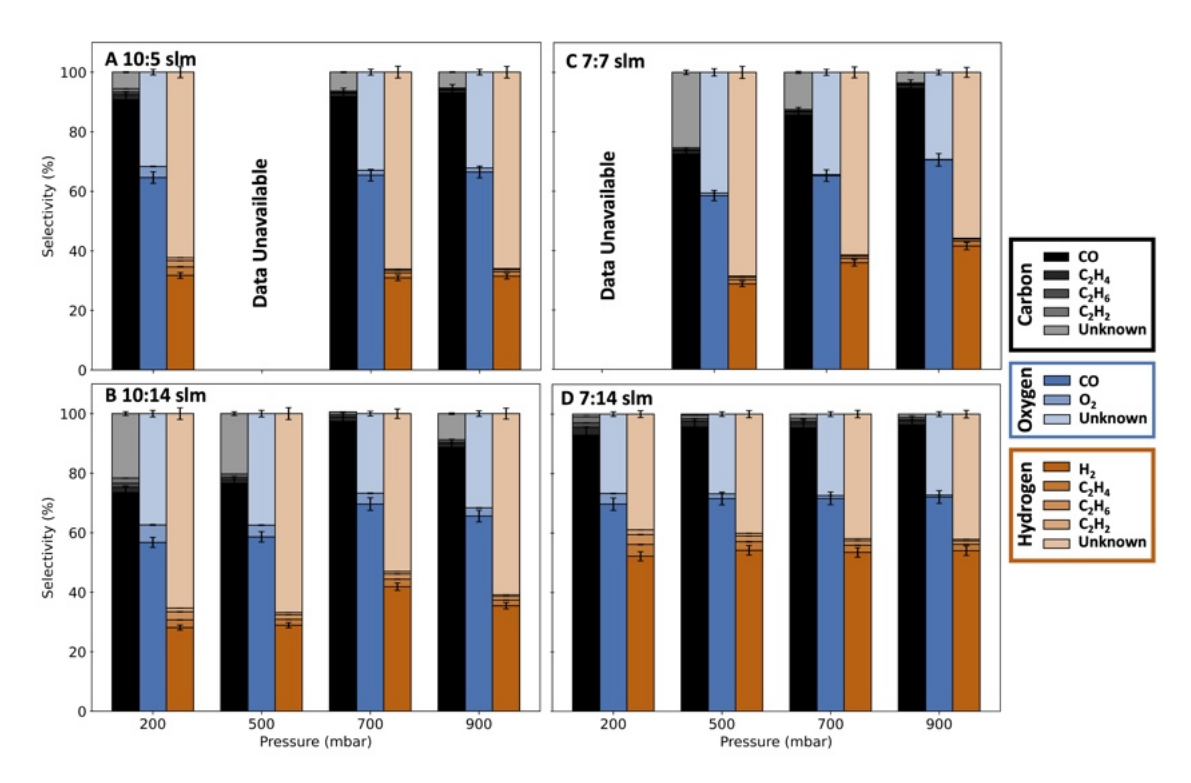


FIGURE 4.8: Selectivity comparison for P = 1250 W for a primary CO_2 flow rate of 10 slm (A and B) and 7 slm (C and D), with different post-plasma injection flow rates of CH_4 (see text). In cases where data collection was not possible due to technical constraints, the corresponding data points are marked as 'Data Unavailable.'

All conditions show a high selectivity toward CO formation, particularly prominent in the 10:5 slm and 7:14 slm, CO_2 : CH_4 ratio configurations. The relatively low syngas ratio observed in our experiments (as previously shown in *Figure 4.7*) can be directly attributed to suboptimal H_2 selectivity, which prevents achieving higher H_2 :CO ratios under the conditions presented in this work (i.e., SEI to the discharge gas). The 7:14 slm CO_2 : CH_4 ratio demonstrates the strongest selectivity toward H_2 , corresponding with an absolute H_2 outflow rate of ~ 1.5 slm (vs. 14 slm of CH_4 input flow rate). To gain deeper insight into the low CH_4 conversion and H_2 selectivity, we employed the 0D chemical kinetic model to elucidate the dominant reaction mechanisms.

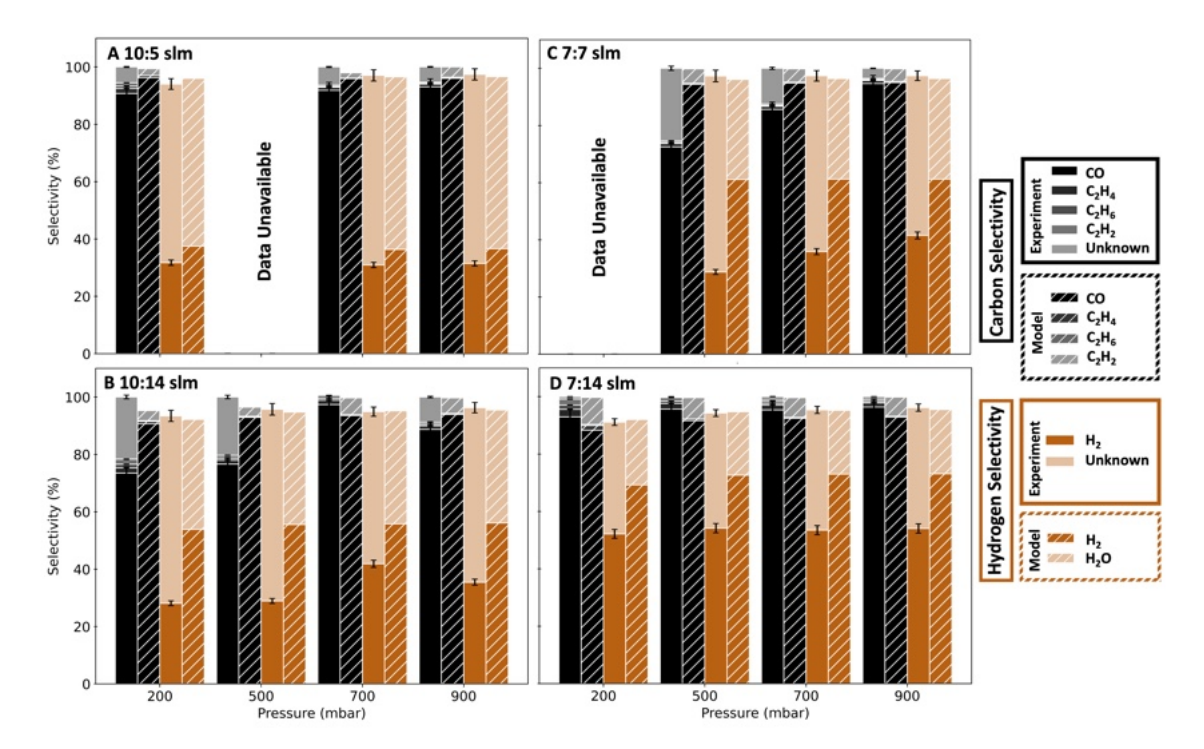


FIGURE 4.9: Comparison between experimental and calculated selectivities at P=1250 W for a primary CO_2 flow rate of 10 slm (A and B) and 7 slm (C and D), with different post-plasma injection flow rates of CH_4 . Only the selectivities towards hydrogen and carbon are plotted, because the O-based selectivities do not provide additional information. In cases where data collection was not possible due to technical constraints, the corresponding data points are marked as 'Data Unavailable.'

As shown in Figure 4.9, the model aligns reasonably well with the experimental selectivities across most conditions; however, note that the model tends to considerably overestimate the H_2 selectivity, which is especially prominent at higher CH_4 fractions. Similarly, the model does not accurately capture the selectivity towards the C_xH_y hydrocarbons, particularly at low pressure (p < 500 mbar); although the reader should note that the total selectivity of C_2H_x species found in the experiments was low across all conditions ($< \sim 6\%$ for C-based, and $< \sim 10\%$ for H-based selectivity), and due to their low concentrations, exhibit a high uncertainty (see Appendix B, Section B.3.1). As a result, it is difficult to highlight their individual contributions to selectivity.

As an example, for a ratio of 7:7 slm, we find the C-based selectivity of C_xH_y to be ~1.8% at 900 mbar with an even distribution between species (see Appendix B, Section B.3.1., whereas the model shows ~4.8%, with the greatest contribution from C_2H_2 (~4.4%). This discrepancy suggests that the reactive pathways leading to C_xH_y hydrocarbons and species constituting the unknown C fraction are not sufficiently represented by the global model, as they would require accurate resolution of the temperature gradients and species

transport within the reactor, but this is outside the scope of a 0D model which cannot describe these complex dynamics. Nevertheless, the overall agreement is quite reasonable, especially for the main DRM metrics, i.e., CO_2 and CH_4 conversion and CO and H_2 selectivity. Multidimensional kinetic simulations employing the GRIMECH 3.0 mechanism could potentially improve the selectivity toward C_xH_y gaseous species by resolving kinetic pathways that require accurate modeling of temperature gradients and species transport. However, given that the reaction mechanism does not account for solid carbon formation [46], the overestimation of H_2 selectivity would likely persist. Thus, to adequately model solid carbon formation, the GRIMECH set would need to be complemented with additional mechanisms, such as the polycyclic aromatic hydrocarbon (PAH) mechanism, which is highly complex and comprises an extensive number of species, rendering it impractical for multidimensional modeling. While this would be an interesting avenue for future research, it falls outside the scope of the present study.

A high percentage of unknown O-based and H-based selectivity is reported across all conditions (Figure 4.8). Particularly, for ratios of 10:5 and 7:14 slm (CO₂:CH₄), we observe a pattern of missing H and O atoms in proportions close to 2:1, suggesting substantial H₂O formation with minimal unaccounted carbon. The model provides important insights into the reaction pathways responsible for this H₂O formation, showing that when CH₄ is injected into the high-temperature post-plasma region as a reactive quenching agent, it scavenges O atoms, predominantly through the reaction $CH_4 + O \rightarrow CH_3 + OH$, and subsequently CH_3 will further consume O atoms via reactions $CH_3 + O \rightarrow H + CH_2O$ and $CH_3 + O \rightarrow H + H_2 + CO$. As CH_4 is rapidly oxidized to CO in the complex reaction pathways stated above, H atoms are released that subsequently react with CO₂ via the reaction $CO_2 + H \rightarrow CO + OH$. This represents part of the RWGS reaction mechanism, where the equilibrium between CO₂, H₂, CO, and H₂O is governed by temperature. Our model reveals that H₂O formation peaks at a concentration of approximately 20% when gas temperatures reach \sim 2800 K, following the water-gas shift equilibrium. However, as the temperature rapidly decreases below 2000 K, the reaction kinetics slow down considerably, effectively "freezing" the H₂O concentration around 6%, despite the equilibrium favoring its decomposition at lower temperatures. This kinetic limitation prevents the formation of H₂, resulting in the low H₂ selectivity observed in our experiments, as explained in detail in Appendix B, B.2.1. Consequently, although the post-plasma CH₄ injection enhances CO₂ conversion through a reaction with H atoms (as shown in the high absolute conversion compared to pure CO_2 conversion in Figure 4.3), it simultaneously promotes substantial H_2O formation, explaining the significant fraction of unknown H and O atoms in the selectivity, as shown in Figure 4.8.

This trade-off between improved CO₂ conversion and H₂O formation represents a key limitation in achieving higher syngas ratios in our current reactor configuration at this relatively low SEI, which confirms the modeling results published by Albrecht et al. [8]. Importantly, our model reveals that higher SEI and CH_4 ratios (240 kJ/mol or ~ 12 eV/molecule, 1:4 ratio of CO₂: CH₄) may result in a higher conversion of both CO₂ and CH_4 , yielding a significantly better syngas ratio (\sim 2), as discussed in detail in Appendix B, B.2.2. However, we note that this SEI is much higher than typical inputs found in literature, with the highest reported values found to range between 7 – 8 eV/molecule [43, 49]. Importantly, it is expected that solid carbon formation will increase at higher CH_4 fractions and elevated SEI values, as this is inherent to the stoichiometry of the DRM process under CH₄-rich conditions, where insufficient oxygen is available to oxidize all CH₄, resulting in the formation of hydrocarbons that either remain in the gas phase or nucleate into solid carbon, enabling high syngas ratios. In the model calculations, excess CH_4 is converted exclusively into gaseous C_xH_y hydrocarbons, without contributing to solid carbon formation. Thus, the impact on CO and H₂ yields will ultimately depend on the extent of solid carbon formation. Therefore, experimental validation of higher SEI conditions would be valuable to assess whether the promising syngas yields and ratios predicted by the model, which excludes solid carbon formation, can be realized in practice.

Notably, as reported in Figures 4.8 and 4.9, selectivity patterns remain largely independent of pressure. An exception to this is observed in the unknown fraction of species (obtained from carbon, hydrogen, and oxygen balance). The fraction of unknown solid carbon was found to be minimal across all conditions and not observed at p < 700 mbar, which is in line with the selectivity data reported in Figure 4.8. For example, the unknown C fraction in Figure 4.8B at 900 mbar is likely attributed to solid carbon, which correlates with our observations of a 'flame-like' plume in the post-plasma region under these conditions. Furthermore, a minimal amount of solid carbon was found in the cyclone separator. Although the model points to substantial H_2O formation, the unknown values for 10:14 and 7:7 slm, $CO_2:CH_4$ at $p \le 500$ mbar, as shown in Figure 4.8, display a slightly different trend, we find a large fraction of unknown C atoms (between $\sim 10-25\%$).

Therefore, the unknown fraction of C under these conditions suggests the formation of products beyond the measured gaseous species and likely points towards the formation of chemical products that will be examined below.

Quantification of liquid products helps us to understand these trends further. To limit the number of samples, we collected a single liquid sample for each CO_2 : CH_4 ratio investigated, meaning for both power conditions and all pressure sets, which was analyzed using the methods outlined in $Appendix\ B$, B.1.1, to determine the composition. In each of the samples collected, the liquid was yellow, with the 7:7, CO_2 : CH_4 mixture being the darkest. The samples exhibited 'a strong, sweet, petrol-like odor', typically associated with hazardous chemicals. We also note that all the post-plasma bellows were stained yellow. The analysis revealed that although the liquid was predominantly water (as the model predicts, which correlates with high unknown O and H selectivity data presented in $Figure\ 4.8A,D$, and at higher pressure in $Figure\ 4.8B,C$) three other main compounds were identified: formaldehyde, acetic acid, and formic acid. Each of these species are present at all ratios of CO_2 : CH_4 ; however, the concentration varies according to the ratio, as shown in $Figure\ 4.10$.

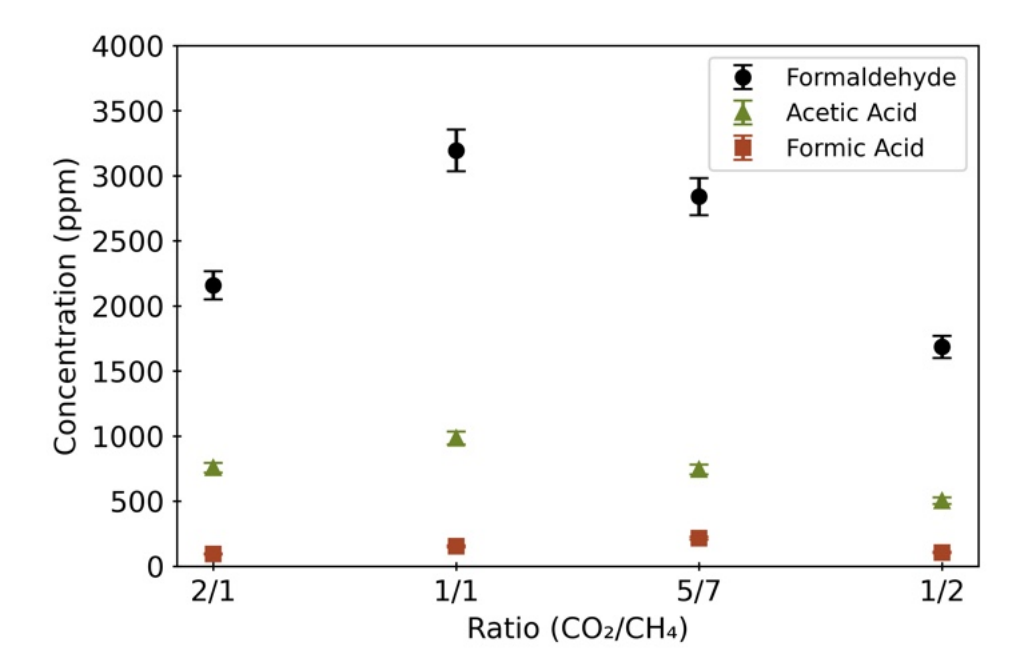


FIGURE 4.10: Concentration (ppm) of the three main components found in each data set (ratio CO₂:CH₄). The highest concentration of formaldehyde, the second highest concentration of a single constituent other than water, was found in the 7:7 slm and 10:14 slm ratios, where we observed the largest unknown quantities of C, O, and H species.

As shown in Figure 4.10, formaldehyde, acetic acid, and formic acid are detected, with formaldehyde as the highest concentration at $\sim 3200 \pm 160$ ppm at 7:7 slm CO₂:CH₄ ratio. The reader should keep in mind that although the samples were taken per ratio, based on the selectivity data, a correlation between the oxygenates detected and the unknown species ratios in the 7:7 slm and 10:14 slm CO₂:CH₄ samples suggests that these molecules of interest are likely formed in greatest concentration at p \leq 500 mbar at P = 1250 W (Figure 4.8B and 4.8C). The extreme temperatures (T >> 1000 K) found in the reactive volume and afterglow generate radicals that can produce a variety of compounds from CH₄:CO₂. Furthermore, we link the dependency between the model and experimental selectivity (Figure 4.9) to the significant fraction of unknown C (from for e.g., hydrocarbons, aromatics, oxygenates), which is not captured by the model since GRIMECH 3.0 is exclusively a gas-phase reaction mechanism, and therefore, it does not include reactive pathways leading to solid carbon formation. Noting the oxygenate measured in the water fraction are too dilute to explain the substantial unidentified carbon fraction, we believe that the majority of the unknown carbon fraction consists of solid carbon carried away as nanoparticles by the flow at lower pressure, where coagulation/agglomeration may not occur and therefore would not be captured by the cyclone separator. Consequently, the model over predicts the gaseous carbon species, particularly CO and C_xH_y . In reality, the gaseous CO that would ultimately contribute to solid carbon formation would consume H atoms while simultaneously generating H₂O due to stoichiometric constraints, both factors contributing to the observed overestimation of H₂ selectivity by the model.

However, we conjecture that CH_4 fragmentation and CO_2 dissociation (CO + O) may lead to the formation of these oxygenates, and especially $CO + H_2$ can form formaldehyde [50], which could also explain the reduction in CO and H_2 selectivity under these conditions (Figure 4.8B and 4.8C), although a reaction between $\cdot CH_3$ and O is also possible [51]. As shown in Figure 4.11, we investigated the total carbon count and analyzed the spectrum of the 7:7 slm sample using UV-Vis, as the presence of these oxygenates did not fully explain the yellow hue of the liquid collected.

Figure 4.11A presents the theoretical total carbon count calculated from the concentration in the samples detected using High-Performance Liquid Chromatography (HPLC) and the measured Total Organic Carbon (TOC) in the sample. Comparison of both allows us to assess the completeness of compound identification. The difference is small, indicating that much of the carbon-containing species have been accounted for in the analysis. The

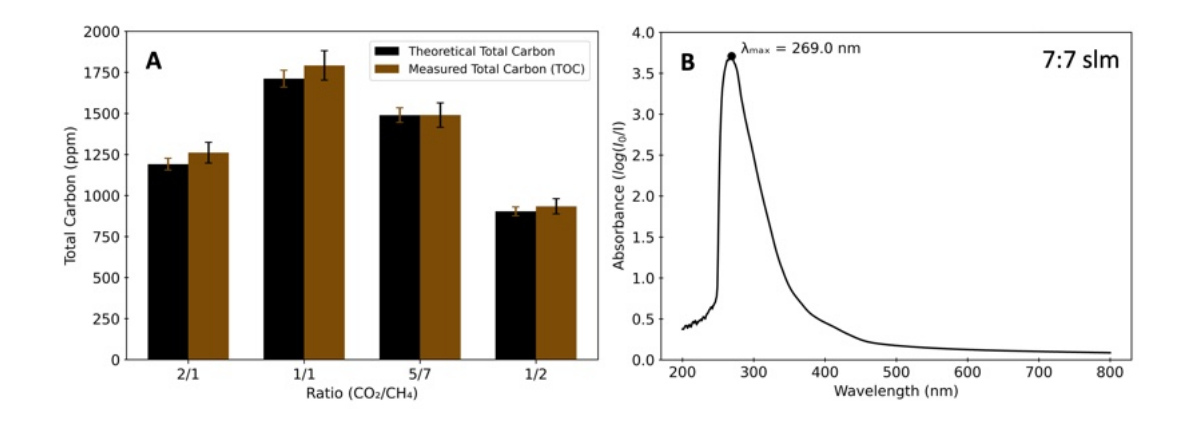


FIGURE 4.11: A: Theoretical total carbon count of the samples, as measured by HPLC (black), and measured by TOC analysis. B: UV-Vis spectrum from the 7:7 slm sample with a sharp peak (λ_{max}) found at 269 nm, indicative of a $\pi \to \pi^*$ electronic transition in a conjugated system.

UV-Vis analysis (Figure 4.11B) reveals $\lambda_{\rm max}$ at 269 nm, suggesting a $\pi \to \pi^*$ electronic transition from a conjugated system. In general, simple carbonyls (like formaldehyde and acetic acid) absorb only in the deep – mid UV and produce peaks between ~190 – 250 nm [52–54]. Furthermore, the addition of a C=C adjacent to a C=O will bathochromically shift the $\pi \to \pi^*$ band into the visible region [55, 56]. The "sweet, petrol-like" odor of the yellow liquid and $\lambda_{\rm max}$ = 269 nm point towards the presence of e.g., α , β -unsaturated acids, aldehydes, or aromatic hydrocarbons. Therefore, we believe the remaining, uncharacterized liquid to be a mixture of many trace molecules, including aromatic species, as evidenced by the small difference between HPLC-detected compounds and total organic carbon (Figure 4.11A). This complexity makes direct comparison with individual reference compounds challenging, as the observed spectrum likely represents a composite of multiple absorbing species rather than a single compound.

Overall, it is interesting to consider that the formation of these oxygenates, e.g., formaldehyde, can be 'tailored' to some extent, according to the $CO_2:CH_4$ ratio (Figure 4.8) and, given the selectivity data, formed in greater concentrations at lower pressure (i.e., < 500 mbar, Figure 4.8B and 4.8C). This suggests dual injection designs in MW-based plasma reactors can help to control temperature distributions, radical pathways, and thus product formation, such as for the production of oxygenates. The reader should note that the absolute concentrations at a given condition are subject to high uncertainties and further research is needed to accurately resolve the yields and potential for application; however, as a first approach, we made an approximation of the oxygenate production based on the

available gas phase conversion, selectivity data, and liquid phase oxygenate concentrations. We take the 7:7 slm CO₂:CH₄ condition as an example, as it exhibits the highest measured oxygenate concentrations. As noted in *Appendix B*, *B.1*, those concentrations represent an average across all pressure and power data sets, encompassing a total of eight different conditions. As it has been typically reported in literature that the liquid by-product found in admixing DRM conditions is pure water, the experiment was not designed to make a distinction between conditions for the liquid fraction and thus it is not possible to quantify with accuracy, since one would need precise inflow and outflow quantities for a fixed data set.

As a first approximation, we assume that all missing O in the O balance (see Appendix B, B.3.1, Table B.20) can be attributed to H_2O formation, and thus we can estimate the production rate of H_2O , given that the oxygenate concentrations are small compared to the H_2O fraction. Since CO and H_2O are the only dominate O-containing product species, each containing a single O atom, the H_2O production rate can be calculated by multiplying the CO_2 molar flow rate (F_{CO_2}) by the CO_2 conversion (χ_{CO_2}) and the fraction of unidentified oxygen (S_O) . To obtain the oxygenate production rate, we then multiply this value by the corresponding oxygenate concentration (c_{oxy}) , resulting in the following expression for the approximated oxygenate production rate (PR_{oxy}) :

$$PR_{oxy} = F_{CO_2} \times \chi_{CO_2} \times S_O \times c_{oxy} \tag{E4.4}$$

As the oxygenate concentrations represent averages, we also compute the average CO₂ conversion and unknown O fractions across the different conditions. This yields an estimated average PR_{oxy} of formaldehyde (2.1 $\mu mol/s$), acetic acid (0.7 $\mu mol/s$), and formic acid (0.1 $\mu mol/s$).

Our study's main research question was to establish a proof-of-concept for dual injection systems, where we identified (unexpected) oxygenate formation pathways that, in our opinion, warrant a dedicated investigation with more sophisticated multi-phase quantification protocols. Unfortunately, as this was not the initial goal of this study and thus given the data and the limitation of this configuration, we cannot provide accurate resolution of the temporal formation of the liquid fractions. Future work should indeed focus

on time-resolved analysis of all product phases to enable accurate mass balance closure and absolute production rate determination. We believe this is an interesting case for future work, especially because the industrial production of formaldehyde is very energy intensive [57, 58], and it would be of interest to the community to know whether we might be able to optimize the production of these valuable products in warm plasmas with carefully configured injection schemes, allowing for further progress towards electrification of the chemical industry.

In summary, dual injection with CH₄ as a reactive quenching agent in a DRM context presents limitations for application. The low syngas ratios observed across all conditions result primarily from significant H₂O formation through the RWGS reaction, as confirmed by modeling. However, one important merit of the dual injection approach is that solid carbon formation is formed downstream of the discharge, mitigating instabilities associated with carbon coupling to the MW field when formed in the reactive volume. Thus, this approach successfully demonstrates that dual injection allows for higher CH₄ fractions without the plasma instability issues that typically occur with conventional admixing in DRM. Furthermore, the model predicts that at higher SEI and CH₄ ratios (240 kJ/mol, 1:4 CO₂:CH₄), we may yield increased syngas ratios (\sim 2), discussed in detail in Appendix B, B.2.2.

4.3.3 Carbon Formation and Morphology in a Dual Injection Flow

To compare the carbon morphology from the dual injection flow (CO₂ plasma with CH₄ post-plasma injection) with conventional DRM in MW plasma, as e.g., reported in *Kelly et al.* [28], we investigated the structure of the solid carbon collected from the walls of the viewing quartz and in the cyclone separator, observed to be formed at p > 700 mbar. We collected a carbon sample for each CO₂:CH₄ ratio and then treated it using the methods outlined in Appendix B, *Section B.1.2*, to determine the structure. All accompanying analysis was conducted by Robin De Meyer (Ph.D. student within PLASMANT). The deposits were characterized by SEM and TEM, revealing monodisperse samples (apart from one exception observed by TEM, see Appendix B, *Section B.3.2*), and representative images are presented in *Figure 4.12*. Understanding the structure and morphology of the collected carbon can provide additional insights into the cooling rates using reactive postplasma quenching.

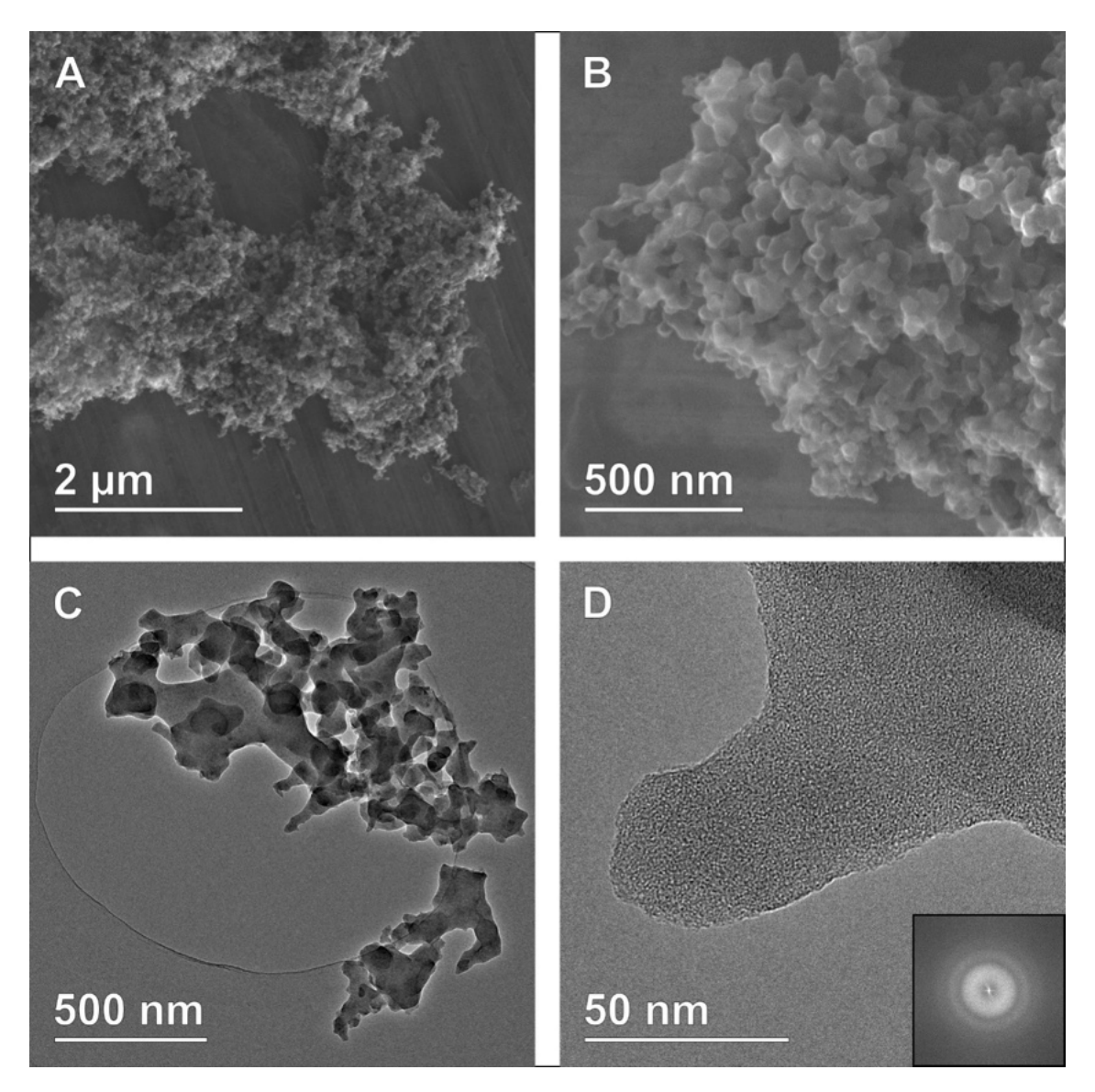


FIGURE 4.12: A, B: SEM images of the deposited carbon materials, revealing large agglomerates, seemingly consisting of many smaller particles (see different scale bar in A and B). C, D: BF-TEM images of the deposited materials. The same morphology of agglomerated particles as found by SEM is observed, but higher magnification images (D) reveal that the particles are fused together, and the material is amorphous, confirmed by Fast Fourier Transform (FFT) (as shown in the inset).

Figures 4.12A and 4.12B show that agglomerates of sub- μ m to several μ m in size are observed in SEM, appearing to consist of many smaller particles, somewhat resembling a carbon black-like morphology [59]; however, the TEM analysis shows that the individual particles are, in fact, completely amorphous (Figure 4.12C and 4.12D). The amorphous structure of the material is confirmed by the high-magnification imaging and the Fast Fourier Transform (FFT) of this image (Figure 4.12D and the inset) revealing no spots or sharp rings in the FFT that would suggest the presence of local crystallinity. This indicates that the formed material is not carbon black, contrary to the carbon materials generated in

conventional DRM in the same MW plasma reactor, including the work by Kelly et al. [28]. Furthermore, the seemingly individual particles observed by low-magnification imaging (Figure 4.12A and 4.12B) are completely fused together at the nanoscale (Figure 4.12C and 4.12D). Therefore, individual primary particles, as commonly defined for carbon black, cannot be readily described, thus preventing the definition of an average particle size for this material.

Studies have shown that the cooling rate plays a critical role in determining the crystallinity and structure of carbon materials formed during plasma-based carbon synthesis [38, 60, 61]. In the case of the fused amorphous carbon structures shown in Figure 4.12C and 4.12D, the post-plasma injection of CH₄ appears to significantly influence the final morphology. Determining the exact parameters of the cooling rate is not straightforward; however, as a first approximation, we consider the cooling rates determined by the 0D model. The model predicts the cooling rate of the total mixture upon CH₄ injection to be in the order of $10^5 - 10^6$ K/s. We note that these values represent the global cooling rate of the simulated gas mixture, which is likely to be significantly lower than the microscopic cooling effects occurring over the length scale of particle diffusion. Literature studying carbon amorphous structures suggests rapid cooling rates trigger the transition to a more disordered morphology. For example, Dozhdikov et al. demonstrated that cooling rates between $10^{12} - 10^{14}$ K/s produce specific structural changes in carbon materials, with higher rates leading to more amorphous structures [62]. In the model developed by Girshick et al., very high cooling rates were shown to "freeze" carbon particles at smaller sizes because the temperature drops below the threshold where significant atomic rearrangement can occur [60]. Moreover, Girshick emphasizes two critical parameters, i.e., monomer concentration and cooling rate, and their influence on nucleation and growth of carbon particles in thermal plasma synthesis [60, 63]. Girshick establishes that high monomer concentration and low cooling rates favor the nucleation of larger and fewer particles, whereas low monomer concentration and high cooling rates produce numerous smaller particles. According to Girshick, this relationship between nucleation rate and growth rate determines final particle morphology. In our case, the counter-flow CH₄ injection likely creates a high cooling rate, potentially diluting the carbon monomer concentration and pushing the system toward numerous small nuclei rather than organized growth.

Girshick also explains that particle formation occurs when supersaturation exceeds a critical threshold [60]. The counter-flow CH₄ injection likely creates a sharp supersaturation gradient that triggers rapid, uncontrolled nucleation throughout the secondary injection region, rather than sequential growth on existing nuclei, as we might find with carbon particles formed around the reactive volume near the plasma in the case of DRM, i.e., when CO₂ and CH₄ are admixed [28]. Fabry et al. also reports that internal mixing, or recirculation cells, significantly affect particle structure [38]. The counter-flow secondary injection of CH₄ is designed to enhance mixing conditions, likely creating a complex flow pattern where the CH₄ counter-flow would disrupt the carbon aggregation process normally found in plasma-based dissociation of CH₄. If the counter-flow injection of CH₄ created an extreme local temperature gradient, as would be expected, carbon precursors would solidify before they could organize into the typical spheroidal primary carbon particles, as previously reported by Kelly et al. [28]. This may explain the completely fused, amorphous structure observed in the TEM images shown in Figure 4.12D.

The amorphous structure represents an interesting morphological state outside of typical plasma-generated carbon materials found in literature [27, 28, 38, 39, 64–66]. In our dual injection system, the particles appear to have undergone partial coagulation, forming the agglomerated structure seen in *Figure 4.12D*, but they lack the energy for surface reorganization that would normally occur in carbon black formation, resulting in completely fused interfaces between particles. Likely, a rapid temperature drop from the counterflow injection of CH₄ into the afterglow region "freezes" the carbon in an amorphous state before proper nucleation, growth, and graphitization can occur, resulting in the fused, completely amorphous morphology observed in the TEM images (*Figure 4.12C* and 4.12D) [60, 67].

We also note that in our dual injection system, no carbon formation was observed in the afterglow viewing quartz below p = 700 mbar. Fabry et al. discusses the thermodynamic equilibrium of the C-H system and how carbon formation has specific pressure and temperature requirements [38]. Additionally, the reactions leading to carbon formation typically involve multiple collision steps [38, 59, 67]. Below 700 mbar, the mean free path increases, reducing collisional frequency, which would affect the kinetics of carbon formation, potentially shifting reaction pathways toward other products. This suggests that pressure affects the balance between different reaction pathways, where the selectivity of carbon species will shift toward gaseous products (such as C_xH_y , CO) or to oxygenate formation, as discussed in Section 4.3.2, rather than condensing into solid carbon. Finally, at lower pressures, the interaction between the CO₂ plasma afterglow and reactive quenching of CH₄ may change significantly. The pressure threshold of 700 mbar might represent a critical point where flow dynamics create appropriate mixing conditions for carbon agglomeration/coagulation, suggesting a minimum pressure environment is needed to achieve the necessary supersaturation, residence time, and reaction kinetics for solid carbon growth in a dual injection plasma system. Our findings suggest that pressure may affect the nucleation kinetics or shift the selectivity in dual injection plasma systems. However, given the large unknown fraction of C atoms in the selectivity data, we believe that carbon agglomeration/coagulation maybe be limited at lower pressures, and therefore not detectable in the post-reactive volume (i.e., in the viewing quartz), nor would it be collected in the cyclone separator, which is limited to particles down to 1 μ m with 95% efficiency.

Amorphous carbon can exhibit valuable properties for specific applications; however, the characterization of the carbon materials in this study serves primarily to provide insights into the cooling dynamics of the reactive quenching process rather than to optimize carbon as a product. Nevertheless, it is worth noting that amorphous carbon materials can find applications in various fields depending on their specific morphological and structural characteristics. For instance, highly porous amorphous carbons with large surface areas are valuable for energy storage applications such as supercapacitors and battery electrodes [68], while dense, non-porous amorphous carbons may be suitable for protective coatings or as reinforcement materials [69, 70]. The fused, completely amorphous morphology observed in our study (Figure 4.12C and 4.12D) suggests a dense, low-porosity structure that would likely be more suitable for applications requiring mechanical strength rather than high surface area applications [71]. However, a comprehensive characterization of properties such as surface area, porosity, electrical conductivity, and mechanical properties would be necessary to fully assess the potential applications of these materials. Since the agglomeration into amorphous solid carbon formation represents only a minor fraction of our products and appears to agglomerate only at higher pressures (p > 700 mbar), our primary focus remains on understanding how the carbon morphology reflects the underlying cooling mechanisms inherent to the dual injection approach.

4.4 Conclusions and Outlook

In this chapter, we investigated the effects of dual injection in a 2.45 GHz CO₂ MW plasma system, where CH₄ was strategically injected as a reactive quenching agent into the high-temperature post-plasma afterglow region. Our findings provide novel insights into how this configuration affects conversion, product selectivity, as well as liquid and carbon formation.

The introduction of CH₄ in the post-plasma region demonstrates approximately a threefold increase in absolute CO₂ conversion compared to pure CO₂ plasma, reaching consistent values of $\sim 28\%$ at 1000 W and 10 slm primary CO_2 flow rate, for different secondary CH₄ flow rates and across the entire investigated pressure range from 200 to 900 mbar. This pressure-independent behavior suggests that post-plasma CH₄ injection effectively mitigates the recombination processes that typically limit CO₂ conversion at higher pressures, which is also convincingly predicted by our model as the RWGS reaction does not show strong pressure dependence. Overall, reactive quenching with CH₄ appears to be more effective at higher SEI input, and when the flow rate of the secondary injection (CH_4) is less than the flow rate of the primary injection (CO_2) . It would be of interest to further explore the parameter space to enhance the CO₂ conversion with reactive quenching. In all the data collected, no characteristic H_{α} emission was observed to indicate upstream migration of CH₄ into the discharge zone, confirming that the secondary injection remained confined to the afterglow region (see Appendix B, Section B.1.3 for additional details). We believe this is likely due to the distance of the secondary injection inlet, or perhaps a suboptimal design profile of the secondary tangential injection. This opens the possibility for future studies to explore alternative injection profiles, such as ring injection geometries, to enhance mixing and potentially to allow for controlled upstream interaction between CH₄ and the plasma volume. Furthermore, investigating the effects of reducing the distance between the secondary injection and the waveguide may help determine the optimal positioning for maximum conversion of both reactive gases while maintaining plasma stability.

The highest CO₂ and CH₄ conversion (55% and 37%, respectively) is achieved at 500 mbar for the 7:7 slm, CO₂:CH₄ ratio at 1250 W, i.e., higher *SEI* conditions, under which solid carbon formation is not observed as an irradiated plume nor does it collect along the quartz walls in the secondary viewing quartz. Furthermore, our study reveals that the limited

carbon formed at higher pressures exhibits an unusual fused amorphous morphology, distinctly different from the spheroidal carbon black particles typically formed during traditional admixed DRM conversion. This atypical morphology is attributed to the high cooling rates (likely $> \sim 10^6~K/s$) created by the counter-flow injection of CH₄, which produces carbon in an amorphous state.

While the dual injection approach improves CO₂ conversion, the syngas ratio shows a maximum H₂:CO ratio of only 0.37 at quasi-atmospheric pressure, and our modeling reveals that the low syngas ratios are likely due to the relatively low SEI applied in this work (due to power supply limitations). This low syngas ratio is attributed to significant H₂O formation, confirmed through our 0D kinetic model analysis. The model revealed that when CH_4 is injected as a reactive quenching agent under limited SEIconditions, partial oxidation of CH₄ by O₂/O radicals generated in the CO₂ discharge proceeds rapidly, and the resulting H atoms react with CO₂ to form CO and OH radicals. The reactive mixture quickly relaxes to the RWGS equilibrium, leading to further CO₂ conversion and ultimately producing H₂O. As temperatures rapidly decrease below 2000 K, these reactions become kinetically limited, preventing H₂ formation and increasing the final H₂O concentration. Given the fast kinetics of the RWGS reaction, suppressing H₂O formation by manipulating the rate of CH₄ addition or the cooling trajectory may be very challenging to achieve in practical applications. Moreover, actively cooling the system to temperatures where partial oxidation of CH₄ remains kinetically feasible but RWGS kinetics is effectively frozen would not be an effective strategy, as it would result in low CH₄ conversion. Indeed, the fraction of oxygen available in the CO₂ plasma is inherently limited. Once all available oxygen is consumed in the partial oxidation of CH₄, maintaining high mixture temperatures remains essential to facilitate the reforming process. Experiments using isotopically labeled ¹³CH₄ or H₂ would be of interest to confirm additional CO formation through the RWGS reaction. Furthermore, our model predicts that a higher SEI will likely yield higher H₂ selectivity, and thus syngas ratios, which could be of interest to future research initiatives.

Therefore, we argue that injecting all CH₄ as close to the discharge (at the end of the waveguide) as possible, coupled with reactor isolation, is the optimal strategy for maximizing the residual CO₂ plasma heat in the reforming process. This approach eliminates the need for alternative strategies such as staged CH₄ addition or temperature-buffered zones. Moreover, higher CO₂ conversion will lead to lower H₂O concentration, following

the constraints imposed by the RWGS equilibrium. As a result, this mechanism would enhance H_2 selectivity and likely improve the syngas ratio. At the SEI used in this study (a limitation of our reactor's maximum power output), the residual heat following CO_2 discharge is insufficient to sustain significant DRM chemistry. The effective SEI applied ($\sim 132~kJ/mol$) are relatively low compared to optimal conditions reported in other DRM studies; however, to avoid impractically high power-to- CO_2 flow rate ratios in the CO_2 discharge, total energy input could be enhanced through methods such as preheating of the CO_2 and CH_4 streams, ideally via heat recovery, which would further improve energy efficiency. Since maintaining elevated temperatures during post-plasma conversion is crucial for optimizing performance, minimizing thermal losses by insulating the reactor could provide additional benefits. Research involving preheating the primary injection gas to help reduce the SEI to the discharge gas may prove to be an advantageous strategy to increase conversion of both reactants.

Importantly, this work demonstrates that dual injection configurations are promising for enhancing CO₂ conversion while minimizing or eliminating carbon deposition, a significant challenge in conventional plasma-based DRM. Moreover, larger fractions of CH₄ can be treated with post-plasma injection. Future research should focus on refining the injection location, increasing the SEI to the discharge gas, and developing reactor designs that enhance mixing dynamics to control product selectivity more precisely. The liquid product analysis identified formaldehyde, acetic acid, and formic acid as the primary oxygenates formed during the process, with the highest concentrations observed in the samples with a 7:7 slm, CO₂:CH₄ ratio. UV-Vis spectroscopy revealed a $\lambda_{\rm max} \sim 269$ nm, suggesting the presence of trace molecules with conjugated systems. These findings indicate that dual injection can potentially be optimized for selective oxygenate production, particularly at sub-atmospheric pressures, where selectivity analysis suggests higher concentrations are likely to form. Additionally, further investigation of the pressuredependent carbon nucleation and coagulation mechanisms could provide valuable insights for designing carbon-free plasma conversion systems or tailoring to higher value molecules (e.g., oxygenates).

Our experimental data reveals significant insights into the complex interplay between plasma dynamics, flow geometry, reaction thermodynamics, and carbon deposition behavior when introducing CH₄ as a reactive quenching agent. While our results demonstrate proof-of-concept benefits, including enhanced CO₂ conversion, we recognize that the current performance metrics pose significant challenges for industrial scale-up. Several key challenges must be addressed before considering industrial scaling of a dual injection system, including understanding how spatial delivery and injection geometry may affect mixing and injection efficiency, which are important factors for scale-specific reaction. Furthermore, changes to these aspects of the process may affect temperature gradients and cooling rates, which may change product selectivity and kinetic pathways. We also believe it would be of great interest to the community to further understand the potential for warm plasma based oxygenate production through targeted studies with dual injection systems. Understanding this is crucial for realizing additional avenues for electrification of the chemical industry using MW plasma technology.

Therefore, further optimization studies, with for example, higher SEI conditions, altering the injection geometry, as well as investigating changes to gas distribution with injection position, are necessary to evaluate industrial potential, as the energy cost and syngas ratios are far below what would be interesting for industrial applications. Although our modeling work suggests that higher SEI may improve these metrics, experimental validation is needed, which may require substantial process redesign; however, we believe that the primary value of this work lies in the improved mechanistic understanding of plasma-based reactive quenching mechanisms rather than immediate commercial application. The insights gained regarding oxygen scavenging mechanisms and product selectivity shifts with pressure provide a foundation for future research directions. However, these findings not only advance our understanding of plasma-based DRM mechanisms but also provide practical guidance for optimizing process engineering and operation parameters. By leveraging the thermal energy of the plasma afterglow through strategic reactive quenching, this approach represents a step toward more precise control of plasma chemistry and potentially opens new pathways for the selective production of fuels and chemicals from greenhouse gases, contributing to the development of carbon-circular economy technologies.

Bibliography

- [1] E.R. Mercer, S. Van Alphen, C.F.A.M. van Deursen, T.W.H. Righart, W.A. Bongers, R. Snyders, A. Bogaerts, M.C.M. van de Sanden, and F.J.J. Peeters. Post-plasma quenching to improve conversion and energy efficiency in a CO₂ microwave plasma. Fuel, 334:126734, 2023. ISSN 0016-2361. doi: 10.1016/j.fuel.2022.126734.
- [2] C.F.A.M van Deursen, H.M.S. Van Poyer, W.A. Bongers, F.J.J. Peeters, F.M.A Smits, and M.C.M. van de Sanden. Effluent nozzles in reverse-vortex-stabilized microwave CO₂ plasmas for improved energy efficiency. *Journal of CO₂ Utilization*, 88: 102952, 2024. ISSN 2212-9820. doi: 10.1016/j.jcou.2024.102952.
- [3] K. Wang, S. Ceulemans, H. Zhang, I. Tsonev, Y. Zhang, Y. Long, M. Fang, X. Li, J. Yan, and A. Bogaerts. Inhibiting recombination to improve the performance of plasma-based CO₂ conversion. *Chemical Engineering Journal*, 481:148684, 2024. ISSN 1385-8947. doi: 10.1016/j.cej.2024.148684.
- [4] A. Hecimovic, C.K. Kiefer, A. Meindl, R. Antunes, and U. Fantz. Fast gas quenching of microwave plasma effluent for enhanced CO₂ conversion. *Journal of CO₂ Utiliza*tion, 71:102473, 2023. ISSN 2212-9820. doi: 10.1016/j.jcou.2023.102473.
- [5] J. Li, X. Zhang, J. Shen, T. Ran, P. Chen, and Y. Yin. Dissociation of CO₂ by thermal plasma with contracting nozzle quenching. *Journal of CO₂ Utilization*, 21: 72–76, 2017. ISSN 2212-9820. doi: 10.1016/j.jcou.2017.04.003.
- [6] R. Vertongen, I. Tsonev, and A. Bogaerts. Enhancing CO₂ conversion with gas quenching in arc plasma. *Chemical Engineering Journal*, 505:159487, 2025. ISSN 1385-8947. doi: 10.1016/j.cej.2025.159487.
- [7] G. Raposo, A.W. van de Steeg, E.R. Mercer, C.F.A.M. van Deursen, H.J.L. Hendrickx, W.A. Bongers, G.J. van Rooij, M.C.M. van de Sanden, and F.J.J. Peeters.

- Flame bands: CO + O chemiluminescence as a measure of gas temperature. *Journal of Physics D: Applied Physics*, 54(37):374005, 2021. ISSN 0022-3727. doi: 10.1088/1361-6463/ac0924.
- [8] M. Albrechts, I. Tsonev, and A. Bogaerts. Can post-plasma CH₄ injection improve plasma-based dry reforming of methane? A modeling study. *Green Chemistry*, 26 (18):9712–9728, 2024. ISSN 1463-9262. doi: 10.1039/D4GC02889A.
- [9] J. Slaets, E. Morais, and A. Bogaerts. Afterglow quenching in plasma-based dry reforming of methane: a detailed analysis of the post-plasma chemistry via kinetic modelling. RSC sustainability, 2025.
- [10] A. van de Steeg, P. Viegas, A. Silva, T. Butterworth, A. van Bavel, J. Smits, P. Diomede, M. van de Sanden, and G. van Rooij. Redefining the microwave plasma-mediated CO₂ reduction efficiency limit: the role of O-CO₂ association. ACS Energy Letters, 6(8):2876-2881, 2021. ISSN 2380-8195. doi: 10.1021/acsenergylett.1c01206.
- [11] V. Vermeiren and A. Bogaerts. Plasma-based CO₂ conversion: To quench or not to quench? The Journal of Physical Chemistry C, 124(34):18401–18415, 2020. ISSN 1932-7447. doi: 10.1021/acs.jpcc.0c04257.
- [12] A.W. Van de Steeg, L. Vialetto, A.F.S. da Silva, P. Viegas, P. Diomede, M.C.M. Van de Sanden, and G.J. Van Rooij. The chemical origins of plasma contraction and thermalization in CO₂ microwave discharges. The Journal of Physical Chemistry Letters, 13(5):1203–1208, 2022. ISSN 1948-7185. doi: 10.1021/acs.jpclett.1c03731.
- [13] R. Vertongen, G. Trenchev, R. Van Loenhout, and A. Bogaerts. Enhancing CO₂ conversion with plasma reactors in series and O₂ removal. *Journal of CO₂ Utilization*, 66:102252, 2022. ISSN 2212-9820. doi: 10.1016/j.jcou.2022.102252.
- [14] F. Girard-Sahun, O. Biondo, G. Trenchev, G. van Rooij, and A. Bogaerts. Carbon bed post-plasma to enhance the CO₂ conversion and remove o₂ from the product stream. *Chemical Engineering Journal*, 442:136268, 2022. ISSN 1385-8947. doi: 10.1016/j.cej.2022.136268.
- [15] O. Biondo, K. Wang, H. Zhang, and A. Bogaerts. Coupling a CO₂ plasma with a carbon bed: The closer the better. *Chemical Engineering Journal*, 507:160190, 2025. ISSN 1385-8947. doi: 10.1016/j.cej.2025.160190.

- [16] C. O'Modhrain, Y. Gorbanev, and A. Bogaerts. Post-plasma carbon bed design for CO₂ conversion: Does size and insulation matter? *Journal of Energy Chemistry*, 104:312–323, 2025. ISSN 2095-4956. doi: 10.1016/j.jechem.2024.12.066.
- [17] H. Zhang, Q. Tan, Q. Huang, K. Wang, X. Tu, X. Zhao, C. Wu, J. Yan, and X. Li. Boosting the conversion of CO₂ with biochar to clean CO in an atmospheric plasmatron: A synergy of plasma chemistry and thermochemistry. ACS Sustainable Chemistry Engineering, 10(23):7712–7725, 2022. doi: 10.1021/acssuschemeng.2c01778. doi: 10.1021/acssuschemeng.2c01778.
- [18] G.J. Van Rooij, H.N. Akse, W.A. Bongers, and M.C.M. Van De Sanden. Plasma for electrification of chemical industry: A case study on CO₂ reduction. *Plasma Physics and Controlled Fusion*, 60(1):014019, 2017. ISSN 0741-3335. doi: 10.1088/ 1361-6587/aa8f7d.
- [19] N.V. Chekmarev, D.A. Mansfeld, A.V. Vodopyanov, S.V. Sintsov, E.I. Preobrazhensky, and M.A. Remez. Enhancement of CO₂ conversion by counterflow gas quenching of the post-discharge region in microwave plasma sustained by gyrotron radiation. *Journal of CO₂ Utilization*, 82:102759, 2024. ISSN 2212-9820. doi: 10.1016/j.jcou.2024.102759.
- [20] D. Mansfeld, S. Sintsov, N. Chekmarev, and A. Vodopyanov. Conversion of carbon dioxide in microwave plasma torch sustained by gyrotron radiation at frequency of 24 GHz at atmospheric pressure. *Journal of CO₂ Utilization*, 40:101197, 2020. ISSN 2212-9820. doi: 10.1016/j.jcou.2020.101197.
- [21] N.V. Chekmarev, D.A. Mansfeld, E.I. Preobrazhensky, S.V. Sintsov, M.A. Remez, and A.V. Vodopyanov. Suppression of reverse reactions during carbon dioxide decomposition in microwave discharge plasma. *Pisma v Zhurnal Tekhnicheskoi Fiziki*, 49(24):31–34, 2023. ISSN 0320-0116.
- [22] R. Aerts, R. Snoeckx, and A. Bogaerts. In-situ chemical trapping of oxygen in the splitting of carbon dioxide by plasma. *Plasma Processes and Polymers*, 11(10):985– 992, 2014. doi: 10.1002/ppap.201400091.
- [23] Y. Liu, E. Hu, E.A. Khan, and Z. Lai. Synthesis and characterization of ZIF-69 membranes and separation for CO₂/CO mixture. *Journal of Membrane Science*, 353 (1):36–40, 2010. ISSN 0376-7388. doi: 10.1016/j.memsci.2010.02.023.

- [24] A. Brunetti, F. Scura, G. Barbieri, and E. Drioli. Membrane technologies for CO₂ separation. *Journal of Membrane Science*, 359(1):115–125, 2010. ISSN 0376-7388. doi: 10.1016/j.memsci.2009.11.040.
- [25] O. Biondo, A. Hughes, A. van de Steeg, S. Maerivoet, B. Loenders, G. van Rooij, and A. Bogaerts. Power concentration determined by thermodynamic properties in complex gas mixtures: the case of plasma-based dry reforming of methane. *Plasma Sources Science and Technology*, 32(4):045001, 2023. ISSN 0963-0252. doi: 10.1088/1361-6595/acc6ec.
- [26] O. Biondo, C.F.A.M. Van Deursen, A. Hughes, A. van de Steeg, W.A. Bongers, M.C.M. van de Sanden, G. van Rooij, and A. Bogaerts. Avoiding solid carbon deposition in plasma-based dry reforming of methane. *Green Chemistry*, 25(24): 10485–10497, 2023.
- [27] C.H. Cho, J.H. Kim, J.K. Yang, I.S. Park, Y.S. Choi, and I.J. Kang. Dry reforming process using microwave plasma generator with high carbon dioxide conversion efficiency for syngas production. *Fuel*, 2024. ISSN 0016-2361. doi: 10.1016/j.fuel.2023.130707.
- [28] S. Kelly, E. Mercer, R. De Meyer, R-G Ciocarlan, S. Bals, and A. Bogaerts. Microwave plasma-based dry reforming of methane: Reaction performance and carbon formation. *Journal of CO₂ Utilization*, 75:102564, 2023. ISSN 2212-9820. doi: 10.1016/j.jcou.2023.102564.
- [29] M.I. Malik, I.E. Achouri, N. Abatzoglou, and F. Gitzhofer. Intensified performance of methane dry reforming based on non-thermal plasma technology: Recent progress and key challenges. Fuel Processing Technology, 245:107748, 2023. ISSN 0378-3820. doi: 10.1016/j.fuproc.2023.107748.
- [30] H. Sun, J. Lee, and M.S. Bak. Experiments and modeling of atmospheric pressure microwave plasma reforming of a methane-carbon dioxide mixture. *Journal of CO₂ Utilization*, 46:101464, 2021. ISSN 2212-9820. doi: 10.1016/j.jcou.2021.101464.
- [31] B. Wanten. Dry, bi-and oxidative CO₂ reforming of CH₄ in an atmospheric pressure glow discharge reactor: an experimental study. Thesis, 2024.

- [32] B. Wanten, Y. Gorbanev, and A. Bogaerts. Plasma-based conversion of CO₂ and CH₄ into syngas: a dive into the effect of adding water. Fuel, 374:132355, 2024. ISSN 0016-2361.
- [33] B. Wanten, S. Maerivoet, C. Vantomme, J. Slaets, G. Trenchev, and A. Bogaerts. Dry reforming of methane in an atmospheric pressure glow discharge: Confining the plasma to expand the performance. *Journal of CO₂ utilization*, 56:101869, 2022. ISSN 2212-9820.
- [34] S. Van Alphen, B. Wanten, F. Girard-Sahun, J. Slaets, J. Creel, M. Aghaei, and A. Bogaerts. The role of CH₄ in plasma-assisted CO₂ and CH₄ conversion in a rotating gliding arc plasma: Insights revealed by experiments and modeling. ACS Sustainable Chemistry Engineering, 12(42):15715–15728, 2024. ISSN 2168-0485.
- [35] S. Maerivoet, B. Wanten, R. De Meyer, M. Van Hove, S. Van Alphen, and A. Bogaerts. Effect of O₂ on plasma-based dry reforming of methane: Revealing the optimal gas composition via experiments and modeling of an atmospheric pressure glow discharge. ACS Sustainable Chemistry Engineering, 12(30):11419–11434, 2024. ISSN 2168-0485.
- [36] S. Mehariya, A. Iovine, P. Casella, D. Musmarra, A. Figoli, T. Marino, N. Sharma, and A. Molino. Chapter 7 Fischer-Tropsch synthesis of syngas to liquid hydrocarbons, pages 217–248. Academic Press, 2020. ISBN 978-0-12-815936-1. doi: 10.1016/B978-0-12-815936-1.00007-1.
- [37] J.A. Menéndez, A. Arenillas, B. Fidalgo, Y. Fernández, L. Zubizarreta, E.G. Calvo, and J.M. Bermúdez. Microwave heating processes involving carbon materials. Fuel Processing Technology, 91(1):1–8, 2010. ISSN 0378-3820. doi: 10.1016/j.fuproc.2009.08.021.
- [38] F. Fabry, G. Flamant, and L. Fulcheri. Carbon black processing by thermal plasma. analysis of the particle formation mechanism. *Chemical Engineering Science*, 56(6): 2123–2132, 2001. ISSN 0009-2509.
- [39] R. Pristavita, G. Mendoza, Y. Norma, J.L. Meunier, and D. Berk. Carbon blacks produced by thermal plasma: the influence of the reactor geometry on the product morphology. *Plasma Chemistry and Plasma Processing*, 30:267–279, 2010. ISSN 0272-4324.

- [40] J.M. Coulson. Coulson Richardson's Chemical engineering. Vol. 6, Chemical engineering design / J.M. Coulson and J. F. Richardson. Chemical engineering design. Oxford: Butterworth-Heinemann, Oxford, 3rd / r.k. sinnott. edition, 1999.
- [41] B. Wanten, R. Vertongen, R. De Meyer, and A. Bogaerts. Plasma-based CO₂ conversion: How to correctly analyze the performance? *Journal of energy chemistry*, 2023. ISSN 2095-4956.
- [42] W.A. Bongers, H. Bouwmeester, A.J. Wolf, S. Welzel F.J.J. Peeters, D. van den Bekerom, N. den Harder, A. Goede, M. Graswinckel, and P.W. Groen. Plasmadriven dissociation of CO₂ for fuel synthesis. *Plasma Processes and Polymers*, 14(6): 1600126, 2017. ISSN 1612-8850. doi: 10.1002/ppap.201600126.
- [43] A.J. Wolf, F.J.J. Peeters, P.W.C. Groen, W.A. Bongers, and M.C.M. van de Sanden. CO₂ conversion in nonuniform discharges: Disentangling dissociation and recombination mechanisms. *The Journal of Physical Chemistry C*, 124(31):16806–16819, 2020. ISSN 1932-7447. doi: 10.1021/acs.jpcc.0c03637.
- [44] C.K. Kiefer, R. Antunes, A. Hecimovic, A. Meindl, and U. Fantz. CO₂ dissociation using a lab-scale microwave plasma torch: An experimental study in view of industrial application. *Chemical Engineering Journal*, 481:148326, 2024. doi: 10.1016/j.cej. 2023.148326.
- [45] COMSOL AB. COMSOL Multiphysics ® v. 6.0, 2024. URL https://www.comsol.com.
- [46] G. P. Smith, D. M. Golden, M. Frenklach, N. W. Moriarty, B. Eiteneer, M. Goldenberg, C. T. Bowman, R. K. Hanson, S. Song, W. C. Gardiner Jr., V. V. Lissianski, and Z. Qin. GRI-Mech 3.0, 2000. URL http://combustion.berkeley.edu/gri-mech/version30/text30.html.
- [47] I.P. Butylkin, V.K. Zhivotov, E.G. Krasheninnikov, M.F. Krotov, V.D. Rusanov, I.V. Tarasov, and A.A. Fridman. Plasma-chemical process of CO₂ dissociation in a nonequilibrium microwave discharge. *Zhurnal Tekhnicheskoi Fiziki*, 51:925–931, 1981. ISSN 0044-4642.
- [48] D.C.M. van den Bekerom, J.M.P. Linares, T. Verreycken, E.M. van Veldhuizen, S. Nijdam, G. Berden, W.A. Bongers, M.C.M. van de Sanden, and G.J. van Rooij. The importance of thermal dissociation in CO₂ microwave discharges investigated by power

- pulsing and rotational raman scattering. *Plasma Sources Science and Technology*, 28 (5):055015, 2019. ISSN 0963-0252. doi: 10.1088/1361-6595/aaf519.
- [49] H. Kim, S. Song, C.P. Tom, and F. Xie. Carbon dioxide conversion in an atmospheric pressure microwave plasma reactor: Improving efficiencies by enhancing afterglow quenching. *Journal of CO₂ Utilization*, 37:240–247, 2020. doi: 10.1016/j.jcou.2019. 12.011.
- [50] K. Hiraoka, T. Sato, S. Sato, N. Sogoshi, T. Yokoyama, H. Takashima, and S. Kitagawa. Formation of formaldehyde by the tunneling reaction of H with solid CO at 10 K revisited. *The Astrophysical Journal*, 577(1):265, 2002. ISSN 0004-637X. doi: 10.1086/342132.
- [51] W.D. Watson. Interstellar chemistry. Accounts of Chemical Research, 10(6):221–226,
 1977. ISSN 0001-4842. doi: 10.1021/ar50114a005. doi: 10.1021/ar50114a005.
- [52] M.R. Leonardo, L.A.B. da Silva, M.T. Filho, and R.S. da Silva. Release of formaldehyde by 4 endodontic sealers. Oral Surgery, Oral Medicine, Oral Pathology, Oral Radiology and Endodontics, 88(2):221–225, 1999. ISSN 1079-2104. doi: 10.1016/S1079-2104(99)70119-8. doi: 10.1016/S1079-2104(99)70119-8.
- [53] S. Lee, H. Ju, H. Jeon, R.L. Machunda, D. Kim, J.K. Lee, and J. Lee. Electrocatalytic reduction of gas-phased CO₂ on nano-sized sn electrode surface. *ECS Transactions*, 53(29):41, 2013. ISSN 1938-5862. doi: 10.1149/05329.0041ecst.
- [54] G. Ruderman, E.R. Caffarena, I.G. Mogilner, and E.J. Tolosa. Hydrogen bonding of carboxylic acids in aqueous solutions—uv spectroscopy, viscosity, and molecular simulation of acetic acid. *Journal of Solution Chemistry*, 27(10):935–948, 1998. ISSN 1572-8927. doi: 10.1023/A:1022615329598.
- [55] S. Ghosh and S. Nandi. A comprehensive review on uv-visible spectroscopy and its application.
- [56] H.H. Perkampus. UV-VIS Spectroscopy and its Applications. Springer Science Business Media, 2013. ISBN 3642774776.
- [57] J. Puhar, A. Vujanović, P. Awad, and L. Čuček. Reduction of cost, energy and emissions of the formalin production process via methane steam reforming. Systems, 2021. doi: 10.3390/systems9010005.

- [58] C.J. Sebastian, F.N. Adhyaksa, M.T. Kamal, and V.E. Susanto. Optimization of energy consumption in formaldehyde production process using reboiled absorption process. 2024. doi: 10.9767/jcerp.20094.
- [59] J.B. Donnet. Carbon black: science and technology. Routledge, 2018. ISBN 1351462628.
- [60] S.L. Girshick and C.P. Chiu. Homogeneous nucleation of particles from the vapor phase in thermal plasma synthesis. *Plasma Chemistry and Plasma Processing*, 9(3): 355–369, 1989. ISSN 1572-8986. doi: 10.1007/BF01083672.
- [61] T.W. Zerda, W. Xu, H. Yang, and M. Gerspacher. The effects of heating and cooling rates on the structure of carbon black particles. *Rubber Chemistry and Technology*, 71(1):26–37, 1998. ISSN 0035-9475. doi: 10.5254/1.3538469.
- [62] V.S. Dozhdikov, A.Y. Basharin, and P.R. Levashov. Structure studies of graded amorphous carbon obtained by liquid carbon quenching. *Technical Physics*, 69(5): 1170–1180, 2024. ISSN 1063-7842.
- [63] S.L. Girshick, C.P. Chiu, and P.H. McMurry. Modelling particle formation and growth in a plasma synthesis reactor. *Plasma Chemistry and Plasma Processing*, 8 (2):145–157, 1988. ISSN 1572-8986. doi: 10.1007/BF01016154.
- [64] M. Gautier, V. Rohani, and L. Fulcheri. Direct decarbonization of methane by thermal plasma for the production of hydrogen and high value-added carbon black. *International Journal of Hydrogen Energy*, 42(47):28140–28156, 2017. ISSN 0360-3199.
- [65] X.F. Guo and G.J. Kim. Synthesis of ultrafine carbon black by pyrolysis of polymers using a direct current thermal plasma process. *Plasma Chemistry and Plasma Processing*, 30:75–90, 2010. ISSN 0272-4324.
- [66] L. Juan, H. Fangfang, L. Yiwen, Y. Yongxiang, D. Xiaoyan, and X. Liao. A new grade carbon black produced by thermal plasma process. *Plasma Science and Technology*, 5(3):1815, 2003. ISSN 1009-0630.
- [67] R.O. Grisdale. The formation of black carbon. Journal of Applied Physics, 24(9): 1082–1091, 1953. ISSN 0021-8979. doi: 10.1063/1.1721452.

- [68] D.R. Lobato-Peralta, P.U. Okoye, and C. Alegre. A review on carbon materials for electrochemical energy storage applications: State of the art, implementation, and synergy with metallic compounds for supercapacitor and battery electrodes. *Journal* of Power Sources, 617:235140, 2024. doi: 10.1016/j.jpowsour.2024.235140.
- [69] K. Silins, H. Baránková, and L. Bardos. Protective amorphous carbon coatings on glass substrates. AIP Advances, 7(11), 2017. doi: 10.1063/1.5002091.
- [70] C. Bommier, D. Mitlin, and X. Ji. Internal structure na storage mechanisms electrochemical performance relations in carbons. *Progress in Materials Science*, 97: 170–203, 2018. doi: 10.1016/j.pmatsci.2018.04.006.
- [71] M.G. Fyta, C. Mathioudakis, G. Kopidakis, and P.C. Kelires. Structure, stability, and stress properties of amorphous and nanostructured carbon films. *Thin Solid Films*, 482(1):56–62, 2005. doi: 10.1016/j.tsf.2004.11.114.

Chapter 5

Beyond Earth:

Martian Atmosphere Conversion for In-Situ Resource Utilization

In this chapter, we explore the potential of plasma-based In-Situ Resource Utilization (ISRU) on Mars through the conversion of simulant Martian atmosphere ($\sim 96\%$ CO₂, 2% N₂, and 2% Ar) into life-sustaining chemicals. As the Martian surface pressure is less than 1% of the Earth's, it is an ideal environment for plasma-based gas conversion using MW plasma reactors, because the latter can operate in a wide pressure regime, including at low pressures. At 1000 W and 10 ln/min, we produced ~ 76 g/h of O₂, 128 g/h of CO, and ~ 3 g/h of NO_x using a 2.45 GHz waveguided reactor at ~ 3.5 times Mars ambient pressure (25 mbar). The energy cost required to produce O₂ was ~ 0.013 kWh/g, which is very promising compared to recently concluded Mars OXygen In-Situ resource utilization Experiment (MOXIE) experiments on the Mars surface [1]. This marks a crucial step towards realizing human exploration of the Red Planet.

This chapter is derived from the following publication:

[•] Plasma-based Conversion of Martian Atmosphere into Life-sustaining Chemicals: The Benefits of Utilizing Martian Ambient Pressure

S. Kelly* and **E.R. Mercer***, Y. Gorbanev, I. Fedirchyk, C. Verheyen, K. Werner, P. Pullumbi, A. Cowley, A. Bogaerts

https://doi.org/10.1016/j.jcou.2024.102668

The work presented in this chapter was carried out in collaboration with the European Space Agency, and is in co-first authorship with Dr. Seán Kelly, a distinguished post-doctoral mentor whose guidance was instrumental to this research.

5.1 Introduction

In February 2021, the Perseverance rover landed on Mars. It was a mission full of firsts, and on April 20th, the Mars OXygen In-situ resource utilization Experiment (MOXIE) completed its initial test for converting Martian atmosphere into life-sustaining molecules, including O_2 at $\sim 98\%$ purity [2]. Using ~ 120 W of power, the atmospheric gas mixture was brought through a Solid OXide Electrolyzer (SOXE) to produce up to ~ 10 g/h of O_2 at peak efficiency [1]. In total, it is estimated that returning just four astronauts home from the Martian surface would require over 25 metric tons (25 \times 10⁶ g) of O_2 for rocket propellant [3]. This enormous requirement highlights why advancing technologies like MOXIE are so critical. The experiments that MOXIE conducted mark a giant leap forward and show a glimpse of what is possible for utilizing the Martian atmosphere to produce valuable and life-sustaining supplies; however, it is apparent from the sheer magnitude of resources needed for just one mission that the future expansion of human exploration to planets like Mars demands significant improvements or novel technologies to efficiently utilize all of the resources available on the Red Planet.

A recent article by Engeling et al. outlined how plasma-based applications could be used for advanced chemical processing in space to support human life during crewed transit and planetary habitation [4]. This study focused on several plasma-based applications being investigated at the National Aeronautics and Space Administration's (NASA) Kennedy Space Center, including plasma waste gasification, plasma-assisted nutrient recovery, hydrogen plasma Lunar regolith reduction, plasma for space agriculture, plasma-activated water, and plasma cleaning and processing [4]. Moreover, the European Space Agency (ESA) has displayed a keen interest in utilizing plasma-based applications and has undertaken several projects aimed at extracting key molecules from Mars' CO₂-rich atmosphere [5]. Although plasma research is still in its early stages, it can potentially influence future planetary colonization strategies. It is clear from the research conducted by both NASA and ESA that plasma-based ISRU is instrumental in advancing space exploration, as well as realizing future human-led missions to Mars.

MW plasma reactors show great potential in an ISRU context. As an emerging technology, MW plasma reactors have demonstrated favorable energy efficiencies and gas conversion at low-sub-atmospheric pressures, such as those found on the surface of Mars, and many studies have reported encouraging results [6–10]; however, few have applied this technology

in a Mars ISRU context [5, 11, 12]. As discussed in Chapter 2, currently, MW plasmabased gas conversion has a Technology Readiness Level (TRL) of approximately 3 (i.e., achieved experimental proof of concept) [13]. Plasma technology in an ISRU context is less developed than Earth-based applications, with an estimated TRL of 1-2, (i.e., basic principles and technology concepts formulated). Progress for Earth-based applications, however, should significantly speed up the development of plasma technology for ISRU and aerospace, with substantial overlap and complementarity anticipated. By employing MW technology in an ISRU context for Mars, it is possible that we can realize the potential for more efficient and sustainable ISRU here on Earth as well. It has been demonstrated that MW plasma conversion can produce valuable resources like propellants (CO and O₂), O₂ for habitats, and fixed nitrogen (as NO_x) for agriculture at a low energy cost, making it an excellent candidate for local generation [5, 11, 14–16]. In a previous study, Kelly et al. reported that when using MW plasma at sub-atmospheric pressures (i.e., 340 mbar), they could achieve an energy cost of approximately 0.04 kWh/g compared to 0.19 kWh/g reported from the first MOXIE experiments to produce O₂ [2, 5]. In conjunction with 47 g/h of O₂ production, they also showed that other valuable chemicals, such as key molecules like CO and NO_x , can be produced and utilized in an ISRU context.

In an optical analysis comparing pure CO₂ plasma versus a simulated Mars atmosphere plasma conducted by Raposo [12], it is shown that the conversion process in MW plasma may be enhanced by near-Mars surface pressure conditions (i.e., compared to higher operating pressures). Raposo's work demonstrated that when operating at typical Martian surface pressure, the plasma afterglow exhibited distinct temperature and gas fraction profiles [12]. Raposo reported a distinct difference in the afterglow chemistry observed by chemiluminescent enhancement, attributing the observation to NO + O recombination [12]. Furthermore, Raposo states that the presence of Ar plays a significant role in the ionization and dissociation processes [12]. Although more research is needed to confirm these findings, the author infers that the overall rate of CO₂ dissociation is increased in a Martian mixture, likely due to the presence of Ar and N₂. Notably, Raposo reflects a change in the plasma regime from a homogenous to a contracted plasma with increased pressure from 6 mbar to 300 mbar [12]. As discussed in Chapter 2, the resulting shift into a contracted state will decrease the intersection of the plasma filament and the transiting gas, increasing gas slippage and reducing conversion.

In this chapter, we investigate the benefits of using MW plasma technology for the conversion of a Martian atmosphere-like mixture (with a composition of approximately 96% CO_2 , 2% N_2 , and 2% Ar) into life-sustaining chemicals at near-Mars surface pressure conditions (25 mbar). We pay special attention to ascertaining the key performance metrics at these low pressures (i.e., key species production rates and energy costs). These central aspects, crucial to understanding MW plasma technology for gas conversion on Mars, have not been previously investigated. Notably, the conversion process involves dissociating CO_2 and N_2 molecules, creating target products, such as CO, O_2 , and NO_x , which can be utilized as building blocks for liquid bi-propellants and fertilizers [15]. The proposed method can provide valuable resources for future human missions to Mars.

5.2 Experimental Methods

The experiments used a forward vortex waveguided configuration with a 2.45 GHz solidstate power supply composed of laterally diffused metal oxide semiconductor (LDMOS) power amplifiers, as shown in the schematic in *Figure 5.1* and thoroughly discussed in Chapter 2. The output from the amplifiers is combined and guided through an isolator and auto-tuner to the WR340 coupling chamber. A 27 mm inner diameter quartz tube is perpendicularly mounted through the waveguide terminated by a sliding short, where plasma ignition occurs. The auto-tuner matches the electric field transition into the resonance chamber such that the reflected power is kept below 1% for all conditions. The gas is injected using a helical swirl inlet to sustain a vortex flow within the discharge area. After that ignition, a surface-wave mode is generated and sustained, isolating the plasma discharge from the quartz tube walls.

The post-plasma composition was analyzed using Non-Dispersive InfraRed and UltraViolet (NDIR/UV) absorption spectrometry (Rosemount X-STREAM XEGP Continuous Gas Analyzer) for NO, NO₂, CO, CO₂ molecules, whereas O₂ was measured using an Infra-Red luminescent quenched absorption technique (Pyroscience GmbH FDO2 Optical Oxygen Sensor). In calibrating these diagnostic instruments, we utilize pre-mixed calibration gases (Air Liquide, e.g., NO, 16 % in Helium and NO₂, 7.8 % in Helium). Crosschecks using Gas Chromatography (GC) with Interscience Compact GC to corroborate calibration. This GC features two channels, each equipped with a Thermal Conductivity Detector (TCD), Carboxen, and Molsieve columns (1010 PLOT and 5A, respectively).

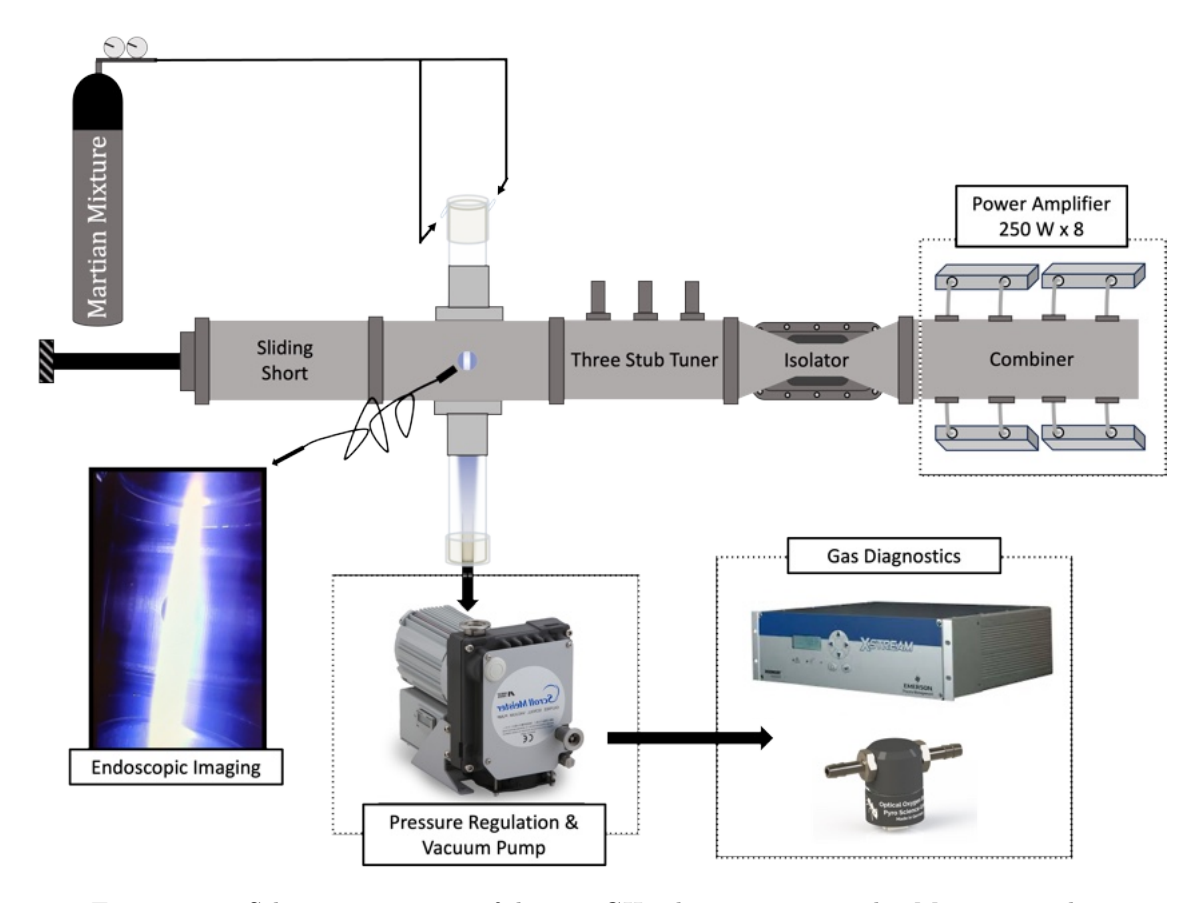


FIGURE 5.1: Schematic overview of the 2.45 GHz plasma reactor with a Martian simulant atmosphere at 25 mbar pressure and 1 kW power. The ignition occurs in the coupling chamber of the rectangular WR340 waveguide, where the plasma is stabilized in the center of the quartz tube. The viewing port allows for real-time plasma imaging, as seen in the image of the plasma filament.

These are used to detect O_2 , N_2 , and CO, while two RT Q-bond columns (one with a length of 3 m and the other 10 m) are utilized for the detection of CO_2 [5]. The primary gas converted in our experiments is CO_2 ($\sim 96\%$ of the Martian atmosphere), with oxidation of the small N_2 content ($\sim 2\%$). The argon fraction ($\sim 2\%$) is not converted due to its inertness. The key overall reactions for consideration are therefore:

$$2 \text{ CO}_2 \rightleftharpoons 2 \text{ CO} + \text{O}_2$$
 (R5.1)

$$O_2 + N_2 \rightleftharpoons 2 \text{ NO}$$
 (R5.2)

$$2 O_2 + N_2 \rightleftharpoons 2 NO_2$$
 (R5.3)

During any gas conversion process, the changes in stoichiometric proportions result in changes in the molar flow rate in the plasma exhaust compared to the inlet flow rate.

In our experimental setup, CO_2 is the primary component of the gas fraction. When it is converted into CO and O_2 , it leads to an expansion of the flow rate, which means an increase in the molar flow rate. The extent of this increase is directly related to the degree of conversion. It's worth noting that the formation of NO_2 results in gas contraction; however, due to the relatively small proportion of N_2 and an even smaller fraction of NO_2 formed in comparison to CO and O_2 , this contraction effect is expected to be negligible when compared to the expansion resulting from CO_2 conversion; therefore, it is neglected in our analysis. In our case, given the predominant CO_2 conversion, we can infer the degree of expansion by examining the CO_2 conversion as follows [5, 17]:

$$\alpha = 1 + 0.5 \times \chi \tag{E5.1}$$

$$\chi = \frac{y_i^{\text{In}} - \alpha \times y_i^{\text{Out}}}{y_i^{\text{In}}}$$
 (E5.2)

Where α represents the gas expansion factor (i.e., $\alpha > 1$), χ is the fraction of CO₂ converted, y_i^{In} is the fraction of CO₂ in the mixture when the plasma is off (i.e., 0.96 in our case) and y_i^{Out} is the measured CO₂ fraction when the plasma is on. Notably, we do not add a dilution gas to measure the gas expansion in our experiments, approximating the conversion as a pure CO₂ conversion given the negligible effects of the N₂ conversion in our context [5, 17]. Rearranging E5.1 and E5.2 we can solve them to find α based on the measured CO₂ data:

$$\alpha = \frac{1.5 \times y_i^{\text{In}}}{y_i^{\text{In}} + 0.5 \times y_i^{\text{Out}}}$$
 (E5.3)

Subsequently, when calculating α , we obtain the CO₂ conversion by E5.3. The CO, O₂, and NO_x production rates are calculated based on the fraction of each species measured in the exhaust (y_j), their molar mass (M_j (g/mol)), the inlet mass flow rate (ϕ_{in}) in normal liters per minute (ln/min, EU – 0°C, 1 atm), as well as α .

The individual production rates (PR, g/h) are then calculated for CO, O₂, and NO_x (NO + NO₂) as:

$$PR_j = \frac{y_j \cdot M_j \cdot \alpha \cdot \phi_{\text{in}}}{\nu_m} \cdot 60 \left(\frac{\min}{h}\right)$$
 (E5.4)

where ν_m is the molar volume (22.4 (l/mol)) of a gas for which our mass flow controllers (Bronkhorst) are calibrated. The energy cost (EC, (kWh/g)) to produce CO, O₂, or NO_x is then obtained using:

$$EC_j = \frac{P}{PR_j} \tag{E5.5}$$

where the power (P, kW or kJ/s) is the absorbed MW power measured during steady-state plasma operation. Additional details regarding the setup are described in Chapter 2.

5.3 Results and Discussion

We discuss our experimental results using our solid-state surface-wave MW plasma reactor, modified for operation at reduced pressures close to Martian ambient conditions. All experiments were carried out using the 2.45 GHz MW reactor described in Section 5.2, with a $\phi_{\rm in}=10$ ln/min (i.e., 1,131 g/h CO₂, 30 g/h N₂, and 21.4 g/h Ar mass flow rate for a Martian mixture in a ratio 96:2:2 v/v CO₂:N₂:Ar), a pressure of 25 mbar, and 1000 W of absorbed plasma power. Throughout the text, NO_x indicates the sum of NO and NO₂. For comparison, we have included the reported results from the work on Kelly et al. [5], which were investigated under the same pressure conditions as the MOXIE experiments (340 mbar) [5].

The production rates of CO, O₂, and NO_x ($PR_{\text{CO,O}_2,\text{NO}_x}$) measured in the plasma exhaust are presented in Figure 5.2(A). The measured rates were 127.7 \pm 1.0, 75.7 \pm 0.9, 2.9 \pm 0.1 g/h, respectively, representing increases of approximately 66%, 50%, 100% compared to the conditions reported by Kelly et al. at 340 mbar [5]. Overall, the sampled exhaust mixture has a percentage ratio of approximately 15.9% CO, 8.3% O₂, and 0.3% NO_x.

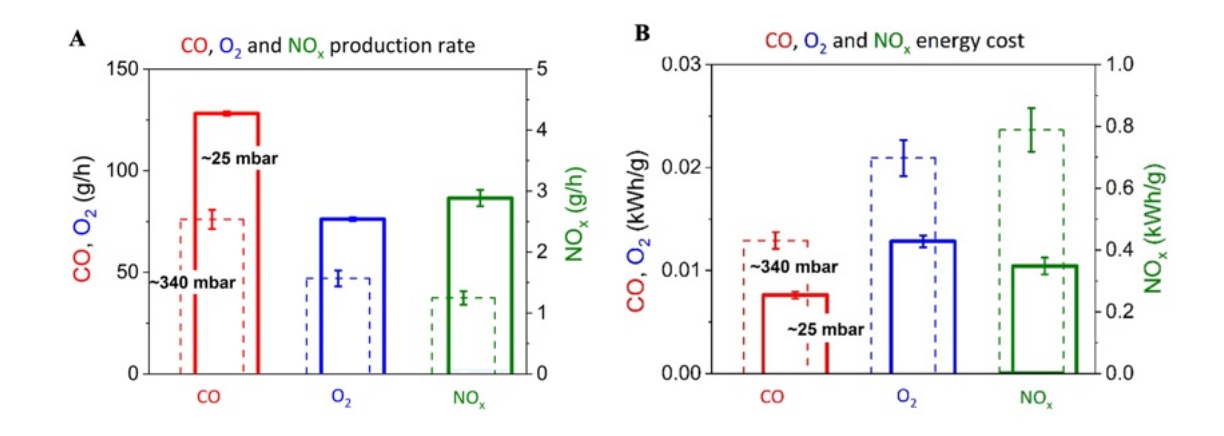


FIGURE 5.2: Comparison of (A) production rate and (B) energy cost at 25 mbar (\sim 3.5 \times Martian atmosphere) with 340 mbar (dashed lines) [5].

The NO_x concentration in the exhaust mixture was equivalent to 3015 \pm 14 ppm, where the primary species produced were NO and NO₂, with a ratio of NO/NO₂ of \sim 9 (i.e., NO concentrations dominate). This corresponds to $\sim 15\%$ of the N₂ inflow being fixed. Thus, we conclude that reducing the pressure closer to Mars' ambient conditions increases the overall production of $CO/O_2/NO_x$, despite a significant reduction in gas residence time under the low-pressure conditions (estimated to be nearly a factor of ten). Furthermore, in Figure 5.2(B) we observe that the corresponding energy cost (EC_{CO,O_2,NO_x}) of producing CO, O₂, and NO_x is 0.0080 ± 0.0004 , 0.013 ± 0.006 kWh/g, and 0.35 ± 0.03 kWh/g, respectively. Given the boost in PR_{CO,O_2,NO_x} , the EC drops similarly by approximately 50 - 70% for O_2 and CO, respectively, and by more than a factor two for NO_x under these reduced pressure conditions compared to the metrics reported by Kelly et al. [5]. It is evident from these results that plasma-based conversion of CO₂ and fixation of N₂ is significantly more productive at pressures similar to the Martian environment. The increased gas velocity at this low pressure (25 mbar) may serve to remove the products from the reactive volume before they can participate in recombination reactions. Furthermore, the gas velocity undergoes dynamic changes as a result of variations in temperature and stoichiometry within the gas mixture. Due to the relatively inert nature of N_2 and CO_2 , considerable energy is required for thermal conversion; however, low-pressure plasmabased conversion provides additional reaction pathways [14]. Given the low pressure reported in our results, electrons have the energy needed to induce excitation towards the lowest vibrational levels in CO_2/N_2 (~ 1 eV), followed by further vibrational-vibrational (V-V) collisions, which enable a "ladder-climbing" process, gradually populating higher vibrational levels (denoted as $CO_2(v)$ and $N_2(v)$).

Production of NO_x (R5.2 and R5.3) in plasma depends on atomic nitrogen (N) and oxygen (O) formation. In a plasma, this can also proceed via an electronically or vibrationally enhanced Zeldovich mechanism consisting of the following reactions [16, 18] (besides the thermal Zeldovich mechanism from the ground-state molecules):

$$O + N_2/N_2(E, v) \rightleftharpoons N + NO$$
 (R5.4)

$$N + O_2/O_2(E, v) \rightleftharpoons O + NO$$
 (R5.5)

The contribution of the first Zeldovich reaction R5.4, is facilitated by electronically or vibrationally excited N_2 molecules. Given the strong N_2 triple bond, the above reaction pair is typically rate-limited by R5.4. Compared to the purely thermal Zeldovich mechanism (i.e., involving only ground state N_2 and O_2), plasma-based conversion has the additional presence of vibrationally or electronically excited N_2 and O_2 molecules, which lower the dissociation threshold required to break the N_2 bond (~ 9.8 eV) by colliding with O atoms (R5.4). The N atoms formed here further react with both ground state and vibrationally/electronically excited O_2 molecules (R5.5) to produce another NO. Moreover, R5.5 also produces an additional O atom, which can again react with ground state and vibrationally/electronically excited N_2 molecules (R5.4). Furthermore, it can oxidize NO to produce NO₂:

$$NO + O \rightleftharpoons NO_2$$
 (R5.6)

It is likely that N_2 molecules in the ground state play a negligible role in NO formation. On the other hand, vibrationally excited $N_2(v)$, mainly from levels near the threshold energy for N_2 oxidation (v = 10 - 14), may contribute significantly more, as the production of $N_2(v)$ requires less energy than of $N_2(E)$ (i.e., the excitation energy for $N_2(v)$ (v = 10 - 14) is in the range 2.7 - 3.7 eV, while for $N_2(E)$ it is over 6.2 eV). This would explain why the energy cost for NO production at 25 mbar is more than a factor two lower than at 340 mbar (see Figure 5.2) [5].

When considering CO₂ dissociation, a similar reaction pathway applies. The overall reaction shown in R5.1 includes the following elementary sub-reactions involving atomic oxygen:

$$CO_2(E, v) \rightleftharpoons CO + O$$
 (R5.7)

$$CO_2(E, v) + O \rightleftharpoons CO + O_2$$
 (R5.8)

where direct dissociation proceeds in R5.7, such as electron impact dissociation, have an energy threshold of 5.5 eV to overcome the (ground state) CO_2 bond energy, but the O atom produced in R5.7 can further react (i.e., R5.8) with CO_2 (and its vibrationally or electronically excited states). This coupling lowers the threshold considerably (e.g., for ground state CO_2 , this lowers the overall energy threshold to 2.9 eV [?]). The production of CO and CO_2 are likely to be primarily formed via R5.8, involving the collision of O atoms with CO_2 , yielding CO and CO_2 . This reaction involves the symmetric stretch and bending vibrational modes of CO_2 , namely $CO_2(v_a-v_d)$ (ranging 0.08-0.33 eV in energy) [19].

Therefore, it is possible that the enhanced conversion results from vibrational excitation, as these levels are stated to be overpopulated in homogeneous or L-mode plasmas at lower pressure (p \ll 100 mbar) [9, 12, 20] due to reduced losses upon collisions with ground state molecules, resulting in a more pronounced vibrational-translational non-equilibrium, which gives rise to efficient routes for conversion [14, 21–23]. An important factor in utilizing the near-ambient Martian pressure (25 mbar), while keeping the same mass flow rate as in the work by *Kelly et at.*, is the limited residence time of the gas in the reactive volume at reduced pressures. At 340 mbar, the gas is estimated to spend approximately 75 ms within the reactive volume (i.e., 0 – 20 cm). At 25 mbar, using the same mass flow rate (i.e., $\phi_{\rm in} = 10 \, {\rm ln/min}$), we estimate the residence time to be approximately 7.5 ms within the reactive volume. Therefore, exploiting the benefits of low-pressure conditions while increasing the gas residence time within the reactive volume, e.g., by applying a lower mass flow rate or creating a longer plasma, could have further benefits to conversion.

5.4 Considerations for Plasma-based ISRU on Mars

As we have outlined, plasma-based conversion of Martian atmosphere enables not only O_2 production but also the formation of CO and NO_x . These life-sustaining molecules can be utilized as ISRU precursors for both fuels and fertilizers. Numerous studies have shown that ISRU on Mars will be essential in realizing cost-effective missions and future colonization of The Red Planet [14, 15, 24]. To explore Mars, we need propulsion systems that require less mass to be launched from Earth, as reaching Mars requires substantial resources, although the exact amount of propellant will depend on the weight of the launch vehicle and mission outline, according to NASA [25]. Plentiful sources of hydrogen have yet to be identified on the surface of Mars; therefore, traditional rocket propellants are likely unavailable for in-situ production. In an article assessing and comparing potential hydrogen-free propellants for an In-situ Mars Ascent Vehicle (IMAV) [26], Conley et al. determined that a liquid propulsion system using a mixture of CO and O₂ was the most favorable regarding performance, safety, and feasibility. The CO/O₂ propellant combination is a top candidate for a Martian in-situ propellant rocket engine, and the feasibility of a pump-fed engine has been detailed in a report by Roncace et al. [27]. As we have shown, plasma conversion of Martian atmosphere can provide a low energy cost method to produce this bipropellant.

In May 2008, the Phoenix Scout Mission landed on the surface of Mars in search of water and signs of life. Within the data, the Martian regolith was found to consist of essential nutrients for plant growth, including both macronutrients, such as oxygen, carbon, hydrogen, nitrogen, potassium, phosphorus, calcium, magnesium, and sulfur, and micronutrients, such as iron, manganese, zinc, copper, molybdenum, boron, and chlorine [28, 29]. However, the Martian regolith was also shown to be laced with an abundance of heavy metals and, of particular interest, perchlorates, which can be highly toxic to humans if ingested or inhaled. This will pose a significant issue for future explorers, as any heavy metals will be taken up by the plants and subsequently consumed by Martian colonists. Moreover, perchlorates pose a chemical hazard to any astronauts on Mars [30–32]. Nevertheless, some studies have been conducted on the feasibility of growing plants on the surface of Mars with fair success using Martian soil simulants [29]; however, it is clear that due to the nature of Martian regolith, inoculation of organic matter and fertilizer to the growth medium will be critical to crop success, a critical resource for self-sufficient

colonies. Although the production of NO_x species from plasma-based application will most likely not be the only source for enrichment of Martian regolith, it is a key product formed in the dissociation of Mars atmosphere that can be utilized in the production of ISRU fertilizers.

5.5 Post-Plasma Separation:

Harnessing the Martian Atmosphere

As outlined in the previous section, plasma-based conversion of Martian atmosphere provides a gateway to produce O_2 , CO, and NO_x as precursors to bi-propellants and fertilizers. The challenge lies in efficiently separating these value-added molecules in the post-plasma effluent mixture. Various separating schemes exist in industry [33–38], including several hybrid designs, combining gas separation by pressure swing adsorption (PSA), vacuum swing adsorption (VSA), or temperature swing adsorption (TSA); however, in theory, the most promising separation scheme for this application is vacuum and temperature swing adsorption (VTSA), to profit from the available low pressure at the Martian surface and the heat generated by the MW reactor.

Furthermore, oxygen transport membranes (OTMs) for O_2 separation can be utilized in the separation from the post-process stream [39]. These are comprised of a material that is conductive for oxygen ions and electronic charge carriers (electrons, defect electrons). The OTMs are referred to as mixed ionic electronic conductor (MIEC) membranes or ion transport membranes (ITMs), with the driving force for O_2 permeation created by the difference of partial pressures of oxygen (pO_2) determined by a gradient of oxygen vacancies across the membrane [40]. The oxygen ion transport mechanism is a thermally activated process; therefore, such membranes work at high temperatures, typically 800° C -1300° C. The post-plasma region of a MW plasma falls well within this temperature range [41, 42]. Among the studied OTM materials, $Ba_{0.5}Sr_{0.5}Co_{0.8}Fe_{0.2}O_{3-\delta}$ (BSCF) appears to be among the most promising for O_2 separation from a gas mixture, showing excellent performance in terms of oxygen flux and separation [39, 43, 44]. Although promising, it should be noted that BSCF has shown inadequate chemical stability when in contact with reacting gases such as CO_2 , CO, and NO_x [44, 45], which poses a significant challenge.

It is theoretically possible to address this by operating the membranes in a "protected" mode. A scheme for this might consider utilizing a VTSA unit for purifying the effluent mixture before these reacting gases come into contact with the OTM. Following this, the permeated oxygen could be removed by vacuum on the permeate side of the membrane, followed by pressurizing or condensing using cryopumping equipment.

Finally, it is feasible to utilize VTSA units to separate and recycle unreacted CO₂, N₂ and Ar back into the reaction stream. This could be achieved by using a multi-layer structure of adsorbers following the conversion characteristics of the plasma reactor, as well as the needs of post-plasma processing, such as protecting the OTM. The separately collected gases could then be pressurized or condensed using cryopumping for storage and later use. In a continuous plasma process, converted gas can be stored in intermediary equipment and, following industrial standards, should be made of at least two capacities installed in parallel that are cyclically compressed and connected to the VTSA unit. In some of the proposed gas separation schemes, particularly relating the introduction of inert gas, such as Ar (recovered and recycled in the separation system), has been considered to enhance the separation performance. It is also feasible to utilize MW-based Mars atmosphere conversion entirely for bi-propellant production, as our results show that it produces a mixture mainly consisting of CO and O₂, which as discussed in Section 5.4, can be used as building blocks for liquid bi-propellants [26, 27].

5.6 Microwave Reactors on Mars

As discussed in Chapter 2, during space applications like ISRU on Mars, available power might be limited (e.g. a few kW from a rover's power system or a few tens of kW from a small nuclear reactor on a habitat). Therefore, energy efficiency is paramount, as 'every watt counts', but so is reliability. Magnetrons at first glance would be attractive for efficiency reasons; however, their limited lifespan is a serious issue in space. A magnetron that lasts 5,000 hours (approximately 7 months continuous) could become a maintenance headache on a Mars mission that is expected to operate for years. Replacing a magnetron on Mars is not trivial. Solid-state devices, rated for $\gg 30,000$ hours, could run for the entire mission without replacement.

Moreover, the mass and volume of the system also matter, and magnetrons require a heavy high-voltage power converter. In a spacecraft design, having to generate and handle kV is undesirable [25]. Solid-state generators only need whatever bus voltage is available (e.g. 28 V DC is common in spacecraft) stepped up to ~ 50 V, which can be done with lightweight switch-mode converters. Thus, for an equivalent MW output, a solidstate system might have higher electronic complexity but lower overall mass and better integration with spacecraft power systems. Additionally, the modular redundancy of solidstate is valuable in space. For example, if a single transistor element fails, the system can continue at slightly reduced power. If a magnetron fails, such as if the vacuum tube breaks, the whole unit can be lost, requiring the mission to carry spares, which is extra mass and the associated extra cost. Furthermore, as discussed in Chapter 2, solid-state systems will not deteriorate in power output or efficiency with time, as is with magnetron sources, making them ideal candidates in an ISRU context. As we outlined in Chapter 2, radiation hardness is a concern on Mars due to the lack of a protective ionosphere [25, 46], and devices made with GaN semiconductors have shown to be more robust against radiation and are already in use in the aerospace sectors [46, 47]. As well, GaN offers benefits in miniaturization and weight reduction [47]. As we have shown in this chapter, semiconductor-based HF generators hold a lot of potential for Mars ISRU missions.

5.7 Conclusion and Outlook

Mars presents favorable low-pressure conditions ideal for efficient conversion through vibrationally-induced dissociation pathways of CO_2 and N_2 using solid-state MW plasma reactors, positioning such devices as promising candidates for In-Situ Resource Utilization (ISRU). However, the potential of these devices in the context of ISRU remains largely untapped [5, 11, 12]. In the MOXIE experiment [1, 2, 48], the energy cost to compress the Martian atmosphere using a scroll pump was about one-third of the total energy cost of the CO_2 conversion into O_2 . Hence, the overall energy cost may be considerably reduced if Mars ambient pressure can be used. In this chapter, we presented our experimental findings from our solid-state surface-wave MW plasma reactor, adapted to operate at pressures closely mirroring Martian ambient conditions, thus avoiding additional costs associated with gas compression. We achieved an O_2 , CO, and NO_x production rate of 75.7 ± 0.9 , 127.7 ± 1.0 g/h, and 2.9 ± 0.1 g/h, respectively. Remarkably, the rate of O_2

production is about 7 times larger than that of the MOXIE experiment ($\sim 10.4 \text{ g/h}$) [1]. This was accomplished at an energy cost of 0.013 kWh/g, hence it is lower compared to the MOXIE experiments, which ranged between $\sim 0.025 - 0.05 \text{ kWh/g}$ for the electrolysis stack alone [1]. In contrast to the work by *Kelly et al.*, who performed experiments at higher pressures ($\sim 340 \text{ mbar}$) [5], the tests conducted at 25 mbar showed an increase of 50 - 70% in O_2 and CO production rates. Moreover, roughly 15% of the incoming N_2 transformed into NO_x , exceeding a twofold gain compared to conditions at higher pressure [5]. This uptick in production, accompanied by a comparable drop in energy cost, was observed despite the gas residence time in the plasma region being reduced (estimated to be by a factor of ten). Our results show that CO_2 conversion and N_2 fixation via plasma are notably more efficient at Martian ambient pressure, likely through the contribution of vibrationally excited 'ladder climbing' mechanisms.

Our MW plasma-based conversion of Martian atmosphere yields a combination of O_2 , CO, and NO_x ; therefore, separation is essential to fully harness these products in an extraterrestrial ISRU context. Although post-plasma separation is out of the scope of this research, we highlight potential gas separation systems and their theoretical integration with a solid-state MW plasma reactor. However, this integration is intricate due to numerous parameters and should be carefully considered. Future studies should focus on utilizing a multi-objective optimization strategy, drawing from comprehensive numerical simulations of the entire process. As of October 2023, various components of the gas separation system, including the MIEC membrane module, the dedicated VTSA, cryopumping systems, and the dual-capacity gas pressurizing system are under construction and simulation at $Air\ Liquide$. These efforts aim to validate the models intended for scaling the design to meet ISRU-specific applications, although we have not been updated on the progress of these studies.

It is clear that exploration and colonization of Mars present enormous challenges that extend beyond just reaching the planet. Establishing a sustainable and self-reliant habitat on a foreign world requires innovative technologies and efficient resource utilization strategies. Plasma-based applications, as highlighted, offer a promising avenue for advanced chemical conversion in the challenging Martian environment. The capability to produce life-sustaining chemicals and propellants from Mars atmosphere points to a future where humanity can truly live off Martian land. Research geared toward the advancement of space exploration also provides valuable insight into sustainable practices that

could benefit civilization as a whole. The lessons learned from these endeavors of achieving ISRU on a foreign planet will undoubtedly shape our approach to sustainability and resource management on our home planet.

Bibliography

- [1] J.A. Hoffman, E.R. Hinterman, M.H. Hecht, D. Rapp, and J.J. Hartvigsen. 18 months of MOXIE (Mars oxygen ISRU experiment) operations on the surface of mars preparing for human mars exploration. *Acta Astronautica*, 210:547–553, 2023. doi: 10.1016/j.actaastro.2023.04.045.
- [2] J.A. Hoffman, M.H. Hecht, D. Rapp, J.J. Hartvigsen, J.G. SooHoo, A.M. Aboobaker, J.B. McClean, A.M. Liu, E.D. Hinterman, M. Nasr, S. Hariharan, K.J. Horn, F.E. Meyen, H. Okkels, P. Steen, S. Elangovan, C.R. Graves, P. Khopkar, M.B. Madsen, G.E. Voecks, P.H. Smith, T.L. Skafte, K.R. Araghi, and D.J. Eisenman. Mars Oxygen ISRU Experiment (MOXIE)—preparing for human Mars exploration. Science Advances, 8(35):eabp8636, 2022. doi: 10.1126/sciadv.abp8636.
- [3] K. Fox, A. Johnson, and C. Skelly. NASA's Perseverance Mars rover extracts first oxygen from Red Planet, April 2021. NASA Press Release, April 21, 2021.
- [4] K.W. Engeling and R.P. Gott. Plasma for crewed transit and planetary habitation: Research efforts at kennedy space center. *IEEE Transactions on Plasma Science*, 51 (6):1568–1579, 2023. doi: 10.1109/TPS.2023.3277216.
- [5] S. Kelly, C. Verheyen, A. Cowley, and A. Bogaerts. Producing oxygen and fertilizer with the Martian atmosphere by using microwave plasma. *Chem*, 8(10):2797–2816, 2022. doi: 10.1016/j.chempr.2022.07.015.
- [6] R. Snoeckx and A. Bogaerts. Plasma technology a novel solution for CO₂ conversion? *Chemical Society Reviews*, 46(19):5805–5863, 2017. doi: 10.1039/C6CS00066E.
- [7] V.A. Legasov, V.K. Zhivotov, E.G. Krasheninnikov, M.F. Kroto, B.I. Patrushev, V.D. Rusanov, G.V. Rykunov, A.M. Spektor, A. Fridman, and G.V. Shoiin. A

- nonequilibrium plasma-chemical process of CO₂ dissociation in high-frequency and ultrahigh-frequency discharges. *Soviet Physics Doklady*, 23:44, 1978.
- [8] W.A. Bongers, H.H. Bouwmeester, A.J. Wolf, F.J.J. Peeters, S. Welzel, D. van den Bekerom, N. den Harder, A. Goede, M. Graswinckel, and P.W.C. Groen. Plasmadriven dissociation of CO₂ for fuel synthesis. *Plasma Processes and Polymers*, 14(6): 1600126, 2017. doi: 10.1002/ppap.201600126.
- [9] A.J. Wolf, T.W.H. Righart, F.J.J. Peeters, W.A. Bongers, and M.C.M. Van De Sanden. Implications of thermo-chemical instability on the contracted modes in CO₂ microwave plasmas. *Plasma Sources Science and Technology*, 29(2):025005, 2020. doi: 10.1088/1361-6595/ab5eca.
- [10] P. Viegas, L. Vialetto, A.J. Wolf, F.J.J. Peeters, P.W.C. Groen, T.W.H. Righart, W.A. Bongers, M.C.M. van de Sanden, and P. Diomede. Insight into contraction dynamics of microwave plasmas for CO₂ conversion from plasma chemistry modelling. *Plasma Sources Science and Technology*, 29(10):105014, 2020. doi: 10.1088/1361-6595/abb41c.
- [11] R.R. Wheeler Jr, N.M. Hadley, S.R. Wambolt, J.T. Holtsnider, R. Dewberry, and L.J. Karr. Plasma extraction of oxygen from martian atmosphere. In 45th International Conference on Environmental Systems, 2015.
- [12] G.J.C. Raposo. Plasma in-situ production of fuel and oxygen on Mars. Master's thesis, Técnico Lisboa, 2020.
- [13] H. Lamberts-Van Assche, G. Thomassen, and T. Compernolle. The early-stage design of plasma for the conversion of CO₂ to chemicals: A prospective techno-economic assessment. *Journal of CO₂ Utilization*, 64:102156, 2022. doi: 10.1016/j.jcou.2022. 102156.
- [14] V. Guerra, T. Silva, P. Ogloblina, M. Grofulović, L. Terraz, M.L. da Silva, C.D. Pintassilgo, L.L. Alves, and O. Guaitella. The case for in situ resource utilisation for oxygen production on mars by non-equilibrium plasmas. *Plasma Sources Science and Technology*, 26(11):11LT01, 2017. doi: 10.1088/1361-6595/aa8dcc.
- [15] V. Guerra, T. Silva, N. Pinhão, O. Guaitella, C. Guerra-Garcia, F.J.J. Peeters, M.N. Tsampas, and M.C.M. van de Sanden. Plasmas for in situ resource utilization on

- Mars: Fuels, life support, and agriculture. Journal of Applied Physics, 132(7):070902, 2022. doi: 10.1063/5.0098011.
- [16] Y.B. Zeldvich. The oxidation of nitrogen in combustion and explosions. J. Acta Physicochimica, 21:577, 1946.
- [17] B. Wanten, R. Vertongen, R. De Meyer, and A. Bogaerts. Plasma-based CO₂ conversion: How to correctly analyze the performance? *Journal of Energy Chemistry*, 76:145–158, 2023. doi: 10.1016/j.jechem.2022.10.019.
- [18] K. Wang, S. Ceulemans, H. Zhang, I. Tsonev, Y. Zhang, Y. Long, M. Fang, X. Li, J. Yan, and A. Bogaerts. Inhibiting recombination to improve the performance of plasma-based CO₂ conversion. *Chemical Engineering Journal*, 481:148684, 2024. doi: 10.1016/j.cej.2024.148684.
- [19] T. Kozák and A. Bogaerts. Evaluation of the energy efficiency of CO₂ conversion in microwave discharges using a reaction kinetics model. *Plasma Sources Science and Technology*, 24(1):015024, 2014. doi: 10.1088/0963-0252/24/1/015024.
- [20] L. Vialetto. Modelling of plasma for CO_2 conversion: electron kinetics, chemistry and transport. PhD thesis, Eindhoven University of Technology, 2021.
- [21] A. Bogaerts and G. Centi. Plasma technology for CO₂ conversion: A personal perspective on prospects and gaps. Frontiers in Energy Research, 8:111, 2020. doi: 10.3389/fenrg.2020.00111.
- [22] A. Bogaerts, X. Tu, G. van Rooij, and M.C.M van de Sanden. 28. Plasma-based CO₂ conversion, pages 585–634. De Gruyter, 2019. doi: 10.1515/9783110665147-028.
- [23] I.P. Butylkin, V.K. Zhivotov, E.G., M.F. Krotov, V.D. Rusanov, I.V. Tarasov, and A. Fridman. Plasma-chemical process of CO₂ dissociation in a nonequilibrium microwave discharge. Zhurnal Tekhnicheskoi Fiziki, 51:925–931, 1981.
- [24] J. Gruenwald. Human outposts on Mars: engineering and scientific lessons learned from history. CEAS Space Journal, 6:73–77, 2014. doi: 10.1007/s12567-013-0051-8.
- [25] D. Beaty, S. Borowski, B. Cataldo, J. Charles, C. Conley, D. Craig, J. Elliot, C. Edwards, W. Engelund, D. Eppler, S. Feldman, J. Garvin, S. Hoffman, J. Jones, F. Jordan, S. Klug, J. Levine, J. Mulqueen, G. Noreen, H. Price, S. Quinn, J. Sanders,

- J. Schier, L. Simonsen, G. Tahu, and A. Tripathi. Human exploration of Mars design reference architecture. Technical report, NASA, 2009. URL https://www.nasa.gov/wp-content/uploads/2015/09/373667main_nasa-sp-2009-566-add.pdf.
- [26] J. Conley, D. Lefler, S. Shaw, and A. Marchese. A comparison of preliminary design concepts for liquid, solid and hybrid propelled Mars ascent vehicles using in-situ propellants. In *Third Annual HEDS-UP Forum*, pages 169–185, 2000.
- [27] E. Roncace. In-situ propellant rocket engines for Mars missions ascent vehicle. In 27th Joint Propulsion Conference, page 2445, 1991.
- [28] J.C. Stern, B. Sutter, C. Freissinet, R. Navarro-González, C.P. McKay, P.D. Archer Jr, A. Buch, A.E. Brunner, P. Coll, and J.L. Eigenbrode. Evidence for indigenous nitrogen in sedimentary and aeolian deposits from the curiosity rover investigations at gale crater, Mars. *Proceedings of the National Academy of Sciences*, 112(14): 4245–4250, 2015. doi: 10.1073/pnas.1420932112.
- [29] D. Elizabeth P.S. Kasiviswanathan, L.J. Halverson, and P. Vijayapalani. Farming on Mars: Treatment of basaltic regolith soil and briny water simulants sustains plant growth. *PLoS One*, 17(8):e0272209, 2022. doi: 10.1371/journal.pone.0272209.
- [30] A.F. Davila, D. Willson, J.D. Coates, and C.P. McKay. Perchlorate on Mars: a chemical hazard and a resource for humans. *International Journal of Astrobiology*, 12(4):321–325, 2013. doi: 10.1017/S1473550413000189.
- [31] J. Wadsworth and C.S. Cockell. Perchlorates on Mars enhance the bacteriocidal effects of UV light. Scientific Reports, 7(1):4662, 2017. doi: 10.1038/ s41598-017-04910-3.
- [32] J. Heinz, J. Doellinger, D. Maus, A. Schneider, P. Lasch, H-P Grossart, and D. Schulze-Makuch. Perchlorate-specific proteomic stress responses of debaryomyces hansenii could enable microbial survival in Martian brines. *Environmental Microbiology*, 24(11):5051–5065, 2022. doi: 10.1111/1462-2920.16145.
- [33] F. Raganati, F. Miccio, and P. Ammendola. Adsorption of carbon dioxide for post-combustion capture: a review. *Energy & Fuels*, 35(16):12845–12868, 2021. doi: 10.1021/acs.energyfuels.1c00740.

- [34] W. Liu, Y. Huang, X.J. Zhang, M.X. Fangand, X. Liu, T. Wang, and L. Jiang. Steam-assisted temperature swing adsorption for carbon capture integrated with heat pump. Case Studies in Thermal Engineering, 49:103233, 2023. doi: 10.1016/j.csite. 2023.103233.
- [35] I.A.A.C. Esteves and J.P.B Mota. Simulation of a new hybrid membrane/pressure swing adsorption process for gas separation. *Desalination*, 148(1-3):275–280, 2002. doi: 10.1016/S0011-9164(02)00704-6.
- [36] L-Q Zhu, J-L Tu, and Y-J Shi. Separation of CO, CO₂, N₂ gas mixture for high-purity CO by pressure swing adsorption. Gas Separation & Purification, 5(3):173–176, 1991. doi: 10.1016/0950-4214(91)80023-9.
- [37] J.W. Yoon, T-U Yoon, E-J Kim, A-R Kim, T-S Jung, S-S Han, and Y-S Bae. Highly selective adsorption of CO over CO₂ in a Cu(I)-chelated porous organic polymer. *Journal of Hazardous Materials*, 341:321–327, 2018. doi: 10.1016/j.jhazmat.2017.07. 074.
- [38] S. Kolbadinejad, H. Mashhadimoslem, A. Ghaemi, and M. Bastos-Neto. Deep learning analysis of Ar, Xe, Kr, and O₂ adsorption on activated carbon and zeolites using ANN approach. *Chemical Engineering and Processing-Process Intensification*, 170: 108662, 2022. doi: 10.1016/j.cep.2021.108662.
- [39] S. Baumann, J.M. Serra, M.P. Lobera, S. Escolástico, F. Schulze-Küppers, and W.A. Meulenberg. Ultrahigh oxygen permeation flux through supported $Ba_{0.5}Sr_{0.5}Co_{0.8}Fe_{0.2}O_{3-\delta}$ membranes. *Journal of Membrane Science*, 377(1-2):198–205, 2011. doi: 10.1016/j.memsci.2011.04.050.
- [40] G. Chen, A. Feldhoff, A. Weidenkaff, C. Li, S. Liu, X. Zhu, J. Sunarso, K. Huang, X-Y Wu, and A.F. Ghoniem. Roadmap for sustainable mixed ionic-electronic conducting membranes. Advanced Functional Materials, 32(6):2105702, 2022. doi: 10.1002/adfm.202105702.
- [41] E.R. Mercer, S. van Alphen, C.F.A.M. van Deursen, T.W.H. Righart, W.A. Bongers, R. Snyders, A. Bogaerts, M.C.M. van de Sanden, and F.J.J. Peeters. Post-plasma quenching to improve conversion and energy efficiency in a CO₂ microwave plasma. Fuel, 334:126734, 2023. doi: 10.1016/j.fuel.2022.126734.

- [42] C.F.A.M. van Deursen, H.M.S. Van Poyer, W.A. Bongers, F.J.J. Peeters, F.M.A. Smits, and M.C.M. van de Sanden. Effluent nozzles in reverse-vortex-stabilized microwave CO₂ plasmas for improved energy efficiency. *Journal of CO₂ Utilization*, 88: 102952, 2024. doi: 10.1016/j.jcou.2024.102952.
- [43] J. Van Noyen, V. Middelkoop, C. Buysse, A. Kovalevsky, F. Snijkers, A. Buekenhoudt, S. Mullens, J. Luyten, J. Kretzschmar, and S. Lenaerts. Fabrication of perovskite capillary membranes for high temperature gas separation. *Catalysis Today*, 193(1):172–178, 2012. doi: 10.1016/j.cattod.2012.03.062.
- [44] S. Engels, T. Markus, M. Modigell, and L. Singheiser. Oxygen permeation and stability investigations on MIEC membrane materials under operating conditions for power plant processes. *Journal of Membrane Science*, 370(1):58–69, 2011. doi: 10.1016/j.memsci.2010.12.021.
- [45] M. Arnold, H. Wang, and A. Feldhoff. Influence of CO₂ on the oxygen permeation performance and the microstructure of perovskite-type (Ba_{0.5}Sr_{0.5})(Co_{0.8}Fe_{0.2})O_{3-δ} membranes. Journal of Membrane Science, 293(1-2):44-52, 2007. doi: 10.1016/j. memsci.2007.01.032.
- [46] V. Maiwald, D. Schubert, D. Quantius, and P. Zabel. From space back to Earth: supporting sustainable development with spaceflight technologies. *Sustainable Earth*, 4(1):3, 2021. doi: 10.1186/s42055-021-00042-9.
- [47] U.A.L. Betz, L. Arora, R.A. Assal, H. Azevedo, J. Baldwin, M.S. Becker, S. Bostock, V. Cheng, T. Egle, and N. Ferrari. Game changers in science and technology-now and beyond. *Technological Forecasting and Social Change*, 193:122588, 2023. doi: 10.1016/j.techfore.2023.122588.
- [48] D. Premathilake, R.A. Outlaw, R.A. Quinlan, and C.E. Byvik. Oxygen generation by carbon dioxide glow discharge and separation by permeation through ultrathin silver membranes. *Earth and Space Science*, 6(4):557–564, 2019. doi: 10.1029/2018EA000406.

Chapter 6

Conclusions and Future Outlook

This thesis has advanced MW plasma technology for carbon utilization with a dual focus on terrestrial decarbonization via CO₂ conversion and interplanetary ISRU. Through a series of experiments, we demonstrated that by leveraging thermal management, chemical quenching strategies, and low-pressure operation, marked improvements to both conversion and energy efficiency can be obtained. Furthermore, the fundamental insights gained through this work reveal that strategic thermal management plays a pivotal role in enhancing CO₂ conversion performance.

Chapter 3 showed the effect of inlet gas preheating, which demonstrate that expanding the reactive volume, i.e., the region where temperatures exceed CO₂ dissociation thresholds (>>1500 K), directly correlates with improved conversion, particularly at higher pressures. This relationship between temperature distribution and conversion challenges the conventional understanding of contracted plasma behavior by highlighting how upstream thermal conditions influence downstream reactive chemistry. Importantly, our findings reveal distinct pressure-dependent responses to preheating.

- Preheating is most beneficial at higher pressures (> 300 mbar), where plasma is fully contracted, and substantially benefits conversion by expanding the spatial temperature profile.
- Preheating negatively affects performance at lower pressures (< 300 mbar), as contraction dynamics cause a smaller reactive volume by decreasing the radial temperature profile.

This pressure-dependent behavior reveals that gas density and flow dynamics critically determine spatial temperature distribution beyond what electron density alone would predict. The high-temperature reactive volume in which CO₂ dissociation dominates is not limited to the plasma volume as defined by electronically excited species emission but extends into regions where thermal processes continue to drive chemistry.

Of course, these insights into thermal management extend beyond preheating, specifically with afterglow quenching strategies. Chapter 4 investigated a dual injection configuration, in which CH₄ is introduced as a reactive quenching agent into the afterglow region, demonstrating a significant increase to CO₂ conversion compared to a pure CO₂ plasma. This enhancement remains consistent across various secondary injection flow rates of CH₄, and at varying pressure, specifically, the decrease in performance normally observed at higher pressure in CO₂ plasma is eliminated. Chemical kinetics modeling carried out by Matthias Albrechts reveals underlying mechanisms, showing that CH₄ injection enhances conversion through complementary pathways.

- Reactive quenching with CH₄ allows for effective scavenging of oxygen that would otherwise participate in CO recombination reactions.
- Additional CO₂ conversion is obtained via the Reverse Water-Gas Shift (RWGS) reaction, extending higher conversion to atmospheric pressure.

This enhancement remains consistent across various secondary injection flow rates of CH₄ and varying pressures due to the lack of pressure dependence of the RWGS reaction. Importantly, the decrease in performance normally observed at higher pressure in CO₂ plasma is eliminated through reactive quenching. The model also compared our results from reactive quenching with CH₄ to thermal quenching with Ar. This revealed that upon injection, CH₄ reduces the destruction of CO from $\sim 30\%$ (as observed with Ar) to < 1%, while simultaneously providing additional CO₂ conversion through the RWGS reaction, highlighting the importance of chemical quenching over thermal quenching approaches.

This demonstrates that post-plasma CH₄ injection effectively mitigates the recombination processes that typically limit CO₂ conversion at higher pressures, by CH₄ acting as an O or O₂ scavenger, which has been found to enhance back reactions to CO₂. This highlights the promise of reactive quenching as an approach for enhancing conversion. Again, showing that effective thermal management plays a central role in enhancing CO₂ conversion.

Our findings suggest several promising avenues for future research and development. A logical next approach is through integrated heat recovery systems, which could not only enhance overall system efficiency by recycling thermal energy but also provide insights into whether preheating and quenching strategies can be combined. Our preheating experiments demonstrate that redirecting even small portions of input power (< 14%) for preheating significantly improves energy efficiency and conversion. Implementing heat recovery from downstream processes could thus substantially enhance industrial system performance, potentially extending high-efficiency operation to atmospheric conditions.

As discussed in Chapter 3, preheating CO₂ can come from any downstream process and doesn't necessarily need to be coupled to the effluent gas directly. Therefore, it is interesting to consider the effect of enhanced recombination observed at higher inlet temperatures (i.e., 850 K); this excess heat has the potential to be utilized for reactive quenching, mitigating the enhanced downstream recombination. This approach might result in a lower specific energy input requirement for the system while still increasing the afterglow temperatures needed for higher CH₄ dissociation. The observed pressure-dependent effects of preheating suggest that combining optimal inlet temperature with effective downstream quenching could create a more favorable temperature profile throughout the reactor, maximizing conversion while minimizing energy consumption.

In Chapter 5, we investigated MW plasma performance under Martian atmosphere conditions, which demonstrated that the natural low-pressure environment of Mars (approximately 7 mbar) creates ideal conditions for efficient conversion. The low pressure on Mars naturally complements MW plasma-based conversion by mitigating recombination and possibly favoring vibrationally driven (CO_2 and N_2) dissociation pathways. The Martian atmosphere, composed of approximately 96% CO_2 , presents an ideal feedstock for resource utilization using MW plasma reactors. The demonstrated synergy between low-pressure MW discharges and CO_2 conversion indicates that plasma technology could serve as a valuable complementary approach to electrochemical techniques, like MOXIE, in the Martian environment. Based on the experimental performance metrics observed under simulated Martian conditions, we conclude that MW plasma technology represents a highly promising candidate for ISRU applications on Mars, capable of efficiently producing essential resources such as O_2 , CO, and NO_x from the native atmosphere.

The promising results obtained from our simulated Martian atmosphere experiments reveal significant potential for specialized low-pressure MW plasma applications, yet several fundamental aspects remain unexplored. A critical next step would be to develop a deeper understanding of the mechanisms behind the enhanced performance metrics observed under Martian conditions. Specifically, characterizing the temperature profiles and plasma contraction state at near-Martian atmospheric pressure would provide crucial insights for optimizing system performance. It has been shown that contraction dynamics fundamentally determine both peak temperatures and thermal gradients within the reactive volume, directly influencing conversion and energy efficiency. Additionally, systematically investigating the role of trace gases in the Martian atmosphere, particularly Ar and N₂, could reveal important synergistic effects in plasma-chemical processes. Such investigations would not only advance ISRU technology development for Mars missions but could also inform plasma-based gas conversion applications on Earth, particularly in scenarios where reduced-pressure operation might be advantageous.

The deeper insights garnered from this research enhances our understanding of MW plasma-based CO₂ conversion and points toward promising directions for future development. The insights gained demonstrate that the performance limitations traditionally observed in MW plasma systems can be addressed through strategic approaches to thermal management and flow dynamics, offering pathways toward more efficient and selective processes for both terrestrial and extraterrestrial applications.

Beyond these specific research directions, our work highlights the importance of understanding the interplay between MW engineering, plasma chemistry, and flow dynamics. Across all experimental investigations, the critical thread shows that control over the flow topology in relation to the plasma's thermal and chemical gradients is key to enhancing conversion and energy efficiency. Flow effects on contraction dynamics, or in the case of reactive quenching with dual injection, highlight that carefully managing flow and cooling trajectories greatly affects downstream recombination processes, the reactive volume profile, and overall system efficiency. Advancing our understanding of flow configurations and heat recovery will be crucial to moving toward industrialization. Furthermore, the distinction drawn between plasma volume and reactive volume challenges conventional reactor design approaches, suggesting that optimizing temperature distribution rather than solely focusing on power and flow input could yield more efficient and selective processes. Similarly, the pressure-dependent response to thermal management techniques indicates

that process designs should be tailored to specific operating conditions rather than applying universal approaches. Succinctly, the interplay of flow dynamics, pressure, and power density is key to scale-up.

In conclusion, this thesis has demonstrated that MW plasma technology offers remarkable versatility and potential for addressing global challenges related to resource utilization. The insights gained through this research also have broader implications for sustainable chemical processing. The ability to strategically manage thermal energy and flow dynamics to enhance conversion and selectivity while minimizing unwanted byproducts aligns with the principles of green chemistry. By systematically investigating the effects of thermal management, reactive quenching, and pressure on plasma performance, we have identified key mechanisms that govern conversion and efficiency, providing both fundamental insights and practical guidelines for future development. The pathways identified offer promising directions for advancing MW plasma technology toward industrial implementation, contributing to a more sustainable future here on Earth and beyond.

Appendix A

Thermal Management: Enhancing Efficiency Through Preheating

The work presented in this chapter was carried out at the Dutch Institute for Fundamental Energy Research, in collaboration with the Plasma for Solar Fuels Devices group under the guidance of Prof. Dr. Ir. Richard van de Sanden, and is in co-first authorship with my esteemed colleague, Cas van Deursen.

This chapter is derived from the following publication:

Preheating applied on a 915 MHz CO₂ Microwave Plasma::
 Unlocking the Potential for Heat Recycling in Plasma Systems
 E.R. Mercer* & C.F.A.M. van Deursen*, F.J.J. Peeters, W.A. Bongers, F.M.A. Smits,
 M.C.M. van de Sanden** & A. Bogaerts** (Submitted Manuscript)

A.1 Analysis of Thermal Losses

We utilize Infrared (IR) thermography to gain insight into the thermal losses in the CO_2 MW reactor. These losses can be split into two different terms: radiative and convective. The radiative losses were calculated using Stefan Boltzmann's law (A.1), with the emissivity of the quartz tube being the same as used in the work of van Deursen et al. [1]:

$$P = A\varepsilon\sigma(T_{QT}^{4} - T_{amb}^{4}) \tag{A.1}$$

in which P is the radiated power (W), A is the surface area of the radiating body (m²), ε = emissivity of the radiating body (-), σ is the Stefan Boltzmann constant, T_{QT} is the temperature of the quartz tube (K), and T_{amb} is the ambient temperature of the room (K).

The heat loss (W) through free convection (Q) was calculated according to A.2:

$$Q = hA(T_{QT} - T_{amb}) (A.2)$$

in which A is the surface area over which convection takes place (m²), h is the average heat transfer coefficient (W/m²K) which can be calculated using A.3.

$$h = \frac{Nu \cdot k}{H} \tag{A.3}$$

in which k is the thermal conductivity of air (W/m · K), H is the Height of the tube (m), and Nu is the Nusselt number (-). In all cases in Chapter 3, the airflow outside the quartz tube is considered laminar (Ra $< 10^9$), so Nu can be calculated as:

$$Nu = \frac{0.68 + (0.67Ra^{\frac{1}{4}})}{\left[1 + \left(\frac{0.492}{\Pr}\right)^{\frac{9}{16}}\right]^{\frac{4}{9}}}$$
(A.4)

in which Pr is the Prandtl number (-) and Ra is the Rayleigh number (-).

The value of Pr is calculated according to:

$$Pr = \frac{\nu}{\kappa} \tag{A.5}$$

in which ν is the kinematic viscosity of air (m²s⁻¹), and κ is the thermal diffusivity (m²s⁻¹) of air of the so-called film temperature (T_f, see A.8). The Ra number is calculated as:

$$Ra = Gr \cdot Pr \tag{A.6}$$

where Gr is the Grashof number (-) can be calculated according to:

$$Gr = \frac{G \cdot \alpha \cdot (T_{QT} - T_{amb}) \cdot H^3}{\nu^2} \tag{A.7}$$

in which G is gravitational acceleration (m s⁻²), and α is the expansion coefficient of air (K⁻¹). Furthermore, it is important to note that the fluid properties used in the above formulas should be that of the T_f , which is calculated as follows:

$$T_f = \frac{T_{QT} + T_{amb}}{2} \tag{A.8}$$

with all variables defined above. The calculated radiative and convective losses can then be added together to give the total thermal losses over the quartz tube inside the waveguide, where losses are the largest.

A.2 Thermometric Probes

A.2.1 Optical Emission Spectroscopy Data Treatment

Optical Emission Spectroscopy (OES) measurements were performed to characterize the plasma emission. The acquired spectral data underwent a comprehensive treatment process to ensure accurate quantitative analysis. This section details the step-by-step methodology employed for data processing and analysis.

A.2.1.1 Raw Data Acquisition and Pre-Processing

Spectral measurements were conducted using a USB spectrometer with a wavelength range of 180 – 900 nm. The optical setup (Figure 3.2, Chapter 3) included a focal length of 540 mm and an iris opening of 11.7 mm, which was used to calculate the solid angle of collection. Dark current measurements were acquired for each integration time to account for detector background noise. Raw spectral data underwent dark current subtraction to eliminate detector background noise. The wavelength axis was calibrated using a quadratic correction function:

$$\lambda_{corrected} = ax^2 + bx + c \tag{A.9}$$

where x represents the measured wavelength, and the coefficients (a = -2.797×10⁻⁶, b = 1.003, c = -0.067) were determined through calibration with known spectral lines. This correction compensates for any systematic deviations in the wavelength scale of the spectrometer.

The spectral intensity was calibrated using a reference standard lamp with known spectral radiance. The calibration process involved: 1) Converting raw counts to absolute spectral radiance using calibration factors derived from the reference lamp measurements; 2) Accounting for varying integration times and detector response; 3) Applying solid angle corrections based on the optical geometry. The calibration factors were interpolated across the full wavelength range to ensure continuous correction of the spectral response.

To account for varying integration times used during measurements, the spectral data was normalized $(I(\lambda)_{normalized})$ according to:

$$I(\lambda)_{normalized} = \frac{I(\lambda)_{measured}}{t_{integration}}$$
(A.10)

where $I(\lambda)_{measured}$ is the calibrated intensity and $t_{integration}$ is the integration time in milliseconds (ms). This normalization enables direct comparison between spectra acquired with different exposure times.

The radial emission profile was reconstructed using Abel inversion. The process involved determining the plasma center through fitting a double Gaussian function to the emission profile at 777 nm, an example is shown in *Figure A.1* [2].

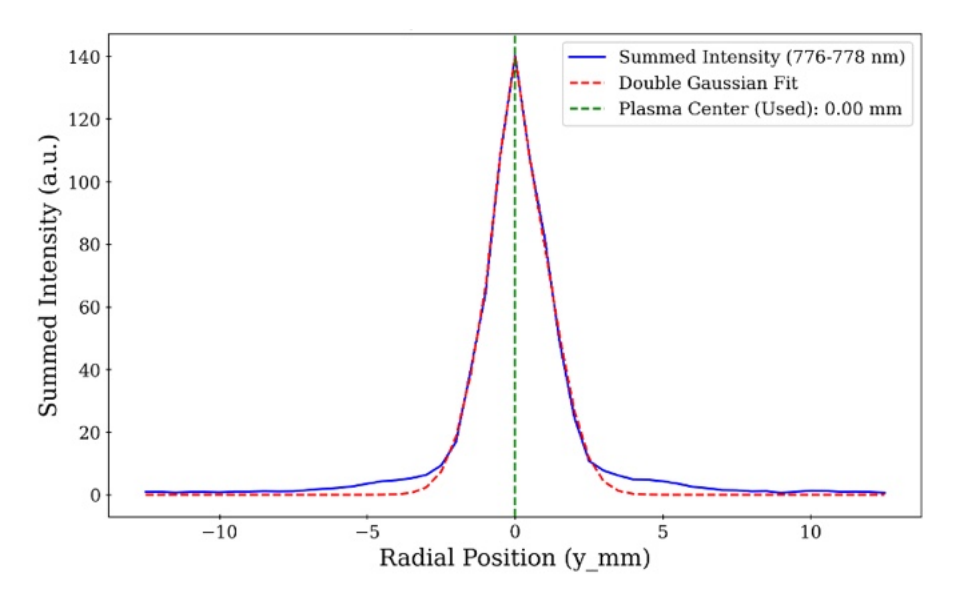


Figure A.1: Summed intensity with double Gaussian fit using the 777 nm emission intensity.

The emission spectra were centered around this determined axis to ensure any offset of captured spectra was corrected. Finally, the Hansen-Law Abel inversion algorithm was applied to reconstruct the radial emission profile ($Figure\ A.2$). The Hansen-Law method was chosen for its stability in handling experimental noise without requiring numerical differentiation of the data. The inversion assumes cylindrical symmetry of the plasma emission.

The calibrated and Abel-inverted spectra were converted to photon flux using the relationship:

$$\Phi(\lambda) = \frac{I(\lambda) \cdot \lambda}{h \cdot c} \tag{A.11}$$

where $\Phi(\lambda)$ is the photon flux at wavelength λ , $I(\lambda)$ is the normalized, calibrated intensity, h is Planck's constant, and c is the speed of light. This conversion provides the absolute number of photons emitted per unit area (photons s⁻¹ m⁻²) and time at each wavelength.

Figure A.3 shows an example spectrum after the preprocessing treatment outlined in this section.

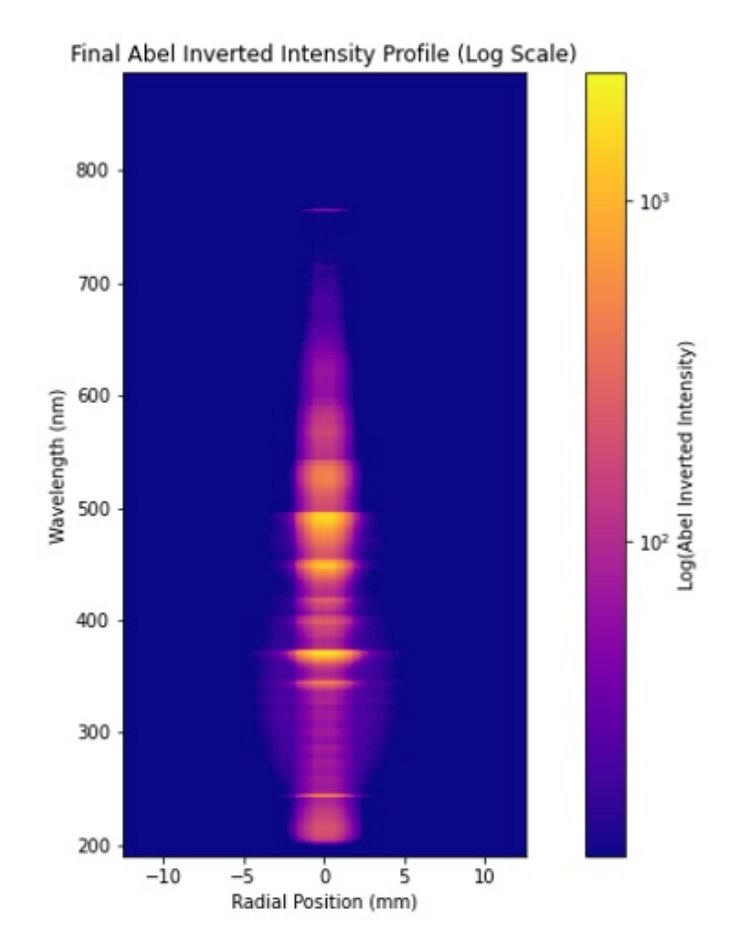


FIGURE A.2: Abel-inverted intensity profile in logarithmic scale.

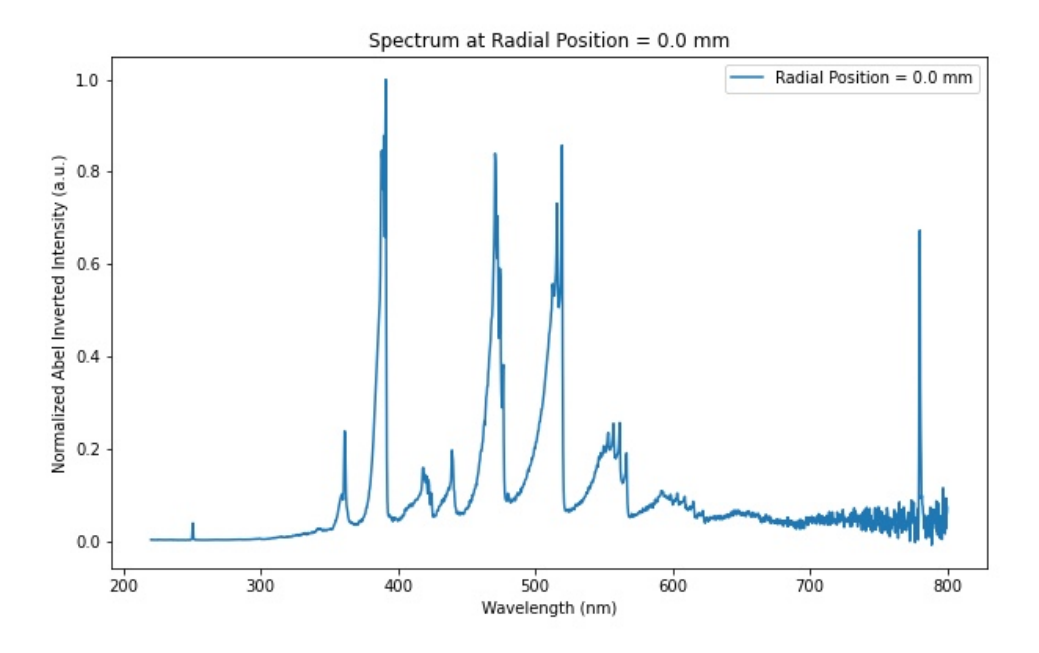


FIGURE A.3: Example spectrum after preprocessing treatment.

A.2.1.2 Uncertainty Considerations

The integrating sphere calibration certificate gives an expanded uncertainty (k = 2), with a range between 0.88 - 1.88% and a mean of 1.19%. We also account for the calibration of the spectrometer while considering possible variations of alignment, temperature, and current stability, uncertainty in each integration time (taken between 1 – 2000 ms), which we estimate to add between $\sim 1-2\%$ uncertainty to our measurement. Therefore, we consider the combined calibration uncertainty to be: $\sqrt{1.19^2 + 1.5^2} = 1.9\%$.

The quadratic fit coefficients (a = -2.797×10^{-6} , b = 1.003, c = -0.067) showed excellent alignment with our data, with a deviation from unity in the linear term (b = 1.003) suggesting wavelength accuracy better than 0.4%.

Dark current subtraction performed for each integration time eliminates systematic bias, and using multiple integration times and normalizing helped reduce random noise; therefore, we estimate the uncertainty to be < 2%.

The optical collection and geometry were well defined in terms of the iris radius (11.7 mm) and focal length (540 mm); therefore, we assume precise calculation of the solid angle, 1.47×10^{-3} sr, with these fixed parameters, and estimate the contribution to our uncertainty to < 1%.

The Hansen-Law method was chosen specifically for stability, and the use of a double-Gaussian fitting for the plasma center determination helps to reduce asymmetries that might occur due to fluctuations in the position of the plasma filament. The assumption of symmetry is further validated by the quality of our fits, which generally showed residuals under 10%. Therefore, we assume the contribution to systematic uncertainty < 3%.

The total uncertainty in the spectra is estimated to be approximately 4.2%. This estimation is derived from quadrature addition of the following components: base calibration uncertainty (1.9%, determined from calibration certificate with k=2 expanded uncertainty of 1.19% and transfer calibration), wavelength calibration (0.4%), detector response (< 2%), optical collection geometry (1%), and Abel inversion process (< 3%). The relatively low total uncertainty is supported by the high quality of the calibration standard (uncertainty range 0.88 - 1.88%) and the implementation of the Hansen-Law method for Abel inversion, as described above.

The data treatment procedure was implemented using Python, utilizing specialized libraries including NumPy for numerical operations, SciPy for signal processing and optimization, and the PyAbel package for Abel inversion. Finally, a Savitzky-Golay filter was applied to reduce noise while preserving spectral features. All raw and processed data were systematically archived to ensure the reproducibility of the analysis.

A.2.2 C₂ Swan Band as a Thermometric Probe using Massive OES

The C₂ $(d^3\Pi_g - a^3\Pi_u)$ Swan band system was analyzed to determine rotational (T_{rot}) and vibrational temperatures (T_{vib}) using the open-source MassiveOES software package, with the relative intensities of these transitions governed by Boltzmann distributions when in thermal equilibrium [3]. The spectral fitting was performed using MassiveOES, which employs a least-squares optimization algorithm to fit synthetic spectra to the experimental data. The $\Delta v = 0$ sequence of the Swan band system was primarily used for determining rotational temperatures, as this region shows the highest sensitivity to T_{rot} .

The uncertainty in the derived temperatures comes from the statistical uncertainty from the fitting routine, estimated through the covariance matrix of the least-squares optimization, uncertainty in molecular constants and transition probabilities, which are estimated to be < 2%, and fitting convergence verification through residual analysis and multiple starting conditions. The reliability of the temperature determination was verified by examining the residuals between experimental and simulated spectra, ensuring no systematic deviations that would indicate non-Boltzmann behavior or other spectroscopic artifacts. The fitting routine showed good convergence across the analyzed dataset. Deviations between T_{rot} and T_{vib} that exceeded 1500 K were excluded from the reported values.

To assess additional uncertainties beyond the residual fitting error, we leveraged the expected radial symmetry of the discharge. Measurements from one side of the centerline (r=0 mm) were reflected and compared against the measurements from the opposite side. The temperature differences between the measured and reflected profiles were incorporated into the total error.

A.2.3 Flame Band Emission Model

Flame band emission spectroscopy was utilized as a secondary temperature diagnostic to capture the periphery temperature surrounding the core plasma region. Flame band spectroscopy measures the emission intensity from the radiative transition of excited CO_2 to ground-state CO_2 after recombination [4]. All spectra were preprocessed using the methods outlined in Section A.2.1. The base of the theoretical background is presented in Chapter 2, Section 2.4.2.

A.2.3.1 Flame Band Fitting Routine and Model Implementation

The fitting routine employs a wavelength-dependent Arrhenius model calibrated using empirical data from spectroscopic measurements combined with independent temperature measurements via rotational Raman scattering [4]. The model incorporates wavelength-dependent activation energies (E_a^{λ}) ranging from ~1100 K at $\lambda > 400$ nm to ~5800 K in the UV region, pre-exponential factors (κ_0^{λ}) following a power law relationship: $\kappa_0^{\lambda} \approx 2.78 \times 10^{-16} \times \lambda^{-4.21}$, and contributions from O₂ Schumann-Runge emission for T > 1500 K. Additional details on the theoretical framework of this approach is outlined in Raposo et al. [4].

The spectral fitting process follows an initial parameter estimation for the temperature (T), intensity scaling factor, and O_2 contribution scale (for T > 1500 K). The optimization uses a least-squares algorithm that minimizes the residuals between the measured spectrum and the model prediction, while accounting for the wavelength-dependent sensitivity and signal-to-noise across the spectral range.

Some known spectral peaks were excluded in the fit (e.g., 360-365 nm, 370-395 nm, 460-480 nm, 505-520 nm, 540-565 nm), and can be observed in Figure A.4 as greyed regions. All fits reported in Chapter 3 had an $R^2 > 0.95$, ensuring that the models accurately captured the spectral features with minimal residual variance, consistent with established standards for reliable quantitative analysis [5].

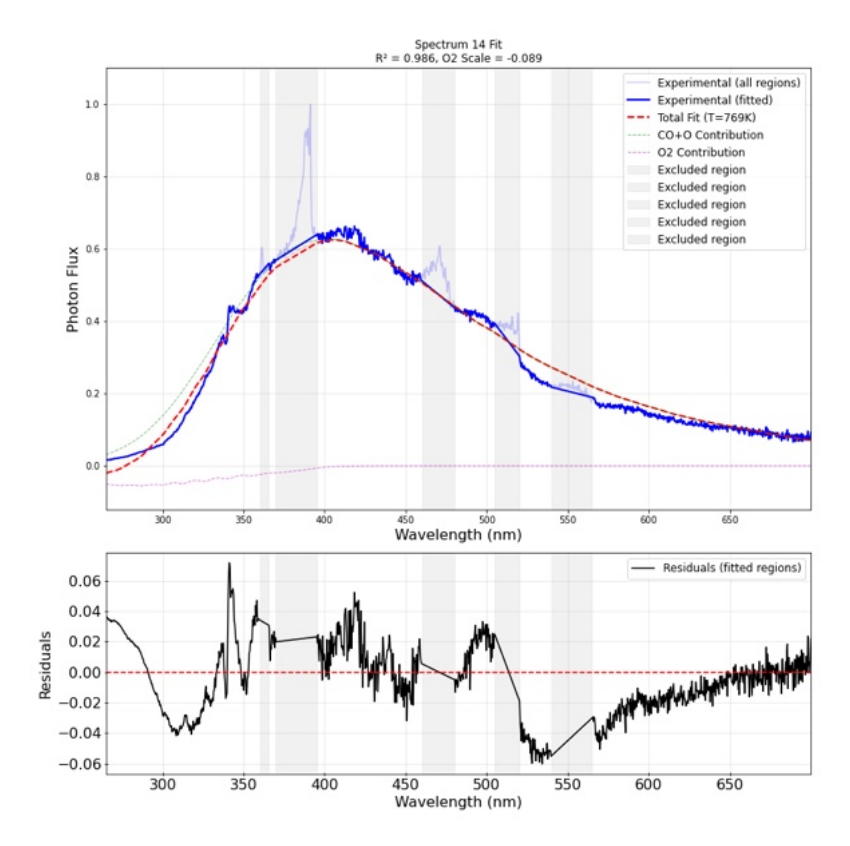


Figure A.4: Example of a fit from $P_{MW}=1000~W,\,T_{\rm inlet}=700~K,\,p=700~mbar,$ mass flow rate = 10~ln/min.

A.2.3.2 Model Limitations

The primary limitation of this spectroscopic method lies in its temperature range validity, which is effectively constrained to below 1500 K. At temperatures exceeding this threshold, the spectral analysis becomes complicated by the emergence of O_2 Schumann-Runge emission bands (180 - 450 nm). The intensity of O_2 emission scales with both the O_2 molar fraction and the CO + O chemiluminescence, introducing additional uncertainty in conditions where O_2 concentrations are not well-characterized or vary significantly with temperature.

The spectral shape exhibits significant temperature dependence, characterized by a systematic shift of the intensity maximum toward shorter wavelengths with increasing temperature, changes in the relative intensities of different spectral regions, and varying contributions from different vibrational levels of the excited states. These effects are empirically accounted for through wavelength-dependent Arrhenius parameters, but the underlying quantum mechanical processes are not fully characterized. The pre-exponential factor (κ_0^{λ}) follows an empirically determined power law, which encompasses changes in natural

radiative lifetimes, quenching probabilities for different excited states, and populations distribution among vibrational levels [4, 6].

The model assumes complete thermalization of the $CO_2(^1B)$ state prior to photon emission, which is supported by collision frequency calculations. At typical operating pressures (> 100 mbar), the time between molecular collisions (< 2 ns) is significantly shorter than the natural radiative lifetime of the $CO_2(^1B)$ state (~200 ns) [6, 7]. However, this introduces pressure-dependent considerations, such as at pressures \ll 100 mbar, where incomplete thermalization may occur, as discussed in Chapter 2, Section 2.4.3. Although these conditions are out of the scope of Chapter 3, where pressure was kept above 200 mbar, they should be considered with future research.

A.2.3.3 Analytical Uncertainties

The total uncertainty in the fitted temperature incorporates systematic components of absolute calibration uncertainties, wavelength-dependent detector response, and optical system throughput variations, discussed in *Section 2.1.2* above. Statistical analysis of the spectral noise propagation, fitting residuals, and parameter correlation effects were utilized in calculating the analytical uncertainty. The temperature uncertainty is calculated using:

$$\delta T = \frac{\delta S}{\frac{dS}{dT}} \tag{A.12}$$

where δS represents the RMS residual and $\frac{dS}{dT}$ is the numerical derivative of the spectrum with respect to temperature.

A.2.3.4 Method Validation

The fitting routine has been validated against independent rotational Raman temperature measurements, literature data for CO flame band emission, and theoretical predictions of spectral features, which have been outlined extensively by $Raposo\ et\ al..$ [4]. Typical uncertainties in the fitted temperatures range from 5-10%. The method provides reliable temperature measurements in the range of $300-1500\ K$, with increasing uncertainty above this range due to the growing contribution of O_2 Schumann-Runge emission; however, the

fitted results did not reveal temperatures above 1000 K for all data (cf. Figure 3.5 in Chapter Three).

A.3 Analytical Techniques and Performance Indicators

We utilized Gas Chromatography (GC) to measure the composition of the post-plasma effluent mixture. From this, the degree of dissociation (conversion, χ) can be calculated using the following formula, which accounts for gas expansion due to the reaction of CO₂ splitting into CO and $\frac{1}{2}$ O₂ [8]:

$$\chi = \frac{1 - y_{\text{CO}_2}^{\text{out}}}{1 + \frac{y_{\text{CO}_2}^{\text{out}}}{2}}$$
 (A.13)

where $y_{\text{CO}_2}^{\text{out}}$ represents the output fraction of CO_2 taken from the GC measurements, with which we calculate the energy efficiency, η , as follows:

$$\eta = \chi \frac{\Delta H_f}{\text{SEI}} \tag{A.14}$$

where ΔH_f is the formation enthalpy (2.93 eV/molecule) of the net reduction reaction of CO₂ to CO, and SEI is the Specific Energy Input (SEI = $\frac{\phi}{P_{\rm MW}}$), both given in the same units, e.g., eV/molecule. For the calculation of the SEI reported in this work, only the MW power is accounted for, not the power to heat CO₂, we consider this as a 'free parameter' in the case of heat recycling.

A.3.1 Conversion Measurements

All conversions reported in this work were determined using a G.A.S. CompactGC 4.0. Samples were taken through a sampling line through which a small part of the effluent was continually flowed, ensuring representative sampling of the plasma exhaust. The GC uses three separate loops, all shown in *Table A.1*.

The effluent composition was then determined from the resultant chromatograms. In order to assess the accuracy of the measurements, the 95% confidence interval of each

Length - ID Column Length - ID Pre-column Species Loop Rt-Q-Bond 4 m - 0.32 mmTC-Molsieve 5A 10 m - 0.53 mm CO_2 1 2 m - 0.32 mmCP-PoraBOND Q 20 m - 0.32 mm2 Rt-Q-Bond CO, O_2, N_2 Rt-Q-Bond 3 m - 0.32 mmTC-Molsieve 5A 10 m - 0.53 mm3 H_2 (not used)

TABLE A.1: Specifications of the loops inside the GC and detected species on each channel.

composition determination was calculated according to equations A.E15 - A.E17, taken from [9].

$$S_{x_{\text{sample}}} = \frac{S_{y/x}}{b} \cdot \sqrt{\frac{1}{m} + \frac{1}{n} + \frac{(y_{\text{sample}} - y_{\text{avg}})^2}{b^2 \cdot \sum_i (x_i - x_{\text{avg}})^2}}$$
 (A.15)

$$x_{\text{sample}} = \frac{(y_0 - a)}{b} \tag{A.16}$$

$$CI_{95} = x_{\text{sample}} \pm t_{(n-2)} \cdot S_{x_{\text{sample}}}$$
(A.17)

in which the standard deviation $(S_{x_{\text{sample}}})$ of each measured component was calculated using the standard deviation of the calibration standards $(\frac{S_{y/x}}{b})$, the slope of the regression line (b), the number of replicas of the measurement (m), the number of calibration standards (n), the response value of the measurement (y_{sample}) , the average response of the calibration standards (y_{avg}) , the concentration (in %) of standard (x_i) , the average concentration (in %) of all standards (x_{avg}) . x_{sample} was determined using the intercept $(y_0 - a)$ and slope of regression line. The student t-value for a two-tailed distribution at n degrees of freedom $(t_{(n-2)})$ was used to determine the 95% confidence interval, which was used to calculate the propagation of errors of the performance metrics reported in this work.

A.4 Power to Heat CO₂

Since the specific heat of CO_2 is not linear with respect to temperature, the power to each standard liter per minute (slm) of CO_2 was calculated using the following formula:

$$\Delta Q = \dot{m} \int_{T_i}^{T_f} C_{p_{\text{CO}_2}}(T) \ dT \tag{A.18}$$

where $C_{p_{\text{CO}_2}}(\text{kJ} \cdot (\text{kg K})^{-1})$ is the specific heat of CO_2 at a given temperature, T (K) is the temperature, and \dot{m} is the mass flow rate of 1 normal liter per minute (ln/min) of CO_2 (3.23 × 10⁻⁵ kg·s⁻¹), as shown in Figure A.5. The power values were calculated from 300 K, using different sources for the specific heat of CO_2 .

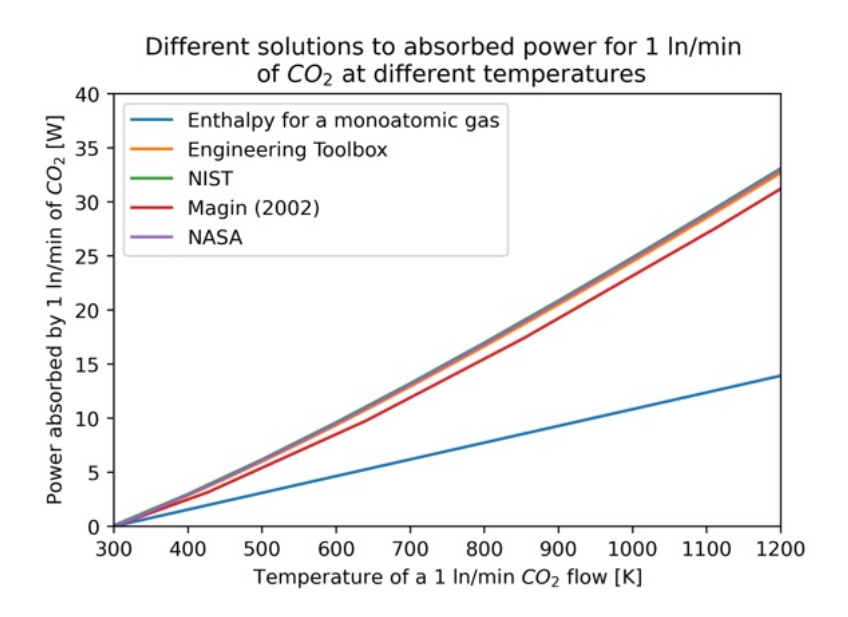


FIGURE A.5: The power absorbed by 1 \ln/\min of CO_2 in watts (W) using different sources for the specific heat of CO_2 .

The final value used for $C_{p_{\text{CO}_2}}$ was obtained from NIST [10]. The added power to CO₂ for a given temperature and mass flow rate was calculated from 300 K for 10 and 20 ln/min [8]. The values for 10 ln/min of CO₂ are $T_{\text{inlet}} = 500$, 700, 850 K and $P_{\text{CO}_2} = 62$, 132, 189 W, respectively. The values for 20 ln/min of CO₂ are $T_{\text{inlet}} = 500$ K and $P_{\text{CO}_2} = 134$ W.

A.5 Additional Results and Discussion

A.5.1 Impact of Preheating at Higher Power

Having established the pressure-dependent effects of preheating at moderate power input (1132 and 1500 W) in Chapter 3, we examine here how these phenomena evolve under higher power conditions (2124 W). This progression is particularly relevant for understanding the scalability of preheating benefits and their interaction with plasma dynamics at elevated power levels. Below are experimental results obtained for $P_{\text{Total}} = 2124 \text{ W}$, $\phi_{\ln/\min} = 20 \text{ ln/min}$, $T_{\text{inlet}} = 300 \text{ K}$ (green) and 500 K (yellow) for different pressures. The total power added to the system was kept constant across all measurements. Error bars are given but fall under the data markers in all cases.

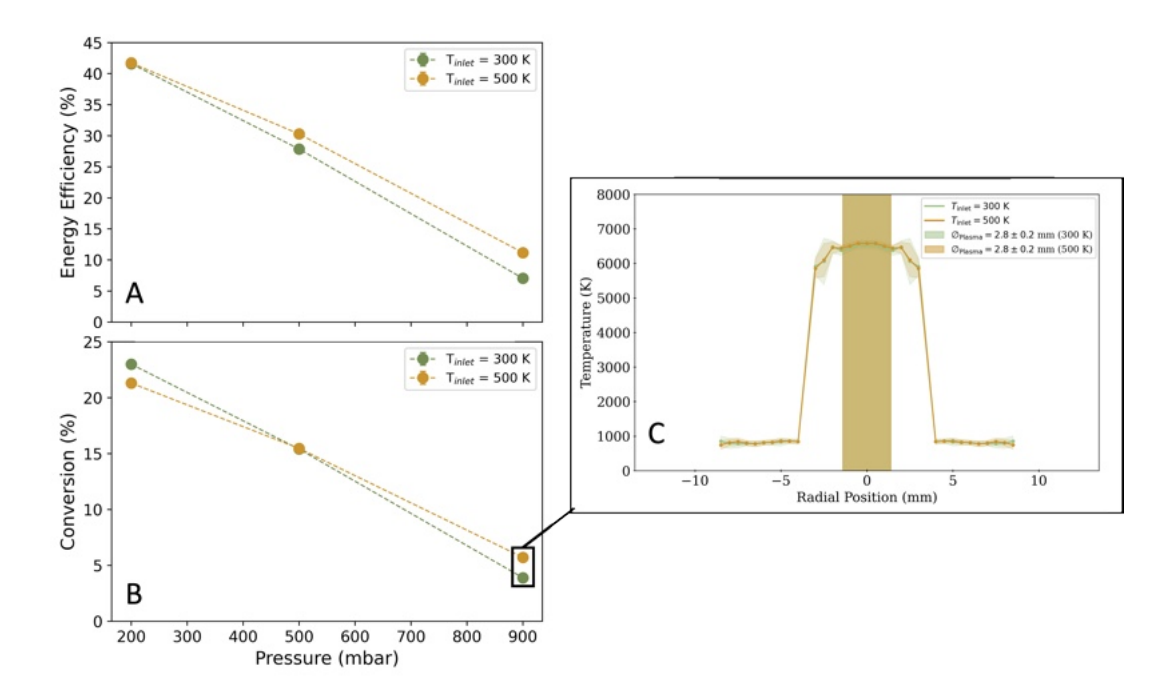


FIGURE A.6: Energy efficiency (A) and conversion (B) plotted for $P_{Total} = 2124 \text{ W}$, $\phi = 20 \text{ ln/min}$, $T_{inlet} = 300 \text{ K}$ (green) and 500 K (yellow), for different pressures, with the corresponding radial temperature profile for 900 mbar (C). Error bars are given but fall under the data markers in all cases.

Figure A.6(A and B) show similar trends to those observed under lower power conditions (Figure 3.3 and 3.4, Chapter 3). At 200 mbar, we again see a decrease in conversion between 300 K and 500 K, from 22.99 \pm 0.08% to 21.30 \pm 0.09%, respectively. At 500 mbar, the conversion is nearly unchanged, at 15.40 \pm 0.06% vs 15.46 \pm 0.07%, between $T_{\rm inlet} = 300$ K and 500 K, respectively. However, we observe an increase in energy efficiency (Figure A.6(A)) due to the exclusion of $P_{\rm CO_2}$ in these calculations.

The most significant improvements occur at near atmospheric pressure (900 mbar), where conversion increases by approximately $\sim 47\%$ compared to baseline conditions, rising from $3.89 \pm 0.03\%$ at $T_{\rm inlet} = 300$ K to $5.71 \pm 0.04\%$ at $T_{\rm inlet} = 500$ K. We see an increase in conversion of more than a factor of 4 when comparing to the 1000 W results, where we observed a $\sim 10\%$ increase in conversion. This suggests that preheating benefits not only persist across power regimes, but the relative impact appears to increase as total power increases. In Figure A.6(C), the radial temperature profile does not show a larger reactive area that reflects the improvements to conversion. It is likely that because the available temperature values from the C_2 swan emission end at 3 mm from the center region for $T_{\rm inlet} = 300$ and 500 K, we are not able to observe the increased reactive area.

A.5.2 Changes to Reactive Volume and Plasma Size

Figure A.7 shows the radial temperature profiles for constant $P_{\text{MW}} = 1000 \text{ W}$ and $P_{\text{total}} = 1132 \text{ W}$ and varying $T_{\text{inlet}} = 300$, 500, and 700 K, which correspond to $P_{\text{CO}_2} = 0$, 62, and 132 W, respectively. The radial temperature profiles are again complementary to the conversion data across different pressure regimes shown in Figure 3.5 in Chapter 3.

In Figure A.7, the temperature profiles show characteristic contracted plasma behavior with steep thermal gradients between the core and peripheral regions. The radial temperature profiles at 200 mbar (top row Figure A.7, A and D) indicate a decrease in the reaction area with increasing $T_{\rm inlet}$ for both $P_{\rm MW}$ and $P_{\rm total}$. In Figure A.7 (middle row, B and E, and bottom row, C and F), we again observe the opposite effect on the reactive area appears at 700 and 900 mbar, where a higher $T_{\rm inlet}$ increases the reactive area (T > 1500 K). We do not observe a significant change in the plasma diameter (FWHM of the 777 atomic oxygen emission) between either high-pressure condition. The reader should note that the data for $T_{\rm inlet} = 500$ K is unavailable for 700 mbar (Figure A.7.C&F) due to plasma instability. However, for the values we have available for p = 900 mbar in Figure A.7C, we can again observe a direct correlation between the reaction area at the height of the plasma and conversion, using the same method as described in Chapter 3, Figure 3.6.

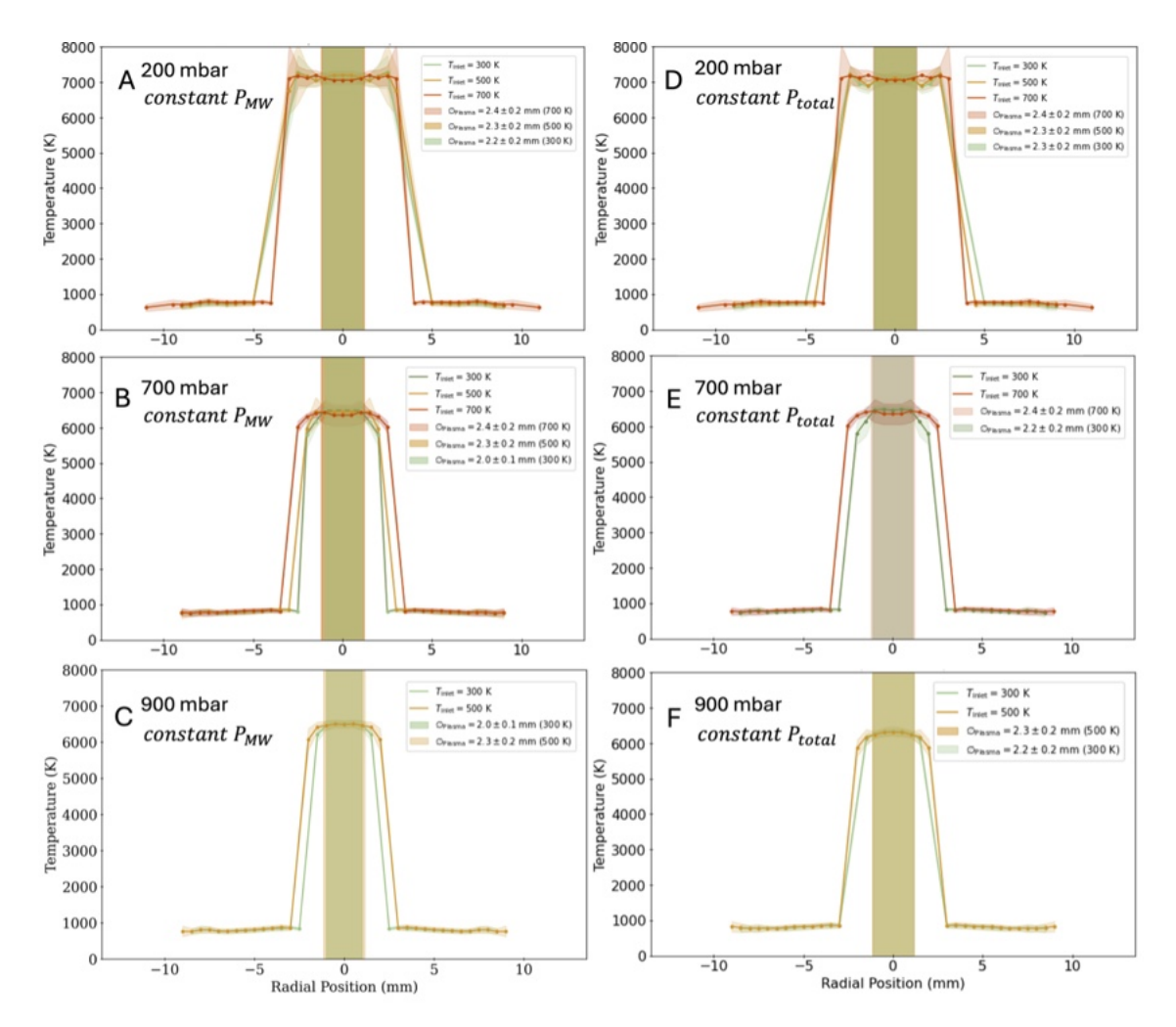


FIGURE A.7: Radial temperature profile plotted for $P_{\rm MW}=1000$ W (lefthand side, A-C) and $P_{\rm total}=1132$ W (righthand side, D-F), $\phi_{\rm ln/min}=10$ ln/min, $T_{\rm inlet}=300$ K (green), 500 K (yellow), 700 K (dark orange), for p = 200 (top row, A and D), 700 (middle row, B and E), and 900 (bottom row, C and F) mbar. The center-shaded region represents the plasma diameter determined by the 777 nm atomic O emission captured by CCD images. The connecting lines between the C_2 swan band (T = \sim 6000 – 7000 K) and the flame band (T < 1500 K) derived temperatures are for visualization purposes only.

Figure A.8 shows that for $P_{\rm MW}=1000$ W, $\phi_{\rm CO_2}=10$ ln/min, p = 900 mbar, $T_{\rm inlet}=300$ (green) and 500 (yellow) K, the reaction area increases for $T_{\rm inlet}=500$ K by $\sim 56\%$ alongside a $\sim 51\%$ increase in conversion compared to baseline conditions.

These findings suggest that while preheating influences the spatial distribution of the plasma and reactive area, it does not fundamentally alter the core plasma properties or peripheral quenching conditions. The pressure-dependent response to preheating implies complex interactions between gas dynamics, thermal gradients, and plasma contraction mechanisms. Further investigation of the emission profiles indicates additional changes to the plasma profile, as shown in $Figure\ A.9$ below.

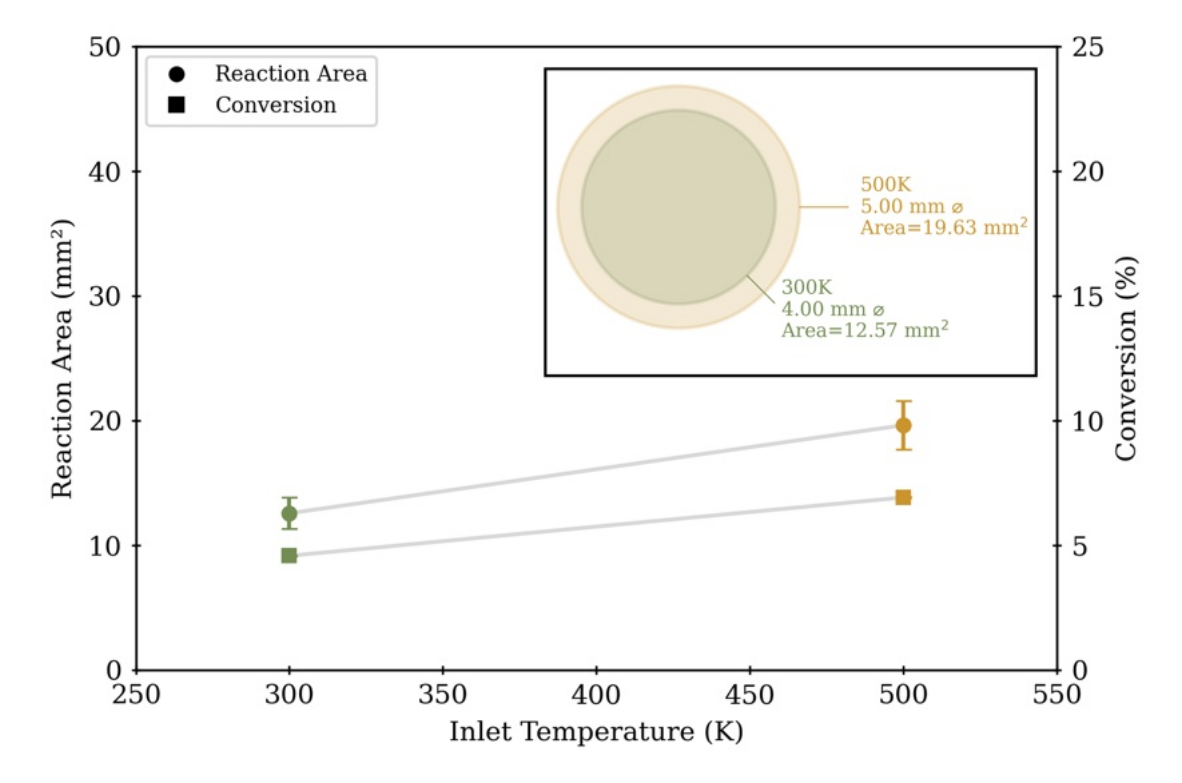


FIGURE A.8: Reaction area (left y-axis) and conversion (right y-axis) as a function of pressure for $P_{\rm MW}=1000~{\rm W},\,\phi_{\rm CO_2}=10~{\rm ln/min},\,p=900~{\rm mbar}$ for $T_{\rm inlet}=300$ (green) and 500 (yellow) K.

Under non-preheated conditions, 200 mbar is at the 'edge' of the hybrid regime, depending on the input power [11]. We observe that the benchmark condition for 200 mbar shows only slight hybrid characteristics, where the center region of the filament is contracted but grows outward towards the tip of the column. With an increase in T_{inlet} , these characteristics become more pronounced, accompanied by a notable decrease in the plasma height (h), as defined by the FWHM of the emission profile for all conditions presented, which will be explored further in Section A.5.4 below. It is clear from these images that contraction dynamics likely contribute to the reduction in the reaction area observed in Figure A.7(A) and A.7(D), as evidenced by the less pronounced hybrid characteristics of the plasma observed at 200 mbar for the 300 K case vs. at 700 K (Figure A.9, top right).

In summary, when comparing plasma characteristics between simulated heat recovery (P_{MW}) held constant) and power redistribution (P_{total}) held constant) experiments, small differences emerge in how the plasma responds to preheating. While both approaches demonstrate temperature-dependent effects on plasma behavior, the magnitude and nature of these changes vary significantly between the two strategies. This will be further elaborated in the next section.

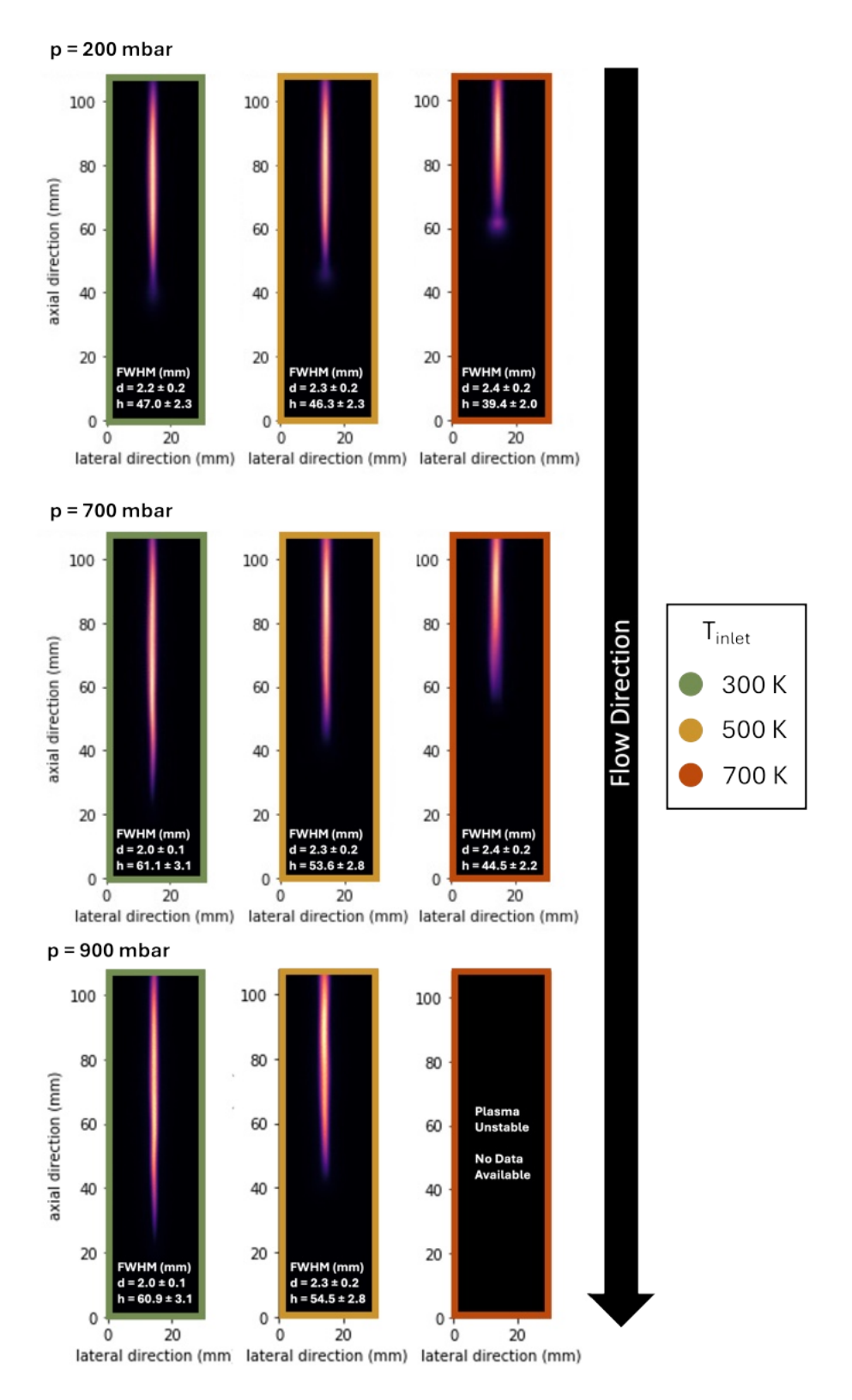


FIGURE A.9: CCD imaging of the 777 atomic oxygen emission for $P_{\rm MW}=1000~{\rm W},\,\phi_{\rm CO_2}=10~{\rm ln/min},\,T_{\rm inlet}=300~{\rm K}$ (green), 500 K (yellow), 700 K (dark orange) for p = 200 (top), 700 (middle), and 900 (bottom) mbar. The data for $T_{\rm inlet}=700~{\rm K}$ at p = 900 mbar is unavailable due to plasma instability under these conditions. The values for the plasma diameter (d) and height (h) are shown at the bottom of each image in white.

A.5.3 Comparative Analysis: Constant Microwave Power vs Constant Total Power

At low pressures (200 mbar), despite maintaining similar core temperatures (~ 7000 K), the reaction area shows distinct responses depending on power distribution. Under constant $P_{\rm MW}$, higher $T_{\rm inlet}$ produces a marked reduction in reactive area, but only at $T_{\rm inlet} = 700$ K. In contrast, when maintaining constant $P_{\rm total}$ by reducing $P_{\rm MW}$ input to compensate for preheating power ($P_{\rm CO_2}$), the reaction area decreases more uniformly across all preheated conditions. This suggests that the plasma's response to preheating is sensitive not only to $T_{\rm inlet}$ but also to the absolute microwave power available for sustaining the discharge, which aligns with the current understanding of plasma contraction dynamics [2, 11, 12].

The behavior at higher pressures (700 - 900 mbar) shows consistent trends between both approaches, with preheating leading to increased reactive area in both cases. However, these effects are more pronounced under constant $P_{\rm MW}$ conditions. A significant increase in plasma diameter was only observed for constant $P_{\rm MW}$. Temperature profiles at 700 mbar demonstrate that increasing inlet temperature from 300 K to 700 K enlarges both the plasma diameter (2.0 mm to 2.4 mm) and the surrounding reactive area, where $T\gg 3000$ K. These findings suggest that absolute microwave power plays a crucial role in determining the magnitude of preheating effects on plasma behavior.

Notably, despite these differences in plasma dimensions and reactive area, core temperatures remain consistent at approximately 6000 - 7000 K across all conditions for both approaches. This consistency in core temperature, regardless of how power is distributed between preheating and microwave input, indicates that the fundamental plasma properties are primarily determined by the thermal-ionization instability, where electron-neutral collisions increase electron density, thus shifting the permittivity, ultimately resulting in a narrowing of the filament. In preheating the inlet gas as a constant pressure, there will be a reduction in the collisionality. For example, at a pressure of 900 mbar, we can calculate the average collisional frequency of CO₂ under two temperature conditions. At 300 K, the collisional frequency approaches approximately 3.9 GHz, while at 900 K, it is about 2.3 GHz, a 41% decrease in collisional frequency.

A.5.4 Axial Contraction of Plasma Filament

We observed that the plasma discharge exhibited notable axial contraction as $T_{\rm inlet}$ increased (cf. also Figure 3.3, Chapter 3), in addition to changes in its radial characteristics at higher pressure. Figure A.10 illustrates this behavior through atomic oxygen 777 nm emission images captured using a 780 nm narrow bandpass filter at different $T_{\rm inlet}$ while maintaining $P_{\rm total} = 1500$ W, p = 900 mbar, and $\phi_{\rm CO_2} = 10$ ln/min.

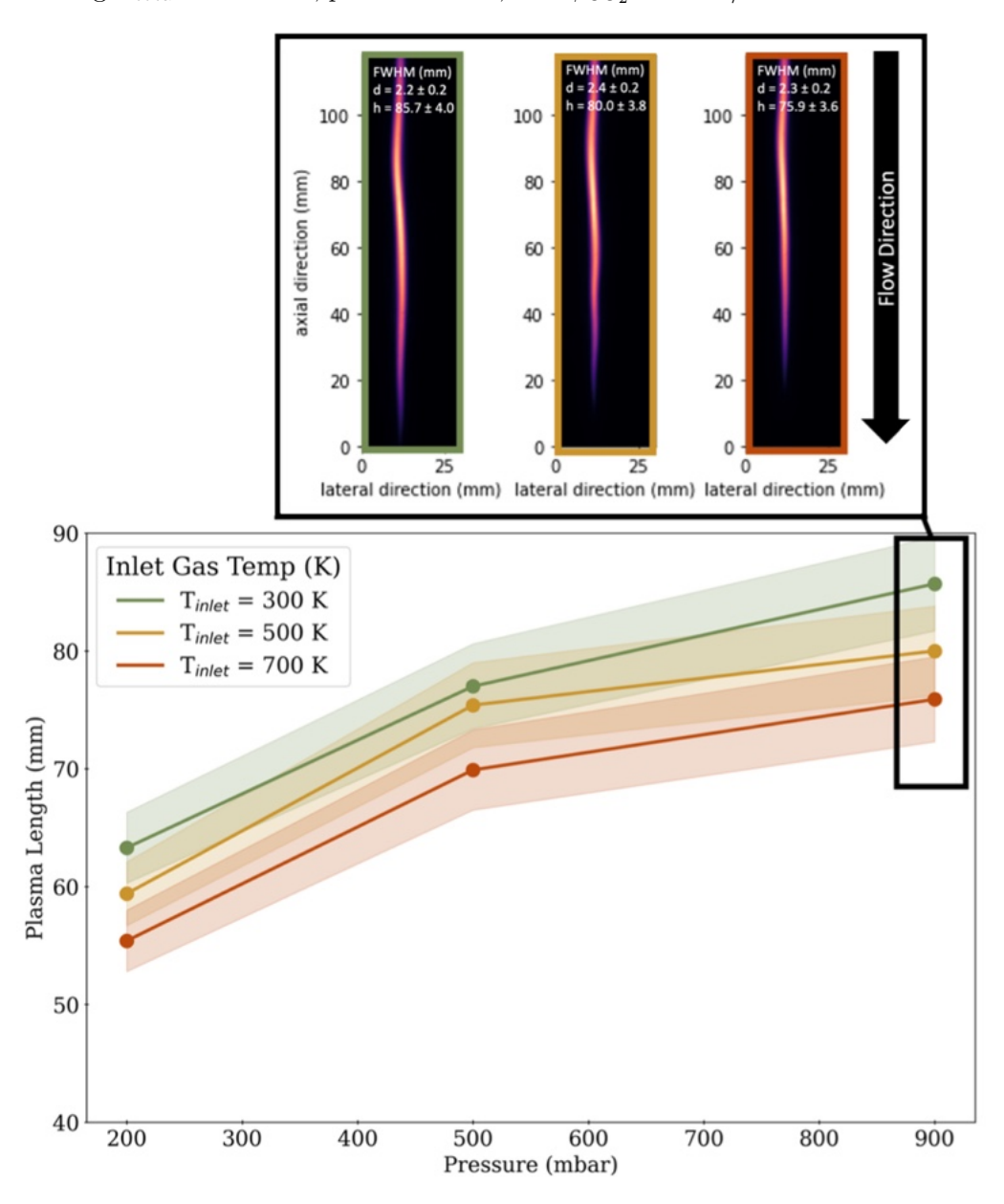


FIGURE A.10: (Top) Images of the atomic oxygen 777 emission as taken with CCD using a 780 nm bandpass filter for $P_{\rm total} = 1500$ W, p = 900 mbar and $\phi_{\rm CO_2} = 10$ ln/min at different $T_{\rm inlet}$. (Bottom) Plasma lengths at different $T_{\rm inlet}$ for $P_{\rm total} = 1500$ W, 10 ln/min plasma, as a function of pressure (mbar).

To determine whether the observed contraction resulted primarily from an increase in volumetric flow rate due to gas expansion from the preheated input gas, experiments were conducted at a constant volumetric flow rate across different $T_{\rm inlet}$. The different conditions tested are visible in Figure A.11.

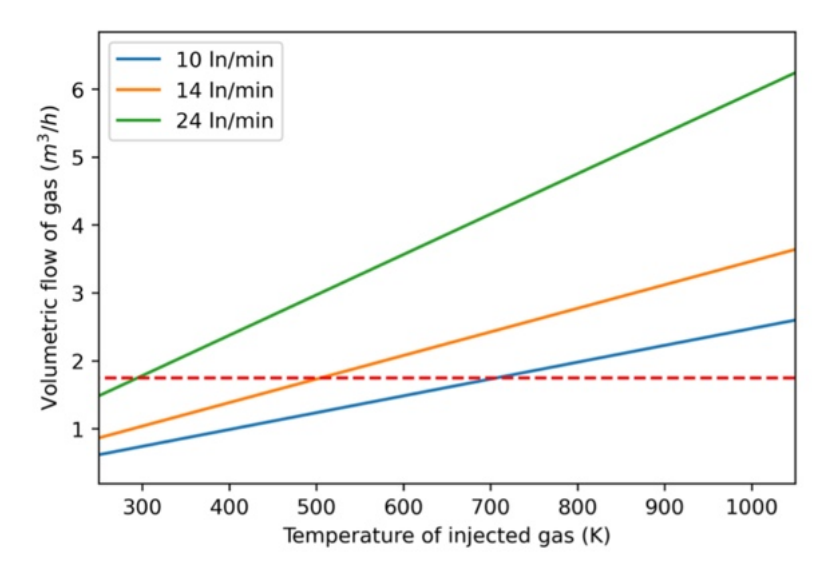


FIGURE A.11: Volumetric flow rate as a function of $T_{\rm inlet}$ for mass flow rates of 10, 14, and 24 ln/min. The intersecting dashed red line shows a constant volumetric flow rate of 1.8 m³/h between the varying $T_{\rm inlet}$ for different mass flow rates (24, 14 and 10 ln/min), giving an equal volumetric flow rate at $T_{\rm inlet} = 300$, 500 and 700 K, respectively. Note that 850 K is not included since the resulting flow rate (\sim 8 ln/min) would be too low to operate without possible damage to the system.

As shown in Figure A.11, to compensate for gas expansion, the mass flow rate was adjusted to maintain an equivalent volumetric flow rate of 1.8 m³/h. The mass flow rate was reduced from 24 ln/min at $T_{\rm inlet} = 300$ K to 14 ln/min at 500 K, and further to 10 ln/min at 700 K.

The results of these constant volumetric flow rate experiments, presented in Figure A.12, revealed nearly identical plasma lengths across the temperature range. This strong correlation between plasma length and volumetric flow rate suggests that the observed axial contraction is primarily driven by changes in the gas flow dynamics rather than direct temperature effects. This finding highlights how preheating alters flow dynamics, affecting both residence time and the spatial distribution of reactive molecular species. This finding provides valuable insight into the mechanisms controlling plasma dimensions and highlights the importance of considering volumetric flow effects when interpreting temperature-dependent plasma behavior.

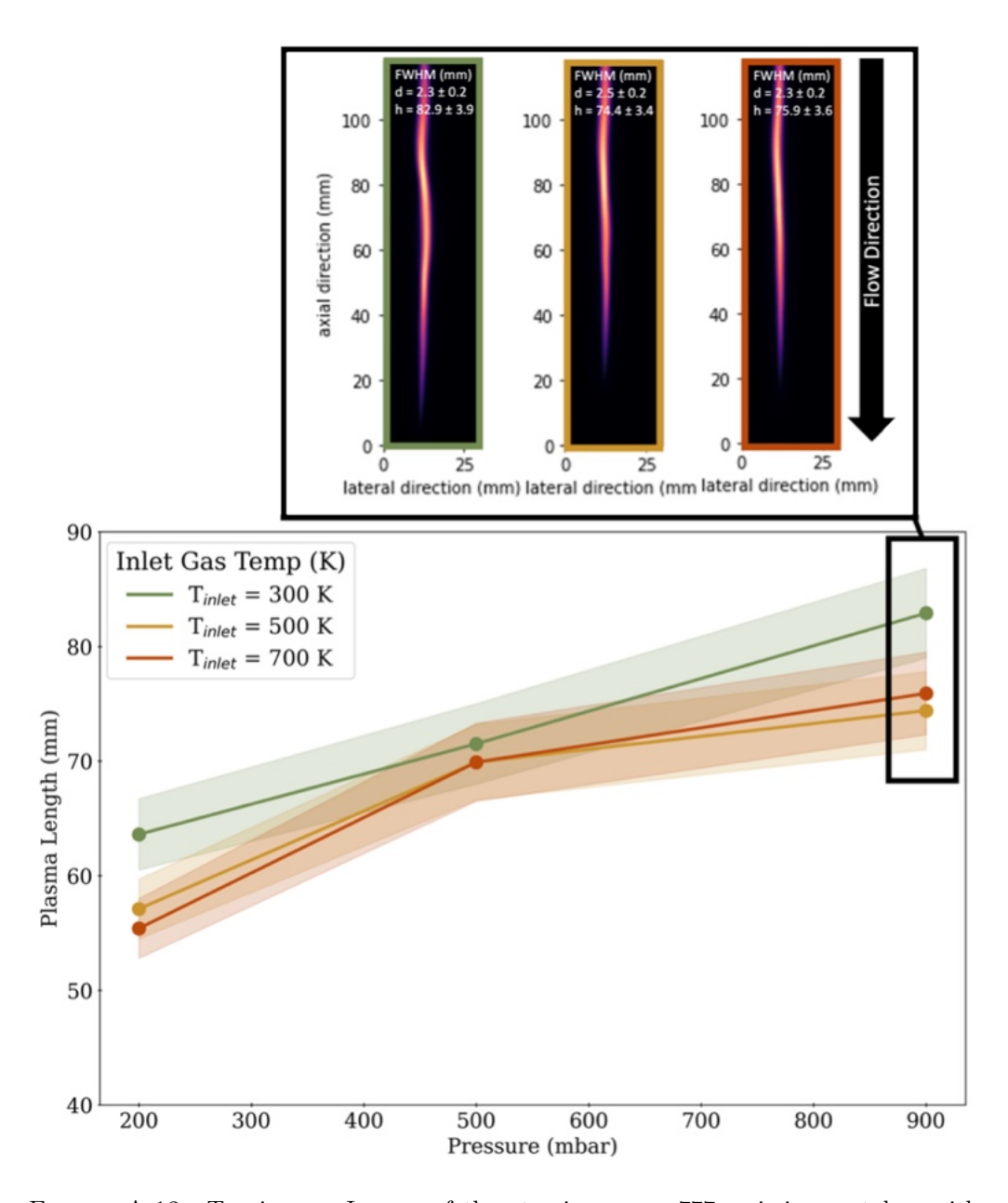


FIGURE A.12: Top image: Images of the atomic oxygen 777 emission as taken with CCD using a 780 nm bandpass filter for $P_{\rm total}=1500~{\rm W}$ at 900 mbar. (Bottom) Plasma lengths at different $T_{\rm inlet}$ for $P_{\rm total}=1500~{\rm W}$, the mass flow rate at 300 K equaled 24 ln/min, 14 ln/min at 500 K, and 10 ln/min at 700 K, as a function of pressure (mbar).

Bibliography

- [1] C.F.A.M. van Deursen, H.M.S. Van Poyer, W.A. Bongers, F.J.J Peeters, F.M.A. Smits, and M.C.M. van de Sanden. Effluent nozzles in reverse-vortex-stabilized microwave CO₂ plasmas for improved energy efficiency. *Journal of CO₂ Utilization*, 88: 102952, 2024. doi: 10.1016/j.jcou.2024.102952.
- [2] A.J. Wolf, T.W.H. Righart, F.J.J. Peeters, P.W.C. Groen, M.C.M. van de Sanden, and W.A. Bongers. Characterization of CO₂ microwave plasma based on the phenomenon of skin-depth-limited contraction. *Plasma Sources Science and Technology*, 28(11):115022, 2019. doi: 10.1088/1361-6595/ab4e61.
- [3] E. Carbone, F. D'Isa, A. Hecimovic, and U. Fantz. Analysis of the C_2 $d^3\Pi_g a^3\Pi_u$ Swan bands as a thermometric probe in CO_2 microwave plasmas. *Plasma Sources Science and Technology*, 2019. doi: 10.1088/1361-6595/ab74b4.
- [4] G. Raposo, A.W. van de Steeg, E.R. Mercer, C.F.A.M. van Deursen, H.J.L. Hendrickx, W.A. Bongers, G.J. van Rooij, M.C.M. van de Sanden, and F.J.J. Peeters. Flame bands: CO + O chemiluminescence as a measure of gas temperature. *Journal of Physics D: Applied Physics*, 54(37):374005, 2021. doi: 10.1088/1361-6463/ac0924.
- [5] N.R. Draper. Applied regression analysis. McGraw-Hill. Inc, 1998.
- [6] A.M. Pravilov and L.G. Smirnova. Spectral distribution of the chemiluminescence rate constant in the O + CO (+ M) and O+ NO (+ He) reactions. *Kinet. and Catal*, 19, 1978.
- [7] P.J. Bruggeman, N. Sadeghi, D.C. Schram, and V. Linss. Gas temperature determination from rotational lines in non-equilibrium plasmas: a review. *Plasma Sources Science and Technology*, 23(2):023001, 2014. doi: 10.1088/0963-0252/23/2/023001.

- [8] B. Wanten, R. Vertongen, R. De Meyer, and A. Bogaerts. Plasma-based CO₂ conversion: How to correctly analyze the performance? *Journal of energy chemistry*, 2023.
- [9] J.N. Miller and J.C. Miller. Statistics and chemometrics for analytical chemistry. Signal, 100:95, 1998.
- [10] National Institute of Standards and Technology. Gas phase heat capacity for CO_2 , May 2023.
- [11] A.J. Wolf, T.W.H. Righart, F.J.J. Peeters, W.A. Bongers, and M.C.M. van de Sanden. Implications of thermo-chemical instability on the contracted modes in CO₂ microwave plasmas. *Plasma Sources Science and Technology*, 29(2):025005, 2020. doi: 10.1088/1361-6595/ab5eca.
- [12] L. Vialetto, A.W. van de Steeg, P. Viegas, S. Longo, G.J. van Rooij, M.C.M. van de Sanden, J. van Dijk, and P. Diomede. Charged particle kinetics and gas heating in CO₂ microwave plasma contraction: comparisons of simulations and experiments. Plasma Sources Science and Technology, 31(5):055005, 2022. doi: 10.1088/1361-6595/ac56c5.

Appendix B

Dual Injection in a CO₂ plasma: Exploring Reactive Quenching

This chapter is derived from the following publication:

Dual Injection in a CO₂ Microwave Plasma:
 Exploring Post-Plasma Quenching with CH₄ and Comparison with DRM
 E.R. Mercer, M. Albrecht, R. De Meyer, I. Fedirchyk, E. Morais, Sara Bals, A. Bogaerts (Submitted Manuscript)

B.1 Analysis

B.1.1 Liquid Analysis

The liquid samples collected from the post-plasma condenser during dual injection experiments were characterized using multiple analytical techniques to identify and quantify various components. Each set of data was defined by a single $CO_2:CH_4$ ratio, meaning for both power conditions and all pressure sets, a single liquid sample was collected (e.g., 1 sample = 7:7 slm $CO_2:CH_4$, 7:7 slm; Power = 1000 and 1250 W, and pressure between 200 – 900 mbar). This approach was chosen to limit the number of samples requiring external analysis and because the experimental setup was not designed to collect individual liquid samples for each condition while in operation.

Since this study represents the first approach to investigating dual injection in a CO₂ MW plasma as a method to utilize reactive quenching, the experimental design prioritized capturing overall trends rather than optimizing sample collection for every parameter combination. As such, certain limitations in data resolution were unavoidable. However, the results provide a foundational understanding of the process, highlighting key trends that will inform future studies where more refined collection strategies can be implemented.

The liquid samples were analyzed using an Interscience Focus GC equipped with a Flame Ionization Detector (FID). Analysis was performed using a Stabilwax column (30 m \times 0.32 mm ID, 1.00 μ m film thickness) through a split/splitline (S/SL) injection. Despite comprehensive analysis, no significant volatile compounds were detected using this method.

High-Performance Liquid Chromatography (HPLC) analysis was performed using a Waters Alliance e2695 system equipped with both PhotoDiode array (PDA) and Refractive Index (RI) detectors. Separation was achieved using a Shodex RSpak KC-811 column (6 μ m particle size, 8.0 × 300 mm), which is specifically designed for organic acid analysis. The mobile phase consisted of 10 mM H₂SO₄ run under isocratic conditions. This analysis successfully identified and quantified formaldehyde, formic acid, and acetic acid in the liquid samples.

Total Organic Carbon (TOC) was measured using a Shimadzu TOC-L analyzer. Samples were appropriately diluted prior to analysis to ensure measurements fell within the calibration range of the instrument. The results from this analysis provided the total carbon content of the liquid samples, which was compared with the sum of carbon-containing compounds identified by the HPLC analysis to assess the completeness of compound identification. Only a small difference was found, and can be seen in *Figure 4.9A*, in Chapter 4.

Gas Chromatography-Mass Spectrometry (GC-MS) analysis was conducted using an Interscience GC 8000 Top system. The separation was performed on an Agilent DB-5MS UI column (30 m \times 0.320 mm, 0.25 μ m film thickness). This technique did not yield significant additional information about the composition of the liquid samples.

Liquid Chromatography-Mass Spectrometry (LC-MS) analysis was performed using a Waters Acquity Arc system. Separation was conducted on a CORTECS C18 Column (90 Å, 2.7 μ m particle size, 4.6 mm \times 50 mm), which is a general-purpose reverse-phase column. A gradient elution method was employed with the following mobile phase composition:

Table B.1: Mapping of the gradient elution employed in LC-MS analysis.

Time (min)	Water (%)	Acetonitrile (ACN%)
Initial	95	5
0.5	95	5
8.0	5	95
8.5	5	95
10	95	5

The flow rate was maintained at 1.2 mL/min. This analysis revealed the presence of an unidentified compound with a molecular weight of 180 g/mol, which was not detected by other analytical methods.

UV-visible spectroscopy (UV-vis, Shimadzu UV-2600i), equipped with a deuterium lamp, a tungsten halogen lamp, and a photomultiplier detector, was used to characterize the chromophoric properties of the liquid samples. This analysis helped identify the absorption maxima and provided insights into the presence of conjugated systems within the unidentified compounds in the liquid products.

B.1.2 Carbon Analysis

All accompanying analysis was conducted by Robin De Meyer (PhD student within PLAS-MANT). After each of the experimental runs, carbon was collected from the bellows and cyclone separator. A set of data is again defined by a single $CO_2:CH_4$ ratio, meaning for both power conditions and all pressure sets, a single sample was collected (e.g., 1 sample = 7:7 slm $CO_2:CH_4$, 7:7 slm; and either 1000 or 1250 W, and one pressure in the range of 200 – 900 mbar, although no carbon formation was observed at p < 700 mbar), for the same reason as explained for the liquid analysis.

A small amount of dark carbonaceous deposits was also found on the reactor walls and in the KF piece downstream of the quartz tube, with only very few deposits found in the cyclone separator. All deposits were collected using a paper tissue for subsequent characterization. The different samples were characterized via scanning electron microscopy (SEM) and transmission electron microscopy (TEM). A portion of the collected material was suspended in acetone (for SEM) or chloroform (for TEM) and dispersed by sonication.

For SEM analysis, a few drops of the suspension were deposited onto an aluminum stub and left to dry before being placed in the SEM for characterization. For TEM analysis, a holey carbon TEM grid was positioned on filter paper, and a few drops of the suspension were applied to the grid and allowed to dry. After a brief drying period, the grid was ready for TEM analysis.

The deposited carbon is analyzed using two methods, Scanning Electron Microscopy (SEM), executed using a ThermoFisher Scientific Quanta FEG 250 operating at 20 kV in high vacuum mode, and Transmission Electron Microscopy (TEM) performed using a ThermoFisher Scientific Tecnai Osiris G20 operating at 200 kV, with images acquired in bright-field TEM (BF-TEM) mode.

B.1.3 Optical Emission Spectroscopy Data Treatment

Optical emission spectroscopy (OES) measurements were performed to characterize the plasma emission. The acquired spectral data (200 – 800 nm) underwent a comprehensive treatment process to ensure accurate quantitative analysis. Spectral measurements were obtained within the resonance chamber of the reactor to determine plasma composition. Spectra were acquired using an Ocean Insight mini spectrometer (HR-4UVV250-5)

equipped with a solarization-resistant fiber with a diameter of 400 μ m (QP400-2-SR) and cosine corrector with Spectralon diffusing material (CC-3-UV-S). For each experimental condition (varying power, pressure, and flow rates), a single-shot spectrum was collected along with an electronic dark measurement.

The raw spectral intensities were calibrated using a standard irradiance calibration to convert arbitrary intensity counts to absolute radiometric units (μ J/count), accounting for the spectrometer's wavelength-dependent response. The collection geometry was calculated accounting for the cosine corrector properties, with a diffuser diameter of 3900 μ m. For the cosine corrector following Lambert's law, the radiance was integrated over a hemisphere (2π sr). The calibrated energy values were then converted to photon flux (photons/s/m²). An adaptive Savitzky-Golay filter was applied to the photon flux data with parameters optimized for spectroscopic data. Different smoothing parameters were applied to baseline and peak regions to preserve spectral features while reducing noise. Finally, the spectra were normalized by their maximum intensity values for comparative analysis across different experimental conditions. An example spectrum is presented in Figure B.1.

The rotational temperatures (T_{rot}) were determined using the Swan band system, C_2 ($d^3\Pi_g - a^3\Pi_u$), within the open source MassiveOES software package by fitting to a simulated spectrum. Here we consider T_{rot} as a reliable proxy for the gas temperature in contracted plasmas [1], which are typically observed at p > 200 mbar [2]. The accuracy of the temperature determination was assessed by analyzing the residuals between experimental and simulated spectra to ensure the absence of systematic deviations indicative of non-Boltzmann behavior or other spectroscopic artifacts. The uncertainties in the extracted temperatures arise from several factors, as described in Appendix A. All temperatures were found to be between $\sim 7000 - 8000$ K, with the lowest pressures (200 mbar) showing somewhat higher temperatures (see Figure B.2), consistent with values reported in the literature [1].

The temperatures were consistent across powers, all overlapping within the error bar, as is typically observed in CO_2 plasmas [1, 3, 4]. Therefore, for better visualization, the values were averaged and presented in *Figure B.2*, with a shaded deviation to show the (small) variability between the two power conditions (1000 and 1250 W), since we do not expect much deviation in temperature between these power conditions, this provides

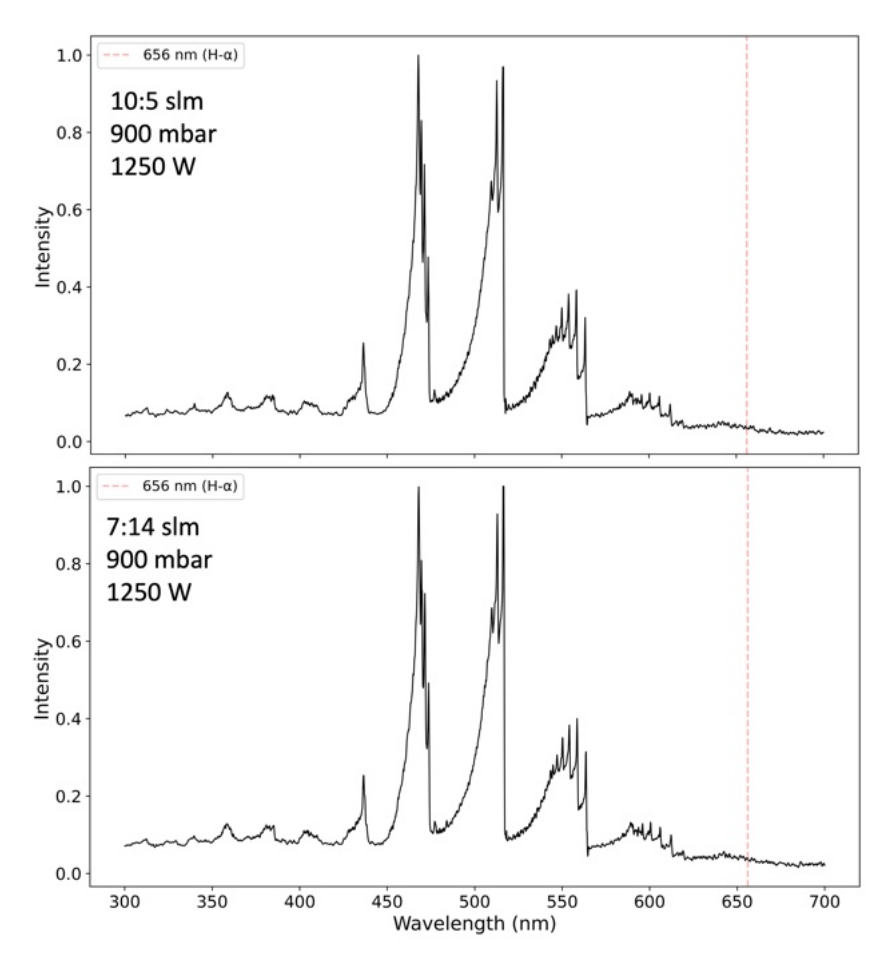


FIGURE B.1: Example of treated spectrum of C_2 ($d^3\Pi_g - a^3\Pi_u$) Swan band, used in MassiveOES fitting, as well as an indicator for where the H_α at ~ 656 nm (red dashed line). No peak was observed in any of the treated spectra.

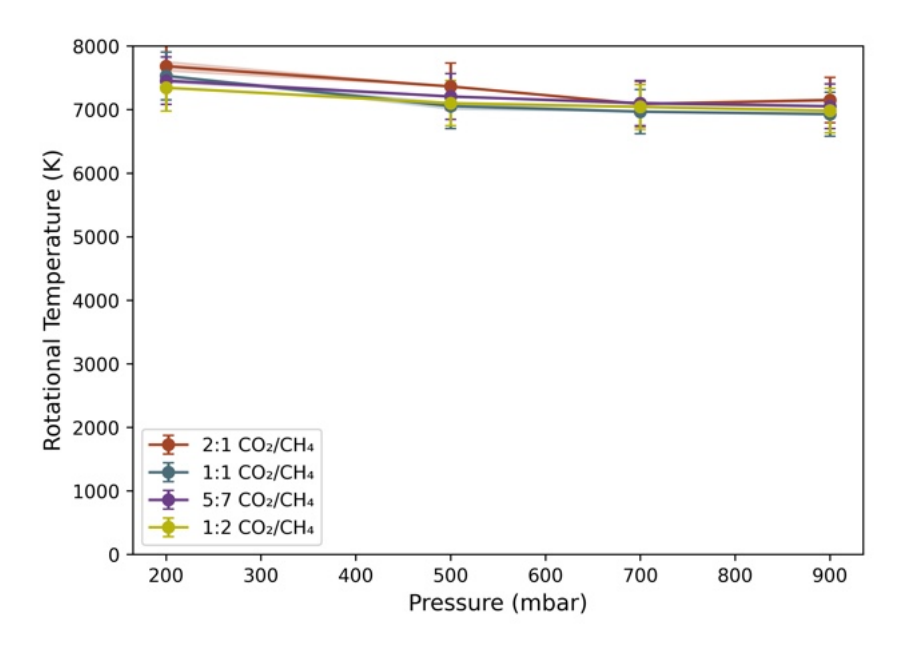


Figure B.2: Averaged rotational temperature between 1000 and 1250 W, as a function of pressure, for the four different $\rm CO_2:CH_4$ ratios investigated.

further indication of the error in this measurement. The presented error bar is taken as a 5% error of this average, as this data was only used as a starting temperature for the model.

The spectra were used during the experiments to monitor whether CH_4 traveled upstream into the reactive volume, as would be indicated by additional peaks from, for example, H_{α} at ~656 nm. The treated data indicated that no CH_4 was detectable within the emission spectra, as two examples are shown in Figure B.1. These spectra were chosen as they represent the 'extreme' circumstances, where we might see the greatest back flow, if present. We expect to observe the H_{α} even in small concentrations, as reported by Kuijpers, who showed that H_{α} can be observed in concentrations as low as 0.75% CH_4 [5]. Therefore, the derived temperatures were taken as the core plasma temperature and used as input for the CO_2 plasma temperature in the 0D model, before CH_4 injection, described in Section S.2.

B.1.4 Secondary Injection Housing

The secondary, counter-flow injection of CH₄ is applied in the afterglow region, 5 cm from the waveguide, where temperatures exceed 1500 K. A diagram is presented in *Figure B.3*. The secondary counter-flow tangential injection was designed to enhance mixing between CH₄ and the post-plasma afterglow region, with two 1 mm inlet nozzles.

B.1.5 Gas Chromatography

Gas sampling was performed using gas chromatography (Agilent 990 MicroGC, two-channel configuration) and an infrared luminescent quenched absorption technique (PyroScience GmbH FDO₂ optical oxygen sensor). The MicroGC system was equipped with two analytical channels, **Channel 1** consists of a Molesieve 5Å column with argon as the carrier gas, used to measure CO, H₂, O₂, and CH₄, and **Channel 2** uses a PoraPLOT U column with helium as the carrier gas, used to measure CO₂, C₂H₂, C₂H₄, and C₂H₆.

Both channels included a CP-PoraBond Q precolumn to improve separation. Before entering the columns, the gas mixture was heated to 70 °C to ensure consistent analysis conditions. The composition of the post-plasma mixture was determined from the chromatograms. In order to assess the accuracy of the measurements, the 95% confidence

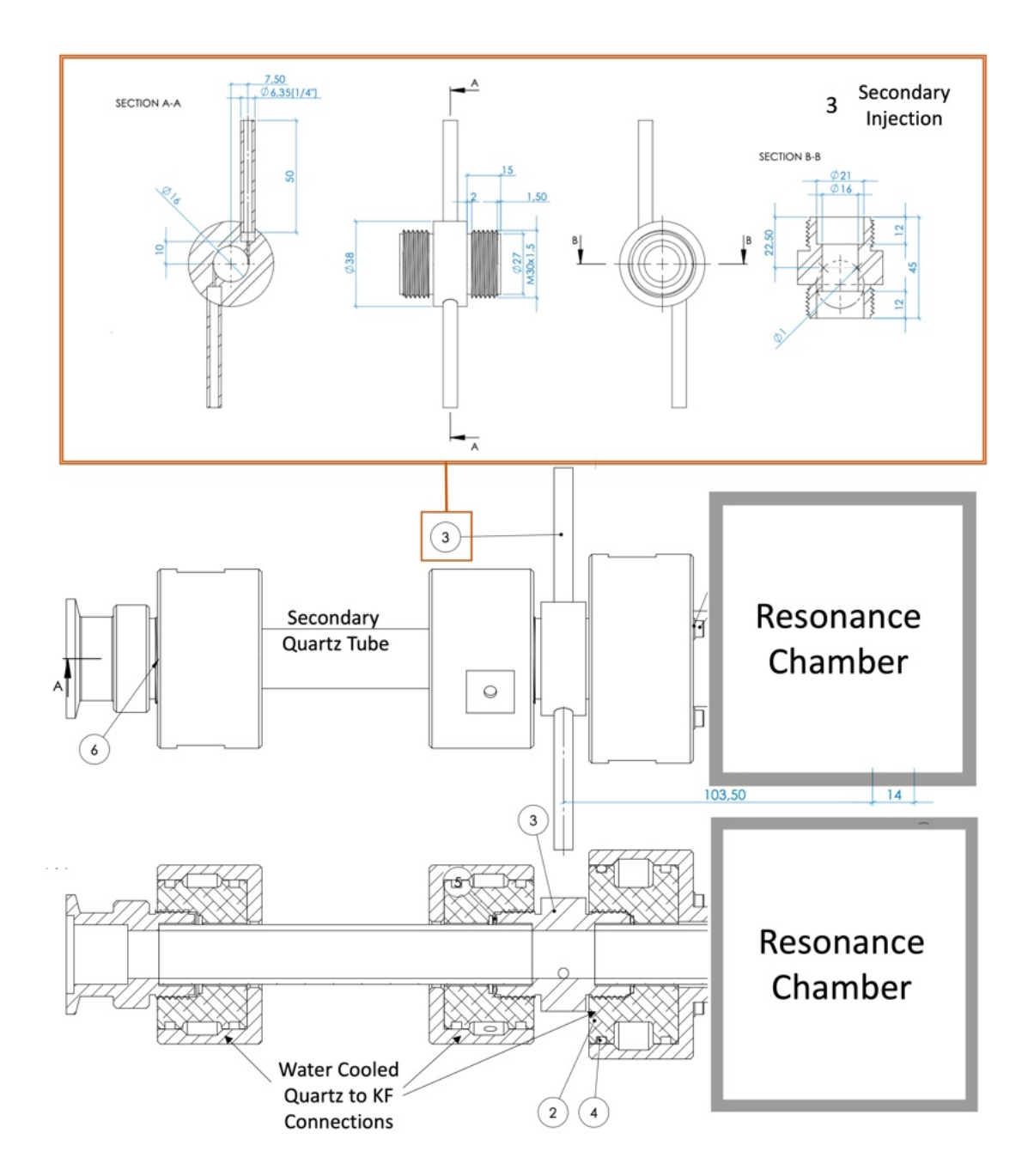


Figure B.3: Schematic drawing of secondary injection housing with post-plasma viewing with a secondary quartz tube. A detailed view of the secondary tangential injection (3) is at the top of the image.

interval of each composition determination was calculated according to the equations outlined in *Appendix A*, *Section A.3.1*.

B.1.6 Performance Calculations

All calculations for the performance metrics shown in this work follow the methods outlined by Wanten et al. [6], to properly account for gas expansion or contraction during the reaction, which is very important to obtain the correct values for the final reported data. We utilized the internal standard method in which nitrogen is mixed downstream before the vacuum pump, as shown in Figure 4.1, in Chapter 4. Therefore, we take both the measured input and output fractions directly so that the flux ratio is equal to the ratio of the obtained fractions of the standard, during the blank (plasma off) and plasma on measurement [6]. The gas expansion coefficient, or flux ratio (α), was calculated using [6]:

$$\alpha = \frac{\dot{n}_{tot}^{out}}{\dot{n}_{tot}^{in}} = \frac{c_{standard}^{in}}{c_{standard}^{out}} = \frac{A_{standard}^{in}}{A_{standard}^{out}}$$
(B.1)

where the molar flow rate (\dot{n}) is assumed constant, with $A_{standard}$ the signal (e.g., peak area in the GC chromatogram) corresponding to the internal standard. The signal and the concentration (c) of the standard are assumed to be linear, and the gas streams are both stable and sufficiently mixed before entering the analytical equipment. $A_{standard}^{in}$ is measured using a blank (or 'plasma off' measurements on the reactants and the internal standard). $A_{standard}^{out}$ is measured during the experimental run, thus giving the relative change in gas expansion or contraction.

The absolute conversion (χ_{abs}) is calculated using:

$$\chi_{abs,i} = \frac{y_i^{in} - \alpha \cdot y_i^{out}}{y_i^{in}} \tag{B.2}$$

where y_i^{in} is the concentration of the inlet reactant (given by a blank measurement), y_i^{out} is the concentration of the unreacted species at the outlet, as measured by GC. This metric only considers a single reactant.

However, when considering the whole input mixture, it is necessary to calculate the effective conversion (χ_{eff}) , which is the weighted χ_{abs} with the fraction of the gas at the inlet (y_i^{in}) :

$$\chi_{eff} = \chi_{abs} \cdot y_i^{in} \tag{B.3}$$

The value for χ_{eff} is used to calculate the total conversion χ_{total} :

$$\chi_{total} = \sum_{i} \chi_{eff_i} \tag{B.4}$$

which takes the sum of the χ_{eff} of each reactant (in our case, CO₂ and CH₄). The value for χ_{total} is used to calculate energy cost (EC_{tot}) :

$$EC_{tot} = \frac{SEI}{\chi_{tot}} \tag{B.5}$$

where SEI is the specific energy input to all reactants (i.e., CO_2 and CH_4) (in kJ/mol, kJ/L, or eV/molecule). Furthermore, the selectivity for a certain reaction product (j) is defined as the ratio of the atoms (a) that are from the conversion of the reactants (i):

$$S_{j,a} = \frac{\mu_{j,a} \cdot \alpha \cdot c_j^{out}}{\sum_i \mu_{i,a} \cdot \left(c_i^{in} - \alpha \cdot c_i^{out}\right)}$$
(B.6)

where $\mu_{j,a}$ is the number of atoms (a) per molecule of j, and $\mu_{i,a}$ is the number of atoms for reactant (i). The measured output concentrations are multiplied with the gas expansion factor, such that the input and output become inflows and outflows instead of concentrations. For the metrics reported, a standard error propagation analysis was derived using the standard deviation in each of the variables (e.g., concentration, as discussed in Section B.1.5, flow rates and power measurements) to determine the overall uncertainty in each value.

B.2 Modeling

B.2.1 Water-Gas Shift Equilibrium and H₂O Formation

As shown in the main text in Section 3.1, the dominant reactions governing CO_2 conversion in our model are:

$$CO_2 + M \rightleftharpoons CO + O + M$$
 (B.R.1)

$$CO_2 + O \rightleftharpoons CO + O_2$$
 (B.R.2)

$$CO_2 + H \rightleftharpoons CO + OH$$
 (B.R.3)

where B.R.1 shows the thermal dissociation reaction (which occurs upon collision with a third body, denoted as M), B.R.2 represents oxidation by O atoms, also leading to dissociation, and B.R.3 is H-mediated conversion. As discussed in the main text, we can assume the chemistry is thermal. The rate coefficients are defined by the GRI-Mech 3.0 reaction mechanism [7], where the reverse rates are calculated according to the principle of detailed balance.

Besides the reduction in back reactions, as explained in Section 4.3.1 in Chapter 4, the addition of CH₄ also leads to a substantial further conversion of CO₂ via B.R.3. The reaction of CO₂ with H atoms is related to the reverse water-gas shift reaction, where H₂ reacts with CO₂ to produce CO and H₂O. As CH₄ is oxidized by the available oxygen, the dissociated hydrogen reacts with CO₂, forming CO and H₂O, following the water-gas shift equilibrium:

$$K_{eq}(T) = \frac{[\text{CO}_2] \cdot [\text{H}_2]}{[\text{CO}] \cdot [\text{H}_2\text{O}]}$$
(B.E8)

where $K_{eq}(T)$ is the temperature-dependent equilibrium constant of the water-gas shift reaction.

Figure B.4 illustrates the formation of H_2O through the reverse water-gas shift reaction. The solid dark blue line represents the H_2O molar fraction obtained from the kinetic simulation, while the dashed light blue line indicates the H_2O molar fraction calculated from the CO₂, CO, and H₂ concentrations in the model, adhering to the equilibrium defined by $K_{eq}(T)$.

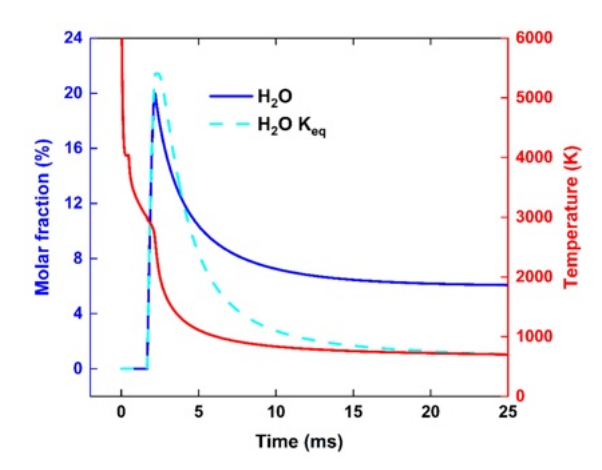


FIGURE B.4: $\rm H_2O$ molar fraction as function of time, calculated by the kinetic simulation (solid dark blue line) and predicted by the water-gas shift equilibrium (dashed light blue line), for a pressure of 500 mbar, a power of 1000 W and $\rm CO_2:CH_4$ ratio of 10:14 slm. The temperature is plotted in red on the right y-axis.

From Figure B.4, it is evident that the H₂O concentration initially follows the water-gas shift equilibrium, reaching a maximum H₂O fraction of 20%, corresponding to a gas temperature of approximately 2800 K, which is plotted on the right y-axis. As the simulation proceeds, the H₂O molar fraction diverges from that predicted by the equilibrium, as the temperature is no longer high enough for the reaction kinetics to keep up with the water-gas shift equilibrium. Since $K_{eq}(T)$ decreases with increasing temperature due to the negative Gibbs free energy of the reaction ($\Delta G^0 = -28.6kJ/mol$), the H₂O fraction predicted by the water-gas shift equilibrium drops below 1% when the temperature falls below 700 K. In contrast, the H₂O molar fraction predicted by the kinetic simulation stabilizes at a molar fraction of 6%, as the kinetics are too slow to degrade the H₂O. This results in a significant amount of H₂O being formed, leading to a relatively low H₂ selectivity of 47%, as shown in Figure 4.6 in Chapter 4.

B.2.2 Model Projections for Higher SEI Conditions

Since the addition of CH₄ to the hot CO₂ mixture leads to further CO₂ conversion via the reverse water-gas shift reaction involving the H atoms generated from CH₄ oxidation, the benefit of increased CO₂ conversion is offset by the loss of H₂, leading to low syngas ratios and lower value products formed (H₂O). Additionally, the CH₄ conversion is relatively

low, as there is insufficient energy in the CO_2 plasma effluent to achieve efficient CH_4 reforming downstream.

The fact that at these lower SEI there is low CH_4 conversion and low H_2 selectivity when CH_4 is injected post-plasma was also predicted by the modeling calculations in *Albrechts* et al. [8], and is confirmed experimentally in this study. These modeling calculations show that increasing the SEI would increase the CH_4 conversion and H_2 selectivity, therefore increasing the syngas ratio.

Therefore, we predict that if the plasma input power could be increased while avoiding plasma instability by injecting CH₄ post-plasma, significantly higher syngas ratios can be obtained. This is supported by the model calculations performed in this work, where for a pressure of 900 mbar, SEI of 267 kJ/mol and CO_2 :CH₄ ratio of 7:14 slm, absolute CO_2 and CH₄ conversions are obtained of 99.4% and 87.8%, respectively, with a syngas ratio of 1.38, where we assumed a more ideal reactor setup with instant CH₄ injection after the plasma and reduction in wall losses by a factor of 10. Applying an $SEI = 240 \ kJ/mol$ and CO_2 :CH₄ ratio of 1:4 yields absolute CO_2 and CH₄ conversions of 99.7% and 74.6%, with an ideal syngas ratio of 2.06. However, it should be noted that in this scenario, 1200 kJ of heat must be applied per mole of CO_2 , likely necessitating a specific and challenging plasma reactor setup.

B.3 Additional Results and Discussion

B.3.1 Additional Results

Comparing the 1000 W data of Figure B.4 with the 1250 W results (Figure 4.7, Chapter 4) reveals several important trends. At the lower power input, all configurations maintain high selectivity toward CO formation, though generally 3-5% lower than at 1250 W. This reduction is most pronounced for the 7:14 slm CO₂:CH₄ ratio (Figure B.4D), particularly at higher pressures.

The selectivity toward H_2 is consistently lower at 1000 W compared to 1250 W across all conditions, indicating less efficient CH_4 conversion at the lower power input. This aligns with the reduced CH_4 conversion observed at 1000 W (discussed in *Figure 4.4* and 4.5

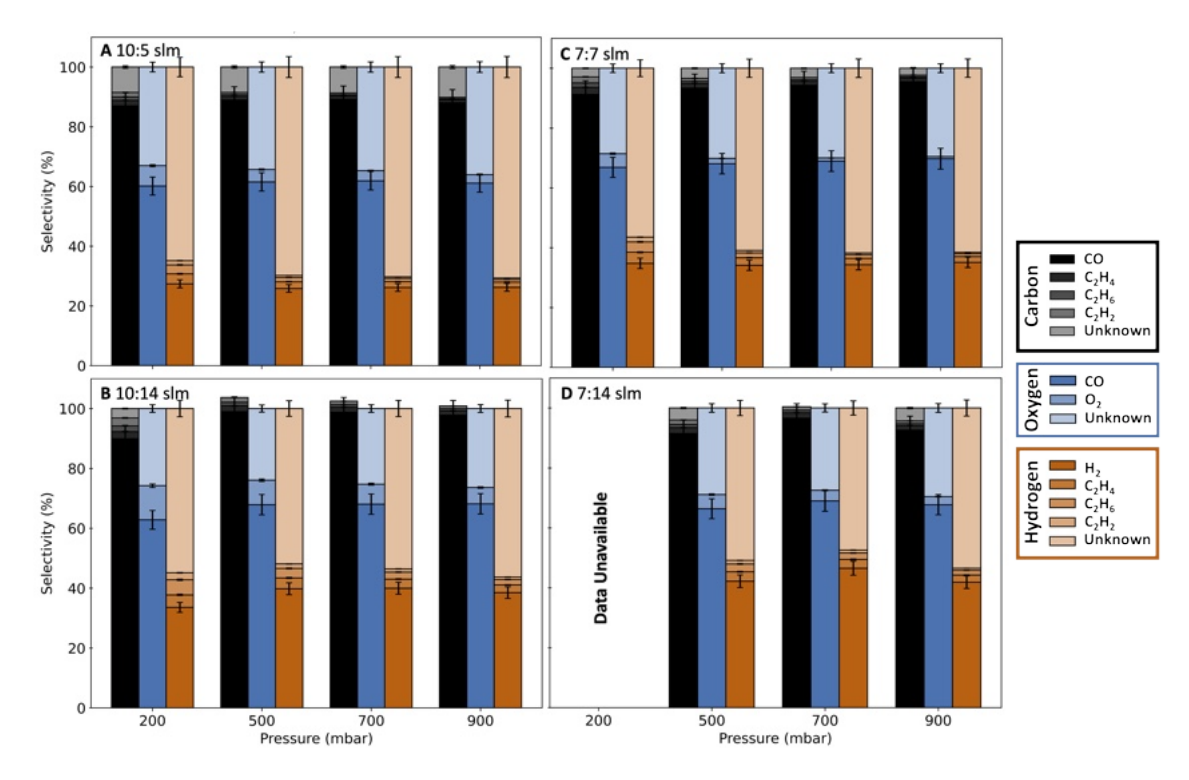


FIGURE B.5: Selectivity data as a function of pressure at p = 1000 W for the primary CO_2 flow rate of 10 slm (A and B) and 7 slm (C and D), with different post-plasma injection flow rates of CH_4 .

in Chapter 4), suggesting that the reduced thermal energy in the afterglow affects both conversion and product distribution.

The formation of C_2 hydrocarbons (C_2H_2 , C_2H_4 , and C_2H_6) appears slightly enhanced at 1000 W, particularly evident in the 10:14 slm and 7:7 slm CO_2 : CH_4 ratio configurations (Figures B.4B and B.4C). This increased selectivity toward C_2H_x species at lower power suggests that the milder temperature conditions in the afterglow region may favor reaction pathways that produce higher hydrocarbons rather than complete reforming to syngas components.

Similar to the 1250 W data, the "unknown" fractions in C, H, and O balances remain; however, the unknown fraction of C atoms remains low in all conditions presented. Therefore, we conclude that the significant unknown component observed in Figure B.4 is likely H_2O , as discussed in Section B.2.2. The unknown fractions of C likely correspond to carbon (at p > 700 mbar) and the liquid oxygenates (formaldehyde, acetic acid, and formic acid) identified and discussed in Figure 4.8 of Chapter 4 (at lower pressure), although here the values for unknown C are much lower than those presented in Chapter 4.

For clarity of the reported values, the conversion (Tables B.2 - B.5), energy cost (Tables B.6 - B.9), selectivity and yield (Tables B.10 - B.33), data are reported below, with the error derived from the error propagation analysis given.

Table B.2: Conversion data (%) for the 10:5 slm, $CO_2:CH_4$ set.

CO ₂ :CH ₄ slm	Power (W)	Pressure (mbar)	Expansion (α)	CO ₂ Conv	CO_2 Conversion (%)		rersion (%)	Total Conversion
				Absolute	Effective	Absolute	Effective	
10:5	1000	200	1.04	28.0 ± 1.4	18.8 ± 0.7	23.5 ± 3.7	7.7 ± 0.9	26.5 ± 1.1
10:5	1000	500	1.04	28.3 ± 1.4	18.9 ± 0.7	23.7 ± 3.7	7.7 ± 0.9	26.8 ± 1.1
10:5	1000	700	1.04	28.2 ± 1.4	18.9 ± 0.7	23.9 ± 3.7	7.8 ± 0.9	26.8 ± 1.1
10:5	1000	900	1.03	28.1 ± 1.4	18.8 ± 0.7	23.9 ± 3.7	7.8 ± 0.9	26.8 ± 1.1
10:5	1250	200	1.05	35.2 ± 1.3	23.6 ± 0.7	32.7 ± 3.6	10.7 ± 0.9	34.4 ± 1.1
10:5	1250	500			No o	lata		
10:5	1250	700	1.05	35.4 ± 1.3	23.7 ± 0.7	32.9 ± 3.6	10.8 ± 0.9	34.6 ± 1.1
10:5	1250	900	1.05	35.6 ± 1.3	23.9 ± 0.7	33.4 ± 3.6	10.9 ± 0.9	34.9 ± 1.1

Table B.3: Conversion data (%) for the 10:14 slm, CO₂:CH₄ set.

$CO_2:CH_4$ slm	Power (W)	Pressure (mbar)	Expansion (α)	CO ₂ Conv	CO_2 Conversion (%)		ersion (%)	Total Conversion
				Absolute	Effective	Absolute	Effective	
10:14	1000	200	1.02	27.6 ± 1.9	11.7 ± 0.7	8.7 ± 2.4	5.0 ± 1.1	16.7 ± 1.3
10:14	1000	500	1.04	27.5 ± 1.9	11.6 ± 0.7	8.1 ± 2.5	4.7 ± 1.1	16.3 ± 1.3
10:14	1000	700	1.04	28.0 ± 1.9	11.8 ± 0.7	8.3 ± 2.4	4.8 ± 1.1	16.7 ± 1.3
10:14	1000	900	1.03	28.3 ± 1.9	11.9 ± 0.7	8.8 ± 2.4	5.1 ± 1.1	17.0 ± 1.3
10:14	1250	200	0.98	39.1 ± 1.6	16.5 ± 0.6	16.8 ± 2.2	9.7 ± 1.0	26.2 ± 1.2
10:14	1250	500	0.98	39.5 ± 1.6	16.7 ± 0.6	16.5 ± 2.2	9.5 ± 1.0	26.2 ± 1.2
10:14	1250	700	1.04	35.5 ± 1.6	15.0 ± 0.6	12.0 ± 2.2	6.9 ± 1.0	21.9 ± 1.2
10:14	1250	900	1.02	39.6 ± 1.8	15.6 ± 0.7	13.9 ± 2.4	8.0 ± 1.1	23.6 ± 1.3

Table B.4: Conversion data (%) for the 7:7 slm, CO₂:CH₄ set.

$CO_2:CH_4$ slm	Power (W)	Pressure (mbar)	Expansion (α)	CO_2 Conv	CO_2 Conversion (%)		CH_4 Conversion (%)		
				Absolute	Effective	Absolute	Effective		
7:7	1000	200	1.06	38.8 ± 1.5	19.6 ± 0.6	19.8 ± 2.6	9.8 ± 0.9	29.4 ± 1.1	
7:7	1000	500	1.06	39.5 ± 1.5	20.0 ± 0.6	19.8 ± 2.6	9.8 ± 0.9	29.8 ± 1.1	
7:7	1000	700	1.06	39.5 ± 1.5	20.0 ± 0.6	20.0 ± 2.6	9.9 ± 0.9	29.9 ± 1.1	
7:7	1000	900	1.06	39.3 ± 1.5	19.9 ± 0.6	19.8 ± 2.6	9.8 ± 0.9	29.6 ± 1.1	
7:7	1250	200			No o	lata			
7:7	1250	500	1.02	54.6 ± 1.3	27.6 ± 0.6	36.7 ± 2.3	18.1 ± 0.9	45.8 ± 1.0	
7:7	1250	700	1.04	52.1 ± 1.3	26.4 ± 0.6	29.9 ± 2.3	14.8 ± 0.9	41.1 ± 1.0	
7:7	1250	900	1.08	49.6 ± 1.4	25.1 ± 0.6	26.6 ± 2.4	13.2 ± 0.9	38.2 ± 1.1	

CO ₂ :CH ₄ slm	Power (W)	Pressure (mbar)	Expansion (α)	CO_2 Conversion (%)		CH ₄ Conve	ersion (%)	Total Conversion
				Absolute	Effective	Absolute	Effective	
7:14	1000	200			No d	ata		
7:14	1000	500	1.03	41.1 ± 1.3	13.9 ± 0.5	10.3 ± 1.6	6.8 ± 0.8	20.7 ± 0.9
7:14	1000	700	1.05	40.3 ± 1.3	13.6 ± 0.5	9.6 ± 1.6	6.3 ± 0.8	20.0 ± 0.9
7:14	1000	900	1.03	40.3 ± 1.3	13.7 ± 0.5	10.3 ± 1.6	6.8 ± 0.8	20.5 ± 0.9
7:14	1250	200	1.07	51.2 ± 1.2	17.3 ± 0.5	14.2 ± 1.5	9.4 ± 0.8	26.7 ± 0.9
7:14	1250	500	1.08	52.3 ± 1.2	17.7 ± 0.5	14.4 ± 1.5	9.5 ± 0.8	27.2 ± 0.9
7:14	1250	700	1.07	52.6 ± 1.2	17.8 ± 0.5	14.6 ± 1.5	9.7 ± 0.8	27.5 ± 0.9
7:14	1250	900	1.07	52.4 ± 1.1	17.7 ± 0.5	14.4 ± 1.5	9.5 ± 0.8	27.3 ± 0.9

Table B.5: Conversion data (%) for the 7:14 slm, CO_2 : CH_4 set.

Table B.6: Specific Energy Input (SEI) and Energy Cost (EC) data for the 10:5 slm, ${\rm CO_2:CH_4~set.}$

$CO_2:CH_4$ slm	Power (W)	Pressure (mbar)	$\begin{array}{c} {\rm SEI} \\ [kJ/mol] \end{array}$	Energy Cost $[kJ/mol]$	$_{[kJ/L]}^{\mathrm{SEI}}$	Energy Cost $[kJ/L]$	$\begin{array}{c} {\rm SEI} \\ [eV/molecule] \end{array}$	Energy Cost $[eV/molecule]$	H ₂ /CO Ratio
10:5	1000	200	98 ± 5	371 ± 19	4.09 ± 0.20	15.40 ± 0.77	1.02 ± 0.05	3.84 ± 0.19	0.17
10:5	1000	500	98 ± 5	367 ± 18	4.09 ± 0.20	15.27 ± 0.76	1.02 ± 0.05	3.81 ± 0.19	0.16
10:5	1000	700	98 ± 5	367 ± 18	4.09 ± 0.20	15.28 ± 0.76	1.02 ± 0.05	3.81 ± 0.19	0.16
10:5	1000	900	98 ± 5	368 ± 18	4.09 ± 0.20	14.86 ± 0.76	1.02 ± 0.05	3.81 ± 0.19	0.17
10:5	1250	200	123 ± 6	357 ± 18	5.11 ± 0.26	14.57 ± 0.74	1.27 ± 0.06	3.70 ± 0.19	0.21
10:5	1250	500				No data			
10:5	1250	700	123 ± 6	356 ± 18	5.11 ± 0.26	14.78 ± 0.74	1.27 ± 0.06	3.68 ± 0.19	0.20
10:5	1250	900	123 ± 6	352 ± 18	5.11 ± 0.26	$14.64 \!\pm 0.73$	1.27 ± 0.06	3.65 ± 0.19	0.20

TABLE B.7: Specific Energy Input (SEI) and Energy Cost (EC) data for the 10:14 slm, $\rm CO_2:CH_4$ set.

CO ₂ :CH ₄ slm	Power (W)	Pressure (mbar)	$\begin{array}{c} {\rm SEI} \\ [kJ/mol] \end{array}$	Energy Cost $[kJ/mol]$	$\begin{array}{c} \mathrm{SEI} \\ [kJ/L] \end{array}$	Energy Cost $[kJ/L]$	$\begin{array}{c} {\rm SEI} \\ [eV/molecule] \end{array}$	Energy Cost $[eV/molecule]$	H ₂ /CO Ratio
10:14	1000	200	62 ± 3	371 ± 19	2.57 ± 0.13	15.41 ± 0.77	0.64 ± 0.03	3.84 ± 0.19	0.21
10:14	1000	500	62 ± 3	380 ± 19	2.57 ± 0.13	15.77 ± 0.79	0.64 ± 0.03	3.93 ± 0.20	0.22
10:14	1000	700	62 ± 3	371 ± 19	2.57 ± 0.13	15.43 ± 0.77	0.64 ± 0.03	3.85 ± 0.19	0.22
10:14	1000	900	62 ± 3	364 ± 18	2.57 ± 0.13	15.12 ± 0.76	0.64 ± 0.03	3.77 ± 0.19	0.22
10:14	1250	200	77 ± 4	295 ± 15	3.21 ± 0.16	12.25 ± 0.61	0.80 ± 0.04	3.05 ± 0.15	0.27
10:14	1250	500	77 ± 4	295 ± 15	3.21 ± 0.16	12.26 ± 0.61	0.80 ± 0.04	3.06 ± 0.15	0.26
10:14	1250	700	77 ± 4	353 ± 18	3.21 ± 0.16	14.67 ± 0.73	0.80 ± 0.04	3.66 ± 0.18	0.26
10:14	1250	900	77 ± 4	327 ± 16	3.21 ± 0.16	13.60 ± 0.68	0.80 ± 0.04	3.39 ± 0.17	0.26

Table B.8: Specific Energy Input (SEI) and Energy Cost (EC) data for the 7:7 slm, $\rm CO_2{:}CH_4$ set.

	- D	- D	CET		CDI		CDI	F G :	TT /00
$CO_2:CH_4$	Power	Pressure	SEI	Energy Cost	SEI	Energy Cost	SEI	Energy Cost	H_2/CO
slm	(W)	(mbar)	[kJ/mol]	[kJ/mol]	[kJ/L]	[kJ/L]	[eV/molecule]	[eV/molecule]	Ratio
7:7	1000	200	106 ± 5	360 ± 19	4.40 ± 0.22	14.96 ± 0.75	1.10 ± 0.05	3.73 ± 0.19	0.24
7:7	1000	500	106 ± 5	355 ± 18	4.40 ± 0.22	14.76 ± 0.74	1.10 ± 0.05	3.68 ± 0.18	0.23
7:7	1000	700	106 ± 5	354 ± 18	4.40 ± 0.22	14.72 ± 0.74	1.10 ± 0.05	3.67 ± 0.18	0.23
7:7	1000	900	106 ± 5	357 ± 18	4.40 ± 0.22	14.84 ± 0.74	1.10 ± 0.05	3.70 ± 0.18	0.23
7:7	1250	200				No data			
7:7	1250	500	132 ± 7	289 ± 18	5.50 ± 0.27	12.01 ± 0.60	1.37 ± 0.07	3.00 ± 0.15	0.30
7:7	1250	700	132 ± 7	322 ± 18	5.50 ± 0.27	13.37 ± 0.67	1.37 ± 0.07	3.33 ± 0.17	0.29
7:7	1250	900	132 ± 7	346 ± 18	5.50 ± 0.27	14.38 ± 0.72	1.37 ± 0.07	3.59 ± 0.18	0.29

Table B.9: Specific Energy Input (SEI) and Energy Cost data for the 7:14 slm, $CO_2:CH_4$ set.

CO ₂ :CH ₄	Power (W)	Pressure (mbar)	$\begin{array}{c} \mathrm{SEI} \\ [kJ/mol] \end{array}$	Energy Cost $[kJ/mol]$	$\begin{array}{c} \mathrm{SEI} \\ [kJ/L] \end{array}$	Energy Cost $[kJ/L]$	$\begin{array}{c} {\rm SEI} \\ [eV/molecule] \end{array}$	Energy Cost $[eV/molecule]$	$ m H_2/CO$ Ratio
7:14	1000	200				No data			
7:14	1000	500	71 ± 4	342 ± 17	2.94 ± 0.15	14.23 ± 0.71	0.73 ± 0.04	3.55 ± 0.18	0.29
7:14	1000	700	71 ± 4	355 ± 18	2.57 ± 0.15	14.74 ± 0.74	0.73 ± 0.04	3.68 ± 0.18	0.29
7:14	1000	900	71 ± 4	346 ± 17	2.57 ± 0.15	14.37 ± 0.72	0.73 ± 0.04	3.58 ± 0.18	0.29
7:14	1250	200	89 ± 4	332 ± 17	3.68 ± 0.18	13.78 ± 0.69	0.92 ± 0.05	3.44 ± 0.17	0.37
7:14	1250	500	89 ± 4	325 ± 16	3.68 ± 0.18	13.51 ± 0.68	0.92 ± 0.05	3.37 ± 0.17	0.38
7:14	1250	700	89 ± 4	322 ± 16	3.68 ± 0.18	13.38 ± 0.67	0.92 ± 0.05	3.34 ± 0.17	0.38
7:14	1250	900	89 ± 4	325 ± 16	3.68 ± 0.18	13.49 ± 0.67	0.92 ± 0.05	3.36 ± 0.17	0.37

Table B.10: Carbon selectivity (%) for the 10:5 slm, $CO_2:CH_4$ set.

Power (W)	Pressure (mbar)	СО	C_2H_4	C_2H_6	C_2H_2	Unknown
1000	200	87.0 ± 2.4	1.8 ± 0.2	1.1 ± 0.1	1.6 ± 0.2	8.5
1000	500	89.0 ± 2.5	1.2 ± 0.2	0.5 ± 0.1	0.7 ± 0.2	8.5
1000	700	89.2 ± 2.5	1.1 ± 0.2	0.4 ± 0.1	0.6 ± 0.2	8.7
1000	900	88.0 ± 2.4	1.0 ± 0.2	0.3 ± 0.1	0.5 ± 0.2	10.1
1250	200	90.7 ± 2.0	1.7 ± 0.1	0.8 ± 0.1	1.2 ± 0.2	5.5
1250	500			No data		
1250	700	91.9 ± 2.0	1.0 ± 0.1	0.3 ± 0.1	0.5 ± 0.2	6.3
1250	900	93.1 ± 2.0	1.0 ± 0.1	0.3 ± 0.1	0.4 ± 0.2	5.3

Table B.11: Carbon selectivity (%) fractions for the 10:14 slm, $\mathrm{CO}_2\mathrm{:CH}_4$ set.

Power (W)	Pressure (mbar)	СО	C_2H_4	C_2H_6	C_2H_2	Unknown
1000	200	89.9 ± 4.5	2.4 ± 0.3	1.9 ± 0.2	2.7 ± 0.3	3.1
1000	500	99.0 ± 5.1	2.0 ± 0.3	1.1 ± 0.2	1.6 ± 0.3	-3.7
1000	700	98.8 ± 5.0	1.7 ± 0.3	0.9 ± 0.1	1.2 ± 0.3	-2.5
1000	900	97.8 ± 4.8	1.5 ± 0.3	0.7 ± 0.1	0.9 ± 0.3	-0.9
1250	200	73.5 ± 2.3	1.8 ± 0.2	1.3 ± 0.1	1.8 ± 0.2	21.7
1250	500	76.6 ± 2.4	1.3 ± 0.2	0.7 ± 0.1	1.0 ± 0.2	20.3
1250	700	97.4 ± 3.5	1.5 ± 0.2	0.7 ± 0.1	1.0 ± 0.2	-0.6
1250	900	88.7 ± 3.2	1.2 ± 0.2	0.5 ± 0.1	0.7 ± 0.2	8.8

Table B.12: Carbon selectivity (%) for the 7:7 slm, CO_2 : CH_4 set.

Power (W)	Pressure (mbar)	СО	C_2H_4	C_2H_6	C_2H_2	Unknown
1000	200	91.2 ± 2.2	2.4 ± 0.2	1.5 ± 0.1	2.0 ± 0.2	2.9
1000	500	93.4 ± 2.3	1.6 ± 0.2	0.7 ± 0.1	1.0 ± 0.2	3.4
1000	700	94.3 ± 2.3	1.3 ± 0.2	0.5 ± 0.1	0.7 ± 0.2	3.1
1000	900	95.5 ± 2.3	1.2 ± 0.2	0.4 ± 0.1	0.6 ± 0.2	2.3
1250	200			No data		
1250	500	72.5 ± 1.2	1.2 ± 0.1	0.4 ± 0.1	0.6 ± 0.1	25.4
1250	700	85.6 ± 1.5	1.1 ± 0.1	0.3 ± 0.1	0.5 ± 0.1	12.5
1250	900	94.7 ± 1.8	1.1 ± 0.1	0.3 ± 0.1	0.4 ± 0.2	3.6

Power (W)	Pressure (mbar)	CO	C_2H_4	C_2H_6	C_2H_2	Unknown
1000	200			No data		
1000	500	91.5 ± 3.5	2.0 ± 0.2	1.1 ± 0.1	1.5 ± 0.3	4.0
1000	700	96.6 ± 3.8	1.8 ± 0.2	0.9 ± 0.1	1.2 ± 0.3	-0.4
1000	900	92.6 ± 3.5	1.5 ± 0.2	0.7 ± 0.1	0.9 ± 0.3	4.3
1250	200	92.9 ± 2.8	2.6 ± 0.2	1.5 ± 0.1	2.1 ± 0.2	0.9
1250	500	95.7 ± 2.8	1.9 ± 0.2	0.9 ± 0.1	1.2 ± 0.2	0.4
1250	700	95.4 ± 2.8	1.6 ± 0.2	0.7 ± 0.1	0.9 ± 0.2	1.4
1250	900	96.4 ± 2.8	1.4 ± 0.2	0.5 ± 0.1	0.7 ± 0.2	1.0

Table B.13: Carbon selectivity (%) for the 7:14 slm, CO₂:CH₄ set.

Table B.14: Carbon yield (%) for the 10:5 slm, $\mathrm{CO}_2\mathrm{:}\mathrm{CH}_4$ set.

Power (W)	Pressure (mbar)	СО	C_2H_4	C_2H_6	C_2H_2	Unknown
1000	200	23.1 ± 0.2	$0.5 \pm 5 e-2$	$0.3 \pm 3e-2$	$0.4 \pm 6e-2$	2.2
1000	500	23.9 ± 0.2	$0.3 \pm 5\text{e-}2$	$0.1 \pm 3e-2$	$0.2 \pm 6e-2$	2.2
1000	700	23.9 ± 0.2	$0.3 \pm 5 \text{e-}2$	$0.1 \pm 3e-2$	$0.2 \pm 6e-2$	2.3
1000	900	23.6 ± 0.2	$0.3 \pm 5 \text{e-}2$	$0.1 \pm 3e-2$	$0.1 \pm 6e-2$	2.7
1250	200	31.2 ± 0.3	$0.6 \pm 5 \text{e-}2$	$0.3 \pm 3e-2$	$0.4 \pm 6 e$ -2	1.9
1250	500			No data		
1250	700	31.8 ± 0.3	$0.4 \pm 5 \text{e-}2$	$0.1 \pm 3e-2$	$0.2 \pm 6e-2$	2.2
1250	900	32.5 ± 0.3	$0.3 \pm 5\text{e-}2$	$0.1 \pm 3e-2$	$0.1 \pm 6\text{e-}2$	1.8

Table B.15: Carbon yield (%) for the 10:14 slm, CO_2 : CH_4 set.

Power (W)	Pressure (mbar)	СО	$\mathrm{C_{2}H_{4}}$	C_2H_6	C_2H_2	Unknown
1000	200	15.3 ± 0.2	$0.4 \pm 4e-2$	$0.3 \pm 2e-2$	$0.5 \pm 5 e-2$	0.2
1000	500	16.5 ± 0.2	$0.3 \pm 4 \text{e-}2$	$0.2 \pm 2e$ -2	$0.3 \pm 5\text{e-}2$	-1.0
1000	700	16.8 ± 0.2	$0.3 \pm 4\text{e-}2$	$0.1 \pm 2e$ -2	$0.2 \pm 5\text{e-}2$	-0.8
1000	900	17.0 ± 0.2	$0.3\pm4\text{e-}2$	$0.1 \pm 2e$ -2	$0.2 \pm 5\text{e-}2$	-0.5
1250	200	19.6 ± 0.2	$0.5\pm4\text{e-}2$	$0.3 \pm 2e$ -2	$0.5 \pm 5\text{e-}2$	5.4
1250	500	20.4 ± 0.2	$0.4 \pm 4 \text{e-}2$	$0.2 \pm 2e$ -2	$0.3 \pm 5\text{e-}2$	5.0
1250	700	21.7 ± 0.2	$0.3\pm4\text{e-}2$	$0.2 \pm 2e$ -2	$0.2 \pm 5\text{e-}2$	-0.6
1250	900	21.3 ± 0.2	$0.3 \pm 4\text{e-}2$	$0.1 \pm 2e$ -2	$0.2 \pm 5\text{e-}2$	1.7

Power (W)	Pressure (mbar)	CO	$\mathrm{C_2H_4}$	C_2H_6	C_2H_2	Unknown
1000	200	27.1 ± 0.2	$0.7 \pm 5e-2$	$0.4 \pm 3e-2$	$0.6 \pm 6e-2$	0.5
1000	500	28.1 ± 0.2	$0.5 \pm 5 \text{e-}2$	$0.2 \pm 3e-2$	$0.3 \pm 6e-2$	0.7
1000	700	28.5 ± 0.2	$0.4 \pm 5 \text{e-}2$	$0.2 \pm 3e-2$	$0.2 \pm 6e-2$	0.6
1000	900	28.6 ± 0.2	$0.4 \pm 5 \text{e-}2$	$0.1 \pm 3e-2$	$0.2 \pm 6e-2$	0.4
1250	200			No data		
1250	500	33.4 ± 0.3	$0.5\pm5\text{e-}2$	$0.2 \pm 3e-2$	$0.3 \pm 6 \text{e-}2$	11.4
1250	700	35.5 ± 0.3	$0.4 \pm 5 \text{e-}2$	$0.1 \pm 3e-2$	$0.2 \pm 6e-2$	4.8
1250	900	36.5 ± 0.3	$0.4 \pm 5 \text{e-}2$	$0.1 \pm 3e-2$	$0.2 \pm 6e-2$	1.0

Table B.16: Carbon yield (%) for the 7:7 slm, $\mathrm{CO}_2\mathrm{:}\mathrm{CH}_4$ set.

Table B.17: Carbon yield (%) for the 7:14 slm, $\mathrm{CO}_2\mathrm{:}\mathrm{CH}_4$ set.

Power (W)	Pressure (mbar)	СО	$\mathrm{C_{2}H_{4}}$	C_2H_6	$\mathrm{C_2H_2}$	Unknown
1000	200			No data		
1000	500	19.4 ± 0.2	$0.4 \pm 4e$ -2	$0.2 \pm 2e$ -2	$0.3 \pm 5 \text{e-}2$	0.3
1000	700	19.8 ± 0.2	$0.4 \pm 4e-2$	$0.2 \pm 2e$ -2	$0.2 \pm 5\text{e-}2$	-0.6
1000	900	19.5 ± 0.2	$0.3\pm4\text{e-}2$	$0.1 \pm 2e$ -2	$0.2 \pm 5\text{e-}2$	0.4
1250	200	25.4 ± 0.2	$0.7\pm4\text{e-}2$	$0.4 \pm 2e$ -2	$0.6 \pm 5 \text{e-}2$	-0.4
1250	500	26.7 ± 0.3	$0.5\pm4\text{e-}2$	$0.2 \pm 2e$ -2	$0.3 \pm 5\text{e-}2$	-0.6
1250	700	26.9 ± 0.3	$0.5\pm4\text{e-}2$	$0.2 \pm 2e$ -2	$0.3 \pm 5\text{e-}2$	-0.3
1250	900	26.9 ± 0.3	$0.4 \pm 4 \text{e-}2$	$0.1 \pm 2e$ -2	$0.2 \pm 5\text{e-}2$	-0.4

Table B.18: Oxygen selectivity (%) for the 10:5 slm, CO_2 : CH_4 set.

Power (W)	Pressure (mbar)	СО	O_2	Unknown
1000	200	60.1 ± 3.2	6.8 ± 1.4	33.0
1000	500	61.5 ± 3.2	4.1 ± 0.9	34.3
1000	700	61.9 ± 3.3	3.4 ± 0.7	34.7
1000	900	61.1 ± 3.2	2.8 ± 0.6	36.0
1250	200	64.6 ± 2.4	3.8 ± 0.6	31.7
1250	500		No data	
1250	700	65.4 ± 2.4	1.7 ± 0.3	32.9
1250	900	66.5 ± 2.4	1.4 ± 0.2	32.2

Power (W)	Pressure (mbar)	СО	O_2	Unknown
1000	200	62.8 ± 5.6	11.4 ± 3.3	25.8
1000	500	67.9 ± 5.9	8.2 ± 2.4	24.0
1000	700	68.0 ± 5.7	6.7 ± 1.9	25.3
1000	900	68.2 ± 5.6	5.5 ± 1.6	26.4
1250	200	56.7 ± 3.0	5.9 ± 1.2	37.4
1250	500	58.6 ± 3.0	3.9 ± 0.8	37.5
1250	700	69.6 ± 3.9	3.7 ± 0.8	26.7
1250	900	65.6 ± 3.6	2.8 ± 0.6	31.6

Table B.19: Oxygen selectivity (%) fractions for the 10:14 slm, $\mathrm{CO}_2\mathrm{:CH}_4$ set.

Table B.20: Oxygen selectivity (%) for the 7:7 slm, $CO_2:CH_4$ set.

Power (W)	Pressure (mbar)	СО	O_2	Unknown
1000	200	66.9 ± 3.0	4.6 ± 0.9	28.6
1000	500	68.1 ± 2.9	1.8 ± 0.3	30.1
1000	700	69.0 ± 2.9	1.1 ± 0.2	30.0
1000	900	69.7 ± 3.0	0.8 ± 0.2	29.5
1250	200		No data	
1250	500	58.5 ± 1.6	0.9 ± 0.1	40.6
1250	700	65.2 ± 1.8	$0.3 \pm 5\text{e-}2$	34.4
1250	900	70.6 ± 2.1	$0.2 \pm 2e$ -2	29.3

Table B.21: Oxygen selectivity (%) for the 7:14 slm, $\mathrm{CO}_2\mathrm{:}\mathrm{CH}_4$ set.

Power (W)	Pressure (mbar)	СО	O_2	Unknown
1000	200		No data	_
1000	500	66.4 ± 4.1	4.8 ± 1.2	28.9
1000	700	69.0 ± 4.3	3.6 ± 0.9	27.5
1000	900	67.7 ± 4.3	2.7 ± 0.7	29.6
1250	200	69.7 ± 3.0	3.6 ± 0.7	26.7
1250	500	71.6 ± 3.0	1.6 ± 0.3	26.8
1250	700	71.7 ± 3.0	1.0 ± 0.2	27.4
1250	900	72.1 ± 3.0	0.7 ± 0.1	27.2

Power (W)	Pressure (mbar)	СО	${\rm O}_2$	Unknown
1000	200	16.8 ± 0.1	1.9 ± 0.1	18.9
1000	500	17.4 ± 0.1	1.2 ± 0.1	19.4
1000	700	17.4 ± 0.1	$1.0 \pm 5\text{e-}2$	19.4
1000	900	17.2 ± 0.1	$0.8\pm4\text{e-}2$	19.8
1250	200	22.7 ± 0.1	1.3 ± 0.1	23.3
1250	500		No data	
1250	700	23.2 ± 0.1	$0.6 \pm 3e-2$	23.8

1250

900

Table B.22: Oxygen yield (%) for the 10:5 slm, $\rm CO_2: CH_4$ set.

Table B.23: Oxygen yield (%) for the 10:14 slm, CO₂:CH₄ set.

 $23.7 \pm 0.1 \quad 0.5 \pm 3e-2$

23.7

Power (W)	Pressure (mbar)	СО	O_2	Unknown
1000	200	17.4 ± 0.2	3.2 ± 0.2	2.8
1000	500	18.7 ± 0.2	2.3 ± 0.1	2.3
1000	700	19.1 ± 0.2	1.9 ± 0.1	2.7
1000	900	19.3 ± 0.2	1.5 ± 0.1	3.1
1250	200	22.2 ± 0.2	2.3 ± 0.1	8.6
1250	500	23.1 ± 0.2	1.6 ± 0.1	8.7
1250	700	24.7 ± 0.2	1.3 ± 0.1	4.0
1250	900	24.2 ± 0.2	$1.0 \pm 5\text{e-}2$	5.9

Table B.24: Oxygen yield (%) for the 7:7 slm, $\mathrm{CO}_2\mathrm{:}\mathrm{CH}_4$ set.

Power (W)	Pressure (mbar)	СО	O_2	Unknown
1000	200	25.9 ± 0.2	1.8 ± 0.1	11.5
1000	500	26.9 ± 0.2	$0.7\pm4\text{e-}2$	12.4
1000	700	27.3 ± 0.2	$0.4 \pm 2e$ -2	12.3
1000	900	27.4 ± 0.2	$0.3 \pm 2e$ -2	12.0
1250	200		No data	
1250	500	32.0 ± 0.2	$0.5 \pm 3e-2$	22.8
1250	700	34.0 ± 0.2	$0.2 \pm 1e-2$	18.6
1250	900	35.0 ± 0.2	$0.1 \pm 4e-3$	15.1

Power (W)	Pressure (mbar)	СО	${\rm O}_2$	Unknown
1000	200		No data	
1000	500	27.3 ± 0.3	2.0 ± 0.1	-1.4
1000	700	27.8 ± 0.3	1.4 ± 0.1	-1.9
1000	900	27.3 ± 0.3	$1.1 \pm 5\text{e-}2$	-1.1
1250	200	35.7 ± 0.3	1.8 ± 0.1	-2.9
1250	500	37.5 ± 0.3	$0.8\pm4\text{e-}2$	-2.9
1250	700	37.7 ± 0.3	$0.5 \pm 3e-2$	-2.6
1250	900	37.8 ± 0.3	$0.3 \pm 2e-2$	-2.7

Table B.25: Oxygen yield (%) for the 7:14 slm, $\mathrm{CO}_2\mathrm{:}\mathrm{CH}_4$ set.

Table B.26: Hydrogen selectivity (%) for the 10:5 slm, CO_2 : CH_4 set.

Power (W)	Pressure (mbar)	H_2	C_2H_4	C_2H_6	C_2H_2	Unknown
1000	200	27.4 ± 2.3	3.3 ± 0.4	3.0 ± 0.3	1.4 ± 0.2	64.9
1000	500	25.8 ± 2.2	2.2 ± 0.3	1.4 ± 0.3	0.7 ± 0.2	69.8
1000	700	26.2 ± 2.2	2.0 ± 0.3	1.1 ± 0.3	0.5 ± 0.2	70.2
1000	900	26.2 ± 2.2	1.8 ± 0.3	0.9 ± 0.3	0.4 ± 0.2	70.7
1250	200	31.7 ± 1.7	2.9 ± 0.3	2.1 ± 0.2	1.0 ± 0.1	62.3
1250	500			No data		
1250	700	30.9 ± 1.7	1.7 ± 0.2	0.8 ± 0.2	0.4 ± 0.1	66.1
1250	900	31.5 ± 1.7	1.6 ± 0.2	0.7 ± 0.2	0.3 ± 0.1	65.9

Table B.27: Hydrogen selectivity (%) fractions for the 10:14 slm, CO_2 : CH_4 set.

Power (W)	Pressure (mbar)	H_2	$\mathrm{C_{2}H_{4}}$	C_2H_6	$\mathrm{C_2H_2}$	Unknown
1000	200	33.6 ± 4.2	4.2 ± 0.6	5.0 ± 0.6	2.3 ± 0.4	54.9
1000	500	39.8 ± 5.1	3.6 ± 0.6	3.2 ± 0.5	1.5 ± 0.3	51.9
1000	700	40.0 ± 4.9	3.0 ± 0.5	2.3 ± 0.4	1.1 ± 0.3	53.6
1000	900	38.5 ± 4.5	2.6 ± 0.5	1.8 ± 0.4	0.8 ± 0.3	56.3
1250	200	28.1 ± 1.9	2.6 ± 0.2	2.7 ± 0.2	1.3 ± 0.1	65.3
1250	500	28.9 ± 1.9	1.9 ± 0.2	1.6 ± 0.2	0.7 ± 0.1	66.8
1250	700	41.9 ± 3.4	2.5 ± 0.4	1.8 ± 0.3	0.8 ± 0.2	53.0
1250	900	35.4 ± 2.7	1.9 ± 0.3	1.2 ± 0.2	0.6 ± 0.2	60.8

Power (W)	Pressure (mbar)	H_2	C_2H_4	C_2H_6	C_2H_2	Unknown
1000	200	34.8 ± 2.1	3.7 ± 0.3	3.5 ± 0.3	1.6 ± 0.2	64.9
1000	500	34.1 ± 2.1	2.5 ± 0.3	1.7 ± 0.2	0.8 ± 0.2	69.8
1000	700	34.3 ± 2.1	2.1 ± 0.3	1.2 ± 0.2	0.6 ± 0.2	70.2
1000	900	35.1 ± 2.1	1.9 ± 0.3	1.0 ± 0.2	0.5 ± 0.2	70.7
1250	200			No data		
1250	500	28.7 ± 1.0	1.5 ± 0.1	0.8 ± 0.1	0.4 ± 0.1	66.2
1250	700	35.9 ± 1.4	1.6 ± 0.2	0.7 ± 0.1	0.3 ± 0.1	66.1
1250	900	41.5 ± 1.7	1.6 ± 0.2	0.7 ± 0.2	0.3 ± 0.1	65.9

Table B.28: Hydrogen selectivity (%) for the 7:7 slm, $\mathrm{CO}_2\mathrm{:}\mathrm{CH}_4$ set.

Table B.29: Hydrogen selectivity (%) for the 7:14 slm, CO_2 : CH_4 set.

Power (W)	Pressure (mbar)	H_2	$\mathrm{C_{2}H_{4}}$	C_2H_6	C_2H_2	Unknown
1000	200			No data		
1000	500	42.2 ± 3.7	3.2 ± 0.4	2.6 ± 0.3	1.2 ± 0.2	50.9
1000	700	46.5 ± 4.3	3.0 ± 0.4	2.1 ± 0.3	1.0 ± 0.2	47.4
1000	900	41.9 ± 3.7	2.4 ± 0.4	1.5 ± 0.3	0.7 ± 0.2	53.5
1250	200	52.2 ± 3.2	4.0 ± 0.3	3.4 ± 0.3	1.6 ± 0.2	39.0
1250	500	54.2 ± 3.3	2.9 ± 0.3	1.9 ± 0.2	0.9 ± 0.2	40.1
1250	700	53.5 ± 3.2	2.5 ± 0.3	1.5 ± 0.2	0.7 ± 0.1	41.9
1250	900	54.1 ± 3.3	2.1 ± 0.3	1.2 ± 0.2	0.5 ± 0.1	42.1

Table B.30: Hydrogen yield (%) for the 10:5 slm, CO_2 : CH_4 set.

Power (W)	Pressure (mbar)	H_2	$\mathrm{C_{2}H_{4}}$	C_2H_6	C_2H_2	Unknown
1000	200	6.4 ± 0.5	0.8 ± 0.1	0.7 ± 0.1	0.3 ± 0.1	22.6
1000	500	6.1 ± 0.5	0.5 ± 0.1	0.3 ± 0.1	0.2 ± 0.1	24.0
1000	700	6.3 ± 0.5	0.5 ± 0.1	0.3 ± 0.1	0.1 ± 0.1	24.3
1000	900	6.3 ± 0.5	0.4 ± 0.1	0.2 ± 0.1	0.1 ± 0.1	24.4
1250	200	10.4 ± 0.5	0.9 ± 0.1	0.7 ± 0.1	0.3 ± 0.1	30.6
1250	500			No data		
1250	700	10.2 ± 0.5	0.6 ± 0.1	0.3 ± 0.1	0.1 ± 0.1	32.1
1250	900	10.5 ± 0.5	0.5 ± 0.1	0.2 ± 0.1	0.1 ± 0.1	32.5

Power (W)	Pressure (mbar)	H_2	C_2H_4	C_2H_6	C_2H_2	Unknown
1000	200	2.9 ± 0.2	$0.4 \pm 4e-2$	$0.4 \pm 3e-2$	$0.2 \pm 2e$ -2	16.1
1000	500	3.2 ± 0.2	$0.3\pm4\text{e-}2$	$0.3 \pm 3e-2$	$0.1 \pm 2e$ -2	14.8
1000	700	3.3 ± 0.2	$0.3\pm4\text{e-}2$	$0.2 \pm 3e-2$	$0.1 \pm 2e$ -2	15.4
1000	900	3.4 ± 0.2	$0.2 \pm 4e\text{-}2$	$0.2 \pm 3e-2$	$0.1 \pm 2e$ -2	16.4
1250	200	4.7 ± 0.2	$0.4 \pm 3e-2$	$0.5 \pm 3e-2$	$0.2 \pm 2e$ -2	32.9
1250	500	4.8 ± 0.2	$0.3 \pm 3e-2$	$0.3 \pm 3e-2$	$0.1 \pm 2e$ -2	32.6
1250	700	5.0 ± 0.2	$0.3\pm4\text{e-}2$	$0.2 \pm 3e-2$	$0.1 \pm 2e$ -2	22.1
1250	900	4.9 ± 0.2	$0.3 \pm 4e-2$	$0.2 \pm 3e-2$	$0.1 \pm 2e$ -2	26.7

Table B.31: Hydrogen yield (%) for the 10:14 slm, CO₂:CH₄ set.

Table B.32: Hydrogen yield (%) for the 7:7 slm, $CO_2:CH_4$ set.

Power (W)	Pressure (mbar)	H_2	$\mathrm{C_{2}H_{4}}$	C_2H_6	$\mathrm{C_2H_2}$	Unknown
1000	200	6.9 ± 0.3	$0.7 \pm 5e-2$	$0.7 \pm 4e-2$	$0.3 \pm 3e-2$	30.5
1000	500	6.8 ± 0.3	$0.5 \pm 5\text{e-}2$	$0.3 \pm 4e-2$	$0.2 \pm 3e-2$	31.5
1000	700	6.9 ± 0.3	$0.4 \pm 5 \text{e-}2$	$0.2 \pm 4e$ -2	$0.1 \pm 3e-2$	31.9
1000	900	6.9 ± 0.3	$0.4 \pm 5 \text{e-}2$	$0.2 \pm 4e$ -2	$0.1 \pm 3e-2$	31.5
1250	200			No data		
1250	500	10.5 ± 0.3	$0.6 \pm 5 \text{e-}2$	$0.3 \pm 4e-2$	$0.1 \pm 3e-2$	61.0
1250	700	10.7 ± 0.3	$0.5 \pm 5\text{e-}2$	$0.2 \pm 4e\text{-}2$	$0.1 \pm 3e-2$	47.5
1250	900	11.0 ± 0.3	$0.4 \pm 5 \text{e-}2$	$0.2 \pm 4\text{e-}2$	$0.1 \pm 3e-2$	40.9

Table B.33: Hydrogen yield (%) for the 7:14 slm, CO_2 : CH_4 set.

Power (W)	Pressure (mbar)	H_2	$\mathrm{C_{2}H_{4}}$	C_2H_6	C_2H_2	Unknown
1000	200			No data		
1000	500	4.3 ± 0.2	$0.3 \pm 3e-2$	$0.3 \pm 3e-2$	$0.1 \pm 2e$ -2	22.1
1000	700	4.4 ± 0.2	$0.3 \pm 3e-2$	$0.2 \pm 3e-2$	$0.1\pm2\text{e-}2$	20.2
1000	900	4.3 ± 0.2	$0.2 \pm 3e-2$	$0.2 \pm 3e-2$	$0.1 \pm 2e$ -2	22.5
1250	200	7.4 ± 0.2	$0.6 \pm 3e-2$	$0.5 \pm 3e-2$	$0.2 \pm 2e$ -2	28.8
1250	500	7.8 ± 0.2	$0.4 \pm 3e-2$	$0.3 \pm 3e-2$	$0.1 \pm 2e$ -2	29.5
1250	700	7.8 ± 0.2	$0.4 \pm 3e-2$	$0.2 \pm 3e-2$	$0.1 \pm 2e$ -2	30.2
1250	900	7.8 ± 0.2	$0.3 \pm 3e-2$	$0.2 \pm 3e-2$	$0.1 \pm 2e$ -2	29.8

B.3.2 Carbon Analysis

During TEM analyses, the particles analyzed were amorphous, as shown and discussed in the main text, except for one group of particles, shown in *Figure B.5* below.

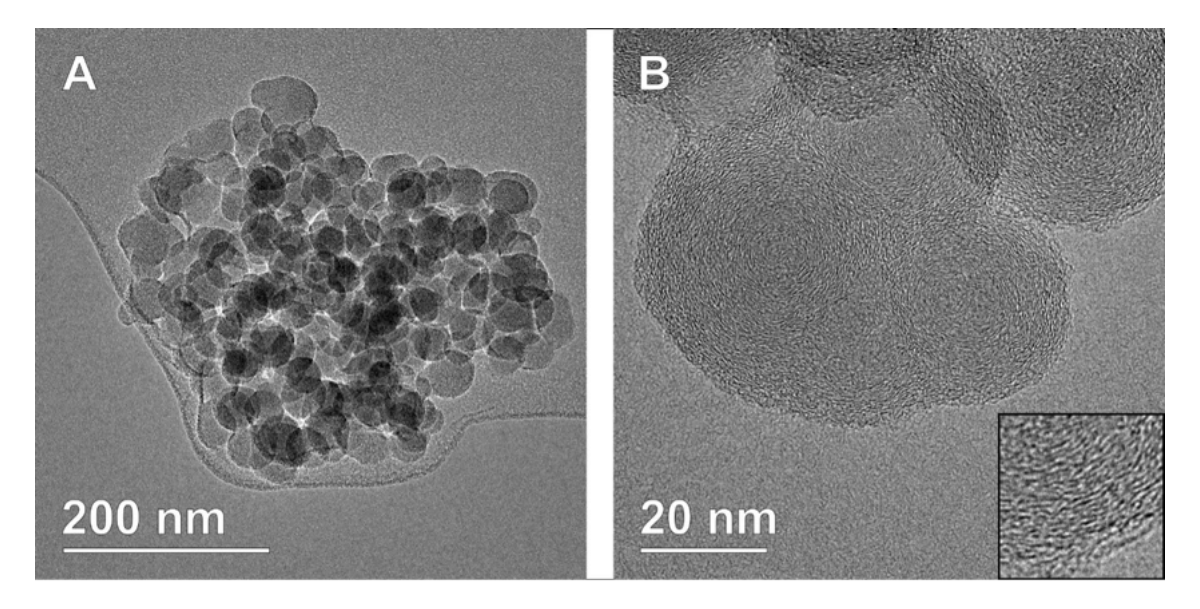


Figure B.6: (A) Group of particles that exhibit a nano-onion-like structure. (B) Higher magnification image of one of the nano-onion particles, presenting the indicative layered structure, highlighted in the inset at double the magnification.

The imaging of the particles in *Figure B.5* exhibited a nano-onion type structure, containing some low-range ordering in the form of concentric layers of carbon, in contrast with the completely amorphous particles observed as the main carbonaceous bi-product, as outlined in Chapter 4 [9]. These particles were rare and are, therefore, not considered a significant part of the produced materials. Still, it does illustrate that the formation of carbon in this system is not trivial and that there may be inhomogeneities in how different gas fractions are treated.

Bibliography

- [1] E. Carbone, F. D'Isa, A. Hecimovic, and U. Fantz. Analysis of the C₂ ($d^3\Pi_g$ - $a^3\Pi_u$) Swan bands as a thermometric probe in CO₂ microwave plasmas. *Plasma Sources* Science and Technology, 2019. doi: 10.1088/1361-6595/ab74b4.
- [2] A.J. Wolf, T.W.H. Righart, F.J.J. Peeters, W.A. Bongers, and M.C.M. van de Sanden. Implications of thermo-chemical instability on the contracted modes in CO₂ microwave plasmas. *Plasma Sources Science and Technology*, 29(2):025005, 2020. doi: 10.1088/ 1361-6595/ab5eca.
- [3] E.R. Mercer, S. Van Alphen, C.F.A.M. van Deursen, T.W.H. Righart, W.A. Bongers, R. Snyders, A. Bogaerts, M.C.M. van de Sanden, and F.J.J. Peeters. Post-plasma quenching to improve conversion and energy efficiency in a CO₂ microwave plasma. Fuel, 334:126734, 2023. doi: 10.1016/j.fuel.2022.126734.
- [4] C.F.A.M. van Deursen, H. Van Poyer, W.A. Bongers, F.J.J. Peeters, F. Smits, and M.C.M. van de Sanden. Effluent nozzles in reverse-vortex-stabilized microwave CO₂ plasmas for improved energy efficiency. *Journal of CO₂ Utilization*, 88:102952, 2024. doi: 10.1016/j.jcou.2024.102952.
- [5] L. Kuijpers. Influence of methane addition to vortex stabilised CO₂ microwave discharges. Master's thesis, Eindhoven University of Technology (TU/e), 2023.
- [6] B. Wanten, R. Vertongen, R. De Meyer, and A. Bogaerts. Plasma-based CO₂ conversion: How to correctly analyze the performance? *Journal of energy chemistry*, 2023.
- [7] G. P. Smith, D. M. Golden, M. Frenklach, N. W. Moriarty, B. Eiteneer, M. Goldenberg, C. T. Bowman, R. K. Hanson, S. Song, W. C. Gardiner Jr., V. V. Lissianski, and

- Z. Qin. GRI-Mech 3.0, 2000. URL http://combustion.berkeley.edu/gri-mech/version30/text30.html.
- [8] M. Albrechts, I. Tsonev, and A. Bogaerts. Can post-plasma CH₄ injection improve plasma-based dry reforming of methane? A modeling study. *Green Chemistry*, 26(18): 9712–9728, 2024. ISSN 1463-9262. doi: 10.1039/D4GC02889A.
- [9] P. Serp and B. Machado. Nanostructured Carbon Materials for Catalysis. The Royal Society of Chemistry, 2015. doi: 10.1039/9781782622567.

Academic Biography

Elizabeth Rose Mercer is a passionate researcher with a lifelong curiosity and joy of problem-solving through science and has specialized in microwave plasma-based technology, with an emphasis on reactor design and modification for sustainable gas conversion. Originally from the United States, Mercer grew up in a rural area of Florida nestled between orange groves and swamp. As a first-generation student, Mercer earned an Associate's Degree in Chemistry at Miami Dade College before securing an internship at the University of Miami with Dr. Eduardo Veliz. This bridged into a two-year undergraduate research project within Prof. Dr. Mare Cudic's lab where Mercer earned an American Chemical Society certified Bachelor of Science in Chemistry from Florida Atlantic University.

After moving to Belgium, Mercer began studying at the University of Antwerp to pursue a Master of Science in Chemistry. During this period, a research internship at the Dutch Institute for Fundamental Energy Research (DIFFER) under the guidance of Prof. Dr. Ir. Richard van de Sanden led to a full thesis project focused on improving post-plasma processes for CO₂ conversion in a 2.45 GHz microwave reactor. This experience marked the beginning of a collaborative relationship with DIFFER, which would later become a pillar of Mercer's Ph.D. work.

Doctoral research conducted at the University of Antwerp within the Plasma Lab for Applications in Sustainability and Medicine - ANTwerp (PLASMANT) group under the supervision of Prof. Dr. Annemie Bogaerts, expanded on these foundations. Mercer's doctoral work focused on microwave plasma-driven conversion of CO₂ into value-added chemicals, with particular attention on improving energy efficiency through process innovations and heat recovery strategies. Key contributions include the design of a dual injection system for Dry Reforming of Methane (DRM), the integration of preheated gas

flows, and the simulation of Martian atmospheric processing in collaboration with the European Space Agency. These efforts aim to advance both Earth-based sustainability solutions and future In-Situ Resource Utilization (ISRU) strategies on Mars.

Beyond the lab, Mercer has been an active community builder. Initiatives such as the Antwerp-Maastricht Plasma Symposium and the Belgian Buddy Project reflect a deep commitment to scientific collaboration and international student support. Leadership within the PLASMANT group's Event Committee further demonstrates a dedication to fostering inclusive and engaged research environments. Mercer has presented work at international conferences, contributed to peer-reviewed publications, and delivered selected talks. With a strong foundation in experimental design and a passion for interdisciplinary problem-solving, Mercer looks forward to continuing a career at the interface of plasma technology and sustainable innovation.

Education

- Ph.D. Chemistry, University of Antwerp
- M.S. Chemistry, University of Antwerp
- B.S. Chemistry, ACS, Florida Atlantic University
- A.S. Chemistry, Miami Dade College

Skill Highlight

- Experimental Expertise: Developed and optimized cutting-edge microwave plasma processes for CO₂ conversion and Dry Reforming of Methane, demonstrating significant improvements in conversion, energy efficiency, and product selectivity, with extensive hands-on experience in advanced diagnostic techniques and process design.
- Collaboration: Built international and interdisciplinary partnerships, including projects with the European Space Agency and the Dutch Institute for Fundamental Energy Research, advancing plasma-based gas conversion using microwave discharges and driving innovation in carbon utilization technologies.
- Networking and Leadership: Established and led initiatives like the Antwerp-Mastricht Plasma Symposium, fostering collaboration among over 40 global researchers and expanding academic networks to strengthen the industrial and scientific impact of plasma-based environmental solutions.

Publications

Journal Articles

• E.R. Mercer, M. Albrechts, R. De Meyer, I. Fedirchyk, E. Morais, S. Bals and A. Bogaerts "Dual Injection in a CO₂ Microwave Plasma: Exploring Post-Plasma Quenching with CH₄ and Comparison with DRM" (Submitted Manuscript)

- E.R. Mercer* and C.F.A.M. Van Deursen*, W. Bongers, F. Smits, F. Peeters, M.C.M. Van de Sanden** and A. Bogaerts** "Preheating Applied on a 915 MHz CO₂ Microwave Plasma: Unlocking the Potential for Heat Recycling in Plasma Systems" (Submitted Manuscript)
- S. Kelly* and E.R. Mercer*, Y. Gorbanev, I. Fedirchyk, C. Verheyen, K. Werner, P. Pullumbi, A. Cowley, and A. Bogaerts "Plasma-based Conversion of Martian Atmosphere into Life-Sustaining Chemicals: the Benefits of Utilizing Martian Ambient Pressure" J. CO₂ Util., vol. 80, 2024, p. 102668, https://doi.org/10.1016/j.jcou.2024.102668
- S. Kelly, E.R. Mercer, R. De Meyer, R.G. Ciocarlan, S. Bals, and A. Bogaerts, "Microwave Plasma-based Dry Reforming of Methane: Reaction Performance and Carbon Formation" *J. CO*₂ *Util.*, vol. 75, p. 102564, 2023, https://doi.org/10.1016/j.jcou.2023.102564
- E.R. Mercer* and S. Van Alphen*, C.F.A.M. van Deursen, T.W.H. Righart, W. Bongers, R. Snyders, A. Bogaerts, M.C.M. van de Sanden, and F.J.J. Peeters "Postplasma Quenching to Improve Conversion and Energy Efficiency in a CO₂ Microwave Plasma" Fuel, vol. 334, p. 126734, 2023, https://doi.org/10.1016/j.fuel. 2022.126734
- G. Raposo, A.W. van de Steeg, E.R. Mercer, C.F.A.M. van Deursen, H.J.L. Hendrickx, W.A. Bongers, G.J. van Rooij, M.C.M. van de Sanden, and F.J.J. Peeters "Flame Bands: CO + O Chemiluminescence as a Measure of Gas Temperature"
 J. Phys. D. Appl. Phys., vol. 54, p.374005, 2021, https://doi.org/10.1088/1361-6463/ac0924

• D.M. Beckwith, F.G. FitzGerald, M.C. Rodriguez Benavente, E.R. Mercer, A.K. Ludwig, M. Michalak, H. Kaltner, J. Kopitz, H.J. Gabius, & M. Cudic "Calorimetric Analysis of the Interplay between Synthetic Tn Antigen-Presenting MUC1 Glycopeptides and Human Macrophage Galactose-Type Lectin," *Biochemistry*, vol. 60(7), p. 547–558, 2021, https://doi.org/10.1021/acs.biochem.0c00942

Conference Contributions

Oral Presentations

Gordon Research Conference, Plasma Processing Science - Andover, New Hampshire
 Selected Speaker, Title: "Preheating in 915 MHz CO₂ Microwave Plasma: Unlocking the Potential for Heat Recycling in Plasma Systems" (2024)

- Antwerp-Maastricht Plasma Symposium University of Maastricht
 Organizer, Plasma-based Gas Conversion, Experimental and Computational Insights (2024)
- CAPTURE Days Vrije Universiteit Brussel
 Oral Presentation, Title: "Preheating in 915 MHz CO₂ Microwave Plasma: Unlocking the Potential for Heat Recycling in Plasma Systems" (2023)
- Antwerp-Maastricht Plasma Symposium University of Antwerp
 Organizer and Presenter, Title: "Plasma-assisted Dry Reforming of Methane in a
 2.45 GHz Microwave Reactor: Improving Conversion and Reactor Design" (2023)
- Unconventional Catalysts, Reactors, and Applications Warwick, United Kingdom Oral Presentation, Title: "Post-Plasma Quenching to Improve Conversion in a CO₂ Microwave Plasma" (2022)
- Hakone XVII, International Symposium on High-Pressure Low-Temperature Plasma
 Oral Presentation, Title: "Post-Plasma Quenching to Improve Conversion in a CO₂
 Microwave Plasma" (2022)
- Life Sciences South Florida STEM Undergraduate Research Symposium Florida International University
 - Oral Presentation, Title: "Synthesis of Glycosylated Building Blocks Bearing Tumor-Associated Carbohydrate Antigens" (2018)
- Undergraduate Research and Inquiry Symposium Florida Atlantic University
 Oral Presentation, Title: "Synthesis of Glycosylated Building Blocks Bearing Tumor-Associated Carbohydrate Antigens" (2017)

Poster Presentations

• European First Year Experience Conference, Future First-Year Students

Poster Presentation, Title: "Navigating Together: a Buddy Programme for International Students at UAntwerp" (2025)

- Gordon Research Conference, Plasma Processing Science Andover, New Hampshire
 Poster Presentation, Title: "Preheating in 915 MHz CO₂ Microwave Plasma: Unlocking the Potential for Heat Recycling in Plasma Systems" (2024)
- Wilhelm and Else Heraeus Seminar: Non-Equilibrium Plasmas for Sustainable Chemistry Physikzentrum Bad Honnef, Germany
 Poster Presentation, Title: "Microwave Plasma Conversion of Martian Atmosphere" (2023)
- ACS National Convention New Orleans, LA
 Poster Presentation, Title: "Synthesis of the Glycosylated Amino Acid Bearing the Thomsen Nouvelle Antigen" (2018)
- Summer Undergraduate Research Symposium Florida Atlantic University
 Poster Presentation, Title: "Synthesis of the Threonine Bearing Thomsen Nouvelle Antigen" (2017)

Grants, Scholarships, and Fellowships

- Gordon Research Conference, Recipient Select (2024)
- Wilhelm and Else Heraeus Seminar, Physikzentrum Bad Honnef (2023)
- Master's Thesis Study Grant, PSFD group, DIFFER (2021)
- Erasmus Grant, International Research Internship, DIFFER (2020)
- Travel Grant Recipient ACS National Convention, University of Florida (2018)
- Summer Undergraduate Research Fellowship, Florida Atlantic University (2017)
- Undergraduate Research Grant, Florida Atlantic University (2017)

Community Building and Networking

Antwerp-Maastricht Plasma Symposium (AMPS)

Initiator and Organizer

Collaboration between PLASMANT and Circular Chemical Engineering Labs

Conceptualized and led AMPS to enable cross-institutional knowledge exchange on plasmabased gas conversion. Curated expert-led sessions, organized lab tours, and facilitated interactive discussions to advance collaborative research in sustainable plasma applications. This annual event facilitates networking among researchers and promotes advances in plasma-based environmental solutions.

Belgian Buddy Project

Founder and Coordinator

University of Antwerp, Faculty of Science

Initiated and led the Belgian Buddy Project to support international students' integration into the Master of Chemistry program. Organized and facilitated mentorship pairs between Belgian and international students, offering academic and cultural acclimation guidance. Developed social activities and structured support networks, which, as of 2024, will lead to an extended implementation across the entire Faculty of Science. The program will also be featured at the European First Year Experience Conference in May 2025.

Event Committee

Founder and Organizer

University of Antwerp, PLASMANT Group

Established and led the Event Committee to promote team building and strengthen connections within the PLASMANT group. Organized and headed activities and events designed to enhance collaboration, foster team spirit, and facilitate a supportive research community.

Acknowledgements

This is the end of a very big chapter of my life, one that took me 17 years to write. Looking back, I can now say how truly special it is to finally see so much of the trials and passion of ones life and work bound together. They say the journey of a thousand miles begins with a single step, but they forget to say that such a journey can never be walked alone. So, to all the people who helped shape my life and career, I acknowledge and extend my deepest gratitude to you.

Professor Eduardo Veliz, you provided me with my first real research experience in supporting my internship at the University of Miami, but more than that, you were the first person to make me feel like I belong in a lab. Your belief changed my life, and I am forever grateful.

Professor Mare Cudic, you kept your promise to help prepare me for graduate school, and I am deeply grateful. Thank you for the countless hours you spent guiding my writing, for trusting me to develop as an independent researcher, and for taking me on as a first-generation student when I needed mentorship most. The skills and confidence you helped me build over those formative years during my bachelor's have carried me through my doctoral program. Without your early guidance and belief in me, I would not have been equipped to successfully navigate my Ph.D. journey.

Professor Spyros Magliveras, you spent a semester sharing your passion for mathematics and for guiding me through the theoretical framework of group theory. I will always fondly remember the afternoons spent in your office toiling away over subgroups and cosets, and I feel forever honored for the time you gifted me.

Professor Richard van de Sanden, you gave me the opportunity to work at DIFFER. The first day walking into the institute was a dream come true for me, and I continue to feel that way every time I visit. Thank you for funding the opportunity for me to come back to DIFFER for my master's thesis, and for inviting me back to complete the preheating project, which made it into this very thesis. Thank you for your unwavering support and reminders that research is about solving your way around the challenges and is better done with a smile.

Professor Annemie Bogaerts, thank you for encouraging me to come to Antwerp for my master's degree and for helping me secure that first Erasmus research internship at DIF-FER, which launched my career in plasma physics and chemistry. I am deeply grateful that you served as my promoter, supported my master's thesis at DIFFER, and most importantly, funded my Ph.D. research, which has allowed me to fulfill what once seemed like an impossible dream. You gave me the autonomy to explore and guide my own research, which helped me develop my expertise and grow as a scientist. Thank you for supporting my extracurricular passions, like the symposium and event committee, which made my experience all the richer. I especially appreciate how you shared in my excitement when experiments went right and were always ready for a quick chat when things weren't going as planned. Your quick email replies, often with a word of encouragement or a small anecdote, came exactly when I needed them most. Thank you for the countless hours you dedicated to helping me edit the work that comprises this thesis and beyond. In the end, this has been such an exciting project and journey, and I am grateful for the entire experience and all the connections you helped me build.

To the entire PLASMANT crew (past and present), it has been one heck of a ride! From Toasty Tuesdays to Teambuilding's, thank you for always making the experience one to remember. To the entire experimentalist team, you rock. It has been an honor to work alongside you. To the Event Committee, and especially to the co-founder Callie, and the OG's Robin and Stein, we had such fun coming up with activities. Thank you for reining me in when I need it most, and indulging some of the more fun ideas, even if they turned out to be THE MOST WORK. I had so much fun planning with you and helping to make PLASMANT a great place to work. Of course, to Lisa, Sara, Helder, Cedric, Rubén, and Mac, I really appreciated the opportunity to get to know you better, even after I transitioned to an 'advisory' position. I hope you continue the work that may on the surface seem frivolous, but that helps to build stronger bonds among colleagues and facilitates greater corporation, which is, in the end, the best way to do science.

To my office mates, old and new, *Pepijn*, *Robin*, *Sara*, and *Priyanka*. I really enjoyed those early days together. I loved our office chair sit sessions, laughing and enjoying those fleeting moments between our research, especially in the first phase of our respective Ph.D. journeys. I will cherish those memories. To *Callie*, *Joran*, and *Mac-Attack*, I loved all our office chats and walks, and koffiekoeken afternoons with tea. A highlight was of course,

our pizza and paint night. Further to those who left before me, *Eline*, *Elise*, *Joachim*, for being amazing people to chat and share space with.

In addition, I must acknowledge the unwavering support of fellow researchers who were instrumental in helping with the work that makes up this thesis and beyond. To Sean for mentoring me when I first came aboard. Especially for including me in the ESA project, which has been a highlight of my career. I am so grateful for the opportunity you provided and that we have been able to stay in touch even after you left PLASMANT officially. I appreciate all your sage advice and always looking out for me. To Senne, for being a mentor when I first started my Ph.D., especially during the COVID lockdown, I am grateful for all the support you gave. To Igor, thank you for always being so supportive and kind to me. I found our afternoons spent in the lab to be fun and fruitful. I extend my deep appreciation to Robin for always lending a hand in the lab and for all the work that led to two papers together. To the invaluable Bart, thank you for always being an excellent lab buddy and for helping me through both personal and experimental challenges. Thank you to Colin for all of the quips and laughs, I had a blast working on the cyclone separator together. To Matthias, I really enjoyed working with you of the dual injection paper, as well as our interesting discussions and problem solving. Thank you as well to Stein for double-checking calculations, I always enjoyed brainstorming bike rides home. To my first 'Belgian Buddy', Vojta, thank you for your tremendous help with thesis edits and support with Overleaf.

I also extend my deep appreciation to Floran for being such a special mentor to me throughout my master's and Ph.D. journey. It is difficult to summarize in a small acknowledgment all that you did to shape my journey. It was always inspiring to chat with you and to problem solve together. I certainly wouldn't have had such a rich experience without your guidance and support. It really means the world to me. Beyond work, the friendship we have developed with the whole 'PTSD group' is so special. To Tim, Bram, Qin, and Cas, you are such amazing friends, and I feel so lucky to have people I can 'shoot the science' with. My journey has been made all the better by your presence in my life. To Tim-Bits, I loved shaping AMPS with you, working to build a stronger collaboration between our teams, it has been an honor to continue not only our friendship, but also our related work. We rock. To Casolita, we have really experienced the Ph.D. journey together. You have been my constant comrade since my master's, and I don't know what I would have done without you. Collaborating with you throughout the preheating project

was truly an honor. I enjoyed the many hours we spent discussing, problem solving, and tag-teaming the mountain of data from our experiments. We did something amazing there, and all our hard work paid off in the end!

To Waldo, Martijn, Aron, Jordy, George, Edwin, Ashley, Lex, Xingyu and the countless others at DIFFER (past and present) who impacted my journey and helped me develop as a researcher, I must extend my sincere gratitude for your active support throughout this journey. Your curiosity and passion were infectious and inspiring, and I will forever be grateful for the opportunity to work with you as esteemed colleagues. It was truly an honor. To Waldo, the official 'Microwave Guru', thank you for sharing your passion for microwave engineering with me and for always being willing to help when I needed you most. Special thanks as well go to Martijn and Aron, whose expertise and assistance were invaluable. I am equally grateful to the electrical department and drawing room staff for their technical guidance and creative solutions that helped overcome numerous challenges. I would also like to express appreciation to the machine shop for their extraordinary craftsmanship, precision, and dedication. Finally, I thank our academic collaborators and the leadership at DIFFER, especially to Richard, for fostering an environment that encourages innovation and interdisciplinary research in the field of plasma physics and sustainable energy technologies.

Furthermore, I extend my sincere gratitude to the machine shop at UAntwerpen, especially Gilles and Eddie, whose exceptional craftsmanship and technical expertise were instrumental in bringing my experimental designs to life. Your precision, innovation, and dedication in fabricating the custom components were vital to the success of my research project. I also always enjoyed visiting you and chatting for a bit in the afternoon or awing over a new piece you were working on. Thank you for always being helpful and kind to me. To the entire ATP team, Priyanka, Herman, Karen, Karel, Arne, and Luc, thank you for always helping me whenever I needed it. You support was integral to my work and I really appreciate you. A special thanks to Herman for ensuring I didn't blow up the lab, to Karel for helping me rip out the madness in the small lab and making it a safer working environment, and to Karen and Priyanka for always being available to listen or help solve a problem.

I must also extend my sincere appreciate to *Hamid* (and the unofficial member of PLAS-MANT, *Shooka*) for your sage wisdom and kindness. Thank you to *Omar* for fun, laughter

filled rides to Eindhoven, as well as being my 'partner in crime' on my T.K. Maxx adventuring. To *Helder* for being an excellent master's student. I am so proud of you for continuing your educational journey in the Ph.D. To *Greg* for your willingness to help in whatever the endeavor was. To *Eduardo*, my work bestie, you inspire me with your endless energy and optimism. Keep it up. Shout out to the G&G.

I extend love and appreciation to the entire *Donnelly & Strain Clan* for always being excited with us, even when it meant we had to be separated by an ocean and six time zones, you supported us with such love and thoughtfulness, which gave us the strength and courage we needed to embark on this crazy journey. It has sometimes been lonely these past six years, with COVID and the separation of time, but you always found a way to ease the pang with a long phone call or an unhinged meme in the family group chat. To my *Mum*, I know you may not have always understood the path I chose, but you always supported me in the best way you knew how. To my brother *Michael* for loving me as I am. To *Sofie*, I thank you for helping me develop the tools to trudge through the journey in becoming my best self.

To my heart, *Chase*, what to say to the man who has helped me achieve my dreams with unwavering support and love. A few lines are not enough to share the million ways you have helped me. Thank you for reading over a thousand drafts, for holding my hand when things were rough, for keeping me alive as I toiled away at my computer for more hours at a time than was healthy, and for being silly with me while dancing the anxiety away. Your encouragement has meant everything and has given me the safety and strength to continue, even when things felt impossible. This journey through our Ph.D.'s has been the greatest adventure (although, who thought this was a good idea!?). But, we made it! And what an incredible time it has been. The memories we have of this unique period of our lives are complex, but they brim with love and laughter, bittersweet in the wind. I cannot wait to see what this next chapter will bring.

Finally, to *Gobbie*, although you are no longer bound to body, I carry you with me in my heart. It was your voice that I heard on the darkest of days when things seemed impossible. You loved us so much and wanted us to live in a world of opportunity. Even if others did not see the value in that, you did. You planted the seed that punched through the earth when all has burned, a fire poppy growing on a barren landscape. A free canvas to build a life I could have never dreamed of. Thank you.

